SAINT-PETERSBURG STATE UNIVERSITY

Printed as a manuscript

Rybkin Artem Gennadievich

Synthesis and electron spin structure of quasi-two-dimensional systems with a combination of spin-orbit and magnetic exchange interactions

Scientific specialty: 1.3.8. Condensed matter physics

submitted in conformity with the requirements
for the degree of doctor of physico-mathematical sciences

Translation from Russian

Scientific consultant:
doctor of physico-mathematical sciences,
professor
Shikin Alexander Mikhailovich

Saint-Petersburg — 2024

Contents

Page

Page

Introduction

Relevance. Spintronics or spin-transport electronics is a field of science and technology dealing with the study of the electron's intrinsic spin and its use along with the electron charge in solid-state electronic devices for information storage, processing and transmission. The first successes in spintronics are connected with the discovery of oscillating long-range magnetic interaction in metallic multilayer structures and its application in devices based on the effect of giant magnetoresistance, in magnetoresistive reading heads of hard disks and in magnetoresistive random-access memory cells. The main element of these devices is a quantum electron well, i.e. a quasi-two-dimensional system representing an ultrathin layer of material in which electrons are restricted in movement perpendicular to the layer due to quantization of the electronic structure. It is well known that the magnetic properties of layered systems with alternating layers of magnetic and noble metals strongly depend on the thickness of the noble metal layers and quantum-dimensional effects observed in these layers [24–28]. In the described devices, the boundary layers of the quantum well are ferromagnetic, which induce spin polarization of the electronic states inside the well due to the exchange interaction and the Pauli exclusion principle. In [29], Co/Cu/Co multilayer structures were investigated and it was found that the magnetic interaction between Co layers has a periodic and oscillating character between antiferromagnetic and ferromagnetic depending on the thickness of the Cu layer (d_{Cu}). The antiferromagnetic coupling strength has the dependence $\sim 1/d_{Cu}^2$ which coincides with that predicted in the case of the Ruderman-Kittel-Kasuya-Yoshida interaction via conduction electrons (RKKY interaction). On the other hand, in the work [25], the spin polarization at the Fermi level of quantum well states (QWS) of sp character in the Cu layer had the same periodicity with film thickness as the magnetic interaction oscillations. Thus, the effect of giant magnetoresistance is related to the formation of QWS in quasi-two-dimensional layers of nonmagnetic materials that mediate the magnetic interaction between bordering layers of magnetic metals.

Further development of spintronics has followed the path of using spin-polarized currents for data storage and processing, because in addition to increasing energy efficiency there is an increase in the speed of such devices [30; 31]. To generate spin currents, spin injection from ferromagnetics into semiconductors [32] has been intensively studied, but the interfaces between these materials have a significant

drawback due to the conductivity mismatch problem, which is solved by using ultrathin dielectric layers between them [33]. Another direction is the generation of spin currents without the use of ferromagnetic materials and external magnetic fields, but using spin-orbit interaction. The spin-orbit interaction induced by an electric field at a two-dimensional interface, the so-called Rashba effect, was originally studied in semiconductor heterostructures [34—36]. Active development of new methods of synthesis and diagnostics of epitaxial quasi-two-dimensional materials under ultrahigh vacuum conditions in the late 1990s allowed to continue studies of spin-orbit interaction in ultrathin layers of light and noble metals on the surfaces of single crystals [37—40]. The study of mechanisms and peculiarities of the process of formation of hybridized electronic states in quasi-two-dimensional materials is still relevant today, as it opens new opportunities for spin control in low-dimensional systems. Especially important is the enhancement of spin-orbit interaction [41; 42] for the observation of such effects as spin Hall effect [43], Rashba-Edelstein effect [44], spin-orbit torque effect [45], quantum spin [46] and anomalous [47] Hall effects (QSHE and QAHE), for observations of Majorana [48] fermions and other fundamental effects. All these effects will certainly find their application in electronics both in the creation of memory elements and logic elements in the existing architecture of computing devices, and in the creation of a completely new architecture of quantum computers and post-silicon electronics. Topological insulators (TI) and graphene-based systems are promising materials for the realization of such effects. Nobel Prizes in Physics in 2010[1] and 2016[2] noted the high significance of the study of quasi-two-dimensional electronic states in both graphene and topological insulators and their promising potential for use in new energy-efficient and fast electronic devices of post-silicon electronics.

Topological insulators – a class of crystalline materials characterized by insulating properties in the bulk but having conductive topological surface states (TSS) with helical Dirac cone spin texture. In these materials, effective generation of spin-polarized currents is possible [49—56]. At the same time, TIs are characterized by a significant ratio between the generated surface spin-polarized currents and the accompanying bulk charge currents [57; 58]. The doping of TIs with magnetic elements can open the energy band gap at the Dirac point, allowing the observation

[1] for groundbreaking experiments regarding the two-dimensional material graphene, awarded to A. Geim and K. Novoselov

[2] for theoretical discoveries of topological phase transitions and topological phases of matter, awarded to D. Thouless, D. Haldane, and M. Kosterlitz

of the quantum anomalous Hall effect [47; 50; 59–61]. Undoubtedly, TIs have high potential for application in spintronics devices and quantum computing [62–64], especially when the Fermi level and Dirac point of TIs are located inside the fundamental band gap.

The discovery of the unique electrical characteristics of graphene (a two-dimensional crystal consisting of a single layer of carbon atoms arranged in the nodes of a hexagonal lattice) has led to an even more active development of a new field of electronics - nanoelectronics, which uses quantum-dimensional effects to operate devices. The use of different characteristics of electronic states for information transfer in quasi-two-dimensional materials has formed a number of directions: spintronics [31] and spin-orbitronics [65], focused on controlling the spin and angular momentum of the electron; valleytronics [66], using local minima of the band structure (valleys) as an effective degree of freedom; 2D topological electronics or topotronics [67], based on the use of topological properties of the band structure of materials, topological superconductors and insulators.

To date, materials and products based on single-layer and multilayer graphene in various forms (e.g., powder, solution, paste, nanoplatelets, functionalized graphene) have already been sold worldwide [68; 69]: graphene-based inks and flexible electronics [70; 71], brake pads with graphene inclusions that improve heat dissipation and increase durability [72], bicycle tires [73], graphene Hall sensors [74], lubricants based on graphene nanocomposites to reduce friction and wear [75], graphene-coated safety helmets, detectors in the visible and infrared spectral range [76], batteries for portable electronic devices and unmanned devices [77], rubber-based materials, packaging with electrostatic protection, cooling systems for electronic chips, audio headphones with graphene membranes [78], lighting devices and many others. The success of utilizing graphene in performance-enhanced consumer products depends primarily on production capacity. Industrial graphene production setups are already being sold worldwide, which is a good basis for launching large-scale production of graphene-based materials and goods.

In recent biological research, graphene is already being used as electrodes in transparent neural implants designed to record and modulate neural activity in order to treat damaged nervous systems [79]. A dense set of small graphene implant electrodes as small as 20 μm is known to simultaneously record electrical and calcium activity in deep layers of the brain [80]. In this study, nitric acid-doped bilayer graphene showed lower ohmic resistance and better mechanical stability than single-

layer graphene. At the same time, the graphene channels were made without using gold, which eliminated artifacts in two-photon calcium imaging measurements. The use of graphene in biomedical research as an electrically conductive channel material is actively expanding due to its optical transparency, flexibility and high electrical conductivity.

Despite the fact that graphene is used in many fields of science and technology, the potential of graphene in micro- and nanoelectronics has not been fully realized. In this regard, the study of graphene and other two-dimensional materials for the purpose of their application in electronic devices is relevant [62; 81–85], as it will not only improve the characteristics of existing devices, but also create a whole direction of post-silicon electronics based on new physical phenomena and laws. In order to use graphene as an active element of electronics, it is necessary to learn how to control its electronic properties. Synthesis of epitaxial structures based on graphene and other two-dimensional materials will allow to obtain new, previously unknown, topological states of matter. Control of spin structure in graphene, i.e. spin splitting of its electronic states and topologically nontrivial band gap in the Dirac point, is one of the most important problems of materials science today, which must be solved for the use of graphene in spintronics and topotronics, especially for the realization of dissipative-free transport. It is known that strong spin-orbit interaction is necessary condition for the observation of effects such as quantum spin Hall effect [86], quantum anomalous Hall effect [87], etc. The second factor affecting the spin structure is the exchange interaction in graphene. In this regard, theoretical and experimental studies of possible magnetic order in two-dimensional carbon systems, such as superatomic graphene [88], triangulene [89], nanographene [90], etc., have attracted special attention. The experimentally unrealized Haldane model based on a graphene lattice with inhomogeneous magnetic field distribution at the atomic scale [91] remains relevant and attractive because it predicts QAHE in a hexagonal two-dimensional lattice. On the other hand, topological edge states have already been demonstrated in germanene [92], which shows that it is fundamentally possible to obtain the QSHE phase in graphene as well as in other 2D structures with hexagonal lattice.

Of great importance is the magnetic proximity effect, which is a promising way to realize the exchange splitting of electronic states [87] without the application of an external magnetic field, which can also be used to realize QAHE, provided that the topological nontriviality of electronic states is preserved. Previously, it was shown

that the contact of graphene with antiferromagnetic oxide can lead to the occurrence of QAHE or quantum valley Hall effect (QVHE) depending on the direction of magnetization [93].

Recent publications on the synthesis of epitaxial graphene by the “face-to-face” method on SiC single crystal show the importance of semiconducting, well-ordered, defect-free graphene in the transition from silicon to graphene electronics [94; 95]. The presence of a 0.6 eV band gap without any localized states inside it, which were previously observed for samples synthesized by the conventional method of thermal decomposition of Si-terminated surface, is shown. Moreover, the zero carbon layer can be grown on both SiC single crystal and 3C-SiC(111) thin layers on Si(111) [96] single crystal. The use of SiC nanofine layers can become the basis of integrated circuits, complementing or replacing silicon elements.

Epitaxial synthesis of nanosystems based on graphene and SiC substrate is still an urgent topic for the scientific community. A large number of works are devoted to fundamental studies of graphene on metal substrates, on which it is difficult to realize quantum effects in spintronics devices and quantum computers due to the electrical shunting of the device metal substrate. Recent publications show the possibility of intercalating and obtaining semiconducting gold under graphene on SiC [97], and measurements of the spin Hall effect in the intercalated Gr/Pb/Au [98] system. Other works report induced superconductivity in graphene in contact with superconductor [99; 100]. Thus, the possibility of intercalation of the zero-layer graphene on SiC, on the one hand, and the observed quantum effects in graphene-based systems using its transfer to a dielectric substrate, on the other hand, indicate the necessity of solving problems on synthesis and investigation of epitaxial layered nanosystems based on graphene and SiC substrate.

Other interesting direction is the use of graphene as an auxiliary material for the synthesis of nanoscale systems by intercalation of atoms under graphene. It is known that chains of magnetic atoms with either strong spin-orbit coupling or spiral magnetic order that interact with superconducting substrates can contain topologically nontrivial Majorana bound states [101]. On the other hand, ultrathin layers of magnetic and heavy metals are still the object of active research. A recent study of a system with two iron monolayers on a tungsten single crystal has shown that the system is a 2D topological magnet [102]. Due to the fact that the atoms on the surface of the above systems are susceptible to oxidation upon exposure to the atmosphere, it is significant to synthesize topological systems with heavy and magnetic metals

directly under the graphene. In this case, graphene can play the role of a protective layer during atmospheric exposure and prevent oxidation of underlying layers, which was previously demonstrated for individual intercalated layers of noble and magnetic metals in the publications [103; 104].

The great potential of the investigated low-dimensional systems lies in the possibility of electrical switching of magnetization via spin-orbit torque, which can be successfully used in the design of fast, energy-efficient, non-volatile high-density magnetic memory. Recently, tremendous efforts have been made to investigate magnetization switching in van der Waals systems with large spin-orbit interaction [45].

The goal of this thesis was to develop the fundamentals and practical approaches for the formation of high-quality systems based on new quasi-two-dimensional materials that maximize the unique properties providing a joint enhancement of spin-orbit and magnetic exchange interactions and, as a consequence, exhibit effects suitable for practical use in modern spintronics.

To achieve this goal, the following main **tasks** were formulated and resolved:

1. Study of spin-dependent quantum-dimensional effects on the example of ultrathin metal layers, study of the influence of a substrate with strong spin-orbit interaction on the electronic structure of thin metal layers.
2. Investigation of semiconductor materials and topological insulators with strong spin-orbit interaction. Determination of the influence of magnetic impurities on the electronic structure. Investigation of the effects of laser radiation interaction with topological insulators.
3. Development of synthesis methods and study of epitaxial graphene on ultrathin single-crystal layers of metals with strong spin-orbit and exchange interactions. Investigation of the influence of strong spin-orbit and exchange interactions on the electronic structure of graphene. Determination of parameters of spin-orbit and exchange interactions in graphene to characterise its topological properties.
4. Development of synthesis methods and study of epitaxial graphene on silicon carbide semiconductor substrate. Study of the possibility of spin-orbit interaction enhancement in graphene/metal/SiC systems.
5. Development of device models based on new low-dimensional materials for spintronics and nanoelectronics applications.

Scientific novelty. The work contains a large number of new experimental and theoretical results and formulated scientific conclusions based on them. The most important of them are summarised below:

1. Spin-resolved photoelectron spectroscopy studies of the pure W(110) surface and ultrathin Al and Au layers on W(110) have been carried out. Spin-polarized surface resonances with linear dispersion and spin structure characteristic of topological surface states were detected on the W(110) surface [3; 105]. For thin layers of Al and Au on W(110), the effects of hybridization between quantum well states localized in the metal layer and interface states at the boundary with the substrate, bulk states of the substrate, surface states of the layer are investigated. The possibility of transferring the strong spin-orbit interaction of the substrate to quantum well states in an ultrathin Al layer up to 15 monolayer is shown [1; 2].
2. Systematic studies of spin splitting of electronic states of graphene on ferromagnetics and nonmagnetic sp and d metals have been carried out [12–15]. The effect of giant Rashba splitting in graphene on Au monolayer, incomplete Pt monolayer and on Pt(111) substrate is found, absolutely not achievable earlier in isolated graphene. At contact of graphene with metals with high atomic numbers (Au, Pt) in contrast to metals with significantly lower atomic numbers (Co, Ni, Cu) the effect of induced spin polarization of graphene states is observed. It is shown that this effect is due to the formation of hybrid bonds between π states of graphene and d states of heavy metal and can be successfully used in the design of spin devices, in particular, with the participation of the candidate proposed and patented design of graphene spin filter [20].
3. Magnetically doped ternary topological insulators were investigated by pump-probe method [17] and a 2D photoelectric effect, the magnitude of which depends on the location of the Dirac point relative to the Fermi level and the edge of the valence band, was revealed.
4. A systematic study of magnetically doped BiTeI semiconductors with different concentrations of magnetic impurities [19] made it possible to identify the influence of magnetic impurities on the magnetic and electronic properties of the materials under study. It was shown that the variation of the band gap with increasing concentration is non-monotonic.

5. A new approach to the synthesis of epitaxial nanothin Pt_5Gd alloy via intercalation under graphene has been developed [5]. Nanothin epitaxial Pt_xGd alloys on the surface of Pt(111) single crystal coated with well-oriented graphene were synthesized, and the electronic and atomic structures at different synthesis stages were investigated. It is shown that the alloy has a thickness of about 3 nm and is terminated by a Pt layer under the graphene. According to scanning tunnelling microscopy data, the top layer of the alloy has a “kagome” structure, and moreover, a moiré pattern between the nanothin alloy and the Pt(111) single crystal is observed. Controlling the doping of graphene through changing the stoichiometry of the alloy opens new possibilities in the development of modern electronics. Due to the well-known catalytic activity of the Pt_5Gd alloy, the synthesized thin film system is promising for the production of catalysts.
6. A model of graphene information recording device for magnetoresistive random-access memory SOT-MRAM (magnetoresistive RAM that uses spin-orbit interaction to switch magnetic states for data storage) has been developed [5; 21]. The principle of recording information in SOT-MRAM is based on passing an electric current through a material with a strong spin-orbit interaction to generate a spin current and realize the spin-orbit torque effect.
7. Well-oriented single-domain graphene on Co(0001) was synthesized by chemical vapor deposition method [16]. Previously, it was only possible to synthesize graphene with multidomain crystal structure, in which the unique electronic structure in the form of Dirac mini-cone is not observed. This result is not only of fundamental importance, but also of applied significance for spintronics, since a record high spin polarization of the states of the graphene/ferromagnet interface was demonstrated for a single-domain system.
8. Magneto-spin-orbit graphene on a metal substrate has been synthesized and investigated [4; 6]. The technique for synthesizing single-domain graphene on Co(0001) made it possible to create a new material – magneto-spin-orbit graphene, and to impart to it the properties of cobalt and gold – magnetism and spin-orbit interaction. It is shown that magnetization of the cobalt substrate leads to asymmetric spin splitting of graphene states in opposite $\overline{K}$ points of the graphene Brillouin zone. The study of the surface by

scanning tunnelling microscopy revealed the formation of loop dislocations at the boundary between the intercalated gold monolayer and the cobalt layer with the formation of single cobalt atoms and clusters under the graphene, which leads to its magnetization.

9. The ferrimagnetic ordering on two sublattices of magneto-spin-orbit graphene was found and the electro-optical effect of the Hall voltage appearance of different polarity depending on the direction of circular polarization of the incident radiation was predicted; a device for direct detection of circularly polarized radiation in the mid-IR range was developed [6; 22]. Spin-polarized Dirac-like states at the $\overline{\Gamma}$ point near the Fermi level have been detected both for a system with a monolayer of Au on the surface of a Co(0001) thin film and for a similar system with ferrimagnetic graphene on the surface. It is found that these states are characteristic of ferrimagnetic ordering in the Au monolayer and possess strong linear magnetic dichroism.
10. To implement magneto-spin-orbit graphene on a non-metallic substrate, the candidate worked out a technique for synthesizing a zero (buffer) layer of graphene on a 6H-SiC(0001) substrate and studied its electronic structure in a wide energy range using theoretical and experimental methods [8–10]. A comprehensive study of the intercalation of noble metal Pt and magnetic metal Co atoms under the zero layer of graphene on SiC(0001) has been carried out. It is shown that the intercalation of Pt or Co atoms leads to the transformation of the zero layer into a graphene monolayer. The intercalation of Co results in the formation of quasi-freestanding monolayer graphene on a magnetic ultrathin layer of cobalt silicides with $CoSi/CoSi_2$ stoichiometry. The ferromagnetic ordering of magnetic moments in the surface plane of the synthesized system was found to be due to the CoSi layer under the graphene. Thus, quasi-freestanding graphene was synthesized, which is in contact with the magnetic substrate and retains the electronic structure in the form of a Dirac cone in the region of the $\overline{K}$ point. As a result of Pt intercalation, a Rashba-type spin-orbit splitting of π electronic states, anomalously high for isolated graphene and previously experimentally unattainable in graphene systems, was found. The obtained results are the basis for further implementation of magneto-spin-orbit graphene on

a semiconductor substrate and are important for the future application of graphene in spintronics.

Practical significance. The obtained results and developed methods of synthesis of graphene-based systems in contact with magnetic and noble metals, leading to its functionalization and modification of its properties, can be successfully used for effective application in nanoelectronics and spintronics. Based on the scientific research conducted with the participation of the author, 3 patents of the Russian Federation for inventions were received [20–22].

Models of electronic devices based on graphene and its contact with heavy metals (Au and Pt) have been developed: an improved graphene spin filter and an information recording device for spin-orbit torque magnetoresistive random-access memory (SOT-MRAM) operating without the use of an external magnetic field. The developed model of the graphene spin filter device [20] is designed to form groups of polarized electrons with a given spin orientation in solid-state electronics devices, as well as the selection and separation of such electrons. Such devices allowing manipulation of spin-polarized electrons can be used as information processing and transmission tools. Another promising application of graphene has been reflected in an information recording device for SOT-MRAM [21], where graphene and metal monolayers are proposed to be used, which enhance the spin-orbit interaction in graphene and significantly improve the performance of the RAM storage cell. The thermal stability of the system under real conditions is demonstrated [18], which is a standard requirement for CMOS storage systems. On the basis of ferrimagnetic graphene in its contact with heavy and magnetic metals, a device for direct detection of circularly polarized radiation in the mid-infrared range [22] has been developed. The invention can be used in the field of optoelectronics and valleytronics and is intended for use in optoelectronic integrated circuits on the micrometer scale.

The 2D photovoltaic effect in magnetically doped topological insulators studied in this work can be applied in optoelectronic logic devices or in devices for converting visible and infrared energy into electric current.

Synthesized graphene on SiC semiconductor substrate can be actively used as building blocks of post-silicon electronics microchips with improved energy efficiency and fast performance. Synthesis of graphene by intercalation on SiC thin layers on Si(111) [96] is one of the possible smooth transitions from silicon technologies to spintronics and 2D topological electronics.

Methodology and research methods. The thesis contains mainly experimental results. To investigate the atomic, crystalline and electronic energy structure of the studied systems, a whole set of modern methods and approaches was used, including those realized at megascience facilities, third generation synchrotron radiation sources, a unique scientific setup “Nanolab” of the SPbSU Science Park and a number of others. Theoretical density functional theory (DFT) calculations were used to interpret the experimental results and characterize the electronic and magnetic structure of the samples. Ultrahigh vacuum conditions both during the synthesis of the systems and further measurements ensured high atomic surface purity. All synthesized systems possessed a well-ordered crystal structure, which allowed characterizing their band structure using photoelectron spectroscopy with angular resolution (ARPES). X-ray photoelectron spectroscopy (XPS) was used to analyze the elemental and chemical structure of the surface and the depth of the layers. Low-energy electron diffraction (LEED) was used to analyze the crystal structure and preliminary orientation of the samples before the ARPES measurements. Scanning tunnelling microscopy (STM) was used to investigate the surface of the samples, including with atomic resolution. The local electron energy structure was measured by scanning tunnelling spectroscopy (STS). The methods used in this work have high surface sensitivity required for studying the surface of single-crystal solids and two-dimensional quantum materials synthesized on their surface.

Validity and approbation of the results. The high degree of reliability of the results is ensured by their reproducibility in various experiments, the use of the most modern world-class equipment and the application of a wide range of complementary methods, as well as agreement with the results of theoretical calculations and with the results obtained by other authors on the basis of published articles on the subject of the thesis. The main results of the work were presented and discussed at the following Russian and international schools, seminars and conferences: First Interdisciplinary Workshop of the German-Russian Interdisciplinary Science Center “Structure and Dynamics of Matter” (Berlin, 2010), WE-Heraeus-Seminar “Rashba and related spin-orbit effects in metals” (Bad Honnef, 2010), Second Surface Science School “Technologies and measurements on Atomic Scale” (Khosta, 2012), German-Russian Conference on Fundamentals and Applications of Nanoscience (Berlin, 2012), 2014 Tenth International Vacuum Electron Sources Conference (Saint Petersburg, 2014), 22nd All-Russian Scientific and Technical Conference “Vacuum Equipment and Technologies – 2015” (Saint Petersburg, 2015), 14th International

Conference “Advanced Carbon NanoStructures” (Saint Petersburg, 2019), EMN Amsterdam Meeting 2019 on Energy Materials Nanotechnology (Amsterdam, 2019), the Fourth STEPS Symposium on Photon Science (Tokyo, 2019), the XV, XXV and XXVI International Symposium “Nanophysics and Nanoelectronics” (Nizhny Novgorod, 2011; online format, 2021 and 2022), the XXIII, XXXIV and XXXV Symposium “Modern Chemical Physics” (Shepsi, 2011, 2022, 2023), the Third Russian-Chinese Scientific and Technical Forum “High-Tech Technologies: From Science to Implementation” (Harbin, 2023), as well as at scientific seminars at MIPT and SPbU.

Personal contribution. All presented results were obtained by the author personally or in co-authorship with his direct participation. The author made a decisive contribution to the formulation of scientific problems, direct creation and commissioning of experimental facilities, conducting experiments, data processing and analysis, and preparation of research results for publication in scientific journals. A significant part of the research was carried out at the unique scientific setup “Nanolab” of the SPbSU Science Park, which was designed, assembled and put into operation with the direct participation of the author. The theoretical results were obtained in co-authorship with A. V. Eryzhenkov, A. V. Tarasov and D. Yu. Usachev; the candidate participated in the formulation of theoretical problems taking into account the measured experimental structural parameters, comparison of experimental and theoretical results, their interpretation and presentation. Preparation for publication of the obtained results was carried out jointly with co-authors, and the contribution of the candidate was either determining or weighty. Of the 23 papers on the subject of the thesis, 11 were prepared personally by the author. Author’s contribution by published works:

- publication [1] in the journal Phys. Rev. B – formulation of the experimental task (80%), experiment preparation and measurements at BESSY II synchrotron (70%), processing of experimental results and their analysis (100%), preparation of research results for publication (100%), writing the manuscript of the article and its publication (60%);
- publication [2] in the journal Phys. Rev. B – formulation of the experimental task (80%), experiment preparation and measurements at BESSY II synchrotron (70%), processing of experimental results and their analysis (100%), preparation of research results for publication (100%), writing the manuscript of the article and its publication (60%);

– publication [3] in the journal Phys. Rev. B – formulation of the experimental task (80%), experiment preparation and measurements at BESSY II synchrotron (70%), processing of experimental results and their analysis (100%), preparation of research results for publication (60%), writing the manuscript of the article and its publication (60%);
– publication [4] in the journal Nano Lett. – formulation of the experimental task (70%), experiment preparation and measurements at Nanolab setup and BESSY II synchrotron (70%), processing of experimental results and their analysis (60%), preparation of research results for publication (70%), writing the manuscript of the article and its publication (60%);
– publication [5] in the journal App. Surf. Sci. – formulation of the experimental and theoretical tasks (90%), experiment preparation and measurements at Nanolab setup, HiSOR synchrotron and OSMOS CNR-Elettra microscopy laboratory (70%), processing of experimental results and their analysis (100%), analysis of theoretical results (50%), preparation of research results for publication (80%), writing the manuscript of the article and its publication (80%);
– publication [6] in the journal Phys. Rev. Lett. – formulation of the experimental and theoretical tasks (80%), experiment preparation and measurements at Nanolab setup, BESSY II, Elettra, and HiSOR synchrotrons (80%), processing of experimental results and their analysis (100%), analysis of theoretical results (50%), preparation of research results for publication (80%), writing the manuscript of the article and its publication (80%);
– publication [7] in the journal “Pis’ma v ZhETF” – formulation of the experimental and theoretical tasks (80%), experiment preparation and measurements at Nanolab setup (80%), processing of experimental results and their analysis (100%), analysis of theoretical results (70%), preparation of research results for publication (80%), writing the manuscript of the article and its publication (80%);
– publication [8] in the journal Phys. Rev. B – formulation of the experimental and theoretical tasks (50%), experiment preparation and measurements at Univer-M setup (90%), processing of experimental results and their analysis (50%), preparation of research results for publication (50%), writing the manuscript of the article and its publication (50%);

- publication [9] in the journal FTT – formulation of the experimental task (50%), experiment preparation and measurements at Univer-M and Nanolab setups (80%), processing of experimental results and their analysis (50%), preparation of research results for publication (50%), writing the manuscript of the article and its publication (50%);
- publication [10] in the journal Symmetry – formulation of the experimental and theoretical tasks (80%), experiment preparation and measurements at Nanolab setup (80%), processing of experimental results and their analysis (70%), analysis of theoretical results (50%), preparation of research results for publication (100%), writing the manuscript of the article and its publication (70%);
- chapter [11] in the book “Quantum Structures for Post-Silicon Electronics” – formulation of the experimental task (15%), experiment preparation and measurements at BESSY II, Elettra, and HiSOR synchrotrons and at Nanolab setup (15%), processing of experimental results and their analysis (15%), preparation of research results for publication (15%), writing the manuscript of the article and its publication (15%);
- publication [12] in the journal Nat. Comm. – formulation of the experimental task (30%), experiment preparation and measurements at the BESSY II synchrotron (50%), processing of experimental results and their analysis (30%), preparation of research results for publication (30%), writing the manuscript of the article and its publication (30%);
- publication [13] in the journal Nanotechnology – formulation of the experimental task (30%), experiment preparation and measurements at BESSY II synchrotron and at Nanolab setup (40%), processing of experimental results and their analysis (30%), preparation of research results for publication (30%), writing the manuscript of the article and its publication (30%);
- publication [14] in the journal New J. Phys. – formulation of the experimental task (30%), experimental preparation and measurements at BESSY II synchrotron (60%), processing of experimental results and their analysis (60%), preparation of experimental results for publication (80%), writing the manuscript of the article and its publication (30%);
- publication [15] in the journal Phys. Rev. B – formulation of the experimental task (30%), experimental preparation and measurements at BESSY II

synchrotron (40%), processing of experimental results and their analysis (30%), writing the manuscript of the article and its publication (20%);

- publication [16] in the journal Nano Lett. – experiment preparation and measurements at Nanolab setup (60%), processing of experimental results and their analysis (20%), writing the manuscript of the article and its publication (10%);
- publication [17] in the journal 2D Materials – formulation of the experimental task (30%), experiment preparation and measurements at LASOR Center, University of Tokyo (40%), processing of experimental results and their analysis (30%), preparation of experimental results for publication (30%), writing the manuscript of the article and its publication (30%);
- publication [18] in the journal Nanotechnology – formulation of the experimental task (50%), experiment preparation and measurements at BESSY II synchrotron and Nanolab setup (40%), processing of experimental results and their analysis (50%), preparation of experimental results for publication (50%), writing the manuscript of the article and its publication (45%);
- publication [19] in the journal Sci. Rep. – formulation of the experimental task (20%), experiment preparation and measurements at BESSY II, Elettra and HiSOR synchrotrons and at Nanolab setup (30%), processing of experimental results and their analysis (20%), preparation of experimental results for publication (20%), writing the manuscript of the article and its publication (20%);
- patents [20–22] and certificate of state registration of computer program [23] - in equal shares between co-authors.

Publications. The candidate is the author of 80 printed works on the dissertation specialty in periodical scientific journals. The main results on the dissertation subject are stated in 19 printed works, of which 18 are published in periodical scientific journals indexed by Web of Science, Scopus and RINC. Three patents [20–22] and one computer program [23] have been registered.

Volume and structure of the work. The dissertation consists of an introduction, 7 chapters, a conclusion, a list of acronyms, a list of references and an author's list of publications on the dissertation subject. The full volume of the dissertation is 289 pages, including 97 figures and 4 tables. The list of references contains 560 titles.

Main scientific results.

1. Magneto-spin-orbit graphene possessing strong induced spin-orbit and exchange interactions, with n- and p-type doping of its electronic structure depending on the amount of intercalated gold under highly oriented graphene on Co(0001)/W(110) substrate. Formation of loop dislocations under graphene at the Au and Co layers boundary. The effect of asymmetric spin splitting of π electron states of magneto-spin-orbit graphene in opposite $\overline{\mathrm{K}}$ points of the Brillouin zone [4; 6; 23]. The personal contribution is at least 80%.
2. Ferrimagnetic ordering on sublattices of n-doped quasi-freestanding graphene and in the underlying gold monolayer on Co(0001)/W(110) substrate. The experimentally measured value of the band gap (80 ± 25 meV) of magnetic character in the graphene electronic structure [6; 22]. Preservation of ferrimagnetic ordering in graphene on Au/Co loop dislocations of different sizes [7]. The personal contribution is at least 80%.
3. Giant Rashba effect in graphene on Au monolayer [12—14; 20] and on Pt(111) substrate [15], not achievable earlier in freestanding graphene. The personal contribution is at least 55%.
4. Giant Rashba-type spin-orbit splitting (up to 200 meV) of π electron states of graphene obtained by intercalation of an incomplete platinum monolayer under zero layer graphene on SiC(0001) [10]. The personal contribution is at least 80%.
5. Methods of formation of highly oriented graphene at elevated temperatures by chemical vapor deposition on Co(0001)/W(110) [16] and on Pt(111) [5; 15]. The personal contribution is at least 80%.
6. Thermal stability of graphene on intercalated Au monolayer when heated to temperatures of 600 – 650 °C [18; 21]. The personal contribution is at least 80%.
7. Giant two-dimensional near-IR photovoltaic effect in a topological insulator with a high filling of the upper Dirac cone states and a Dirac point located inside the fundamental band gap [17]. The personal contribution is at least 60%.
8. Synthesis of zero layer graphene with reconstruction of $(6\sqrt{3} \times 6\sqrt{3})\mathrm{R}30^\circ + (5 \times 5)$ on Si-terminated $6H$-SiC(0001) surface by stepwise high-temperature annealing under ultrahigh vacuum conditions to

temperatures 1150 – 1170 °C [8; 9]. The personal contribution is at least 80%.

9. Synthesis of graphene on ultrathin layers of CoSi and $CoSi_2$ cobalt silicides on SiC(0001) by intercalation of cobalt atoms under zero layer graphene on SiC(0001). More efficient intercalation by adsorption of Co atoms onto the surface of the heated sample than in the case of adsorption onto the surface of the room temperature sample followed by annealing. Ferromagnetic ordering in the synthesized system [8; 9]. The personal contribution is at least 80%.
10. Synthesis of ordered nanothin epitaxial layer of Pt_5Gd alloy under graphene. Surface termination of the alloy by an atomic Pt layer with a "kagome" structure [5]. The personal contribution is at least 80%.
11. Spin polarization of surface d resonances in the W(110) pseudo-gap opened by spin-orbit interaction, their linear dispersion, and spin structure in the $\bar{\Gamma}\bar{S}$ direction of the surface Brillouin zone characteristic of topological surface states [2; 3]. The personal contribution is at least 80%.
12. Spin-dependent hybridization effects between quantum well states and interface states at the boundary of thin Al layers with W(110) substrate leading to anomalously high spin splitting of quantum well states not typical for freestanding Al layers [1; 2]. The personal contribution is at least 80%.
13. Magnetic character of the observed band gap in the electronic structure of magnetically doped BiTeI semiconductors (see the article [19] and pp. 111, 120 – 124 of the work [11]). The personal contribution is at least 60%.

Thesis statements to be defended:

1. The anomalously high value of spin splitting ($\sim$ 0.4 eV) of quantum well states in Al films (up to 15 monolayers) on W(110) is due to the spin-dependent avoided-crossing effect of dispersion dependences of interface states and quantum well states [1; 2]. The presence on the W(110) surface of spin-polarized surface resonances with a linear dispersion dependence in the $\bar{\Gamma}\bar{S}$ direction of the surface Brillouin zone and a spin structure characteristic of topological surface states [3].
2. Giant two-dimensional photovoltaic effect in the near-IR range in magnetically doped topological insulators, the magnitude of which depends on the stoichiometric composition of topological insulators and on the position of the Dirac point relative to the Fermi level and the valence band edge [17].

3. Non-monotonic variation of the Kramers point band gap and the saturation magnetization in magnetically doped BiTeI semiconductors with an increase in the concentration of magnetic atoms indicates the magnetic nature of the band gap [11; 19].
4. Synthesis methods of highly oriented graphene on Co(0001)/W(110) and Pt(111) substrates by chemical vapor deposition from propylene molecules at elevated temperatures (640 – 660 °C for Co(0001)/W(110) and 900 – 1050 °C for Pt(111)) [5; 15; 16].
5. Methodology of intercalation of gadolinium atoms under highly oriented graphene on a Pt(111) single crystal, allowing the synthesis of a nanothin epitaxial layer of Pt_5Gd alloy under graphene with control over the position of the Dirac point of graphene relative to the Fermi level [5].
6. Synthesis methods of quasi-freestanding graphene on metal and semiconductor substrates:
   – synthesis method of magneto-spin-orbit graphene with induced spin-orbit and exchange interactions by intercalation of gold atoms under graphene on Co(0001)/W(110) with asymmetric in magnitude spin splitting of π electronic states of graphene in the vicinity of the $\overline{\mathrm{K}}$ point of the Brillouin zone [4; 12–14; 18];
   – synthesis method of graphene on ultrathin layers of cobalt silicides CoSi and $CoSi_2$ on SiC(0001) by intercalation of cobalt atoms under zero-layer graphene on SiC(0001), allowing to obtain ferromagnetic ordering in the synthesized system with the maximum value of coercivity 180 Oe in the temperature range 2 – 300 K [8; 9].
7. The giant Rashba-type spin-orbit splitting (up to 200 meV) of π electron states of graphene, obtained by intercalating an incomplete platinum monolayer under a zero-layer graphene on SiC(0001), in the vicinity of the $\overline{\mathrm{K}}$ point of graphene Brillouin zone is associated with a reduction in the distance between graphene and platinum atoms for corrugated graphene [10].
8. Sublattice ferrimagnetic ordering of quasi-freestanding graphene with n-type doping and in the underlying gold monolayer on the Co(0001)/W(110) substrate leads to the opening of a band gap of magnetic character in the electronic structure of graphene and the formation of a spin-polarized state at the Au – Co boundary with conical dispersion near the Fermi level and with the effect of strong linear magnetic dichroism [6; 7; 22].

The conducted studies and the obtained results in the form of the formulated defended thesis statements contributed to the development of the direction on the synthesis of quasi-two-dimensional systems with a combination of spin-orbit and magnetic exchange interactions using two methods:

– the proximity effect between the ordered layer of light element atoms (e.g., C and Al) and the ordered layers of heavy (e.g., W, Au, and Pt) and magnetic (e.g., Ni, Co, and Gd) element atoms,

– doping of single-crystal systems with strong spin-orbit interaction (e.g., BiTeI and topological insulators) with atoms of magnetic elements (Mn, V).

This scientific and technical direction is represented by the first experimental works [106–108] to obtain graphene with a combination of induced spin-orbit and magnetic exchange interactions and is relevant for the synthesis of new spintronics materials - sources of spin-polarized currents.

1. Current state of research in the field of synthesis and control of electronic spin structure of quasi-two-dimensional systems

1.1 Spin-orbit interaction in solid state physics

The spin-orbit interaction (coupling) is a relativistic effect related to the interaction of the intrinsic mechanical momentum of a particle (spin) with its orbital momentum in the potential field. In atomic physics, the spin-orbit interaction of the electron is taken into account as a Pauli term in the non-relativistic approximation of the Dirac equation [109]:

$$H_{SO} = -\frac{\hbar}{4m_0^2c^2}\boldsymbol{\sigma} \cdot \boldsymbol{p} \times \nabla V, \tag{1.1}$$

where $\hbar$ is Planck's constant, m_0 is the mass of a free electron, c is the speed of light, $\boldsymbol{p}$ – the momentum operator, V is the Coulomb potential of the atomic nucleus, and $\boldsymbol{\sigma} = (\sigma_x, \sigma_y, \sigma_z)$ is the vector of Pauli spin matrices. In an atom, the spin-orbit coupling leads to an additional energy splitting of electron levels, to the appearance of the so-called fine structure of spectroscopic lines of the atom.

In a crystalline solid, the electronic structure is characterized by energy bands $E_n(\boldsymbol{k})$ with a band index n and a quasi-wave vector $\boldsymbol{k}$. Spin-orbit coupling has a strong influence on the structure of the energy band $E_n(\boldsymbol{k})$. In the first publications, Roger J. Elliott [110] and Gene Dresselhaus [111] noted the effect of spin-orbit interaction on the band structure of Bloch electrons. R. D. Elliott showed that if the crystal structure has inversion symmetry, there is a two-fold degeneracy in the spin of the energy bands $E_n(\boldsymbol{k})$ for each quasi-wave vector $\boldsymbol{k}$ throughout the Brillouin zone. D. Dresselhaus investigated the spin-orbit interaction in semiconductors with inversion-asymmetric structure of zinc blende ZnS, which is the crystal structure of many III–V and II–VI semiconductors such as GaAs, InSb, and CdTe. He predicted anisotropic spin splitting of the dispersion dependence (dispersion) $E(\boldsymbol{k})$, whose magnitude has a cubic dependence on the quasi-wave vector $\boldsymbol{k}$ for bands with Γ_6 symmetry and known as "spin-orbit splitting of Dresselhaus".

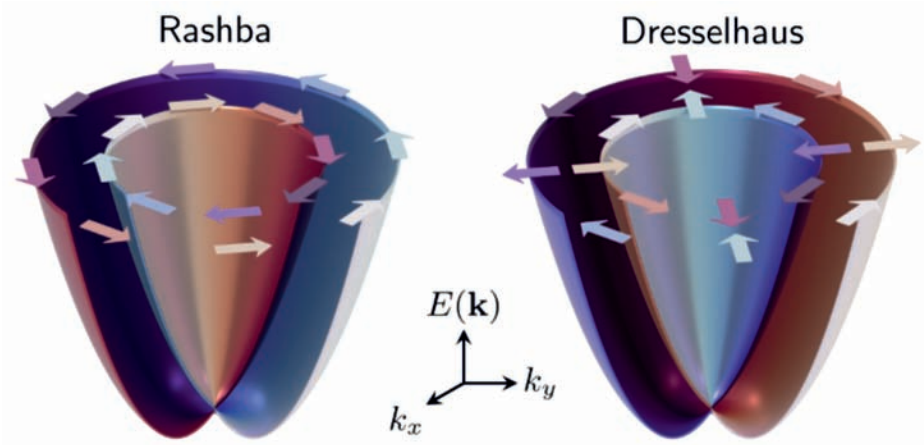

Figure 1.1 — Spin textures of electron bands for a two-dimensional free electron gas in the case of Dresselhaus-type and Rashba-type spin-orbit interactions. Rashba Hamiltonian $H_R = \alpha_R(\sigma_x p_y - \sigma_y p_x)$, Dresselhaus Hamiltonian $H_D = \beta_D(\sigma_x p_x - \sigma_y p_y)$. The figure is taken from the article [112].

The study of spin-orbit interaction in semiconductors with inversion-asymmetric wurtzite structure (e.g. GaN, CdS and ZnO) carried out by E. I. Rashba and V. I. Sheka [34] showed that the spin splitting of the s electron dispersion $E(\boldsymbol{k})$ near the Γ point is linear in $\boldsymbol{k}$ and isotropic for $\boldsymbol{k}$ perpendicular to the wurtzite axis c. It is precisely this dependence of the spin splitting on $\boldsymbol{k}$ that is associated with the "Rashba spin-orbit interaction".

On the example of semiconductors of two different structural types it has been shown that there is a removal of spin degeneracy of electronic states as a result of spin-orbit interaction and violation of the inversion symmetry in the crystal. If we consider the model of a two-dimensional electron gas, the patterns of spin orientation in $\boldsymbol{k}$ space will be significantly different for the Dresselhaus-type splitting and the Rashba-type splitting. In the case of Rashba splitting, we have a helical spin texture with the spin direction $\boldsymbol{s}$ always perpendicular to the wave vector $\boldsymbol{k}$ (see Fig. 1.1).

The table 1 summarizes the conditions under which spin degeneracy is observed in solids. However, it is possible to remove the spin degeneracy by breaking not only the inversion symmetry in space, but also in time. Kramers' theorem states [113] that if the Hamiltonian operator of a system with half-integer total spin commutes with the time reversal operator $[H,T]$=0, then for any eigenstate $|n\rangle$ the state $T|n\rangle$ will also be an eigenstate of the Hamiltonian with the same energy, i.e., $E_\uparrow(\boldsymbol{k}) = E_\downarrow(-\boldsymbol{k})$. Thus, it is possible to break the Kramers degeneracy by applying an external magnetic field or by doping the solid with magnetic metal atoms to produce intrinsic magnetization in the solid.

Inversion symmetry in space: $E_{\uparrow}(\boldsymbol{k}) = E_{\uparrow}(-\boldsymbol{k})$ Inversion symmetry in time (time reversal symmetry): $E_{\uparrow}(\boldsymbol{k}) = E_{\downarrow}(-\boldsymbol{k})$	$\Rightarrow$	Spin degeneracy (magnetic field $B = 0$): $E_{\uparrow}(\boldsymbol{k}) = E_{\downarrow}(\boldsymbol{k})$

Table 1 — Spin degeneracy in a solid in the absence of an external magnetic field due to the joint effect of inversion symmetry in space and time.

1.1.1 Spin-orbit interaction in quasi-two-dimensional structures

Quasi-two-dimensional structures are crystal structures with dimensional restriction along one of three spatial axes, which leads to restriction of charge carriers motion along the restriction axis and free motion in other directions. Examples of quasi-two-dimensional structures are heterostructures, quantum wells, superlattices, and single crystal surfaces. Due to the fact that in such structures there is a two-dimensional interface between layers of different elemental composition and structure and/or surface, the spatial inversion symmetry is violated. Violation of the spatial inversion symmetry (at the two-dimensional boundary or surface) leads to the removal of spin degeneracy and splitting of electronic states. Thus, the spin-orbit coupling opens new possibilities in manipulating the spin of charge carriers in quasi-two-dimensional structures for spintronics applications.

The widespread use of ARPES method with spin resolution in the 2000s ensured active research for years to come into quasi-two-dimensional systems and solid surfaces, in which a strong intra-atomic potential gradient led to spin splitting of electron states. The first study of spin-orbit splitting on a metal surface was made for an Au(111) single crystal using the ARPES method in 1996 [114]. The authors pointed out the importance of both the surface potential gradient and the strong Coulomb potential of the nucleus. The influence of the Coulomb potential of the nucleus on the spin-orbit splitting of surface states was further confirmed in the works [115—117], including the study of the surfaces of W(110) and Mo(110) single crystals coated with monolayers of Li, Ag, and Au atoms. Let us consider the reasons that underlie the effect of substrate-induced spin-orbit interaction in ultra-thin metal layers.

The simplest Rashba-Bychkov [118] model for a two-dimensional electron gas has shown that in the presence of a potential gradient perpendicular to the localization

plane, the dispersion dependence splits into two spin components as a result of the spin-orbit interaction (see Fig. 1.7 (a)). The dispersion law has the following form:

$$E_{\pm}(\boldsymbol{k}_{\parallel}) = \frac{\hbar^2|\boldsymbol{k}_{\parallel}|^2}{2m^*} \pm \alpha_R|\boldsymbol{k}_{\parallel}|, \tag{1.2}$$

where $\boldsymbol{k}_{\parallel}$ is the two-dimensional quasi-wave vector for the electronic state in the (x,y) plane, m^* is the effective mass and the constant $\alpha_R \sim \nabla V = dV/\,dz$.

If we compare the value of the experimental spin-orbit splitting ($\sim$ 110 meV) of the Au(111) surface states with the value predicted on the basis of the Rashba-Bychkov model with a limiting surface potential equal to the work function, it appears that the value of the experimental splitting is much larger than the value predicted by the model ($\sim 10^{-3}$ meV) [116]. This implies that the intra-atomic potential of atoms on the surface has a significant effect on the spin-orbit splitting of surface states. In Ref. [106], it was shown that the asymmetry of the wave function of interface state with respect to the surface Gd atoms leads to an effective electric field causing the Rashba effect.

Indeed, in a quasi-two-dimensional system, the Rashba constant can be calculated using the equation [119; 120]:

$$\alpha_R = \int \frac{1}{c^2}\frac{dV(\boldsymbol{r})}{dz}|\psi_{k\|}(\boldsymbol{r})|^2 d\boldsymbol{r}, \tag{1.3}$$

where $V(\boldsymbol{r})$ is the one-electron potential, $\psi(\boldsymbol{r})$ is the wave function, the z-axis is perpendicular to the surface of the quasi-two-dimensional system, and the integral is taken over the whole unit cell. The equation shows that the spin splitting is caused by the asymmetry of the potential $V(\boldsymbol{r})$ and/or the probability density of the wave function (charge density) $|\psi_{k\|}(\boldsymbol{r})|^2$. Thus, the strength of the Rashba effect can be controlled by such physical parameters as the gradient of the intra-atomic potential (atomic number Z) and the asymmetry of the wave function of the electronic state relative to the atomic nucleus. Figure 1.2 shows the different contributions to the Rashba constant α_R of spin splitting of quantum well states (QWS) in ultrathin Ag films on Au(111) single crystal. Inset (a) shows the case of a free film for which the total α_R will be zero due to the compensation of the contributions from the left and right parts of the film. For the case of Ag film on Au(111) single crystal, the penetration of the QWS wave function deep into the Au(111) single crystal occurs. Figure 1.2(b) shows the main contributions to the Rashba constant, which can be

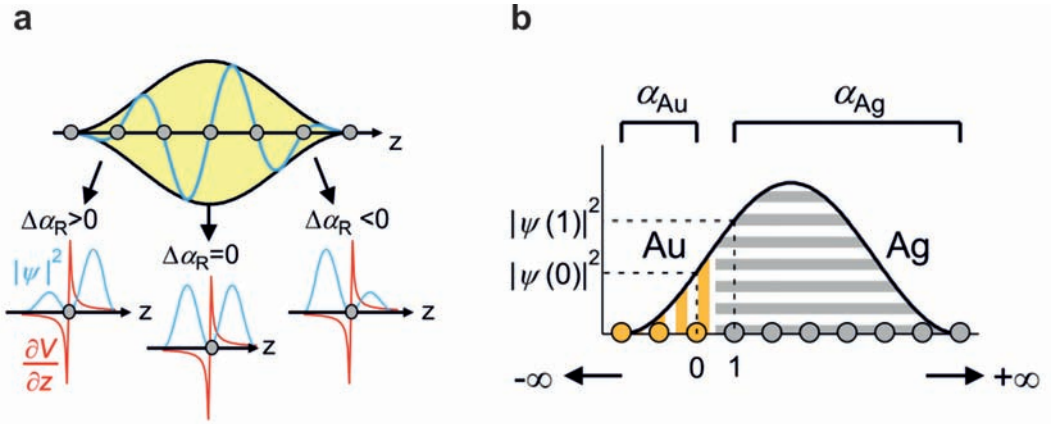

Figure 1.2 — (a) Schematic representation of the relation between the charge density distribution of QWS and the layer-resolved Rashba effect. The blue curves show the charge density distribution, and their envelope is shown by the black curve. The red curves denote the potential gradient dV/dz, which increases near the cores. (b) Schematic representation of the decomposition of α_R into contributions from the Au substrate and the Ag film. The figure is taken from the paper [120].

calculated by the following formula [120]:

$$\alpha_R \propto \left\langle \left| \frac{dV}{dz} \right| \right\rangle_{Au} |\psi_{env}(0)|^2 - \left\langle \left| \frac{dV}{dz} \right| \right\rangle_{Ag} |\psi_{env}(1)|^2. \tag{1.4}$$

It turned out that the Rashba effect in ultrathin films is determined by the QWS charge density at the interface between the film and the substrate and the ratio of the gradients of the intra-atomic potentials of the substrate and film atoms. For a stronger Rashba effect, it is required to choose film and substrate materials with the largest difference in atomic number, but it should be taken into account that the electronic structure of the substrate should have a band gap in which QWS of the film will be formed. That is why, in this work, ultrathin layers of light elements were synthesized in contact with substrates of heavy elements to study the effect of induced spin-orbit splitting of surface electronic states. In particular, ultrathin Al ($Z = 13$) layers on W(110) single crystal ($Z = 74$) and graphene ($Z = 6$) on Au ($Z = 79$) and Pt ($Z = 78$) monolayers on different substrates, including Pt(111) single crystal, were synthesized.

1.1.2 Intrinsic spin-orbit interaction in graphene and the quantum spin Hall effect

It is known that due to the small charge of the carbon atoms nucleus (atomic number Z), the spin-orbit interaction has an insignificant effect on its electronic structure, the splitting does not exceed 24-50 μeV at the $\overline{\mathrm{K}}$ point of graphene [121]. On the one hand, this provides a large spin relaxation length in graphene [122—124]. Spin-polarized current control has been successfully implemented in Datta-and-Das spin transistor based on graphene [35; 125]. On the other hand, free graphene cannot be a source of spin-polarized electrons; it is necessary to use a source and drain made of magnetic materials and with a given magnetization, which significantly complicates the design of the device. Another possible solution to the problem of generating spin-polarized currents in graphene is to enhance its intrinsic spin-orbit interaction.

The intrinsic spin-orbit interaction and the Rashba-type spin-orbit interaction arise in graphene due to "mixing" between π and σ bands due to the atomic spin-orbit interaction in the former case and due to a combination of the atomic spin-orbit interaction and the Stark interaction in the latter case [126]. Charles Kane and Eugene Mele in their work [46; 86] showed that if the Rashba-type spin-orbit interaction is smaller than the intrinsic spin-orbit interaction, then the quantum spin Hall effect (QSHE) can be observed in graphene [127]. In the open band gap at the Dirac point, edge states insensitive to scattering are formed, since their directionality is uniquely related to the spin direction. The authors, using the tight-binding method, wrote down the graphene Hamiltonian, which generalizes the Haldane model by including spin with spin-orbit interactions invariant to time reversal (the Haldane model and Chern numbers will be discussed in more detail in Section 1.14):

$$H = -t\sum_{\langle i,j\rangle}\hat{c}_i^{\dagger}\hat{c}_j + i\lambda_{SO}\sum_{\langle\langle i,j\rangle\rangle}\nu_{ij}\hat{c}_i^{\dagger}s^z\hat{c}_j + i\lambda_R\sum_{\langle i,j\rangle}\hat{c}_i^{\dagger}(\boldsymbol{s}\times\tilde{\mathbf{d}}_{ij})_z\hat{c}_j + \lambda_{\upsilon}\sum_i \xi_i\hat{c}_i^{\dagger}\hat{c}_i, \quad (1.5)$$

where *i, j* denote the nearest neighbor sites in the sublattice A(B), the fermion operator $\hat{c}_i^{\dagger}$ ($\hat{c}_i$) creates (annihilates) an electron at the *i* site, and the same for the *j* site, *t* is the hopping parameter, λ_{SO} is the intrinsic spin-orbit interaction constant, $\nu_{ij} = (2/\sqrt{3})(\tilde{\boldsymbol{d}}_1 \times \tilde{\boldsymbol{d}}_2)_z = \pm 1$, where $\tilde{\boldsymbol{d}}_1$ and $\tilde{\boldsymbol{d}}_2$ are unit vectors along the two bonds when an electron jumps from site j to site i, the next-nearest neighboring site, s^z is the Pauli matrix describing the electron spin, λ_R is the Rashba spin-orbit coupling

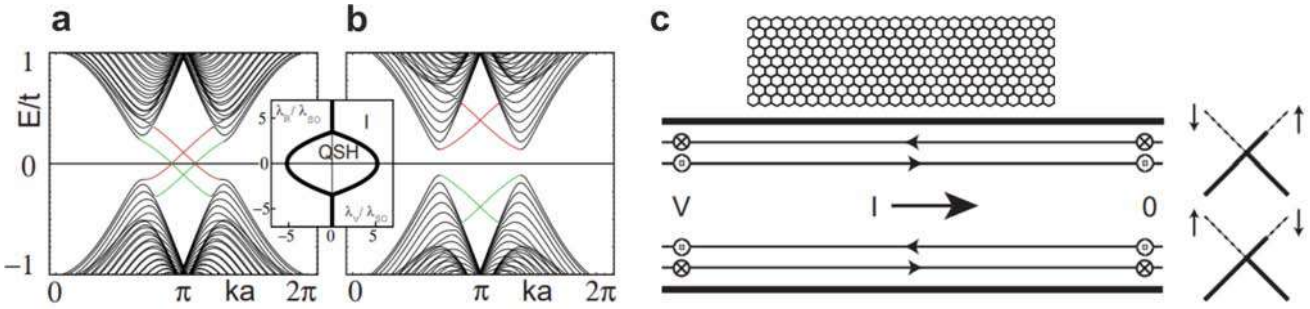

Figure 1.3 — Energy bands for a one-dimensional zigzag ribbon of graphene for the QSHE phase at $\lambda_\upsilon = 0.1t$ (a) and the insulator phase at $\lambda_\upsilon = 0.4t$ (b). In both cases, $\lambda_{SO} = 0.06t$ and $\lambda_R = 0.05t$. The edge states at different boundaries are shown in different colors. The inset shows the phase diagram as a function of λ_υ and λ_R for $0 < \lambda_{SO} < t$. (c) Schematic diagrams showing the two-terminal geometry for measuring the current I = ($2e^2$/h)V flowing into the right junction. The diagrams on the right show the populations of the edge states. Parts of the figure are taken from the articles [46; 86].

constant, $\tilde{\boldsymbol{d}}_{ij}$ is the unit lattice vector pointing from site j to site i, and $\boldsymbol{s}$ is the vector of Pauli matrices.

The first term is the usual nearest neighbor hopping term, which describes the formation of a linear dispersion of π states at the $\bar{\mathrm{K}}$ point. The second term, representing the intrinsic spin-orbit interaction, couples the second neighbor sites with a spin-dependent amplitude, with $\nu_{ij} = \pm 1$ if the electron makes a left (right) rotation to reach the second neighbor. The third term is a Rashba-type spin-orbit interaction, which breaks the $z \to -z$ mirror symmetry, and is due to the perpendicular electric field or the interaction with the substrate. The fourth term is a sublattice staggered potential ($\xi_i = \pm 1$), breaking the in-plane two-rotation symmetry. It was included in the model to describe the transition between the QSHE phase and a simple insulator. Figures 1.3 (a,b) show the energy bands of a graphene strip with zigzag edges calculated by the tight-binding method for the QSHE phase and the insulator phase. Both phases have a bulk energy gap and edge states, but in the QSHE phase the edge states cross the energy gap in pairs. The population of these states changes when a voltage is applied, which ensures the flow of spin-polarized currents along the edges of the graphene strip with opposite spin directions for the opposite edges (see Figure 1.3 (c)).

It should be noted that C. Kane and E. Mele used two conjugate copies of the Haldane model for spin-up electrons (valence band Chern numbers ± 1) and spin-

down electrons (valence band Chern numbers ∓ 1). Since the total valence band Chern number was zero, the quantum anomalous Hall effect was absent. However, the authors found by numerical calculation that if time-reversal invariance is not violated, the edge states are in fact protected by a previously unexpected topological invariant $\mathbb{Z}_2$ related to the Kramers degeneracy. Their pioneering work initiated the development of a new direction in spintronics – dissipationless transport using nontrivial topological edge states.

One of the ways to enhance the intrinsic spin-orbit interaction predicted theoretically is the arrangement of adatoms In and Tl [128], Os and Ir [129] in hollow positions on graphene (in the center of the hexagon). However, this effect could not be registered in either transport measurements or ARPES measurements [130–133]. In [132], it was suggested that this discrepancy between theory and these experiments may be due to the masking of the band gap opening by the broadening of the Dirac states in the ARPES experiment due to the disorder in graphene introduced by thallium adatoms with corresponding scattering contributions. In theoretical work [134] on the spin-orbit interaction in graphene with Pb adatoms, it was shown that different contributions to the spin-orbit interaction arise depending on the position of the adatoms. Adatoms placed in hollow positions open the band gap at the Dirac point and induce intrinsic spin-orbit interaction. However, at another placement of adatoms, randomly or in a rectangular supercell commensurate with graphene with the $c(4 \times 2)$ adatom structure relative to the substrate, there is an enhancement of the spin-orbit interaction of the Rashba type without opening the band gap. On the other hand, experimental studies on the electronic structure of graphene partially and fully intercalated with Pb atoms with the formation of $c(4 \times 2)$ structure on Ir(111) [135] and Pt(111) [136], respectively, indicated a possible state of QSHE in graphene due to the registration of edge states and a band gap in graphene. Further experimental investigation of the Gr/Pb/Ir(111) system did not confirm the presence of a band gap at the Dirac point due to the fact that the intrinsic spin-orbit interaction was smaller than the Rashba spin-orbit interaction [137].

Other known methods for increasing the intrinsic spin-orbit interaction are hydrogenation [138] or fluorination [139] of graphene, the corresponding concentrations of which of 0.05% and 0.06% led to an increase in the intrinsic spin-orbit interaction to 2.5 meV and 9.1 meV The enhancement of the intrinsic spin-orbit interaction has been successfully demonstrated for graphene by observing the spin Hall effect even at room temperatures [98; 138–140]. At the same time,

the observation of the quantum version of the spin Hall effect requires the synthesis of graphene-based epitaxial structures whose sublattice equivalence will be violated. This problem has not yet been solved for graphene-based systems.

Recent work [141] using STM/STS technique was the first to reveal the topological state of QSHE in a monovalent 2D material, germanene, epitaxially grown on a $\mathrm{GePt_2}$ alloy. The grown system has a buffer layer of germanium atoms between germanene and the alloy similar to graphene on SiC with a buffer layer of carbon in between. However, in the case of germanene, corrugation is observed in the form of different vertical positions of sublattice atoms, which allows for a nontrivial band gap due to sublattice symmetry breaking and inhomogeneous charge distribution on the sublattices [142]. Germanene is an analog of graphene, but was also chosen by the authors of the paper due to the stronger intrinsic spin-orbit interaction, since it depends on the atomic number of the element and is $\sim Z^4$. It is shown theoretically [143] that the magnitude of the spin-orbit band gap in germanene should be $\sim$ 4.0 meV and $\sim$ 23.9 meV for planar and corrugated germanene, respectively. It should be noted that the corrugated structure is stable for germanene as well as for silicene. The edge states in the work [141] were measured by dI/dV scanning tunneling spectroscopy at the edge of the germanene layer. The experiment revealed a $\sim$ 70 meV band gap, which is almost completely closed when an electric field is applied. Depending on the magnitude of the applied electric field, a topological phase transition from the topological state of the QSHE to a trivial insulator was observed through the closure of the band gap (close to zero value). This work, published in 2023, is the first known experimental evidence of the existence of the QSHE phase in a monovalent 2D material.

The conducted studies of graphene and graphene-like structures show that to observe the topological phase of the QSHE in these materials, it is necessary to use an element with a high atomic number as adatoms or an underlying substrate layer and deviations from the planar structure of layers with a violation of the equivalence of the graphene sublattices and graphene-like structures to increase intrinsic spin-orbit interaction. Enhancement of the spin-orbit interaction can be achieved in the epitaxial synthesis of graphene by adsorption and intercalation of heavy metals or by transferring graphene to the corresponding layers with heavy metals. However, as will be shown below, for graphene intercalated with gold atoms, an increase in the spin-orbit interaction of the Rashba type is observed without opening the band gap

due to the formation of a graphene/metal moiré superstructure with a size of several unit cells of graphene.

1.1.3 Induced Rashba-type spin-orbit interaction and its combination with magnetic exchange interaction

In most materials with a strong atomic spin-orbit interaction, the inversion-breaking crystal field acts as a perturbation, so that the resulting Rashba-type spin splitting is only a fraction of the spin-orbit energy (see Fig. 1.4 (a)). In contrast, if we have a strong crystal field, the spin-orbit interaction acts as a perturbation, and hence the spin splitting fully reflects the atomic spin-orbit interaction (see Fig. 1.4 (b)). Therefore, the optimal compromise between these two energy scales will result in the maximum Rashba-type spin splitting. For example, the compound $\mathrm{PtCoO_2}$ is characterized by a maximum Rashba-type spin splitting $\sim$ 60 meV, which corresponds to the Co $3d$ atomic spin-orbit splitting [144] and is achieved under crystal field dominance [145]. Another work [146] proposes a different mechanism to explain the spin-orbit interaction and considers the large Rashba-type spin splitting in bulk materials as a result of the avoided-crossing effect of dispersion dependences in the electronic structure. This observation confirms that orbital “mixing” is a key factor for creating materials with strong Rashba-like spin-orbit interactions. However, a general theory with clear recommendations for the development of materials with maximum Rashba-type spin splitting both in the bulk and at the interfaces has not yet been created, and the above works indicate further directions for the development of research in the field of searching for materials for spintronics.

In Chapter 3, on the example of induced spin-orbit splitting of quantum well states in ultrathin layers of aluminum, we will show that the main factor of anomalous splitting in such a quasi-two-dimensional system is hybridization of QWS with interface states and substrate states. We will call the spin splitting anomalous if it exceeds the atomic spin-orbit splitting of the elements that make up the quasi-two-dimensional system. In the case of ultrathin aluminum layers, these values are larger than the value of the atomic spin-orbit splitting $\sim$ 22 – 25 meV for Al $3p$ [147; 148].

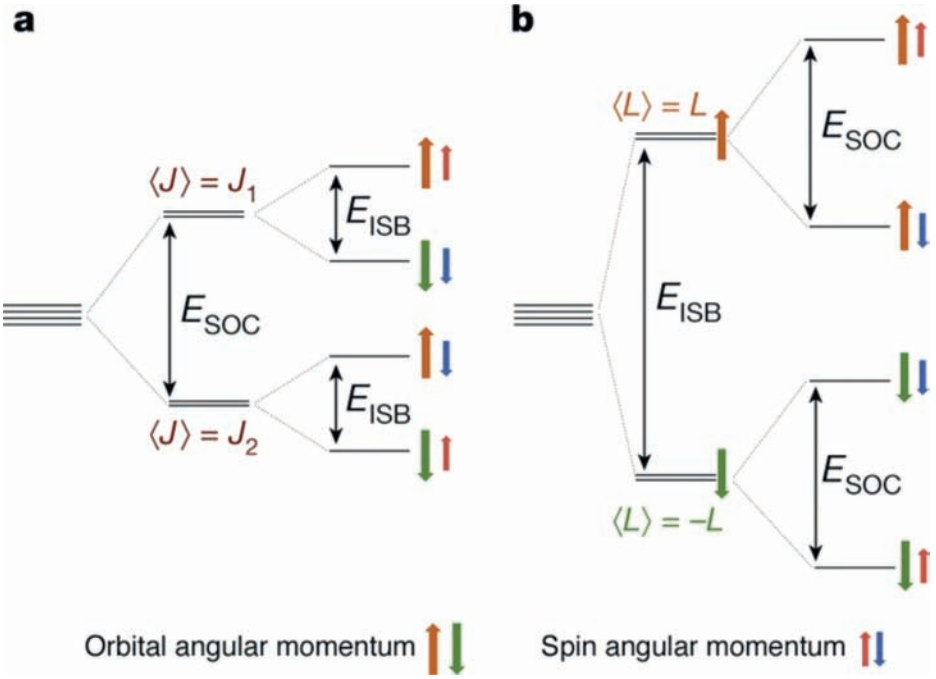

Figure 1.4 — Schematic of the splitting of electronic levels under inversion symmetry breaking and spin-orbit interaction. (a) The case of spin-orbit interaction dominance, the interaction of orbital and spin angular momenta leads to the splitting of states with different total angular momentum J. The inclusion of the crystal field and breaking of the inversion symmetry leads to further splitting of states with opposite momentum $\boldsymbol{k}$. (b) The case of dominance of the non-centrosymmetric crystal field, which removes the degeneracy between orbital states with opposite momentum $\boldsymbol{k}$. Further inclusion of the spin-orbit interaction leads to the splitting of states with spin $\boldsymbol{s}$ parallel and antiparallel to the orbital angular momentum $\boldsymbol{L}$. The orange and green arrows denote the orbital angular momentum; the red and blue arrows denote the spin angular momentum. The figure is taken from the article [145].

It is known that the contact of graphene with heavy metals can lead to the induced giant Rashba effect in graphene [12; 14; 149; 150]. In this case, the hybridization of π states of graphene and d states of heavy metal [14] plays the main role in the substrate-induced effect, while the magnitude of the Rashba-type spin splitting remains constant in the vicinity of the $\bar{\mathrm{K}}$ point [12; 14]. Theoretical works [121; 151; 152] considering the Rashba-type spin-orbit interaction also confirm the conservation of the splitting value in the vicinity of the $\bar{\mathrm{K}}$ point, but do not take into account the influence of the substrate. The Hamiltonian of graphene with the Rashba spin-orbit interaction term H_R in the $\overline{\mathrm{K}}$ and $\overline{\mathrm{K}}'$ valleys and its eigenvalues

$E(\boldsymbol{k})$ are determined by the following expression [153]:

$$\begin{gathered} H_R = \frac{\lambda_R}{2}(\tau\sigma_x s_y - \sigma_y s_x), \\ E(\boldsymbol{k}) = \frac{\nu \cdot \mu}{2}(\sqrt{\lambda_R + 4(\hbar v_F k)2} - \mu\lambda_R), \nu, \mu = \pm 1, \end{gathered} \tag{1.6}$$

$\tau = \pm 1$ corresponds to two non-equivalent valleys $\overline{\mathrm{K}}$ and $\overline{\mathrm{K}}'$, $\sigma_{x,y}$ and $s_{x,y}$ are Pauli matrices denoting the pseudospin (acting on A,B sublattices) and real spin, the product $\nu \cdot \mu$ defines the electronic and hole subbands. Figure 1.5 shows data from a spin-ARPES experiment with a Rashba-type spin splitting. Outside the hybridization region of π states of graphene and $5d$ states of gold, the magnitude of the spin splitting of π states of graphene reaches $\sim$ 100 meV, and the splitting itself is called the giant Rashba splitting in Ref. [12].

In theoretical works [154—156], which considered the moiré superstructure with a substrate, a significant increase in the splitting value was shown only in the region of hybridization with the metal d states. The discovered contradiction has not been resolved until now, as it required more detailed studies of the structure of the graphene-metal boundary, its deviation from the model structure with a flat heavy metal layer, and the development of new theoretical models. In this connection, in Chapter 6 the causes of the giant Rashba effect in graphene will be discussed using the Gr/Pt/SiC system as an example.

Although the induced Rashba-type spin-orbit interaction cannot lead to the QSHE phase, its combination with magnetic exchange interaction can lead to unique characteristics of the electronic structure to create spin-polarized currents in spintronics.

As early as 1928, Werner Heisenberg concluded that ferromagnetic order must have an electrostatic origin, realized at the quantum mechanical level, due to the smallness of purely magnetic interactions [157]. He found that the Coulomb repulsion between electrons

$$U(\boldsymbol{r_1},\boldsymbol{r_2}) = \frac{1}{4\pi\varepsilon_0}\frac{e^2}{|\boldsymbol{r_1} - \boldsymbol{r_2}|}, \tag{1.7}$$

in combination with the Pauli principle gives a strong effective field consistent with experiment. If we consider a system like a hydrogen molecule consisting of two electrons and their atomic orbitals Φ_L and Φ_R, the evaluation of the Coulomb interaction $E_C = \int \Psi_\pm^* U \Psi_\pm d\boldsymbol{r_1} d\boldsymbol{r_2}$, where $\Psi_\pm$ are symmetric and antisymmetric

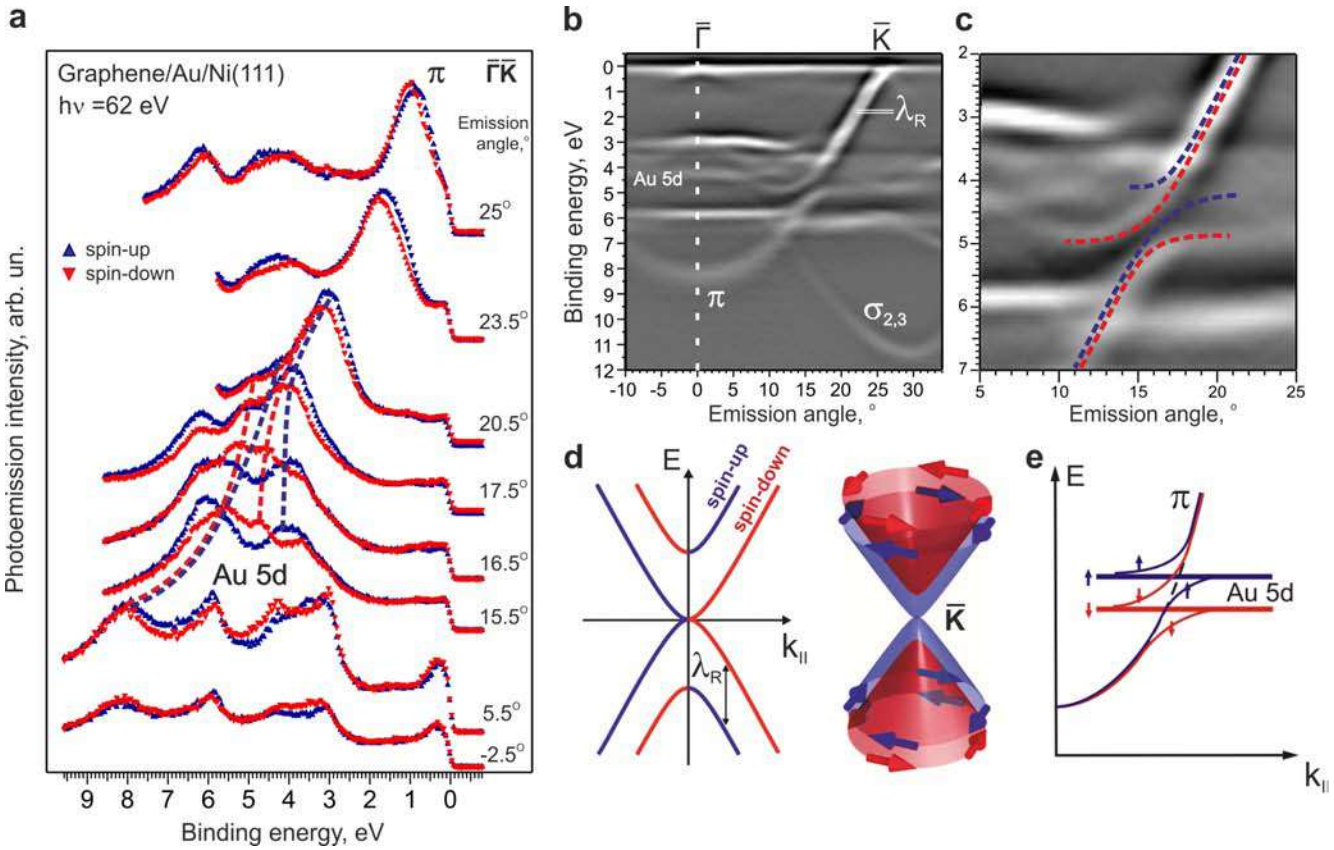

Figure 1.5 — (a) A series of spin-ARPES spectra of Gr/Au/Ni/W(110) system measured at different polar angles relative to the surface normal in the $\overline{\Gamma}\,\overline{\mathrm{K}}$ direction of the graphene Brillouin zone. ARPES intensity map as the second derivative $\mathrm{d}^2\mathrm{N}(\mathrm{E},\mathrm{k}_{\|})/\mathrm{dE}^2$ in the same direction (b), including the hybridization region of π states of graphene and $5d$ states of gold on an enlarged scale (c). A model of the Rashba-type spin splitting of π states of graphene outside the region of intersection of the dispersion dependences of π states of graphene and $5d$ states of gold (d) and a model of the spin-dependent avoided-crossing effect of the dispersion dependences of graphene and gold states (e).

combinations of wave functions, gives the energy splitting $\pm J_{ex}$:

$$J_{ex} = \int \Phi_L^*(\boldsymbol{r_1})\Phi_R^*(\boldsymbol{r_2})U(\boldsymbol{r_1},\boldsymbol{r_2})\Phi_R(\boldsymbol{r_1})\Phi_L(\boldsymbol{r_2})d\boldsymbol{r_1}d\boldsymbol{r_2}. \qquad (1.8)$$

Thus, when two neighboring atoms have unpaired electrons, the parallelism or antiparallelism of the electron spins affects whether the electrons can share the same orbital as a result of exchange interaction. If the exchange integral J_{ex} is positive, the energy of the ferromagnetic (FM) state is lower than the energy of the antiferromagnetic (AFM) state, which favors the alignment of the spin directions $\uparrow\uparrow$. Since the exchange interaction is of electrostatic origin, it is found to be of the correct order of magnitude to explain ferromagnetism.

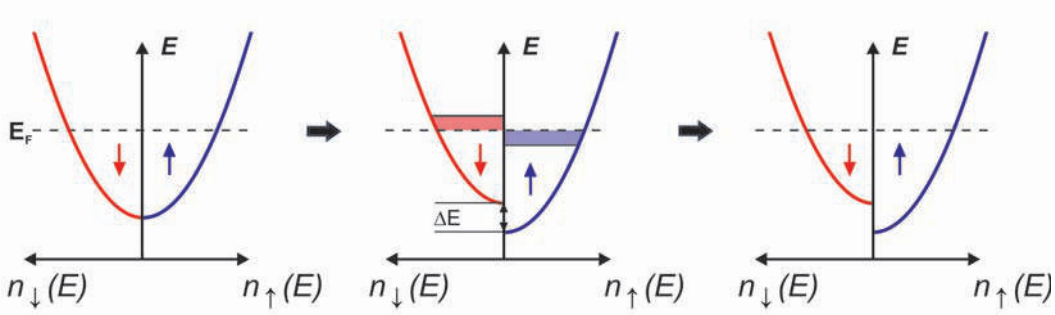

Figure 1.6 — Density of states $n(E_F)$ with spin resolution for paramagnetic metal: without external magnetic field, with external magnetic field and after "alignment" of the Fermi level as a result of spin flipping.

Let us consider the simplest model of magnetic materials – the Stoner [158] model of the formation of band magnetism. Figure 1.6 shows the change in the density of states of a paramagnetic metal when an external magnetic field B_{ext} is applied, which first of all leads to the appearance of Zeeman splitting for states with spin-up and spin-down $\Delta E = 2\mu_B B_{ext}$, where $\mu_B = e\hbar/2m_e$ – the Bohr magneton. The spin flip for some states near the Fermi level E_F restores the total Fermi energy for both spin subsystems, leading to a common magnetic moment $M = N_\uparrow - N_\downarrow$. The model predicts ferromagnetism for high densities of states at the Fermi level (for transition d metals), when the paramagnetic state becomes unstable and the Stoner criterion $n(E_F) > 1/I$ is satisfied, where I is the electron-electron interaction parameter. In the case of transition metals, where both longitudinal and transverse magnetic fluctuations are important, the most appropriate model for describing magnetism and calculating the Curie point value is the Hubbard model. We will consider it on the example of superatomic graphene in the next section.

So, let us return to the consideration of the influence of the combination of spin-orbit and magnetic exchange interactions on the electronic structure of the solid. It has been shown that the time reversal symmetry T plays an essential role in the formation of the spin texture of surface states. Figure 1.7 illustrates the dispersion relations of a free electron gas with the Rashba and Zeeman fields. The Rashba surface state arises at a wave vector k_{TRIM} (or corresponding momentum $p = \hbar k_{TRIM}$) that is invariant with respect to time reversal (TRIM), with double degeneracy at the point k_{TRIM} according to Kramers' theorem ($\Delta E(k_{TRIM}) = 0$). In contrast, Zeeman-type surface states [159; 160] exist at points without TRIM and with $\Delta E(k_{non-TRIM}) > 0$, as shown in Fig. 1.7 (b). If the Zeeman field is directed parallel to the surface, in this case the dispersion relations of the Rashba-type states undergo a change: an

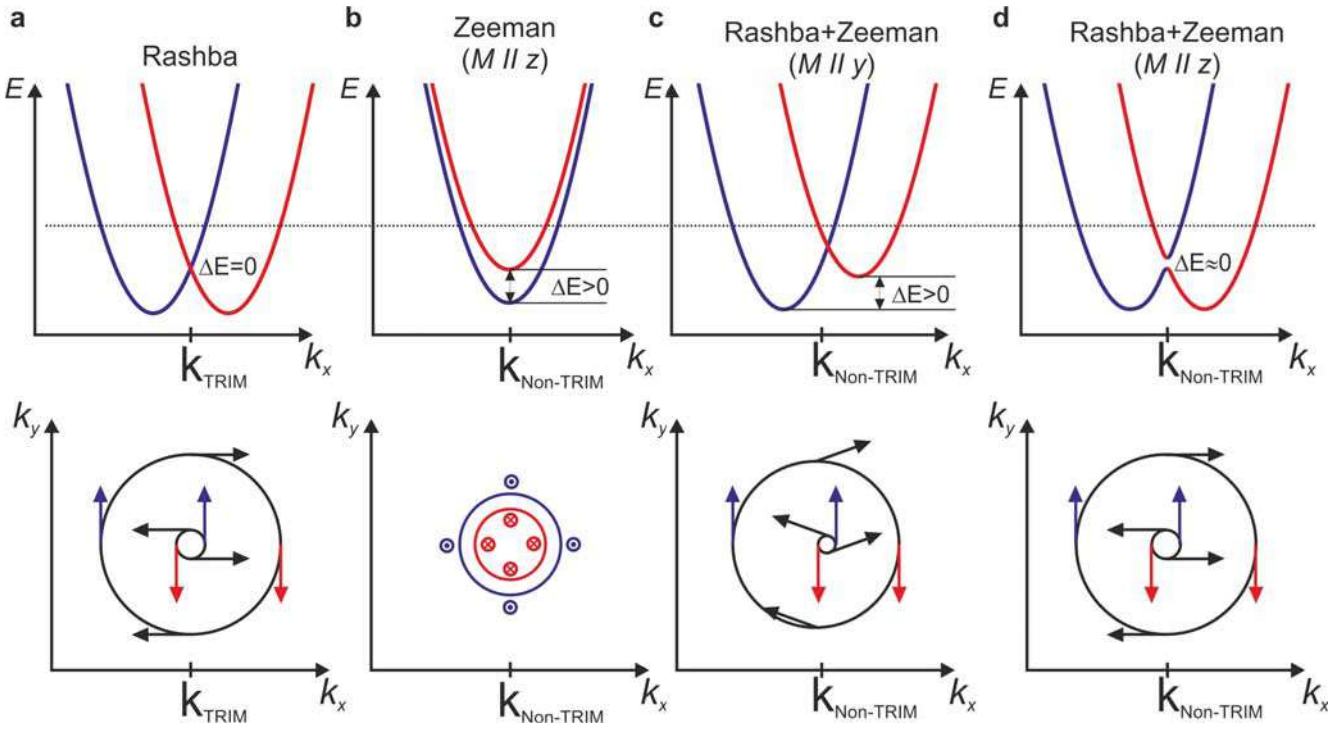

Figure 1.7 — Sketches of surface state bands for k points without (a) and with (b,c,d) violation of time reversal symmetry, Rashba-type and Zeeman-type, respectively. The red and blue colors show the spin orientation in the $-y$ and $+y$ directions for the two branches of surface states.

asymmetric spin splitting appears near the $k_{non-TRIM}$ point (Fig. 1.7(c)), similar to that predicted for the π states of graphene in the Ref. [108]. In the case of a Zeeman field perpendicular to the surface of a two-dimensional electron gas, the spin texture characteristic of the Rashba gas will generally be preserved, but near the $k_{non-TRIM}$ point there will be a spin component perpendicular to the surface, along the z direction. Similar "hedgehog" shaped spin textures were found in Gr/Au/Fe in [150], in V-doped BiTeI [161], and in Sn/SiC(0001) [162]. The "hedgehog" spin texture will allow to expand the application of graphene and other quasi-two-dimensional systems in electronics, but only if the Fermi level is adjusted to the band gap region, for example, by changing the Au concentration under the graphene or by adsorption of atoms onto the surface of the quasi-two-dimensional system. The presence of electronic states on the Fermi surface with a defined spin direction will ensure the generation of spin-polarized currents when an electric field is applied [153].

The combination of spin-orbit and magnetic exchange interactions can be realized by the hybridization of surface states of a quasi-two-dimensional system with the substrate states. As shown in Fig. 1.8, at the intersection of the bands of Rashba-type spin-split states and exchange-split bands of a bulk state or quantum well

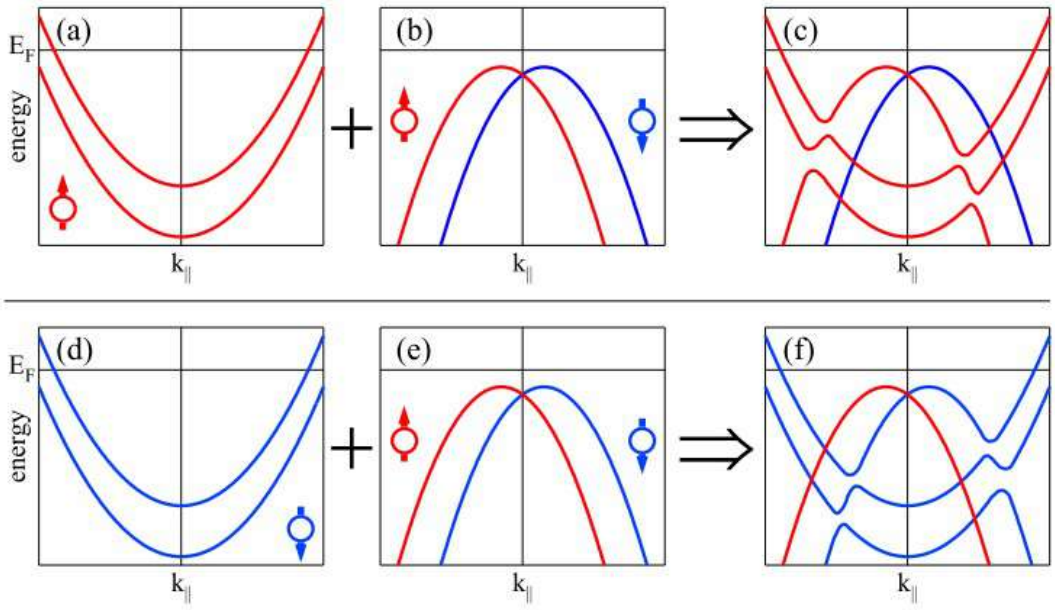

Figure 1.8 — Schematic representation of the interaction of spin-polarized QWSs ((a) and (d)) and spin-split Rashba-type surface states ((b) and (e)). Depending on the spin orientation of the QWS, spin-selective hybridization with the surface states leads to an asymmetric $\boldsymbol{k} \leftrightarrow -\boldsymbol{k}$ band structure in (c) and (f). Figure is taken from [163].

state, there is a spin-dependent avoided-crossing effect leading to an asymmetric band structure with band gaps [163]. The formation of asymmetrically arranged band gaps as a result of this interaction, in turn, will allow the observation of transport effects such as magnetoresistance anisotropy and current-induced magnetization [163].

In conclusion, it is important to note that not only spin-orbit and magnetic exchange interactions lead to spin splitting of electronic states, but also the violation of inversion symmetry in two-dimensional hexagonal structures can lead to an anomalous valley Hall effect associated with the appearance of transverse conduction due to the different behavior of charge carriers, electrons and holes, depending on their belonging to the opposite $\overline{\mathrm{K}}$ and $\overline{\mathrm{K}}'$ valleys. For example, graphene, silicene, and other quasi-two-dimensional structures can be used in spin filters based on the spin-valley scattering effect on non-equivalent sublattices of a two-dimensional hexagonal structure and non-equivalent magnetic moments in opposite valleys, as well as in other valleytronic devices based on valley-dependent Berry phase effects [164; 165]. Figure 1.9 shows a method for generating and detecting valley polarization. An applied electric field E_y in the plane of the figure leads to the accumulation of electrons at opposite edges of the sample with opposite valley indices, i.e., the chemical potential has different values in opposite valleys ($\mu_1 \neq \mu_2$). The flowing current $j_x \sim (\mu_1 - \mu_2)E_y$ can be registered as a transverse Hall voltage occurring

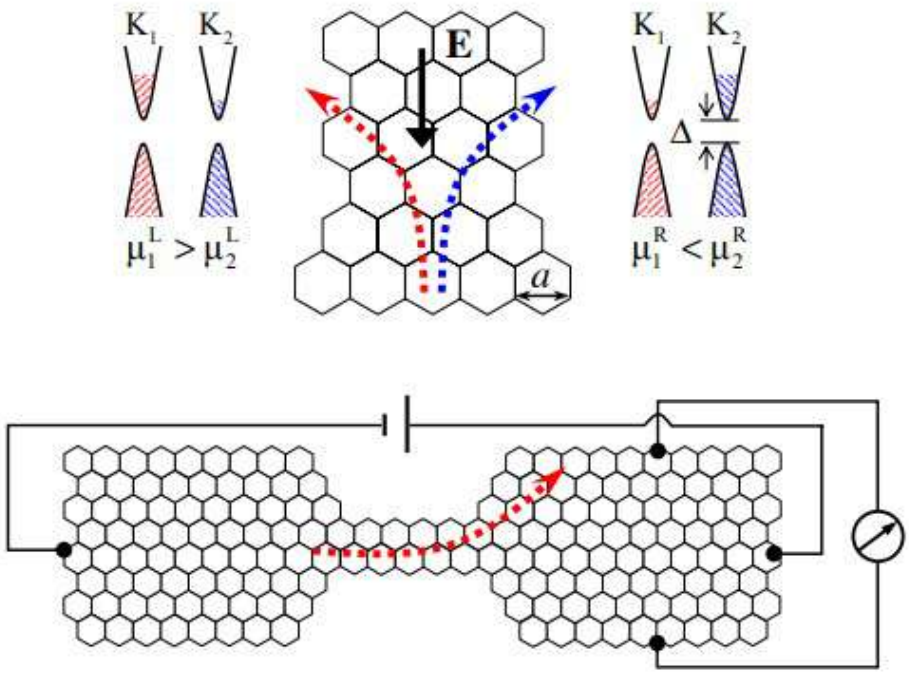

Figure 1.9 — Schematic diagram of valley polarization generation and detection. The lower part of the figure shows the method for detecting valley polarized current as transverse Hall voltage. The figure is taken from [164].

at the edges of the sample. In Chapter 7 a new quasi-two-dimensional system based on ferrimagnetic graphene with inversion symmetry breaking, leading to the manifestation of a Hall voltage when irradiated with circularly polarized infrared radiation (the circular dichroism Hall effect), will be presented.

1.2 Magnetic proximity effect

The magnetic proximity effect of van der Waals materials with magnetic materials is one of the most successfully used to enhance the exchange interaction [166–169] and to obtain new systems with topological properties [87; 170]. Enhancement of the exchange interaction in a layer of atoms of a non-magnetic material on a magnetic metal was studied by O. Krupin on the example of a metal-oxide surface layer system $p(1\times1)$O/Gd(0001) [106]. In this work, it has been shown that exchange-split interface states are formed in the near-surface layer, which are additionally split due to the Rashba-type spin-orbit interaction. The enhancement of the spin-orbit interaction was associated with the asymmetry of the wave function

of the interface states near the Gd atoms and, consequently, with the presence of an effective electric field gradient. The spin splitting scheme proposed in this work for the states of nearly free electrons in the presence of both the Rashba effect and ferromagnetic magnetization was verified in Refs. [107; 108]. However, no significant spin splitting of π states of graphene was detected (less than 45 meV) [108], indicating the absence of both giant Rashba splitting in graphene and its magnetization in general (no exchange splitting of π states at the $\bar{\Gamma}$ point). The lack of proximity effect in contact with magnetic $3d$ metals led to further search for systems based on graphene and ferromagnetic and antiferromagnetic compounds [170; 171].

The contact of graphene with a layered antiferromagnet Cr_2O_3 was successfully utilized in a theoretical study to achieve a topological phase in graphene [93]. In this case, the magnetization change in a antiferromagnetic thin layer, which can be realized electrically, led to a transition between different topological phases: from the QAHE phase with magnetization perpendicular to the graphene surface to the QVHE phase with magnetization along the surface through the valley-polarized quantum anomalous Hall effect phase (VP-QAHE). Such a set of topological phases can also be observed when crossing an antiferromagnetic domain wall. Thus, it has been shown that direct contact with chromium atoms leads to an increase in spin-orbit and exchange interactions in graphene with the possibility of obtaining different topological phases.

Another way to influence the electronic structure of graphene was proposed to co-doping graphene with magnetic $3d$ metal atoms and boron atoms at specific locations, which theoretically led to the enhancement of intrinsic spin-orbit interaction and the possibility of observing the QAHE phase in graphene [172]. In the works [173; 174] it is shown that for low concentrations of boron atoms doping graphene (< 5 at. %) there is a substitution of carbon atoms only in one of the graphene sublattices. The indicated concentrations of boron atoms are sufficient to obtain the QAHE phase in graphene [172], but the location of the Dirac point significantly deeper than the Fermi level requires the application of a gate voltage to shift the Dirac point. The fabrication of the gate contact, as well as the rejection of the single-crystal substrate significantly complicates further realization of the device based on co-doped graphene.

On the other hand, magnetization in graphene can appear in contact with non-magnetic atoms, such as adsorption of hydrogen atoms onto the surface of graphene [138; 175] or when the second layer of graphene is arranged with a small angle rotation in the surface plane with respect to the first layer of graphene, in the

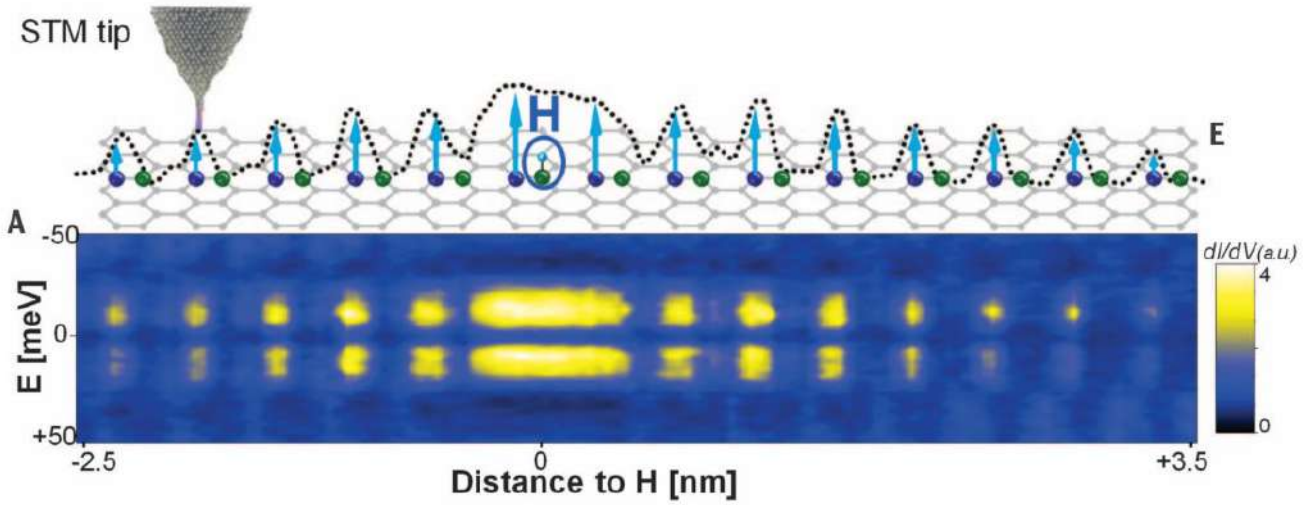

Figure 1.10 — Conductivity map dI/dV(x,E) along a straight line passing through the adsorbed hydrogen atom. The spectra were obtained at a tunnel junction resistance of 3 GΩ (U_t = 100 mV, I_t = 33 pA). Figure is taken from [175].

so-called twisted graphene [176]. If we remove one p_z orbital from the graphene π band, double filling of the π state by two electrons with different spins will not be possible due to electrostatic Coulomb repulsion (additional energy U will be required to fill the state). This would lead to the filling of the π state with only one electron and a total magnetic moment [177]. As it turns out, the STM/STS technique is quite a sensitive method to detect the local density of states near defects and confirm the magnetic moment $\sim 0.1\mu_B$ on the graphene sublattice atoms in the region of adsorbed H atom when compared with the theoretical curve [175]. Figure 1.10 shows the conductivity map, which is a set of STM curves measured in the constant current mode when scanning along a straight line. Both the STM curve and the map visualize only one sublattice of graphene, which according to the DFT calculation results has unidirectional magnetic moments perpendicular to the surface. The presence of magnetic moments on carbon atoms is confirmed by the registration of spin splitting $\sim$ 20 meV on the conductivity map. In this case, the adsorption of hydrogen atoms onto one of the sublattices is required to observe macroscopic magnetization in graphene. Due to the fact that hydrogen atoms can be adsorbed on different sublattices even at low concentrations, it is very difficult to obtain magnetized graphene by adsorption. Rotating graphene layers relative to each other to obtain magnetized graphene over a large area was more promising, but was accomplished by exfoliating graphene [176], which has technological difficulties within the framework of industrial production. For this reason, Chapter 7 will present a comprehensive study of ferrimagnetic epitaxial graphene over large sample areas

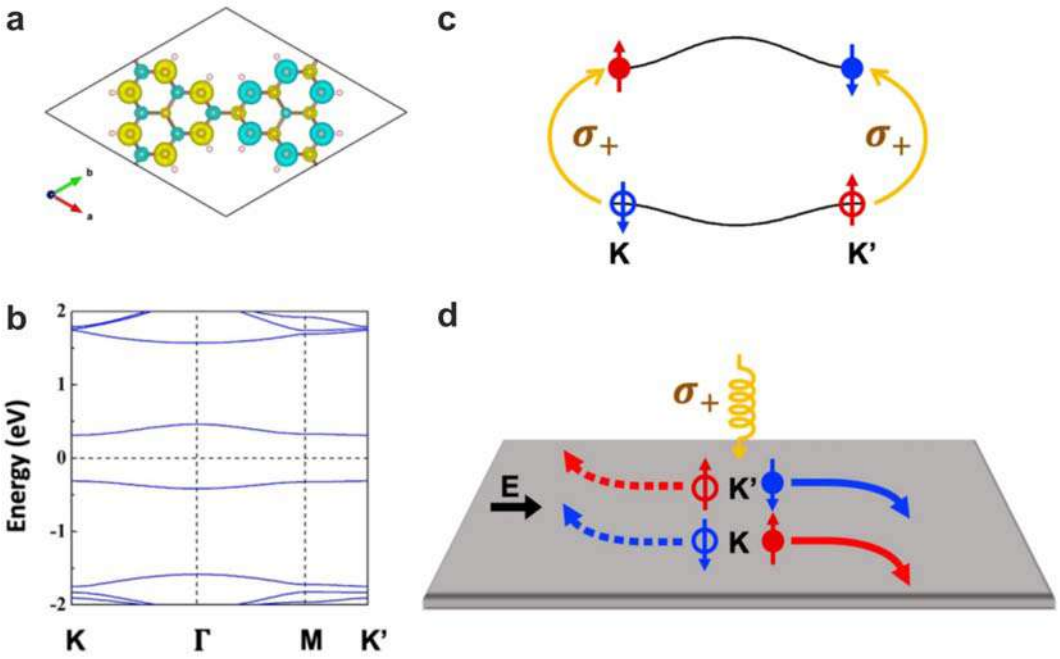

Figure 1.11 — (a) Atomic structure of superatomic graphene, where brown spheres represent carbon atoms and light pink spheres represent hydrogen atoms, with a spatial distribution of spin density difference ($\rho_{up}(r)$ - $\rho_{down}(r)$)/2, where yellow and blue colors denote positive and negative isosurfaces. (b) Band structure of superatomic graphene. (c) Schematic illustration of excited electronic states of superatomic graphene by circularly polarized radiation with σ_+ polarization. The electron with spin up/down is excited into the conduction band in the $\overline{\mathrm{K}}/\overline{\mathrm{K}}'$ valley, while the hole with spin down/up remains in the valence band. (d) Hall effect of circular dichroism of electrons and holes excited by σ_+ radiation. Electrons with spin up/down from the $\overline{\mathrm{K}}/\overline{\mathrm{K}}'$ valley accumulate at the bottom edge of the sample. Figure is taken from [178].

$\sim 100\times100$ nm^2 and show the visualization of only one graphene sublattice by STM/STS methods.

In [178], the possibility of antiferromagnetic ordering on graphene sublattices was predicted on the example of superatomic graphene with a large unit cell. The voids were artificially created in graphene, and the broken bonds of carbon atoms were passivated by hydrogen atoms (see Fig. 1.11 (a)). In such a material, a Mott insulator state with the formation of 0.6 eV band gap due to strong Coulomb repulsion was observed (Fig. 1.11 (b)), and the sublattice atoms of superatomic graphene were magnetized in the opposite way. Berry curvatures were shown to have opposite sign for different valleys, spins, and valence/conduction bands. The observed unique chirality with respect to spin-up and spin-down states of the same valley led to the prediction of the circular dichroism Hall effect (Fig. 1.11 (c-d)): the polarity of the

Hall voltage depends on the polarization sign of the incident circularly polarized radiation. For a more detailed study of the band structure, the authors calculated the hexagonal two-dimensional structure by the tight binding method using the Hubbard model [179], the Hamiltonian of which can be expressed as follows:

$$H = -t \sum_{\langle i,j \rangle \alpha} (\hat{c}^{\dagger}_{i\alpha} \hat{c}_{j\alpha} + \hat{c}^{\dagger}_{j\alpha} \hat{c}_{i\alpha}) + U \sum_{i} \hat{n}_{i\uparrow} \hat{n}_{i\downarrow}, \tag{1.9}$$

where $\hat{c}^{\dagger}_{i\alpha}$ ($\hat{c}_{i\alpha}$) is a fermionic operator that creates (annihilates) an electron in the *i* site with spin α ($\uparrow, \downarrow$), and similar for the *j* site, *t* – the hopping parameter, $\hat{n}_{i\alpha}$ – the spin density operator ($\hat{n}_{i\alpha} = \hat{c}^{\dagger}_{i\alpha} \hat{c}_{i\alpha}$) and *U* – the repulsive force of electrons at the site. The obtained results were in good agreement with those obtained by the DFT method for the following parameters: $t = 0.1$ eV and $U = 0.63$ eV. The Hubbard model describes the conductor-insulator transition, which is determined by the competition between Coulomb repulsion (U) and kinetic energy (t). In the case of superatomic graphene, the Mott insulator transition criterion is fulfilled $U/t > 4.3$ [180], which leads to the opening of the band gap at the Dirac point and antiferromagnetic ordering on the sublattices of superatomic graphene.

Based on the above results, we can conclude that the control of magnetic properties of quasi-two-dimensional materials is possible using the magnetic proximity effect with compounds that include magnetic elements and with adatoms of hydrogen and other elements. But it should be noted that spin-orbit interaction also opens a new way to electrically control magnetic properties, for example, giving the possibility of manipulating the magnetization of adatoms. Since the orbital motion of the electron can be controlled by external electric fields, the application of an electric field perpendicular to the surface of graphene with adsorbed $5d$ transition metal atoms leads to a rotation of the magnetization of the adatoms from the surface plane to the perpendicular direction due to the magnetoelectric effect [181]. In general, the hybrid system experiences a topological metal-dielectric phase transition. For the out-of-plane magnetization of $5d$ metal atoms, the Chern number of all occupied states takes an integer value of +2, which means that there are two dissipation-free and topologically protected edge states on each side of the graphene ribbon with adatoms. These systems are candidates for further transport measurements.

Due to the fact that the observation of quantum spin and anomalous Hall effects in graphene and graphene-like materials requires induced spin-orbit interaction, and for quantum anomalous Hall effect and magnetization of the two-dimensional layer, it

seems important to study the electronic structure in order to separate the contributions of spin-orbit and magnetic exchange interactions in graphene.

1.3 Quantum anomalous Hall effect

The Hall effect was discovered by Edwin Herbert Hall in 1879. This effect results in the separation of the current flowing in an external magnetic field into its components of positively charged particles and negatively charged particles and can be measured as a transverse voltage on the sample (see Fig. 1.12 (a)). Later, the anomalous Hall effect without the application of an external magnetic field was observed in ferromagnetic materials by Hall himself. These effects were observed at the macroscopic level, and a century later new varieties of the Hall effect were discovered at the microscopic level (see Fig. 1.12 (c-h)). In 1980, Klaus von Klitzing discovered the quantum Hall effect (QHE) in the silicon metal-oxide-semiconductor field-effect transistor structure [183], which consists in quantization of the transverse

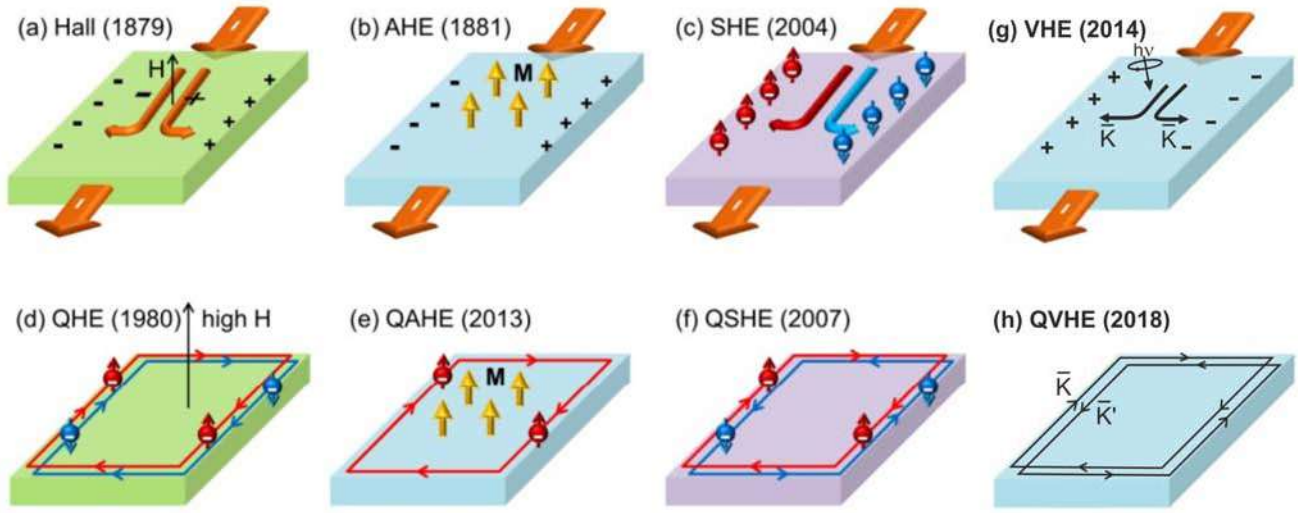

Figure 1.12 — Hall effect family: Hall effect (a), anomalous Hall effect (b), spin Hall effect (c), quantum Hall effect (d), quantum anomalous Hall effect (e), quantum spin Hall effect (f), valley Hall effect using circular radiation (or circular dichroism Hall effect) (g), and quantum valley Hall effect (h). In parentheses are the year of discovery, H – external magnetic field, and M – internal spontaneous magnetization. Part of figure (a) – (f) is taken from [182].

resistance or conductivity of a two-dimensional electron gas at low temperatures and in strong magnetic fields. The transverse resistance increases stepwise with increasing magnetic field and has a plateau when the Fermi level is located between the Landau levels – energy levels of a charged particle in a magnetic field $E(n) = E_0 + \hbar\omega_c(n + 1/2)$ (cyclotron frequency $\omega_c = eB/m^*$):

$$R_{xy} = \frac{V_{Hall}}{I_x} = \frac{h}{e^2\nu}, \tag{1.10}$$

where ν takes integer or fractional values for integer QHE or fractional QHE, respectively. The filling factor ν is defined by the formula as the ratio of the densities of states per unit area for a two-dimensional electron gas and for Landau levels:

$$\nu = \frac{n_{2D}}{n_B} = \frac{h}{eB}n_{2D}. \tag{1.11}$$

Typical dependences of the longitudinal and transverse resistances in the integer Hall effect are shown in Fig. 1.13 (a). As the magnetic field increases, the Landau levels cross the Fermi level, which leads to a sharp change in the longitudinal resistance R_x and an increase in the Hall resistance R_H by an amount h/e^2. The longitudinal resistance becomes very small in the plateau region of the Hall resistance, that is, current flow without dissipation at low temperatures is observed. In [185], it was shown that the integer quantum Hall effect can be interpreted on the basis of the model of edge states. Indeed, at the edges of the sample, the cyclotron orbitals of electrons break (Fig. 1.13 (b)), which leads to the formation of edge states that participate in the longitudinal current I_x. Moreover, when the polarity of the applied voltage or the direction of the magnetic field is reversed, the current will flow along the opposite edge of the sample. Fig. 1.13 (c) shows the Landau levels near the edges of the sample for the potential well model. The current carried by each edge state I_x is quantized and equals $(e/h)\Delta\mu$, where $\Delta\mu$ is the difference in the electrochemical potential at the edges of the sample ($eV_{Hall} = \Delta\mu$). In [186; 187], it was found that the acquisition of the Berry phase [188] by particles under the influence of a magnetic field is responsible for the quantization of conductivity in the Hall effect. The quantum Hall effect, characterized by the topological number ν [189], was the first example of realizing topological properties of electronic structure in experiment. Despite the great potential of dissipation-free edge states of QHE for future electronic devices, the need for strong magnetic fields and, as a consequence, high power consumption prevents their further application.

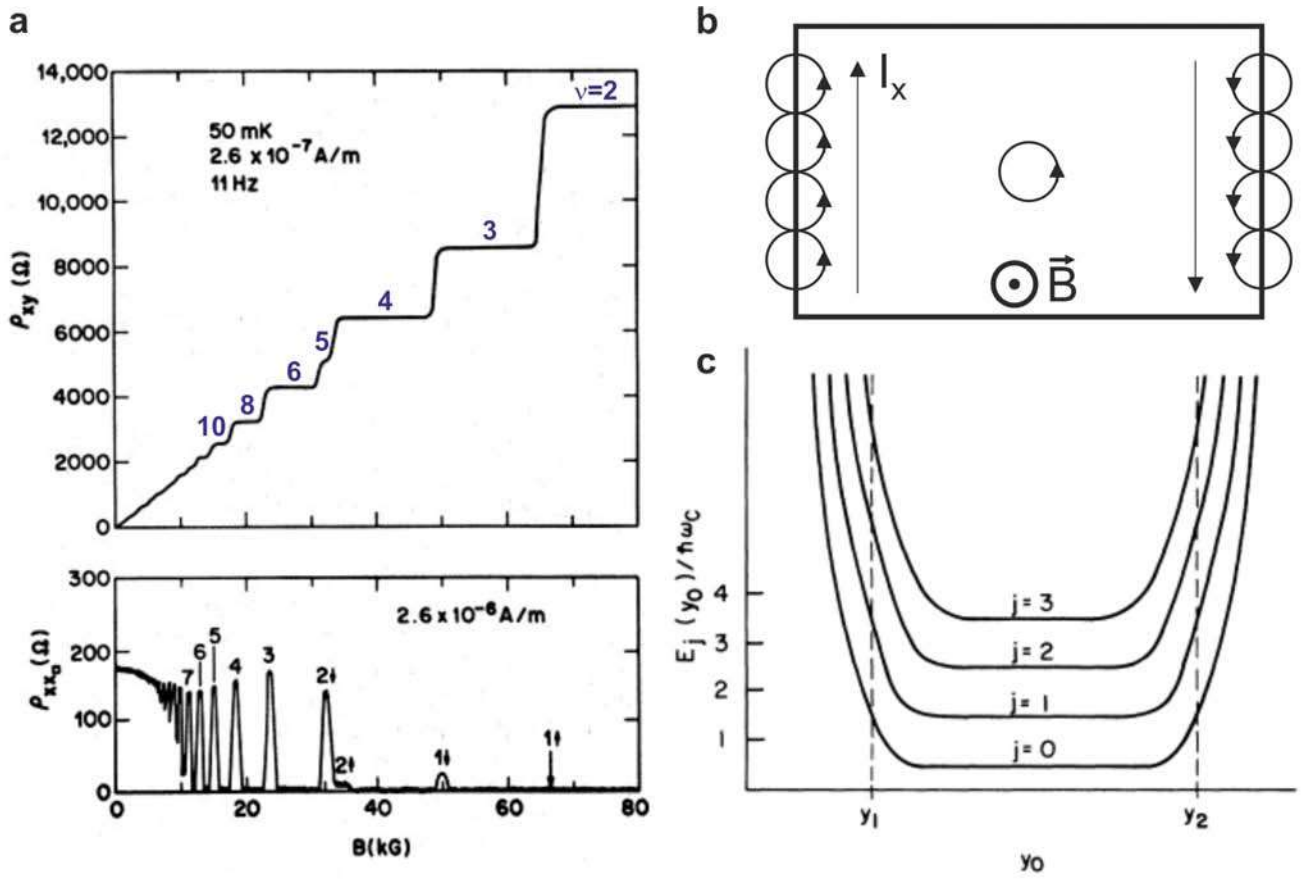

Figure 1.13 — Experimental dependences of the Hall resistance $R_H = \rho_{xy}$ and resistivity $\rho_{xx} \sim R_x$ of the $GaAs - Al_xGa_{1-x}As$ heterostructure on the magnetic field at a fixed carrier density corresponding to the gate voltage $V_g = 0$ (a). Semiclassical description of edge states (b). Electrons collide with the edge while moving along the cyclotron orbit, which leads to the appearance of an edge current. Behavior of Landau levels near the edges of the sample in the case of an infinitely high potential well (c). Part of the figure (a) is taken from [184], (c) – from [185].

In his “toy” model, the future Nobel laureate D. Haldane showed the possibility of observing the topological phase in a two-dimensional hexagonal material with non-equivalent sublattices and an external inhomogeneous magnetic field with zero total flux. The main factors determining the observation of the quantum anomalous Hall effect were the violation of sublattice symmetry and time reversal symmetry. This work was the basis for understanding a new subclass of topological insulators – two-dimensional Chern insulators characterized by a non-zero Chern number or chiral edge states on opposite edges of the two-dimensional insulator. In this case, the

anomalous Hall conductivity can be calculated by the TKNN formula [93; 189]:

$$\sigma_{xy} = \frac{e^2}{h} C = \frac{e^2}{h} \frac{1}{2\pi} \sum_n \int_{BZ} f_n \Omega^n(\boldsymbol{k}) d\boldsymbol{k} = \\ = -\frac{e^2}{h} \frac{1}{2\pi} \sum_n \int_{BZ} f_n \sum_{n' \neq n} \frac{2Im < \Psi_{n\boldsymbol{k}} | \nu_x | \Psi_{n'\boldsymbol{k}} >< | \Psi_{n'\boldsymbol{k}} | \nu_y | \Psi_{n\boldsymbol{k}} >}{(\varepsilon_{n'\boldsymbol{k}} - \varepsilon_{n\boldsymbol{k}})^2} d\boldsymbol{k}, \tag{1.12}$$

where h is the Planck constant, C is the Chern number of all occupied states obtained by integration over the $\boldsymbol{k}$-space of Berry curvatures $\Omega_n(k)$, n is the zone index, f_n is the Fermi-Dirac distribution function, $\nu_{x,y} = dH/dk_{x,y}$ – velocity operator, $\varepsilon_{n\boldsymbol{k}}$ and $\Psi_{n\boldsymbol{k}}$ are eigenvalues and eigenfunctions of the Hamiltonian at a given point $\boldsymbol{k}$ within the Brillouin zone.

The Chern invariant (Chern number) can be physically explained in terms of the geometric or Berry phase of wave functions $\Psi_{n\boldsymbol{k}}$. When we traverse a closed contour C in the space of $\boldsymbol{k}$ vectors, the gauge-invariant Berry phase $\gamma = \oint_c i < \Psi_{n\boldsymbol{k}} | \nabla_{\boldsymbol{k}} | \Psi_{n\boldsymbol{k}} > d\boldsymbol{k}$ accumulates, where the argument of the integral $\boldsymbol{A}_n = i < \Psi_{n\boldsymbol{k}} | \nabla_{\boldsymbol{k}} | \Psi_{n\boldsymbol{k}} >$ is the Berry connection. Using Stokes' theorem, the Berry phase γ can be expressed as the surface integral of another quantity $\boldsymbol{\Omega^n}$, which is the Berry curvature (or Berry field) and is defined as the rotor of the Berry connection ($\boldsymbol{\Omega^n} = \nabla \times \boldsymbol{A}_n$). Thus, the Chern invariant is an integer that accounts for the total flux of the Berry field in the Brillouin zone, and the conductivity formula itself 1.12 is a simplified expression of the Kubo formula for a quasi-two-dimensional periodic system, which defines the linear response of an observable quantity to a time-dependent perturbation [190].

The quantum anomalous Hall effect was discovered in 2013 in thin films of Cr-doped magnetic topological insulator $(Bi,Sb)_2Te_3$ [47]. At zero magnetic field, the anomalous Hall resistance as a function of gate voltage reaches the predicted quantized value of h/e^2 ($\sim$ 25.8 kΩ), which is accompanied by a significant drop in longitudinal resistance (see Fig. 1.14 (b)). Thus, the existence of edge currents is confirmed by the practically zero longitudinal resistance for the magnetized sample. In a strong magnetic field, the longitudinal resistance disappears, while the Hall resistance remains at a quantized value (see Fig. 1.14 (e-f)). This behavior proves that the system is in the same quantum Hall effect state in magnetic fields up to $\sim$ 18 T as at zero field.

It has been found that doping other 3D topological insulators with magnetic atoms, including the magnetically doped TI [182; 191; 192] investigated in Chapter 4,

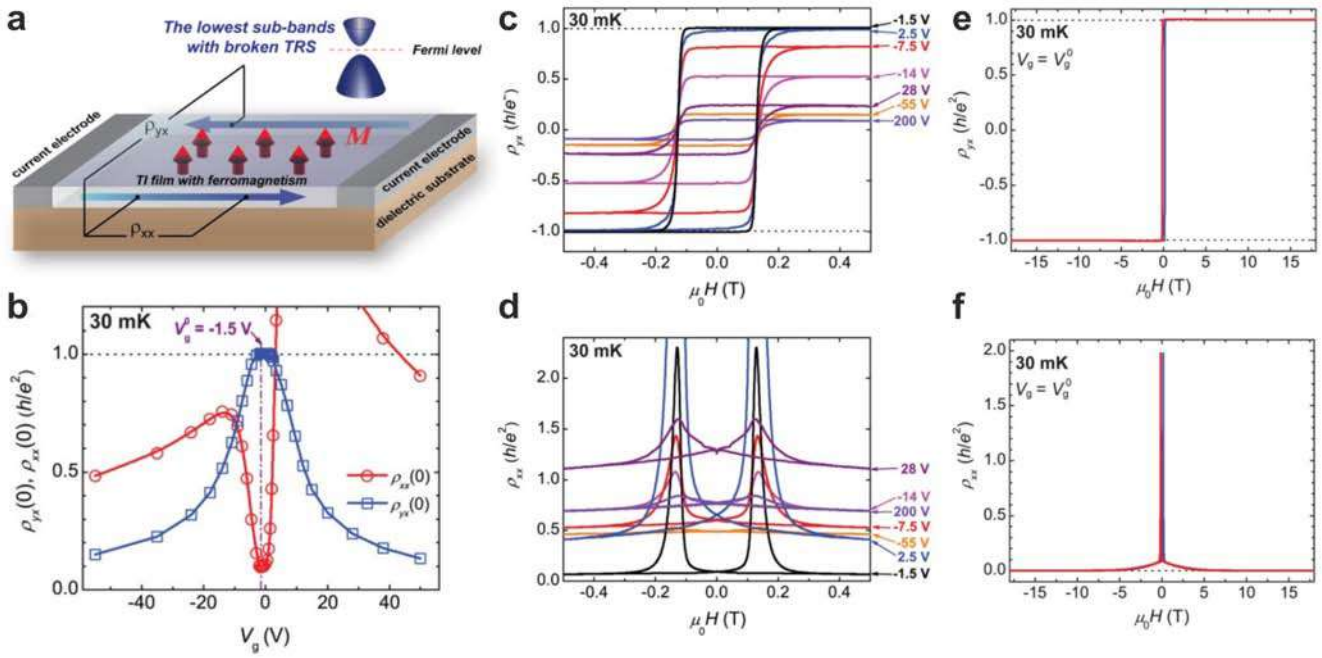

Figure 1.14 — Schematic image (a) illustrating the QAHE in a thin film of Cr-doped TI $(Bi,Sb)_2Te_3$. The magnetization direction (M) is shown by red arrows. The chemical potential of the film was controlled using a gate voltage applied to the backside of the dielectric substrate. Dependence of the longitudinal and transverse resistivity $\rho_{xx}(0)$ (red circles) and $\rho_{yx}(0)$ (blue squares) on the gate voltage V_g (b). Dependence of $\rho_{yx}(0)$ (c) and $\rho_{xx}(0)$ (d) on the magnetic field at different V_g. Dependence of $\rho_{yx}(0)$ (e) and $\rho_{xx}(0)$ (f) on the magnetic field, including the region of strong magnetic fields, at constant V_g^0 corresponding to the neutral charge of the sample. The figure is taken from [47].

also induces magnetism and breaks T symmetry, i.e., the doping results in the formation of a Chern insulator. Three-dimensional topological insulators are characterized by Dirac surface states, which are formed in the band gap of TI (Fig. 1.15). Doping with magnetic atoms leads to the appearance of magnetization and the opening of the band gap for surface states, in which an edge one-dimensional state involved in Hall conduction is formed.

The classical version of the anomalous Hall effect was observed in graphene in contact with adsorbed Eu atoms [193] or thin EuO layers [194]. These experiments confirm the possibility of magnetization of graphene in a ferromagnetic manner as a result of the proximity effect. The observation of a quantum version of the anomalous Hall effect requires a good epitaxial correspondence of the layers and a certain ratio of spin-orbit and exchange interactions in graphene. In [195], the quantum anomalous Hall effect in graphene was predicted by calculating Chern numbers for reference

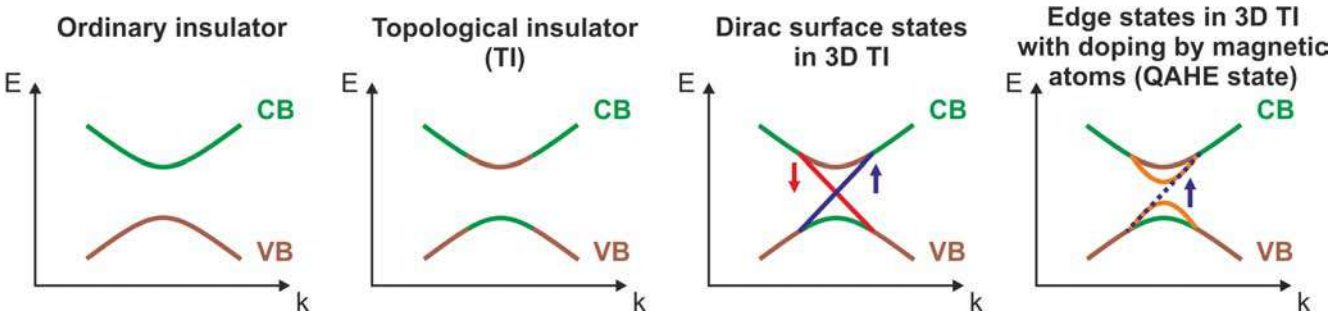

Figure 1.15 — Comparison of the electronic structure of a trivial insulator and topological insulators. The valence band and conduction band are shown in brown and green colors. In a topological insulator there is an inversion between these bands as a result of strong spin-orbit interaction. The red and blue solid lines show the quasi-two-dimensional surface states of Dirac fermions, and the dashed line shows the edge one-dimensional state.

systems. Accounting for the exchange field as a staggered order revealed the quantum anomalous Hall effect in flat graphene with Chern number C = 1, with one spin edge state at the boundary of the graphene nanoribbon. Remarkably, the combination of the intrinsic spin-orbit interaction and homogeneous exchange interaction yields topologically protected helical states whose spin is opposite at opposite zigzag edges. Rotating the magnetization from perpendicular to the in-plane direction makes the system trivial, thus allowing topological phase transitions to be controlled. The authors of this paper have shown that the staggered exchange interaction model is realized in graphene on the Ising antiferromagnetic $MnPSe_3$ even in the case of the incommensurability of the hexagonal lattice of Mn and graphene atoms. Further, in the experimental work [196] the quantum anomalous Hall effect in graphene in contact with antiferromagnetic $CrPS_4$ up to room temperature was found.

The interest in quasi-two-dimensional systems with the realization of QAHE is related not only to the possibility of creating new energy-efficient and fast electronics devices, but also to the possibility of creating topological quantum computer qubits based on anyons, two-dimensional quasiparticles possessing intermediate statistical properties between bosons and fermions [197]. In recent publications, fractional quantum Hall anomalous effects have been found in superlattices based on twisted $MoTe_2$ layers and five-layer rhombohedral graphene and hexagonal boron nitride [198; 199]. The existence of flat bands with high Chern number indicates the possibility of more exotic states of fractional anomalous Hall effect with non-Abelian anyons, on the basis of which topological quantum computing can be realized [200].

Summarizing the considered results of research in the field of synthesis and control of the electronic spin structure of quasi-two-dimensional systems, we can conclude that the main efforts of the world community are directed to the search for quasi-two-dimensional systems and the realization of devices based on them using the effects of quantization of the electronic structure and quantum Hall effects. However, in these works, quasi-two-dimensional layers obtained by exfoliation or chemical vapor deposition (CVD) were transferred to a dielectric substrate, and further device design did not assume epitaxiality of the used layers. Because of this, anomalous (light-induced) and spin Hall effects were initially measured, but their quantum versions were not detected. To observe quantum Hall effects, high ordering and epitaxiality of layers are required so that the overall electronic structure of the system has strictly defined topological properties. A significant part of the published work was carried out using mechanically exfoliated, which is incompatible with industrial production on the scale of a whole monocrystalline wafer – substrate. One candidate for device design is the SiC semiconductor substrate, which enables the production of graphene by intercalation of a zero-layer graphene. The epitaxial synthesis of layered nanosystems based on graphene and SiC substrate will be discussed in Chapters 5 and 6.

The necessity to synthesize new epitaxial quasi-two-dimensional materials, including layered nanostructures, which, due to their unique properties, will be used in computer technologies, data storage systems and quantum computing and determined the main vector of research of this work.

2. Methods

2.1 Basic experimental research methods

To solve the problems set within the framework of this thesis, a modern complex of methods for the study of the surface of solids was used. The main research methods were:

- X-ray photoelectron spectroscopy (XPS);
- ultraviolet photoelectron spectroscopy with angular resolution (ARPES), including spin-resolved (spin-ARPES) and time-resolved spectroscopy;
- low-energy electron diffraction (LEED);
- scanning tunneling microscopy (STM) and spectroscopy (STS), including cooling down to 1 K;
- scanning electron microscopy (SEM) and transmission electron microscopy (TEM);
- measurement of magnetic properties of materials in a wide range of magnetic fields and temperatures using superconducting quantum interferometer (SQUID);
- density functional theory (DFT) method for calculating the electronic band structure.

Much of the research presented in this thesis was performed using the unique scientific setup Nanolab and the photoelectron spectroscopy setup Univer-M at the Resource Center “Physical Methods of Surface Investigation” (SPbU Research Park). Nanolab was designed, fabricated and commissioned for about 4 years (see Fig. 2.1). After the final stage of commissioning in 2013, many unique scientific results were obtained with its help and several candidate and doctoral theses were defended. The uniqueness of the Nanolab setup is determined by the set of tools for the development and implementation of methods for the creation of solid-state low-dimensional systems and new composite nanomaterials promising for use in modern high-tech production, as well as methods for the study of their electronic energy and crystal structure, such as photoelectron spectroscopy (ARPES and spin-ARPES), scanning probe microscopy of atomic and subatomic resolution (STM/STS and atomic

force microscopy), LEED and Auger-electron spectroscopy. The main feature of Nanolab setup is that it implements a combination of scanning probe microscopy and photoelectron spectroscopy methods with angular and spin resolution. These are the two main groups of methods that allow to obtain the most complete information about the electronic structure of solids, as well as to visualize the structure of surfaces and nano-objects at the atomic level. At the same time, the photoelectron spectroscopy and probe microscopy modules have their own sample loading and preparation chambers, which allow the synthesis of samples and their study without violating ultrahigh vacuum conditions (base pressure $\sim 2\times10^{-10}$ mbar).

Other equipment of the SPbU Research Park was also used for the research: Zeiss Auriga Laser and Zeiss Merlin scanning electron microscopes, Zeiss Libra 200FE transmission electron microscope in the interdisciplinary resource center “Nanotechnology”, Oxford IonFab 300 ion-beam etcher in the resource center “Nanofabrication of Photoactive Materials (Nanophotonics)”, Quantum Design MPMS SQUID VSM magnetometer in the resource center “Diagnostics of Functional Materials for Medicine, Pharmacology and Nanoelectronics”, Thermo Fisher Scientific Escalab 250Xi photoelectron spectrometer in the resource center “Physical Methods of Surface Investigation”.

Part of the research using photoelectron spectroscopy was carried out at third-generation synchrotron radiation centers:

- at the RGBL, UE112_PGM-1, UE112_PGM-2b-1[3], UE56-2_PGM-2, U125-2_SGM and U125_PGM (RGBL2) beamlines of the BESSY II synchrotron (Helmholtz-Zentrum Berlin, Germany) using SPECS Phoibos 150 and VG Scienta R4000 hemispherical energy analyzers with Mott spin detectors, operating at energies of 26 and 25 kV, respectively, in the part of studies of W(110), Al/W(110), Gr/Pt(111), magnetically doped BiTeI, Au/Co(0001) and Gr/Au/Co(0001)/W(110) systems;
- at the BaDElPh beamline of the Elettra synchrotron (Trieste, Italy), in the part of studies of magnetically doped BiTeI and Gr/Au/Co(0001)/W(110) systems;
- on the scanning tunneling microscope SPECS SPM 150 AARHUS at the joint microscopy laboratory OSMOS CNR-Elettra, in the part of studies of the Gt/Pt$_x$Gd/Pt(111) systems;
- at the BL-1 and BL-9 beamlines of the HiSOR synchrotron (Hiroshima, Japan), in the part of studies of the magnetically-doped BiTeI, Gt/Pt$_x$Gd/Pt(111) and Gr/Au/Co(0001)/W(110) systems;

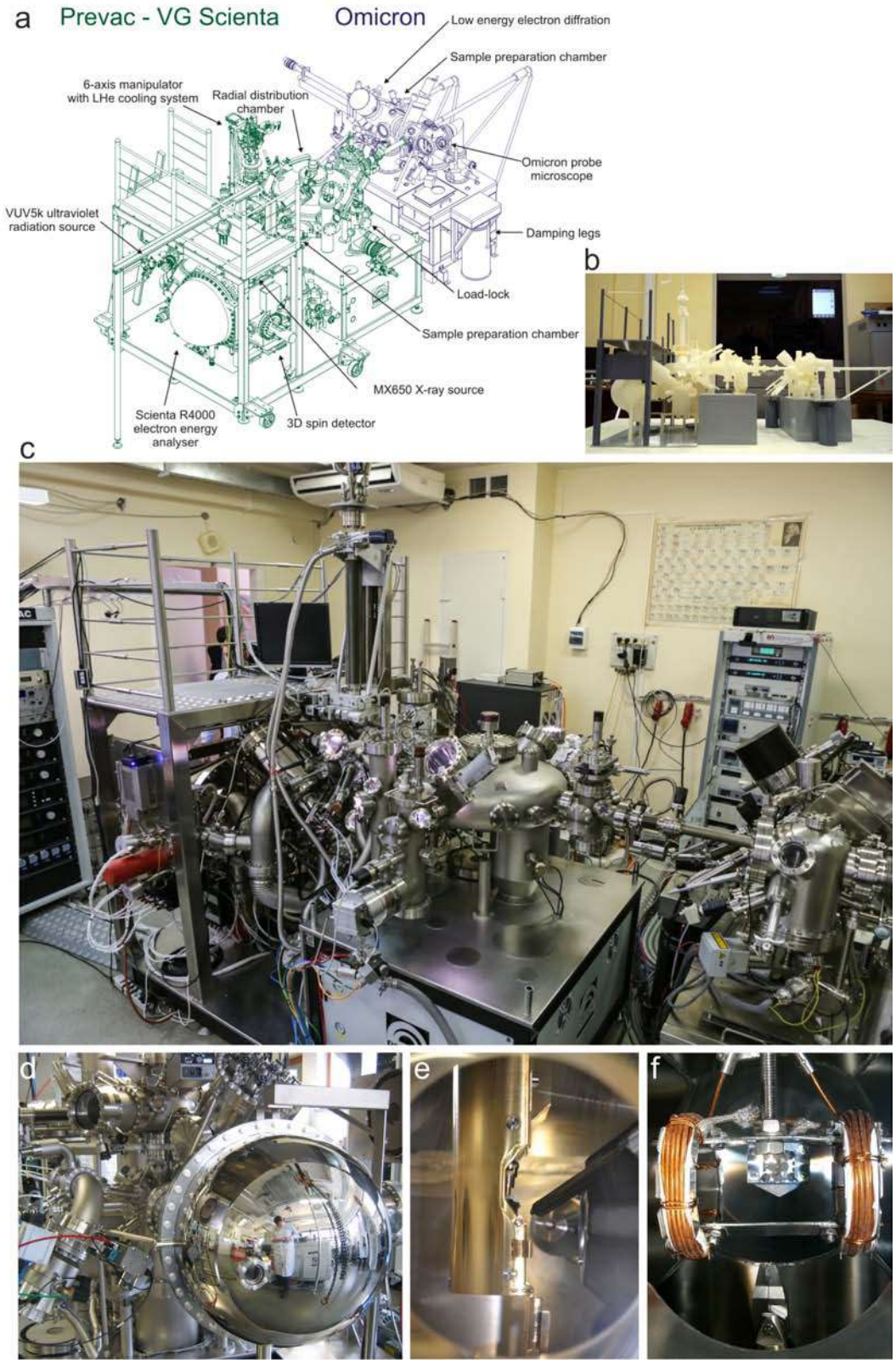

Figure 2.1 — (a) 3D drawing of the Nanolab setup, (b) 3D model printed on a printer, (c) general view of the setup in the lab room, (d) view of the VG Scienta R4000 hemispherical analyzer during factory acceptance tests, (e) view of the six-axis cryogenic manipulator and analyzer lenses in the analysis chamber, (f) Helmholtz coils for sample magnetization.

– at the laser ARPES and spin-ARPES setups at the HiSOR synchrotron, in the part of studies of the Gr/Au/Co(0001)/W(110) systems.

Time-resolved studies of magnetically doped topological insulators by two-photon time-resolved ARPES were performed at the Laser and Synchrotron Research (LASOR) Center of the Institute of Solid State Physics, University of Tokyo. Figure 2.2 shows a schematic of the setup consisting of a pulsed laser source, pump and probe pulse lines, and a hemispherical energy analyzer. The angle of incidence of the laser beam was 45° relative to the surface normal. The corresponding ARPES dispersion maps were measured in the direction perpendicular to the plane of incidence of the laser beam. The probe pulse was linearly p-polarized and had a photon energy of 5.9 eV. The pump pulse was s-polarized with hν = 1.48 eV. The duration of each individual pulse was only 170 fs. The pulses were repeated every 4 μs. The time delay between the pump and probe pulses for time-resolved measurements was varied from -4 ps before the pump pulse generation to 822 ps after the pump pulse generation (see Fig. 2.3). To measure the photovoltaic effect, the shift of the ARPES dispersion map generated by the pump pulse and the dispersion modification when the pump pulse power was varied from 2 to 20 mW were analyzed. The time delay between the pump and probe pulses for this experiment was chosen to be (4 μs – 4 ps), i.e., just before the generation of the next pump pulse. All measurements were performed at the sample temperature T = 11 K. A detailed description of the setup and the geometry of the experiment have been published in [201–203].

To perform STS measurements of the Gr/Au/Co(0001)/W(110) system, a scanning tunneling microscope JT-STM SPECS at the MIPT Center for Advanced Methods of Mesophysics and Nanotechnology was used. The setup has a three-chamber configuration for loading samples, preparing them, and performing measurements. The measuring chamber includes a cryostat with reservoirs for liquid nitrogen and liquid helium. The uniqueness of the microscope lies in the ability to cool the sample to a temperature of 1 K using the Joule-Thomson effect and control the magnetic field up to 3 Tesla during the experiment.

It should be noted that in all experimental setups the base pressure was maintained at a level of no more than 2×10^{-10} mbar, which ensured high surface cleanliness from adsorbed residual gas molecules during the experiment.

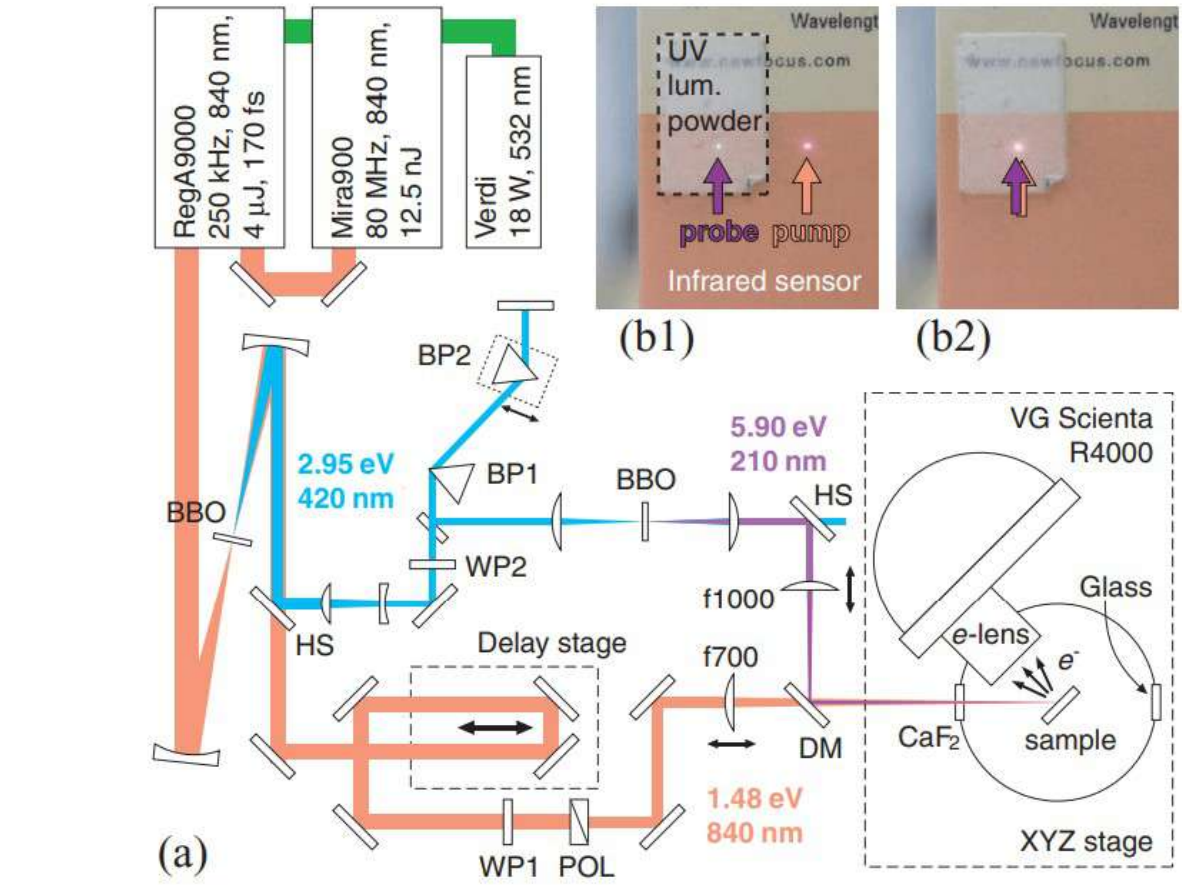

Figure 2.2 — (a) Schematic of a two-photon ARPES setup with a time delay line, (b) sensor device for visualizing the infrared pump beam and the ultraviolet probe beam. Images are taken before (b1) and after (b2) beam alignment. Figure is taken from [201].

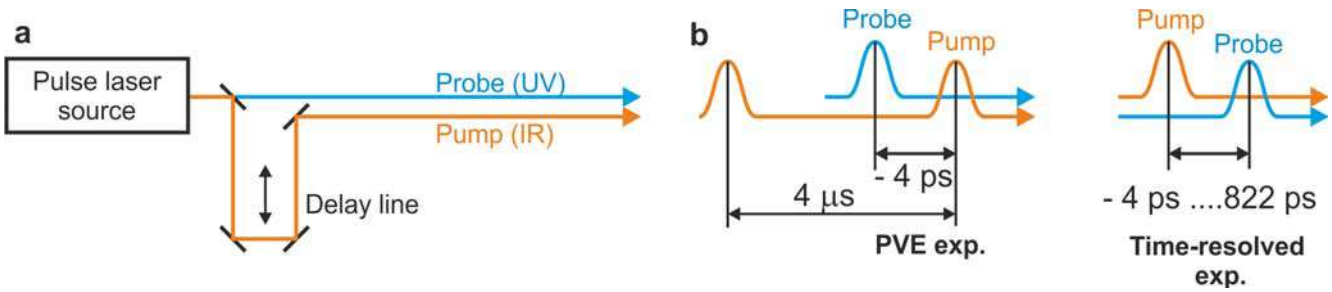

Figure 2.3 — (a) Schematic illustration of the pump-probe experiment. The time delay used in the various experiments is shown in tab (b).

2.2 Photoelectron spectroscopy method

The method of photoelectron spectroscopy is one of the modern methods for the study of occupied electronic states in solids. This method is based on the photoeffect phenomenon and consists in the registration of photoelectrons emitted from a solid when absorption of photons and transition of electrons between the ground and excited states takes place. When the energy $h\nu$ of an incident photon on the solid surface exceeds the sum of the binding energy E_{bin} and the work function from the solid Φ, some electrons leave the solid and are registered at the kinetic energy E_{kin} determined by the expression:

$$E_{\text{kin}} = h\nu - E_{\text{bin}} - \Phi, \tag{2.1}$$

with E_{kin} counting from the vacuum level and E_{bin} counting from the Fermi level. Thus, without taking into account electron scattering effects, the energy distribution of the escaped photoelectrons directly reflects the energy structure of the solid.

The most commonly used model to explain photoelectron spectra is the three-step model [204], which divides the photoelectron emission process into three independent steps. In the first step, photoexcitation of the electron occurs. Since the photon in the ultraviolet energy range has negligibly small momentum (including the energy region of 5 – 70 eV, which is used in this thesis), the quasi-wave vector $\vec{k_i}$ of the ground state is preserved up to the reciprocal lattice vector $\vec{G}$:

$$\vec{k}_f = \vec{k}_i + \vec{G}, \tag{2.2}$$

where the indices i and k correspond to the ground and excited states of the electron. The law of energy conservation is written in the following form:

$$E(\vec{k}_f) = E(\vec{k}_i) + h\nu, \tag{2.3}$$

Thus, the photoexcitation transition will be direct in the reduced Brillouin zone (see Fig. 2.4) and can occur only when the energy difference between the ground and excited states is equal to the photon energy. In the framework of perturbation theory, the probability of such a transition P_{if} is described by Fermi's golden rule [204; 205]:

$$P_{if} = \frac{2\pi}{\hbar} |< \psi_i | H' | \psi_f >|^2 \delta(E_f - E_i - h\nu), \tag{2.4}$$

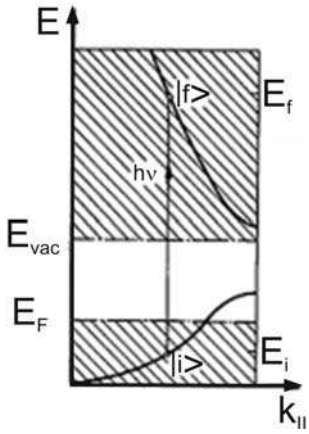

Figure 2.4 — Energy diagram of photoexcitation at the direct transition.

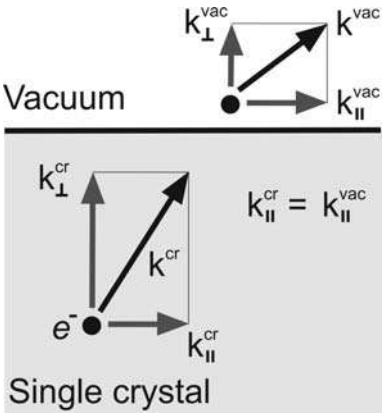

Figure 2.5 — Transmission of an electron through a surface potential barrier.

where $H' = \frac{e}{2mc}(\boldsymbol{A}\cdot\boldsymbol{p}+\boldsymbol{p}\cdot\boldsymbol{A})+\frac{e^2}{2mc^2}\boldsymbol{A}\cdot\boldsymbol{A}$ is a term of the Hamiltonian, describing the interaction between the electron and the electromagnetic field with vector potential $\boldsymbol{A}$ (scalar potential $\varphi = 0$). In the dipole approximation valid for radiation in the ultraviolet range (the photon momentum is small, i.e., the wavelength is longer than the localization region of electron orbitals), the transition matrix element can be written as follows [204]:

$$M_{if} \propto |<\psi_i|\boldsymbol{r}|\psi_f>| = \int \psi_i \boldsymbol{r} \psi_f d\boldsymbol{r}. \tag{2.5}$$

Hence, if the matrix element for any transition is zero, the transition is forbidden in the dipole approximation.

The next step of the three-step model is the transport of an excited electron to the surface of a solid body. The number of electrons that can leave the solid without scattering and escape into the vacuum depends exponentially on the escape depth d (the thickness of the layer through which the transport takes place):

$$N = N_0 e^{-\frac{d}{\lambda}}, \tag{2.6}$$

where λ is the mean free path length with respect to inelastic scattering, which for elements is determined by the empirical formula [206]:

$$\lambda = \frac{538}{E^2} + 0.41\sqrt{aE} \quad \text{(monolayers)}, \tag{2.7}$$

where E is the kinetic energy of electrons in electro-volts, a is the thickness of the monolayer in nm. Considering the equation 2.7 for kinetic energies of 10 – 300 eV,

we obtain that the mean free path length corresponds to the first few atomic layers of the solid surface. Photoelectron spectroscopy of the valence band using appropriate photon energies is a surface-sensitive technique.

The last step of the three-step model is the escape of the photoelectron into the vacuum through the surface potential barrier. Understanding this process is essential in determining the dispersion dependence of the initial state $E(\vec{k_i})$. The quasi-wave vector of an electron in a crystal can be decomposed into components parallel and perpendicular to the surface (see Fig. 2.5):

$$\vec{k}^{\text{cr}} = \vec{k}^{\text{cr}}_{\perp} + \vec{k}^{\text{cr}}_{\parallel} \tag{2.8}$$

As shown in Fig. 2.5, when a photoelectron passes the surface potential barrier, only the component of the quasi-wave vector parallel to the surface is preserved, although it can change to the surface reciprocal lattice vector $\vec{g}$, that is:

$$\vec{k}^{\text{vac}}_{\parallel} = \vec{k}^{\text{cr}}_{\parallel} + \vec{g} \tag{2.9}$$

As a result of refraction, the electron will move in a new direction, determined by the emission angle θ, when it enters the vacuum. Since the energy of a free electron is expressed as $E_{\text{kin}} = \frac{\hbar|\vec{k}|^2}{2m}$ and $|\vec{k}_{\parallel}| = |\vec{k}| \cdot \sin\theta$, then we obtain the relation for the wave vector component parallel surface that is essential for photoelectron spectroscopy with angular resolution:

$$|\vec{k}^{\text{vac}}_{\parallel}| = |\vec{k}^{\text{cr}}_{\parallel}| = \sqrt{\frac{2m}{\hbar^2} E_{\text{kin}}} \cdot \sin\theta \approx 0.52\sqrt{E_{\text{kin}}(\text{eV})} \cdot \sin\theta \tag{2.10}$$

If we register photoelectrons emitting at some angle θ and measure their kinetic energy, the wave vector component $|\vec{k}^{\text{cr}}_{\parallel}|$ can be easily obtained from the equation 2.10. Thus, the energy distribution of electrons measured for each polar angle θ gives us information about the band structure $E(\vec{k}_{\parallel})$ of the initial states in the single crystal (the final state under photoexcitation with photon energies above 50 eV is described not by a Bloch wave but by a plane wave, which is practically not modulated by the crystal potential). The situation with the wave vector component perpendicular to the surface is somewhat more complicated due to the fact that it decreases during the transfer across the surface because of the difference in the energy levels inside the crystal and in vacuum. It can be determined using the formula:

$$|\vec{k}^{\text{cr}}_{\perp}| = \sqrt{|\vec{k}^{\text{vac}}_{\perp}|^2 + \frac{2mV_0}{\hbar^2}}, \tag{2.11}$$

where V_0 is the internal potential of the crystal, which determines the difference of energies inside the crystal and in vacuum. If we measure the photoelectron emission in the direction normal to the surface of the single crystal ($k_{\|} = 0$) as a function of photon energy, the dispersion dependence of the initial state $E(\vec{k}_{\perp})$ can be easily obtained if the dispersion of the final state is known (at $h\nu > 50$ eV the final state can be considered as a plane wave).

Although the three-step model makes the photoelectron emission process clear and simple to discuss, it is rather complicated for the interpretation of experimental results and, as a rule, the one-step model is used instead. The basic idea of the one-step model is to describe the actual process of excitation, photoelectron transport to the crystal surface, and escape into the vacuum as a single quantum mechanical process including all multiple scattering events. In the framework of this model, the so-called time-inverse wavefunction of the low-energy electron diffraction state is used as the final state wavefunction in the equation 2.4. In the LEED method, an incident monochromatic electron beam is elastically scattered by atoms in the crystal, and the scattered waves are summed to form a diffraction pattern. Now, if we change the direction of the incoming beam, we get a monochromatic electron wave that originates from surface layers of the crystal (and attenuates deep into the crystal), similar to the electron wave produced by the photoelectron emission process. The use of inverse LEED wave function as the final state wave function has been successful for theoretical modeling of photoelectron emission spectra [207].

The method of photoelectron spectroscopy with angular resolution is widely used to measure dispersion dependence and symmetry of energy bands in solids. Initially, photoelectron spectroscopy covered two relatively narrow energy ranges realized in laboratory conditions: the first range is provided by the presence of gas-discharge sources ($h\nu \approx 10$ – 48 eV), and the second range is associated with a widespread source of photons - X-ray tubes using the radiation of K_{α} lines of some elements (mainly Mg and Al, photon energies of 1486.6 and 1253.6 eV, respectively). The wide energy gap between these two ranges has led to a natural separation into ultraviolet photoelectron spectroscopy (UPS), which is used in analysis of valence band, and X-ray photoelectron spectroscopy (XPS), which investigates both the valence band and the core levels. Angle-resolved photoelectron spectroscopy (ARPES) is commonly understood as angle-resolved UPS. In recent years, the use of a continuous-spectrum photon source, which is synchrotron radiation produced by the ultra-relativistic motion of charged particles in a storage ring, has found

increasing practical application. With the help of monochromators in this case it is possible to obtain monochromatic radiation, which in addition can be adjusted in energy from soft ultraviolet to hard X-rays. The use of a synchrotron allows us to obtain monochromatic radiation with high energy resolution and high intensity, which is extremely important for the measurement of spin polarization of emitted photoelectrons.

2.2.1 Angle-resolved XPS for analyzing layer depths and thicknesses

The Bouguer–Beer–Lambert law determines the attenuation of a monochromatic light beam when propagating in an absorbing medium, but is valid for the linear motion of electrons in a solid:

$$I = I_0 e^{-d/\lambda}, \tag{2.12}$$

where I_0 is the intensity of the electron beam before attenuation, λ is the mean free path length with respect to inelastic scattering, and I is the intensity after passing through a layer of thickness d in the perpendicular direction. If the electrons leave the solid at an angle θ relative to the normal to the surface, their path, and hence the attenuation of the intensity, increases:

$$I = I_0 e^{-d/(\lambda cos\theta)}. \tag{2.13}$$

If we calculate the logarithm of the ratio of XPS peak intensities for a certain angle θ and for normal emission, then its value will be proportional to the average depth of occurrence of the element of this peak. Thus, calculating the ratios of element peaks intensities allows us to determine the order of their location from the surface to the depth of the solid.

This thesis considers quasi-two-dimensional systems that consist of several layers of different elements, but may include a substrate element, for example, in case of formation of surface silicide. In this case, the XPS peak of the element is decomposed into components at different energies corresponding to the chemical environment of the element, and the intensity of each component is determined.

Knowing the intensity of XPS peaks of the elements and the depth of their occurrence, it is possible to estimate the thickness of each of the layers.

The simplest way to calculate the intensity of photoelectron emission is to sum the intensity from each layer [208; 209]:

$$I = \sigma\varphi AT \sum_{i=0}^{\infty} n e^{-i \cdot d/(\lambda cos\theta)}, \tag{2.14}$$

where σ is the photoionization cross section of the atomic subshell at excitation energy $h\nu$, φ is the incident photon flux, A is the analysis region, T is the photoelectron detection efficiency (energy analyzer transmission function), n is the concentration of atoms in the layer, d is the interlayer distance, λ is the mean free path length of electrons, and θ is the emission angle.

Using the Taylor series expansion for a semi-infinite homogeneous crystal we obtain:

$$I_{\infty} = \sigma\varphi AT n_{bulk} \frac{1}{1 - e^{-d_{bulk}/(\lambda cos\theta)}} \tag{2.15}$$

And the intensity of a layer of thickness d can be expressed as follows:

$$I = I_{\infty} \cdot (1 - e^{-d/(\lambda cos\theta)}) \tag{2.16}$$

Consider a system consisting of a layer of element A on a substrate of element B. Using equations 2.15 and 2.16, we obtain the ratio of the peak intensities of the elements:

$$\frac{I^A}{I^B} = \frac{I^A_{\infty} \cdot (1 - e^{-d/(\lambda^{A,A} cos\theta)})}{I^B_{\infty} \cdot e^{-d/(\lambda^{B,A} cos\theta)}} \approx \frac{\sigma^A n^A_{bulk} (1 - e^{-d^B_{bulk}/(\lambda^{B,B} cos\theta)}) \cdot (1 - e^{-d/(\lambda^{A,A} cos\theta)})}{\sigma^B n^B_{bulk} (1 - e^{-d^A_{bulk}/(\lambda^{A,A} cos\theta)}) \cdot e^{-d/(\lambda^{B,A} cos\theta)}} \tag{2.17}$$

where $\lambda^{B,A}$ is the mean free path for electrons moving with peak energy B in material A. Using the known values of the ionization cross section, atomic concentration, interlayer distances, and the measured ratio of the XPS peak intensities of elements A and B, we obtain an estimate of the layer thickness d. Similarly, it is possible to estimate the thickness of each layer for a system with several layers. It should be noted that this analysis is based on the following assumptions: the layers and the substrate are uniform in composition and atomic concentration, have flat surfaces, the layers are uniform in thickness, and the effects of photoelectron diffraction and elastic scattering do not significantly affect the thickness estimate.

2.2.2 Geometry of ARPES experiment

The method of photoelectron spectroscopy with angular and spin resolution is based on the measurement of the photoelectron beam intensity for some emission angle and photoelectron energy (Fig. 2.6). The use of a six-axis manipulator allows us to select any point (direction) in the surface Brillouin zone of the sample. The detector can be a set of channelrons (photoelectron multipliers) or a microchannel plate. The advantage of using a microchannel plate is the possibility of simultaneous registration of a range of emission angles ($\pm 15^{\circ}$). In the used energy analyzers with microchannel plates, the output slit of the analyzer was oriented parallel to the manipulator axis R_1, as shown in Fig. 2.6. In this case, the recorded angle range of the microchannel plate corresponds to the angle R_3, which further extends the limited range of manipulator angles along R_3, typically from -5° to 10°. For the same reason, the dispersion dependence of π states of graphene is measured by rotating the sample around the R_1 axis with a wider range of available angles, up to 60° from the normal to the sample surface (for the Nanolab setup). In this work, linear (s and p) and natural polarization of the radiation was used. To measure the spin polarization of a photoelectron beam, it must be physically divided into two beams and directed into two Mott detectors using electron lenses. One of the Mott detectors will measure the S_x and S_z polarizations of the photoelectron beam, while the second one will measure the S_y and S_z polarizations. The S_z polarization is called the out-of-plane component in the case of normal emission, and the S_y polarization is called the Rashba component in the case of measurements for angles along the R_1 axis. It should be noted that the measured spin-resolved dispersion dependences reflect the spin polarization of the initial states only if the spin polarization of the final state and the spin rotation and flip effects depending on the radiation polarization do not contribute significantly to the resulting spin texture during photoelectron emission [210–212].

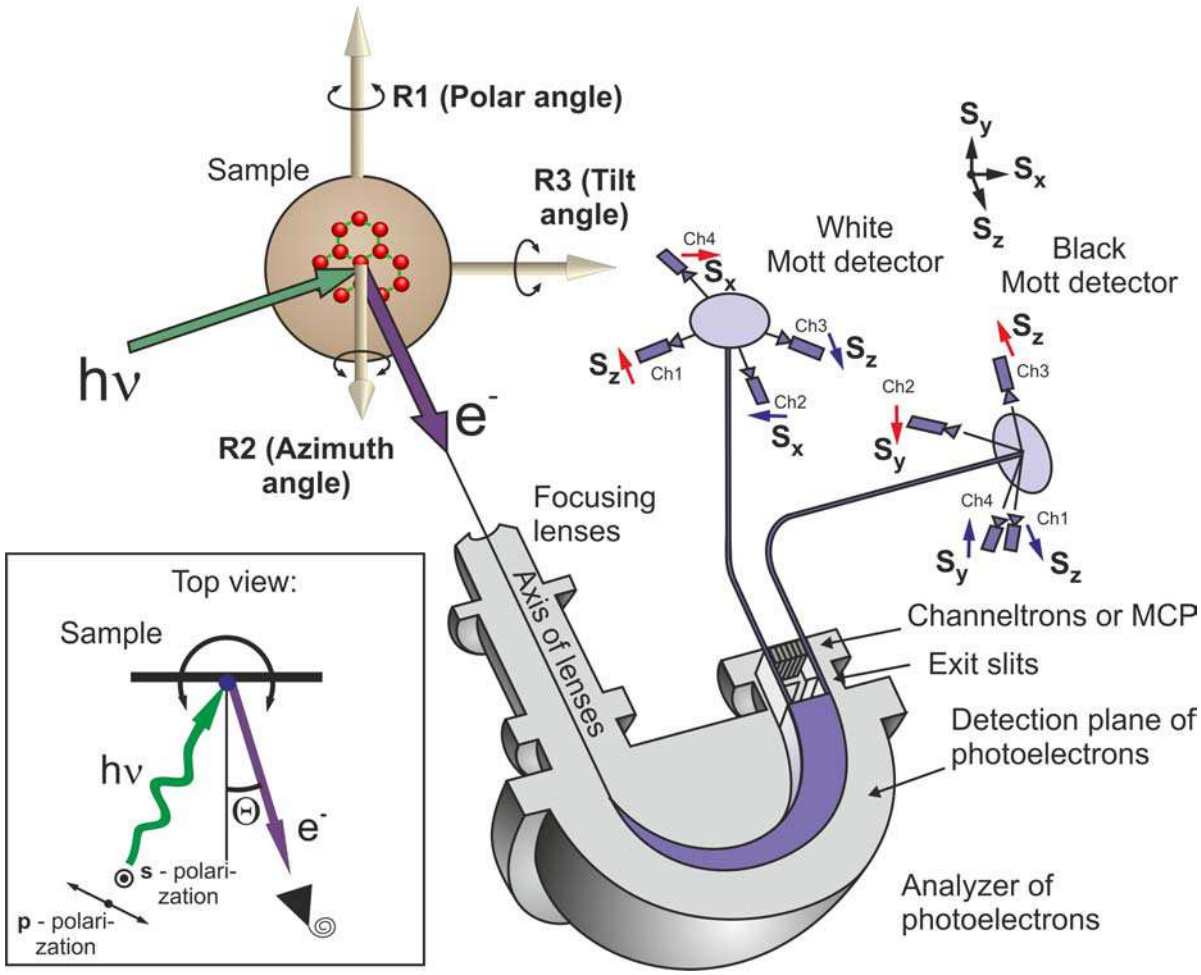

Figure 2.6 — Schematic illustration of a photoelectron spectroscopy experiment.

2.2.3 Procedure for processing spin-resolved ARPES data

Let us start with the calculation of the spin polarization, it can be obtained as follows:

$$P = \frac{1}{S} \times \frac{I_L - I_R}{I_L + I_R}, \tag{2.18}$$

where I_L and I_R are the intensities of scattered photoelectrons collected by the left and right channels of the Mott detector, respectively; S is the Sherman function, equal to 0.14 for the Nanolab detector.

The spin-up and spin-down intensities were calculated as follows:

$$I_{up} = \frac{1+P}{2} \times (I_L + I_R), \quad I_{down} = \frac{1-P}{2} \times (I_L + I_R), \tag{2.19}$$

where I_{up} and I_{down} are the intensities of states with spin-up and spin-down projections on a given axis.

The statistical error of spin polarization can be calculated by the formula [213]:

$$\Delta P = \frac{1}{S\sqrt{I_L + I_R}}. \tag{2.20}$$

To reduce the statistical error, averaging over N points of both the measured data themselves and the polarization curve can be applied. As a rule, this is accompanied by a N-fold decrease in the energy step of the spin spectra, which increases the energy uncertainty but reduces the intensity statistical error.

The polarization curve averaging can be expressed by the formula [214]:

$$P_{aver} = \frac{1}{N}\sum_{n=1}^{N} P_i, \tag{2.21}$$

with a statistical error

$$\Delta P_{aver} = \frac{\Delta P}{\sqrt{N}} = \frac{1}{S\sqrt{N \cdot (I_L + I_R)}}. \tag{2.22}$$

Accordingly, the $\Delta I_{up,down}$ error based on the 2.19 equation can be calculated as

$$\Delta I_{up,down} = \frac{1}{2}\sqrt{I_L + I_R}\sqrt{1 \pm 2P + P^2 + \frac{1}{S^2 N}}. \tag{2.23}$$

Thus, averaging over N points reduces the statistical error of measurements. However, averaging over an excessive number of points should be avoided in order not to lose the energy resolution of the experimental intensity peaks.

2.3 Synthesis and sample preparation

2.3.1 Description of techniques and samples under study

The following techniques, written in co-authorship with the candidate, were used to synthesize the samples and prepare the surface for measurements:

– technique for cleaning the surface of refractory and transition metal single crystals to atomic purity during research (certified at SPbU); describes operations on cleaning of single crystals of refractory metals by the method of

short-term high-temperature annealing and single crystals of transition metals using ion etching under ultra-high vacuum conditions; details of substrate cleaning are also described in Refs. [1; 117; 215; 216];

- technique of permanent deposition of various metals with continuous control of the thicknesses of the deposited layers during research (certified in SPbU); is based on the experimental registration of quantum-dimensional effects in thin metal layers on the surface of single crystals continuously during the increase of the thickness of the deposited film, starting from submonolayer thicknesses, using the ARPES method. The film thickness can be estimated with an accuracy of up to tenths of a monolayer and controlled by the observed spectrum of quantum well states by their energy and number. This technique can be used in the fabrication of precision quantum nanoelectronics devices and new nanostructured materials;
- technique for testing the crystal structure of single crystal surfaces and their orientation for investigation by photoelectron spectroscopy with angular resolution based on high-resolution details of LEED patterns during research (certified at SPbU); is used for correct orientation of a single crystal system in the required crystallographic direction for further investigation by the ARPES method of dispersion of energy bands along the selected directions of the surface Brillouin zone with high symmetry;
- technique for measuring the dispersion of energy bands and the structure of occupied and unoccupied states by photoelectron spectra with high angular and energy resolution during research (certified at SPbU); is used to study the peculiarities of the electronic structure and dispersions of electronic states in the required directions of the Brillouin zone;
- technique of elemental and chemical analysis of solid surfaces by the method of photoelectron spectroscopy of core levels; contains a description of the main required technological operations to determine the presence of elements in the sample and their chemical state using a photoelectron spectrometer Thermo Fisher Scientific Escalab 250Xi;
- technique of manufacturing and preparation of ultrahigh vacuum scanning probe microscope tips for obtaining high resolution; describes the conditions of tip preparation by electrochemical etching and high-temperature annealing under vacuum conditions.

Monocrystalline samples of magnetically doped topological insulators and BiTeI semiconductors with different concentrations of magnetic impurities were synthesized at Novosibirsk State University by the Bridgman-Stockbarger method. The impurity doping is expressed in atomic percentages, where magnetic V(Mn) atoms mainly substitute Bi atoms. The doping level of V(Mn) x% in magnetically doped BiTeI corresponds to the stoichiometry $\mathrm{Bi_{(1-x/100)}V(Mn)_{(x/100)}TeI}$, and in the case of magnetically doped topological insulators $\mathrm{Bi_{2-x/100}V_{x/100}Te_{2.4}Se_{0.6}}$ и $\mathrm{Bi_{1.34-x/100}V_{x/100}Sb_{0.66}Te_3}$. The clean surfaces of the samples were obtained by cleavage under ultrahigh vacuum conditions.

In addition to single-crystal substrates W(110) and Pt(111), *N*-type and semi-insulating Si-terminated 6*H*-SiC(0001) wafers purchased from TankeBlue Semiconductor Co. Ltd. (Beijing, China) were used in this work (catalog numbers W26N0P-CPF and W26S0P-CPF, respectively). Influence on the conditions of zero-layer graphene synthesis and further intercalation depending on the substrate type was not found.

The amount of deposited Al, Co, Au, Pt, and Gd metal layers by physical vapor deposition was controlled using quartz microbalance and varied in the range from units to several tens Å. The annealing temperature of the samples during surface cleaning and further synthesis was determined using Keller CellaTemp PA 20 AF 2/C and PA 29 AF 22/C pyrometers. When synthesizing the zero-layer graphene on 6*H*-SiC(0001), the sample temperature was determined using a Keller CellaTemp PA 20 AF 2/C pyrometer with a luminosity factor of 0.6 for a measurement angle of 60° from surface normal. The use of the same pyrometer and the same measurement conditions ensured a high reproducibility of the synthesis temperature with an accuracy of 20 °C, since otherwise different reconstructions on the surface would be obtained.

Graphene was synthesized by chemical vapor deposition of propylene ($\mathrm{C_3H_6}$). For thin layers of Co(0001) and Pt(111) single crystal, previously unknown conditions for the synthesis of single-domain, well-oriented graphene were found, which will be given in the corresponding chapters of this work.

The Co film was magnetized by a current pulse through coils placed near the sample (see Fig. 2.1 (f)). The peak value of the applied magnetic field at the sample position and the decay time were 0.3 T and $\sim$ 0.2 ms, respectively.

2.3.2 Procedure for cleaning of Pt(111) single crystal

A special procedure was developed for the cleaning of Pt(111) single crystal due to the increasing amount of carbon contamination in the crystal after multiple syntheses of graphene on its surface by propylene cracking. Preparation of a clean and atomically flat Pt(111) single crystal surface is important for the subsequent synthesis of graphene by chemical vapor deposition. The articles [217—222] reported the use of elevated temperatures in the range of 900 – 1230 K to synthesize graphene with dominant 30° rotational domains relative to the platinum substrate. Such a large difference in synthesis temperatures and in the area ratio of 30° rotational domains to other domains may depend on the history of using the single crystal as a substrate for graphene synthesis. It was found that after several repeated graphene syntheses followed by single crystal cleaning, the fraction of misoriented domains with respect to 30° domains of graphene increases. A possible reason for this behavior is the insufficient cleaning of the Pt single crystal from carbon dissolved in the near-surface layer after applying conventional cleaning procedures described elsewhere [15; 217—219; 221; 222]. Moreover, it has been reported that the 30° domain of graphene can be synthesized by carbon segregation at an elevated temperature of 1600°C [223]. After cleaning, angle-resolved XPS measured at a sliding angle to the surface (to increase surface sensitivity) and STM were used to detect the possible presence of carbon-containing nanoclusters. To avoid the formation of clusters, the procedure for preparing the pure surface of Pt(111) single crystal used in [15] was modified:

1. preliminary Ar^+ ion etching of the surface on the Oxford IonFab 300 setup for 10 min at an ion incidence angle of 60°, an energy of 0.5 keV, and a current density of 12 μA/mm^2,
2. transfer to the sample preparation and analysis setup and annealing at 450 °C,
3. Ar^+ ion etching of the surface with ion energies of 1.5 keV and 0.6 keV and a current density of 0.4 μA/mm^2 for 2 hours for each ion energy,
4. short-term annealing for 15 s at 850 °C,
5. repeated O_2 treatment cycles for 1 hour (at 750 °C and partial oxygen pressure of 2.6×10^{-7} mbar) and short-term annealing for 15 s (at 850 °C) until a clean surface was obtained according to LEED, angle-resolved XPS and STM data.

After obtaining a clean Pt(111) surface, graphene was synthesized by cracking propylene (C_3H_6) at a pressure of 1.4×10^{-7} mbar and a sample temperature of 1050 °C for 25 min.

2.4 Density functional theory method

Over the past 30 years, density functional theory has been the main method for quantum mechanical modeling of periodic systems. In the Kohn – Sham formalism, this method replaces the intractable problem of several interacting electrons in the field of atomic nuclei with a simpler problem of independent electrons moving in some effective potential [224]. This effective potential includes the static potential of atomic nuclei, the Coulomb repulsion, the exchange interaction, and the electron correlation. The exact properties of the exchange-correlation potential continue to play a central role in constructing approximations. In recent years, the local density approximation (LDA) and generalized gradient approximation (GGA) have been frequently used, but they do not take into account some features of the potential, such as peaks and steps, which are crucial for predicting the static electric polarizability and band gap, as well as for describing bond breaking and strongly correlated systems [225]. It should be noted that the density functional theory method in combination with structural optimization has proven to be quite accurate and effective in obtaining results in a reasonable time frame. The use of the DFT method with structural optimization in conjunction with neural networks and machine learning has proven to be an effective way to search for new compounds [226; 227].

The electronic structure of the systems investigated in this work was calculated in the OpenMX, VASP and WIEN2k software packages. The systems were modeled as supercells in the approximation of periodic crystalline slabs. These calculations helped to correctly interpret the experimental results obtained and more fully characterize the synthesized systems. Direct work in the corresponding software packages was performed by M. M. Otrokov and A. V. Tarasov. Some of the calculations were performed in the resource center “Computing Center” of the SPbU Science Park.

The first-principles theoretical calculations of the Gr/Pt, ZLG/SiC(0001), and Gr/CoSi/$CoSi_2$ interfaces were performed using the OpenMX package, which

provides a fully relativistic implementation of the DFT with localized pseudo-atomic orbitals [228; 229] and norm-conserving pseudopotentials [230]. The exchange-correlation energy in the Perdew–Burke–Ernzerhof (PBE) scheme of the generalized gradient approximation (GGA) was used [231; 232]. More detailed information regarding the chosen basis functions, k-grid size, total energy convergence criterion and other parameters can be found in the published papers [8; 10].

The theoretical calculation of Gr/Au was performed using the projector augmented wave (PAW) method [233] implemented in the VASP code [234; 235]. The exchange-correlation energy was considered using the generalized gradient approximation GGA [232]. The Hamiltonian contained scalar-relativistic corrections, and the spin-orbit coupling was taken into account by the second variational method [236]. The DFT-D3 approach [237; 238] was used to describe the van der Waals interactions. Additional information on the calculation parameters is published in the article [4].

Theoretical calculations of Gr/Pt_xGd, Au/Co(0001), and Gr/Au/Co(0001) interfaces have been performed by the full-potential augmented plane-wave + local orbitals method [239] implemented in the WIEN2k software code [240], together with the generalized gradient approximation GGA in the PBE version [232]. The spin-orbit interaction was taken into account by the second-variation method with scalar-relativistic orbitals as basis functions [236]. The unfolding of the band structure of the supercell was carried out according to the technique described in the work of O. Rubel et al. [241]. Additional information on the calculation parameters is published in the articles [5—7].

2.5 Auxiliary software

Unit cell drawings were created and presented using VESTA software [242]. STM data processing was performed using Gwyddion software [243] with the functions of base alignment and two-dimensional fast Fourier transform filtering. The remote control unit for the VUV5k ultraviolet radiation source of the photoelectron spectroscopy setup Univer-M was created and used on the basis of Arduino controller.

3. Induced spin-orbit interaction in thin metal layers

The search for new materials for spin filters (valves), the main task of which is the generation of controlled spin-polarized current, has attracted great interest in the spin structure of the surface of single crystals. In the absence of magnetic fields, the spin polarization of the surface is due to spin-orbit interaction, which for quasi-two-dimensional surface or interface states leads to their energy splitting and spin polarization. For a single crystal with inversion symmetry in the volume, energy spin splitting of surface states is observed according to the Rashba-Bychkov model due to the potential gradient perpendicular to the surface (see paragraph 1.1.1). A pioneering experiment by S. LaShell et al. found spin-orbit Rashba splitting for the Au(111) surface state [114; 244]. The situation becomes more complicated in dielectrics, the conducting two-dimensional states in the band gap are divided into two topologically different classes depending on the symmetry of the bulk band structure: trivial (e.g., split Rashba states) and topological states protected by time reversal symmetry. In the first case there is an even number of crossings by surface (edge) states of the Fermi level between two points of the two-dimensional Brillouin zone invariant to time reversal, and in the second case this number is odd [245]. It is natural to ask how the electron states on the surface of heavy metals with strong spin-orbit interaction behave in this regard. In addition to the Au(111) surface state, more complex “topological metal” states were found on the Bi(114) [246] and Sb(111) [247] surfaces, which were associated with the topological surface states of topological insulators [245; 248].

3.1 Electron states of the pure surface of single crystal W(110) and with thin layers of Al

The valence electron states of $5d$ character of pure W(110) surface and modified by the adsorption of Al monolayer have been investigated by spin-resolved ARPES (spin-ARPES). It is known that the two-dimensional states formed in thin metal films on W(110) are strongly influenced by the spin-orbit interaction in the substrate [115; 117; 215; 216; 249]. This was first established for Li/W(110) [115], and spin

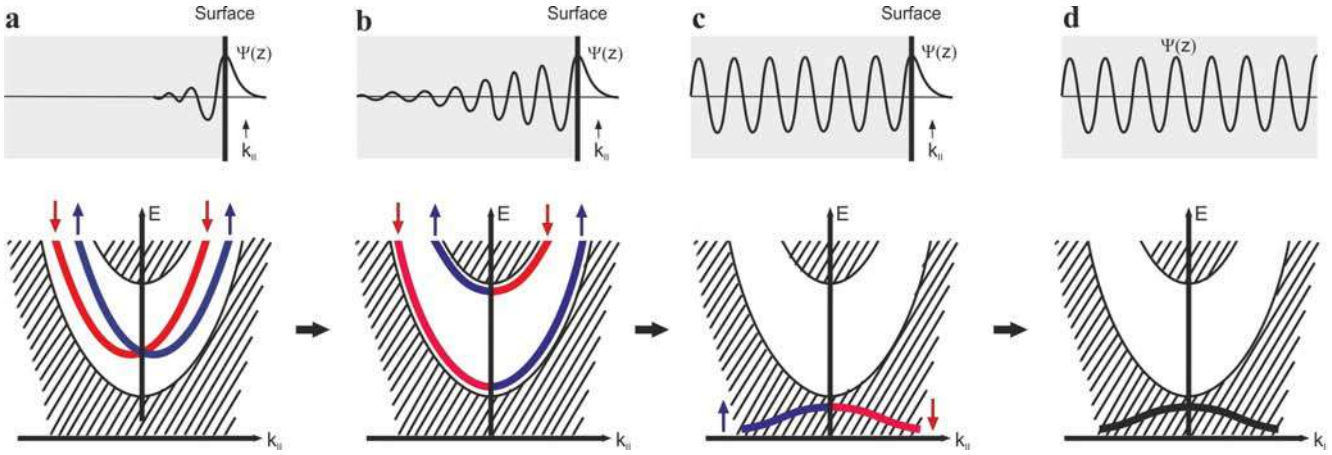

Figure 3.1 — Spin structure of electron states with different localization of the wave function: surface state (a), surface resonances (b), bulk states in the presence of a surface (c), and for an infinite crystal (d). The spin-↑ and spin-↓ states are indicated by blue and red lines, respectively.

polarization of the states was measured for H/W(110) [249]. The adsorbed noble metal layers [117; 215; 216] are also characterized by a large spin-orbit splitting caused by the substrate and uncharacteristic of the layer elements, as it was found to be much smaller on Mo(110) than on W(110) [115; 117].

The classical Rashba effect leads to a shift of quasi-two-dimensional states of opposite spins in opposite $\mathbf{k}_{\|}$ directions, see Fig. 3.1 (a). In [250; 251], it was shown that surface spin polarization depending on $\mathbf{k}_{\|}$ can be observed for bulk bands as well. Although the Kramers degeneracy of the bulk states is not lifted (Fig. 3.1 (c)), polarization appears on the surface due to spin-dependent reflection of Bloch waves from the surface. In a surface-sensitive experiment using the spin-ARPES method, it turns out to be possible to register the spin density beating of bulk states near the surface [250]. In this case, an asymmetric spin structure is observed in the vicinity of the $\bar{\Gamma}$ point (Fig. 3.1 (c)). In the context of the conducted studies, spin-polarized surface resonances W(110) with a dispersion similar to the Dirac cone and a spin structure qualitatively different from the classical Rashba picture and reminiscent of topological surface states were discovered (Fig. 3.1 (b,c)).

The measured dispersion dependences $\mathrm{E}(\mathrm{k}_{\|})$ of the photoelectron emission intensity along the $\bar{\Gamma}\bar{\mathrm{S}}$ direction are shown for a pure W(110) surface in Fig. 3.2 (a) and for a surface covered with 1 monolayer of Al in Fig. 3.2 (b). The assignment of the spectral maxima to the spin-↑ state (blue lines) and spin-↓ state (red lines) in Fig. 3.2 is made on the basis of the spin-ARPES spectra shown in Fig. 3.3. The dispersion dependences of W(110) are in good agreement with earlier measurements

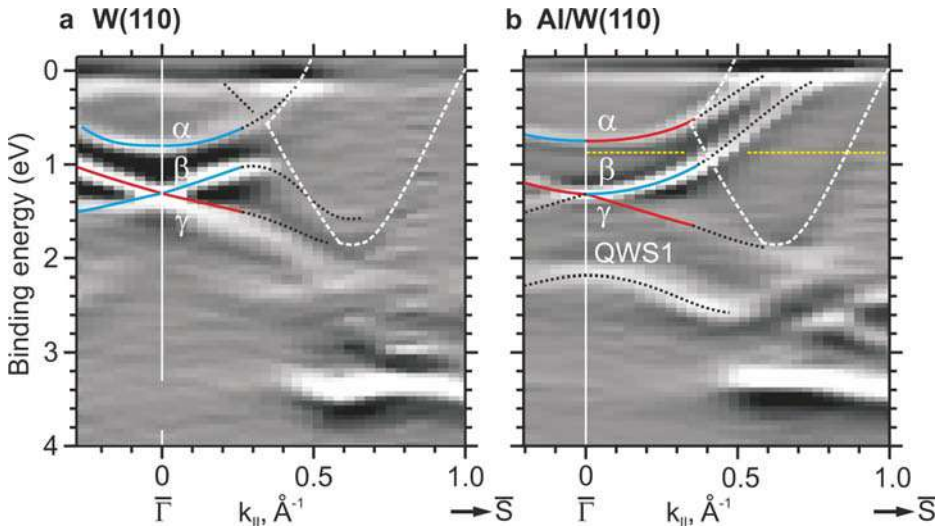

Figure 3.2 — ARPES measurements for pure W(110) (a) and for Al/W(110) (b) as the second energy derivative of the intensity. The distribution of the Rashba spin component in panels (a) and (b) as blue and red lines is adopted from the spin-resolved spectra shown in Fig. 3.3. The black dashed lines show the dispersion of the ARPES intensity maxima in regions where spin-resolved measurements were not available due to insufficient intensity/statistics. The white dashed line highlights the bulk projected gap $\mathbf{k}_{\|}$. The label QWS1 in panel (b) indicates the quantum well state in Al.

in Refs. [115; 252; 253]. In photoelectron emission normal to the surface of the single crystal, the spectra show the most pronounced surface resonance at a binding energy of 1.3 eV, located in the spin-orbit pseudogap [252] (between Γ_{7+} and Γ_{8+} states [254]), to which the β and γ dispersion branches converge (Fig. 3.2 (a)). The dispersion branch of the α state is near the edge of the pseudogap (at the $\bar{\Gamma}$ point at a binding energy of 0.8 eV). The measured branch γ with spin-↓ polarization disperses from 1.3 eV at the $\bar{\Gamma}$ point to 2.3 eV at $k_{\|} = 0.6$ Å^{-1}, where it merges with the edge of the $\bar{\Gamma}\bar{\mathrm{S}}$ projected gap. The oppositely polarized branch β rises and reaches the edge of the gap at 0.4 Å^{-1}. It should be noted that the α state has no second spin-split component, and somewhat surprisingly, its polarization does not change sign at the $\bar{\Gamma}$ point. In Al/W(110), we also observe a separate state α (Fig. 3.2 (b)), and here its spin polarization is clearly antisymmetric, i.e. spin-↓ for $+k_{\|}$ and spin-↑ for $-k_{\|}$. In this system, the β state is pronounced and polarized opposite to the α state. And the γ state in Al/W(110) is much less intense than in pure W(110), but is well distinguishable on the second derivative of the intensity with respect to energy, especially at large angles, see Fig. 3.2 (b). This indicates that the dispersion branches cross the line of constant energy an odd number of times between the points $\bar{\Gamma}$ and $\bar{\mathrm{S}}$ and for a given energy interval between the lower edge of the α branch and the lower

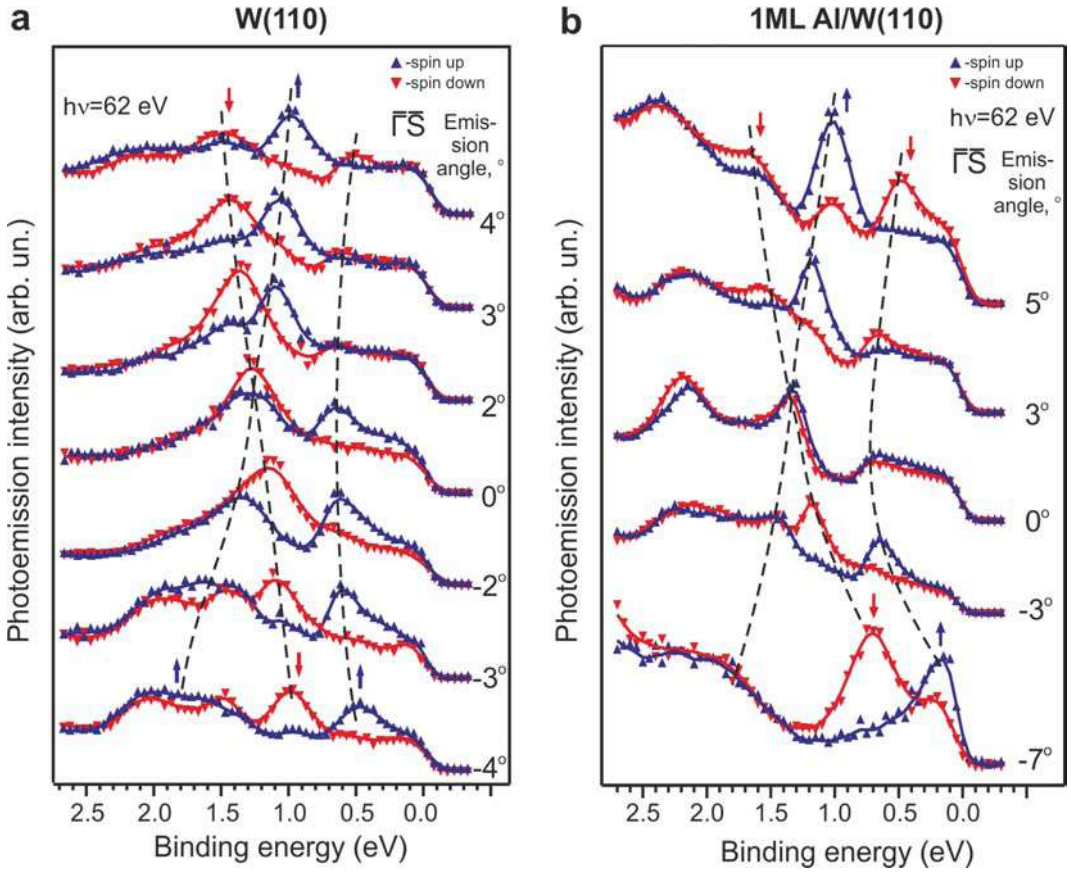

Figure 3.3 — Spin- and angle-resolved dispersion dependences for pure W(110) (a) and for Al/W(110) (b). The photoelectron intensity with spin-↑ is shown by blue triangles pointing upward, and spin-↓ by red triangles pointing downward. The projection of spin onto the axis lying in the plane of the sample and perpendicular to the wave vector component $k_{||}$ (Rashba component) is presented.

edge of the β branch (see the yellow dashed line in Fig. 3.2 (b)), implying a behavior topologically different from the simple Rashba-Bychkov model.

To explain the unusual spin structure of the electronic states of the studied quasi-two-dimensional systems, a comparison with the theoretical spin density distribution shown in Fig. 3.4 and 3.5 was carried out. The *ab initio* calculations were performed in a repeating slab geometry (29 atomic layers) using the self-consistent (in the local density approximation) full-potential method of linearized augmented plane waves (LAPW) [255]. Relativistic effects were taken into account within the two-component approximation [256]. The total projected density of states (DOS) is shown in Fig. 3.4 (a) and (d) for W(110) and Al/W(110), respectively. It is defined as the sum over all (discrete) λ states with energy E and Bloch vector $\mathbf{k}_{||}$: $N(E,\mathbf{k}_{||}) = \sum_{\lambda} \delta(E_{\lambda\mathbf{k}_{||}} - E)$, with the δ function replaced by a Gaussian function with a full width of 0.2 eV at half maximum. The local $\mathbf{k}_{||}$ projected DOS, with depth resolution, is the sum of

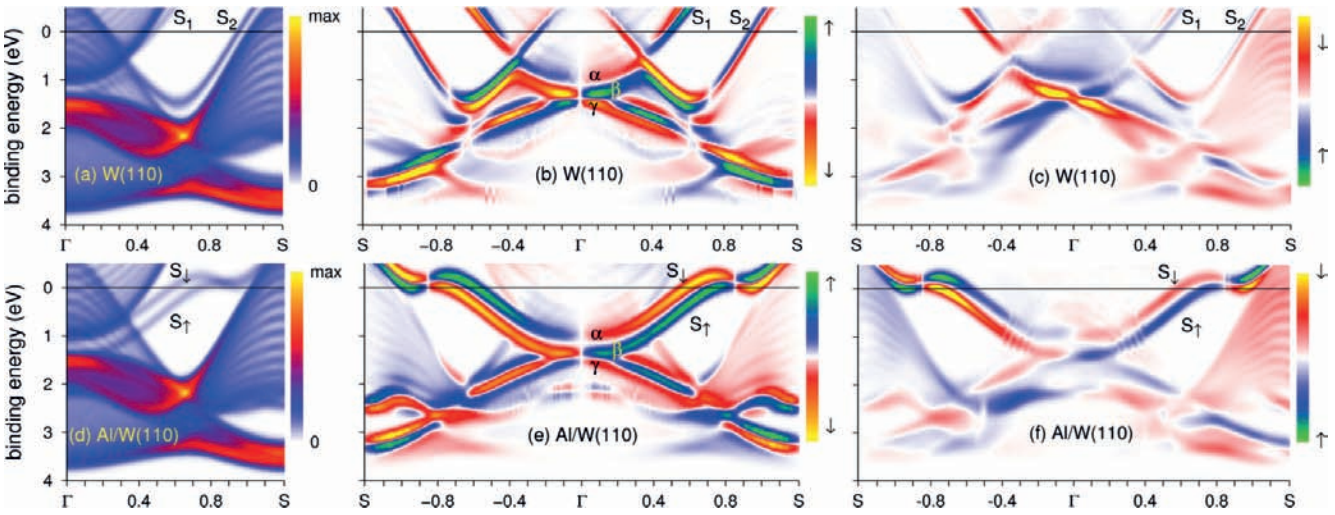

Figure 3.4 — Calculated density of states (DOS) and spin-ARPES intensity maps for W(110) (top row) and Al/W(110) (bottom row). Projected DOS $\mathrm{N(E,k_{\|})}$ along $\bar{\Gamma}\bar{\mathrm{S}}$: total DOS (a) and (d); net-spin spectral density $\mathrm{S(E,k_{\|})}$, (b) and (e); spin-ARPES intensity maps, (c) and (f). The figure is taken from the paper [3]; the calculation was performed by E. E. Krasovskii.

spin densities σ integrated over the plane parallel to the surface $z = const$, with $\mathbf{r} = (\mathbf{r}_{\|},z)$: $\rho^{\sigma}_{\mathbf{k}_{\|}}(z,E) = \int d\mathbf{r}_{\|} \sum_{\lambda} |\psi^{\sigma}_{\lambda\mathbf{k}_{\|}}(\mathbf{r})|^2 \delta(E_{\lambda\mathbf{k}_{\|}} - E)$.

The net-spin spectral density $S(E,\mathbf{k}_{\|})$ (Fig. 3.4 (b,e)) is the integral of the spin density $\rho_{\mathbf{k}_{\|}} = \rho^{\uparrow}_{\mathbf{k}_{\|}} - \rho^{\downarrow}_{\mathbf{k}_{\|}}$ on the interval z from the middle of the slab to the middle of the vacuum region. The real spatial distribution $S(E,\mathbf{k}_{\|})$ is revealed using a partial DOS ΔS with layer-by-layer resolution (Fig. 3.5 (a,b) for W(110) and Fig. 3.5 (e,f) for Al/W(110)), where the integration in both cases is over half of the space from the topmost W layer to the right, i.e., only for the vacuum region for W(110) and for the Al monolayer and vacuum for Al/W(110). Figure 3.5 (c,d) for W(110) and Figure 3.5 (g,h) for Al/W(110) show the charge and spin density distribution in energy and depth for $k_{\|} = 0.1$ Å^{-1}, indicating that the electronic states in the region of the outermost atomic layers are spin-polarized, while weak oscillations $p_{\mathbf{k}_{\|}}(z)$ with lattice periodicity remain in the depth of the crystal [251].

For a pure W(110) surface, two surface states $\mathrm{S_1}$ and $\mathrm{S_2}$ are observed, both of which are spin-split. The structure of the spin DOS has a clear correspondence with the dispersion branches of the ARPES intensity in Fig. 3.2 (a). As shown in Fig. 3.4 (b), the dispersion branches of states $\mathrm{S_{\downarrow}}$ and $\mathrm{S_{\uparrow}}$ join at the point $k_{\|} = +0.3$ Å^{-1} with the branches of states α and β, respectively. The β state has higher spin density and penetrates more deeply into the vacuum than α (see Fig. 3.5 (b-d)). The γ state is the spin-orbit component of the β state with opposite spin: they intersect

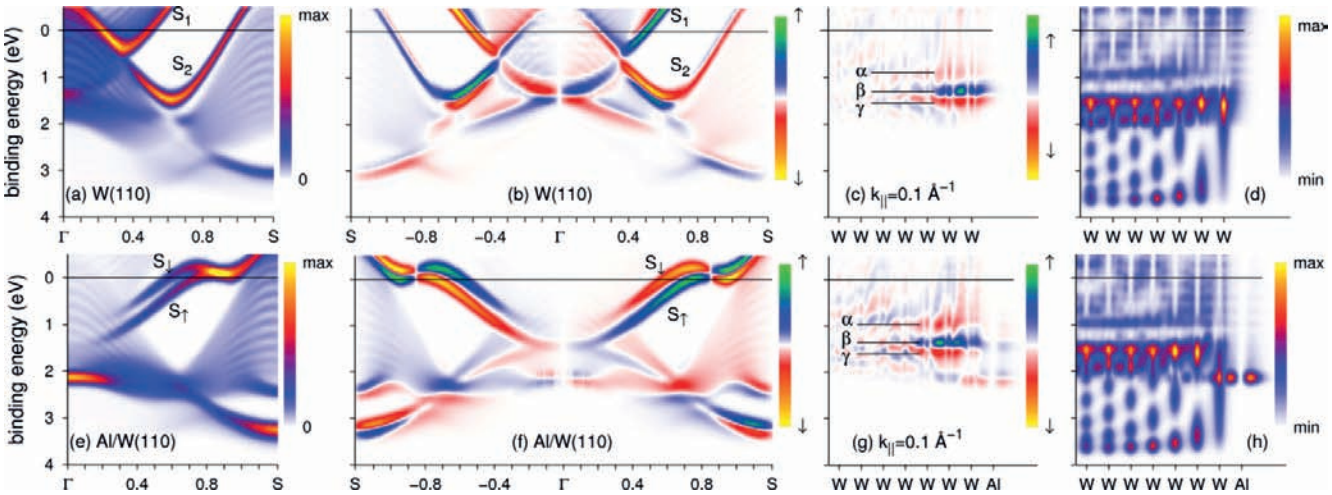

Figure 3.5 — Spatial distribution of total and net-spin spectral density for W(110) (top row) and Al/W(110) (bottom row). Partial DOS from the top W layer and vacuum (a) and from the top W layer, Al layer and vacuum (e), and net-spin DOS ΔS, (b) and (f), see text. Projected local depth-resolved net-spin DOS $\rho(z,E)$, (c) and (g), and total DOS $\rho(z,E)$, (d) and (h) for $k_{\|} = 0.1$ Å^{-1}. Half of the slab is shown, vacuum is on the right. Ticks on the horizontal axis denote atomic layers. The figure is taken from the paper [3], the calculation was performed by E. E. Krasovskii.

at the $\bar{\Gamma}$ point with a linear dispersion relation. The presented Fig. 3.5 (a-d) show that the spin-polarized features have a bulk origin for $k < 0.3$ Å^{-1}. On the other hand, they have a maximum intensity at photon energy $\sim$ 62 eV, and their energy position does not change with photon energy, indicating their quasi-two-dimensional origin (see Fig. 3.6). The intensity of these states has a resonance character depending on the photon energy, which is characteristic of surface states with the appearance of additional intensity peaks in the case of surface indirect transitions to the final state [257]. Thus, summarizing the results of the analysis of experimental and theoretical data we can conclude that the states are surface resonances near the $\bar{\Gamma}$ point, localized also in deeper layers of tungsten than the surface states.

The observed spin structure of electronic states is characteristic of topological insulators, but is found on a metallic surface. This analogy raises the question of whether the linear dispersion dependence is preserved under surface perturbation. The answer is given by comparison with the Al/W(110) system, for which the α and β states are still present inside the continuum of bulk states, but their polarization changes strongly, especially the total spin density S of the α state near $\bar{\Gamma}$ is enhanced (Fig. 3.4 (e)). Interestingly, unlike the pure W(110) surface, the β and γ states do not have a linear dispersion dependence in the vicinity of the $\bar{\Gamma}$ point, but pass through

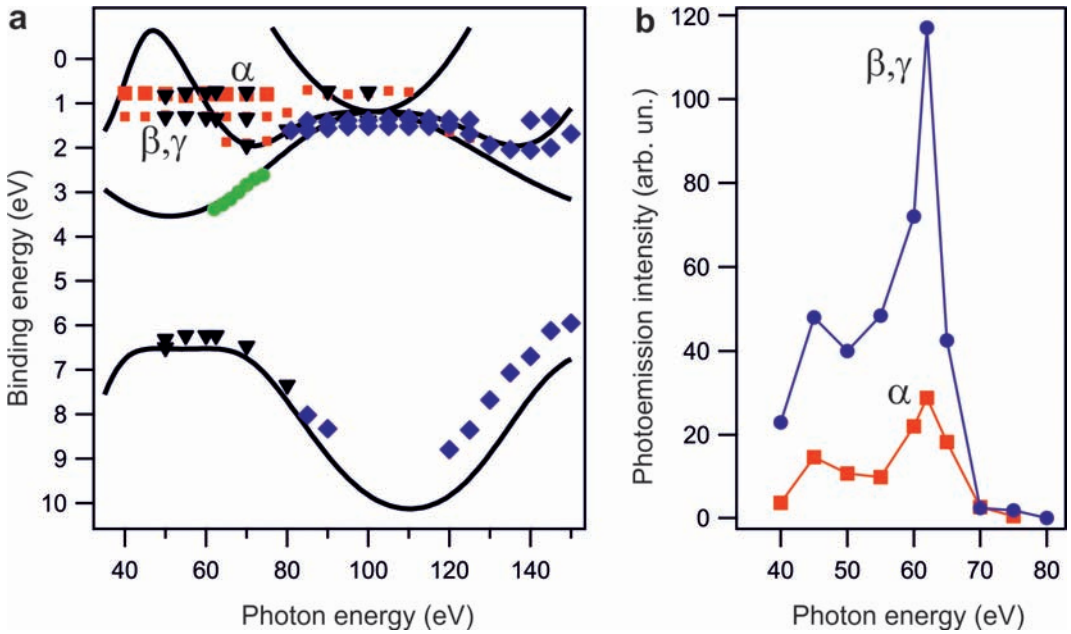

Figure 3.6 — (a) Energy positions of the maxima of photoelectron peaks in the valence band of the pure W(110) surface at normal emission as a function of photon energy. Symbols of different shapes and colors indicate data from different experiments. The lines show the theoretical dependence based on the calculation in the $\bar{\Gamma}\bar{\mathrm{N}}$ direction without the spin-orbit interaction [258]. (b) Dependence of the intensity of tungsten surface resonances on the photon energy.

a turning point. In this case, the surface states change dramatically: instead of two weakly split pairs S_1 and S_2, two strongly polarized states $S_\downarrow$ and $S_\uparrow$ are formed, which connect to the dispersion branches of the states α and β, respectively. Here we encounter the "topological metal" behavior: over a substantial energy interval, only the β state is present, which transitions to the $S_\uparrow$ state as the magnitude of quasi-wave vector increases.

To relate the measured spin polarization of the photoelectron current to the spin structure of the initial states, the *ab initio* one-step photoelectron emission theory described in [250] was applied. The final states are time-reversed low-energy electron diffraction states obtained in the scalar-relativistic approximation using the inverse linearized augmented plane wave method as explained in [259].

In the calculations presented in Fig. 3.4 (c) and (f), the angle of light incidence is fixed at 55° relative to the surface normal, so the left-right asymmetry of the theoretical energy – quasi-wave vector distribution of the total spin photoelectron current is solely a final state effect. The experiment of photoelectron spectroscopy breaks the symmetry of the system, so the spin polarization of the measured current does not correspond to the spin polarization of the initial states: the total intensity

(spin polarization) is not symmetric (antisymmetric) with respect to the $\bar{\Gamma}$ point. This final state effect, in particular, can be seen for the spectrum at $\theta = 0^\circ$ in Fig. 3.3 (a) and the calculated spectrum at $k_\parallel = 0$ in Fig. 3.4 (c), which show both the α peak polarized by spin-$\uparrow$ and the β peak polarized by spin-$\downarrow$, while the resulting spin density in Fig. 3.4 (b) vanishes due to the invariance of the system relative to time reversal. Moreover, both the measured and calculated photoelectron current are much more strongly spin-$\downarrow$ polarized at $-k_\parallel$ than spin-$\uparrow$ polarized at $+k_\parallel$. This also explains the spin-$\uparrow$ polarization of the α branch for both $-k_\parallel$ and $+k_\parallel$, which is stronger at $-k_\parallel$, in agreement with experiment.

Finally, we note the interesting behavior of the $S_\downarrow$ and $S_\uparrow$ states on Al/W(110) at the Fermi level and above, which is outside the measured energy range (Fig. 3.4 (e)). As the magnitude of quasi-wave vector $k_\parallel$ increases toward positive values, the dispersion branches intersect and pass an inflection point (with a decrease in the binding energy of the $S_\downarrow$ state and an increase in the binding energy of the $S_\uparrow$ state). This means that by adjusting the binding energy of the crossing point relative to the E_F level (e.g., by surface doping), one can control the scattering properties of the surface states, since the number of incident and reflected waves changes rapidly with energy. This unusual dispersion dependence near the Fermi level is interesting for applications in spintronics because it opens up the possibility of manipulating surface spin currents across a one-dimensional boundary [260].

To summarize, we can conclude that the spin-split surface states on W(110) and Al/W(110) propagate into the bulk continuum, forming continuous dispersion lines at large $k_\parallel$ intervals with the states in the bulk projected band. This allows us to characterize the spin structure of metallic surfaces in terms of the topology of these lines. Spin-resolved electron density analysis provides important information on the origin and nature of surface states/resonances. Both W(110) and Al/W(110) exhibit a topology that is very different from both the case of spin-split Rashba surface states and the Dirac cone in topological insulators: a change in the sign of the spin polarization of one individual state α in the vicinity of the point $\bar{\Gamma}$. At the same time, dispersion branches with a linear dependence are observed in W(110) in the vicinity of the $\bar{\Gamma}$ point (the β and γ states), which, upon deposition of an Al monolayer, becomes parabolic due to their three-dimensional origin.

The results of this work were first presented at the WE-Heraeus-Seminar “Rashba Effect and Related Spin-Orbit Effects in Metals” [105] and published in [1—3]. The discussion about the topology of spin-polarized states in the vicinity of

the $\bar{\Gamma}$ point W(110) continues. Despite the experimental evidence of the trivial nature of the electron states near the $\bar{\Gamma}$ point [261; 262], the theoretical work [263] shows the importance of the W(110) surface relaxation and the possibility of the existence of metallic topological states. A nonzero compressive strain opens an inverted band gap at the H point of the bulk Brillouin zone of tungsten. At the same time, the mirror Chern number turns out to be nonzero, which confirms the topological character of the formed surface states, which are protected by mirror symmetry, as in crystalline topological insulators.

3.2 Avoided-crossing effect of dispersion dependences of quantum well states and substrate states

Quantum-dimensional effects can strongly modify the electronic structure and properties of metallic layers (films) and multilayer systems [24; 264]. The layer thickness is the main, but not the only important parameter for quantization. The electronic band structure of the layer material and the barrier material also has a significant influence on the electronic structure of the quantum system. In the simple case of a quantum film, the barriers are the interfaces with the vacuum and with the substrate. Intuitively, it is clear that only the absolute bulk projected band gap in the substrate provides electron confinement in the quantum film. However, as experience shows, a local (relative) band gap that exists only for a certain range of electron energy and wave vector, or a band gap for a certain wave function symmetry (e.g., s, p, and d character) that appears for different atomic numbers of the layer and the substrate, leads to electron confinement and quantum well states (QWSs). Explanation of these different cases within the same system was made with the help of the phase accumulation model, which calculates the phases of electronic states accumulated during reflection from the barriers (interfaces) of the quantum film [24; 265–268]. The phase of the reflected wave depends on the energy and the width of the band gap in the substrate. The dependence of the QWSs on the electronic structure of the substrate was first investigated as a function of the film thickness, i.e., the width of the quantum well [267–270]. In these studies, the two-dimensional quasi-wave vector $k_{\parallel}$ in the film plane was kept zero, corresponding to the center of the two-dimensional

surface Brillouin zone, and in photoelectron spectroscopy with angular resolution – to emission in the direction normal to the film surface. The effect of the substrate's band gap width has been studied by ARPES for Ag films on Cu(111) [267] and Ni(111) [269], and for Au on W(110) [270]. At certain values of $k_{||}$ outside the normal emission, the influence of the electronic structure of the substrate can manifest itself in a change in the effective mass of electrons, leading to a change in the curvature of the QWS dispersion $E(k_{||})$ [271; 272].

It has been found that in thin quantum films the effective mass increases strongly [271; 272]. Moreover, away from the center of the Brillouin zone, the QWS dispersions experience kinks where they enter the substrate band gap in Al/Si(111) [273] and Ag/Ge(111) [274–277]. Similar kinks and splittings near the edges of substrate band gap were observed in Ag/Si(100) [278], Mg/W(110) [279–281] and Cu/Co(100) [282]. It has been observed that the effect of crossing states between the QWS and substrate states plays a significant role and can lead to the evolution of a QWS of a certain quantum number into a QWS with a different quantum number [282]. Replacement of the vacuum interface with a different material also leads to strong changes in the phases of the QWSs [283; 284] and similar effects of modification of the QWS dispersion dependences as those caused by the substrate, including kinks (e.g., for Ag(111) layers coated with one third of a monolayer of Bi [285; 286]). The splitting of the QWS peak at the edge of the substrate band gap was observed for Ag/Ge(111) and was interpreted as a multi-electron effect [287]. On the other hand, the ARPES method is closely related to the registration of final state effects in the process of photoelectron emission. However, if one studies the QWS behavior in the deposited layer of the material of interest instead of direct transitions for bulk single crystal, the influence of the final state effects can be avoided [269; 273]. Thus, the substrate states with band gap positions can be recovered by analyzing the QWS dispersion, which is especially interesting for high electron correlation, for example, in semiconductors [273] and correlated d metals [269]. For an Ag layer on W(110) with a thickness of 1 monolayer (ML) (2 ML in ref [270]), it was demonstrated that the interaction of QWSs with the substrate through the effect of preventing the crossing of dispersion dependences (the avoided-crossing effect) allows one to recognize the parity of substrate states [288].

The substrate affects also the spin electronic structure of the adsorbed film and can lead to the induced spin polarization of QWSs. In particular, the appearance of the induced spin polarization of QWSs at the Fermi level due to the exchange

interaction in the noble metal layers located between the ferromagnetic layers is the main reason for the long-range oscillating magnetic interaction in spin valves with giant magnetoresistance [24–28]. The influence of the substrate on the spin polarization of QWSs has also been revealed in the study of materials with strong spin-orbit interaction [37; 38; 40; 289]. Substrate-induced spin-orbit splitting was found for interface and quantum well states in monolayers and ultrathin films of noble metals (Cu, Ag and Au) on the heavy metal substrate W(110) [37; 38; 40; 289]. If only the material of the quantum film and not the substrate possesses strong spin-orbit interaction, this also leads to spin-orbit splitting of the QWSs, which was observed for Pb/Si(111) [39]. The observed energy splitting of the QWSs in light metal Mg films [279; 281] formed the basis of a project to investigate Al quantum films on W(110). The main questions to be answered in the studies were formulated as follows: how do the QWSs in Al layer interact with substrate states and what is the effect of film thickness; how do the parabolic dispersions of QWSs change when crossing substrate bands in contrast to the behavior of a quasi-free electrons; how is the spin structure of QWSs modified by the substrate compared to the QWSs of a free film, and how can this be explained in terms of the avoided-crossing effect?

Figure 3.7 shows the dispersion dependences $E(k_{\parallel})$ of interface and quantum well states of ultrathin Al films on W(110), measured in the $\bar{\Gamma}\bar{S}$ direction of the surface Brillouin zone for different Al thicknesses. In Fig. 3.7 (a), the corresponding dispersion dependences for the pure W(110) single crystal surface are shown for comparison. The edges of the bulk projected band gap of W(110) are marked by dashed lines [258]. The characteristic features of the electronic structure of the atomically pure W(110) surface are surface resonances of $5d$ character [252] located at normal emission (emission angle $0°$) at binding energies of about 0.8 and 1.3 eV, the dispersion branches of which extend up to the border of the local W band gap. As shown in the previous paragraph, two dispersion branches with linear dependence along the $\bar{\Gamma}\bar{S}$ direction intersect in the region of binding energy of $\sim$ 1.3 eV and near $\overline{\Gamma}$ point. After deposition of 1 to 3 monolayers of Al, these states are transformed into Al-W interface states, which already propagate into the W band gap region (see the blue and red lines in Fig. 3.7 (b)).

The resulting interface states, marked as $I^{'}$ and $I^{''}$, have the maximum intensity in the center of the band gap. The states practically become dispersionless, preserving their splitting inside the entire band gap. In addition, at a thickness of 2 ML Al, a QWS with n = 0 is formed (marked as SS in Fig. 3.7). As the thickness of the Al film

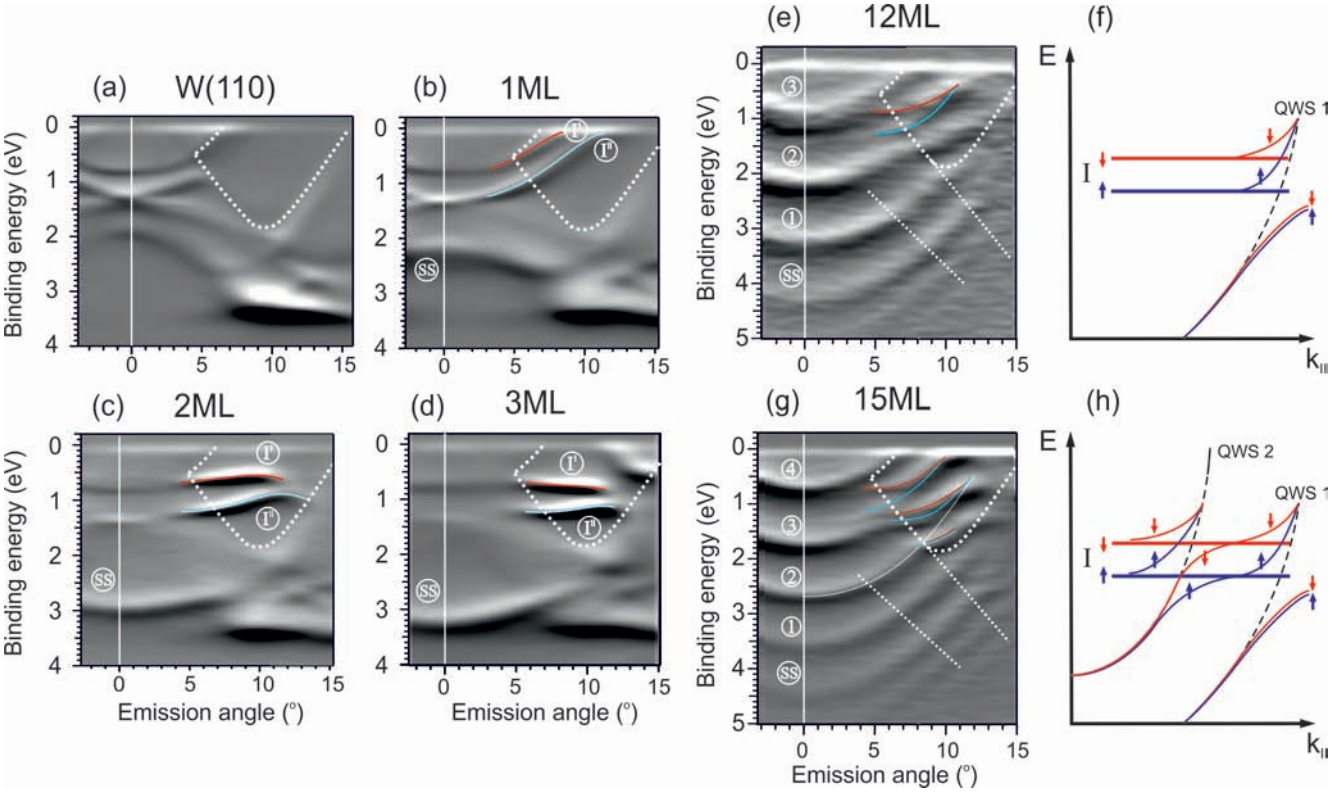

Figure 3.7 — ARPES intensity maps measured for a pure W(110) surface at photon energy hν = 65 eV (a) and for 1 – 15 ML Al on W(110) at photon energy hν = 62 eV (b-e,g). The labels I^{I} and I^{II} denote the interface states formed at thicknesses of 1, 2, and 3 ML. The SS label corresponds to the Al(111) surface state, and labels 1 to 4 correspond to the QWSs. The data are presented as the first derivative of the intensity with respect to the binding energy. The edges of the W projected band gap onto the surface are marked with dashed lines, and the edges of the W band of 6*p* character are marked with two straight dashed lines. The interaction between the QWSs and interface states is shown by lines in blue for spin-up and red for spin-down, according to spin-ARPES measurements. The sketches in (f) and (h) show the intersection of the spin-split interface states by one (f) and two (h) QWSs.

increases, this state transitions to the Al(111) surface state. It is located at a binding energy of about 3 eV at normal emission and has a parabolic dispersion with breaks in the places of intersection with the edge of the projected W band of $6p$ character.

Increasing the thickness of the Al layer from 2 ML (Fig. 3.7 (c)) to 3 ML (Fig. 3.7 (d)) does not lead to a strong modification of the dispersion dependences of the interface and quantum well states. They are very similar to those observed at 2 ML Al, however, with some energy shift of the SS state (to the binding energy of $\sim$ 3.2 eV) and a slight modification of the interface states in the W-derived band gap.

The interface states for 3 ML Al are clearly visible and are marked with red and blue lines ($I^{'}$ and $I^{''}$) for comparison with other dispersion dependences presented in Fig. 3.7. As noted above, these states are formed by hybridization between the electronic states of the W surface and the deposited Al layer and are localized at the interface. At a thickness of 3 ML, the intersection of the dispersion branches of the interface ($I^{'}$ and $I^{''}$) and SS state does not occur and they do not affect each other. The interface states are modified when the second and third atomic layers of Al are deposited. After the completion of the formation of 3 monolayers, these states stabilize, and further deposition of Al does not lead to fundamental changes in their energy and splitting.

To analyze the spin structure of the split interface states, the corresponding spin-resolved spectra for 3 ML Al and thicker layers were measured. In Fig. 3.8 (a) and (b), the corresponding series of spin-integrated and spin-resolved ARPES spectra are shown for different polar angles with respect to the surface normal. The values of the polar angles are shown on the right side of the presented spectra. The spin-integrated photoelectron emission spectra (Fig. 3.8 (a)) corresponding to the spin-resolved spectra in Fig. 3.8 (b) are marked with blue lines. Figure 3.8 (b) shows that the interface states $I^{'}$ and $I^{''}$ are almost completely spin polarized. The corresponding spin orientations are consistent with the Rashba model and are shown in Fig. 3.8 (a) and (b) by red and blue symbols and corresponding arrows. The W-derived band gap region is shown by thin black lines. The presented spin-resolved spectra indicate the spin polarization of the interface states and allow an accurate determination of their energies.

For the thickness of 12 ML Al (Fig. 3.7 (e)), the region of spin-polarized interface states in $k_{||}$-space is crossed by the dispersion branch of the quantum well state with n = 2, and its significant modification occurs. The QWS is split into two parts with opposite spin directions due to the Rashba effect. Consequently, each part of

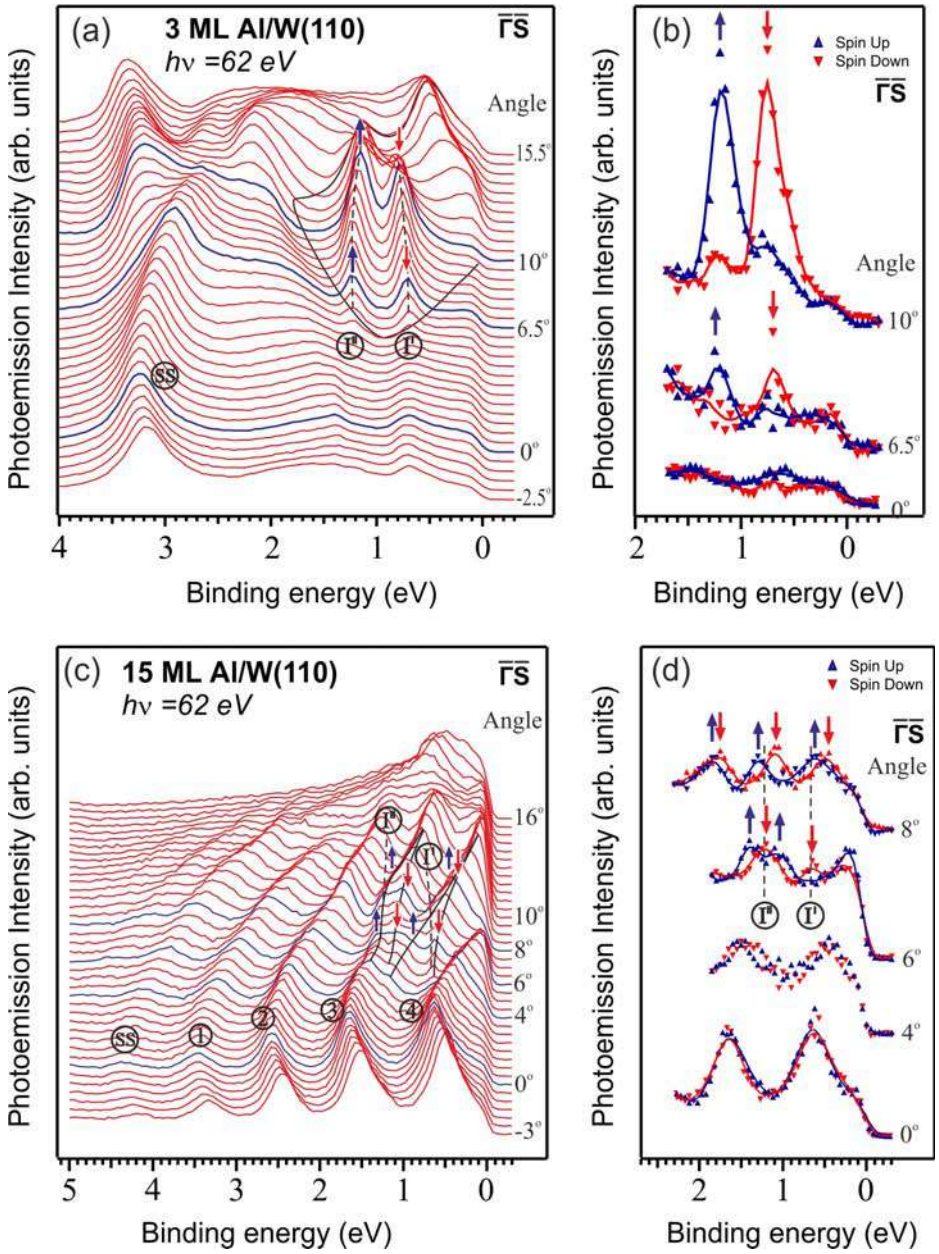

Figure 3.8 — A series of spin-integrated and spin-resolved ARPES spectra for different polar angles for 3 ML Al (a,b) and 15 ML Al (c,d) on W(110) surface. The states with different spin projection are marked with blue and red symbols and corresponding arrows. The labels I^{I} and I^{II} denote interface states, and SS denotes the surface state of Al(111). The blue lines in (a,c) correspond to the polar angles for which the spin-resolved spectra were measured and are shown in panels (b,d), respectively. The thin black line shows the border of the bulk projected band gap of W(110).

the QWS interacts with the interface states with the same spin projection. In the region of the expected intersection of the QWS and spin-polarized interface states, there is a avoided-crossing effect that violates the parabolic dispersion dependence of the QWS. A sketch of such a spin-dependent avoided-crossing effect of the dispersion branches is shown in Fig. 3.7 (f). There is significant spin splitting at the expected intersection site. In regions away from this intersection, the spin splitting is much smaller, and the QWS dispersion in these regions, is independent of the avoided-crossing effect. Thus, as a result of the avoided-crossing effect, a "branching" of hybridized spin-split states is formed. For polar angles < 10°, a pronounced spin splitting is observed at the intersection of QWS with n = 2 and interface states and a significantly smaller spin splitting far from the intersection (for polar angles > 10°).

At a thickness of 15 ML Al, two dispersion branches of the QWSs cross the interface states (Fig. 3.7 (g)). As a result, the formation of at least three pronounced curved dispersion branches (Fig. 3.8 (c)) and four spin-polarized branches in the W band gap region (Fig. 3.8 (d)) is observed in photoelectron emission spectra. This situation is represented as a sketch in Fig. 3.7 (h). When the QWSs cross the W 6*p* states (the edges of the band are shown in Fig. 3.7 by dashed lines in the energy region between 2 and 4 eV), some bending of the QWS branches is also observed. However, in this case their modification is less significant. Moreover, no large spin polarization of the QWSs in this region is observed. Only some broadening of the peaks and curvature of the dispersion branches in the crossing region take place. The observed changes in the electronic structure are close to those described for the systems Al/Si(111) [273], Ag/Si(100) [278], and Ag/Ge(111) [275; 277; 287].

Thus, we observe strong changes in the dispersion dependences of the QWSs derived from the Al *sp* band in Al(111) films on W(110). Some of them exhibit large spin-orbit splitting, unexpected for Al with its small nuclear charge (Z = 13). By detailed studies of different thicknesses, we were able to distinguish between a range of small thicknesses (1–3 ML) and a range of large thicknesses (4 – 15 ML). The range of small thicknesses allows observing states with anomalously large (∼ 0.5 eV) spin-orbit splitting independent of $k_{||}$ using the ARPES method. They appear inside the bulk projected band gap of W(110) and refer to the Al-W interface states, the nature of which is related to the electronic structure of the W(110) surface. In the higher thickness range, the QWSs are both outside and inside the bulk projected band gap of W(110) with higher two-dimensional localization and photoelectron emission intensity in the latter case. When the dispersion branches $E(k_{||})$ of these QWSs cross

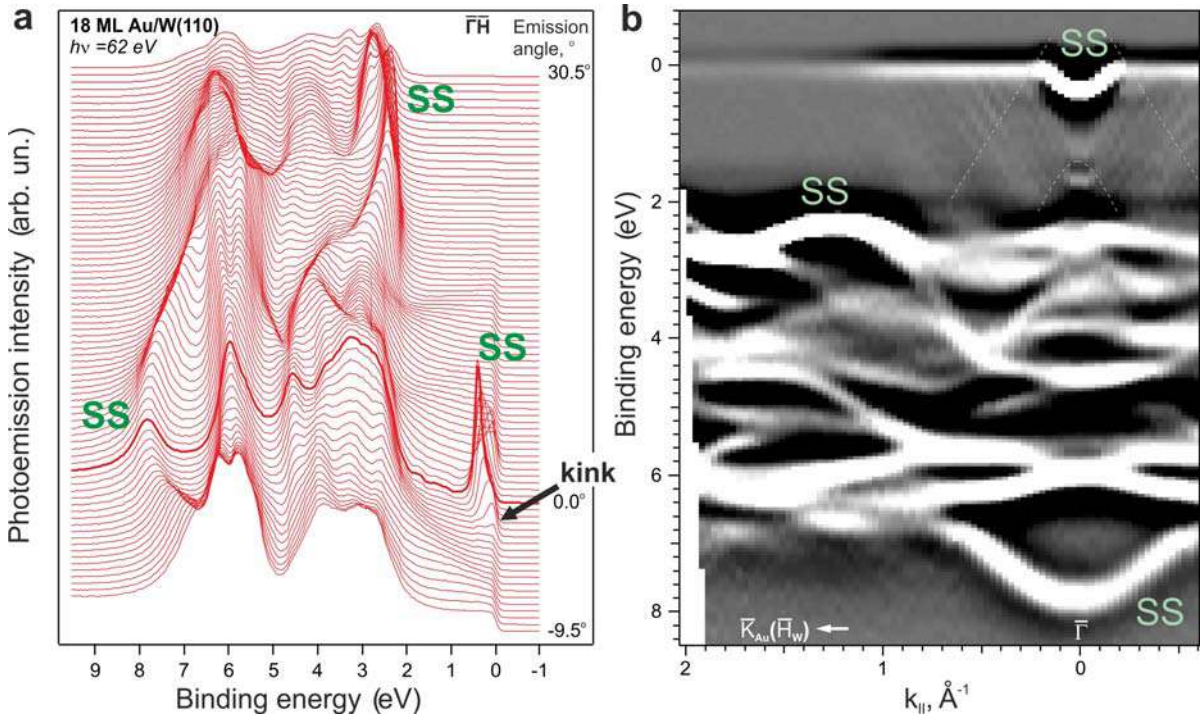

Figure 3.9 — (a) A series of spin-integrated ARPES spectra for different polar angles for 18 ML Au. (b) ARPES intensity map in the form of the second energy derivative. The dotted lines mark the edges of the band of W 6p states. The photon energy $h\nu$ is 62 eV.

the corresponding branches of the interface states, they interact in the crossing region. The interaction leads to the formation of hybridized binding and antibonding states located at higher and lower binding energies than the expected intersection and the opening of the corresponding local energy band gap. Each state is found to interact with a state of the same spin. Since the interacting interface states are initially spin polarized with a large spin-orbit splitting, the resulting binding and antibonding states are different for each spin orientation. Where the two QWSs branches cross the interface states, the spin-dependent avoided-crossing effect leads to the formation of a characteristic “loop” of spin-split hybridized states.

The observed spin-dependent avoided-crossing effect has a general character valid for any system in which states with pronounced spin splitting intersect with states with weaker splitting. Thus, a large spin-orbit splitting is observed for electronic states localized on atoms of a light element such as Al, even when these atoms are located in a quantum film at a distance of several interatomic distances from the heavy element.

The effects of hybridization of the QWSs and *sp* substrate states are of a general nature and can also be demonstrated by the example of an 18 ML thick Au(111) film

on W(110). Figure 3.9 shows the ARPES data in the $\bar{\Gamma}\bar{H}$ direction of the surface Brillouin zone of W(110), which corresponds to the $\bar{\Gamma}\bar{K}$ direction for Au(111). The electronic structure calculations of the Au(111) single crystal presented in [290] are in excellent agreement with the measured dispersion dependences. Some intense surface states are labeled as "SS" in the figure. The parabolic dispersion branches of the QWSs in the Au layer experience kinks in the region of localization of substrate states of *sp* character, marked by dashed lines in Fig. 3.9 (b). The kinks are evidence of a change in the effective mass of nearly free QWSs upon hybridization with the bulk states of the substrate, i.e., there is a deeper penetration of QWSs into the substrate. Similarly, the parabolic dispersion dependence of the Au(111) surface state when approaching the localization region of the Au(111) *sp* band and the corresponding QWSs experiences a kink due to their hybridization and deeper penetration of surface state into the Au(111) layer. This kink is shown in Fig. 3.9 (b) by an arrow. In [291], the time-resolved ARPES method was used to show the behavior of the dispersion dependence of the surface state in more detail, including the energy region above the Fermi level.

In this section we have shown on the example of ultrathin layers of Al and Au on the surface of single crystal W(110) that QWSs formed in thin layers can hybridize with interface states at the boundary of the single crystal, with the bulk states of the substrate and with the surface states of the metal layer. Hybridization is observed in the form of avoided-crossing effects and bends of dispersion dependences. At the same time, the ARPES study of electronic states in thin layers allows us to obtain information not only on the surface structure, but also on the structure of the interface between the metal layer and the substrate and on the structure of the substrate itself. Thus, by analyzing the behavior of dispersion dependences, it is possible to obtain information about localized electronic states in the depth of the grown epitaxial system, which are inaccessible for direct measurement due to the surface sensitivity of the ARPES method.

3.3 Findings

The spin polarization of electronic states of W(110) and Al/W(110) surfaces has been investigated by photoelectron spectroscopy with angular and spin resolution. Spin-polarized surface resonances with a Dirac cone-like dispersion $E(k_{\parallel})$ and a spin structure qualitatively different from the classical Rashba-Bychkov model and reminiscent of topological surface states have been found on both surfaces. It is found that the photoelectron emission process affects the spin polarization of the intensity, in particular, it causes polarization of the spectra at normal emission. Nevertheless, the measured spin polarization of electronic states is a property of the ground state and is analogous to the Rashba-type spin polarization of bulk states on the surface.

Despite the low atomic number, the electronic states in Al films are characterized by large spin-orbit splitting during epitaxial growth on W(110). The spin-ARPES experiment revealed two types of spin-split states as a result of spin-orbit interaction: quantum well states with Rashba-type splitting proportional to the electron wave vector $k_{\parallel}$ in the film plane (Rashba parameter $\alpha_R \sim 7 \times 10^{-2}$ eV·Å), and interface states at the substrate boundary with large splitting ($\sim$ 0.5 eV). The dispersion dependences $E(k_{\parallel})$ of this pair of interface states change insignificantly with increasing layer thickness up to three Al monolayers. For thicker layers, a pronounced spin-dependent avoided-crossing effect of the dispersion branches of quantum well states with interface states is observed, which leads to their enhanced spin-orbit splitting in Al layers up to 15 monolayers thick.

4. Study of magnetically doped systems with strong spin-orbit interaction

Topological insulators (TIs) are new materials that have a bulk band gap like conventional insulators, but cannot be adiabatically coupled to them by a smooth change of the Hamiltonian parameters and have topologically protected conducting states at their edge or surface [245]. These states are possible due to a combination of spin-orbit interaction and time reversal symmetry. Two-dimensional (2D) topological insulators (Chern insulators) exhibit the quantum spin Hall effect, which is a close relative of the integer quantum Hall effect. A three-dimensional (3D) topological insulator is characterized by spin-polarized two-dimensional Dirac fermions on its surface and the corresponding $\mathbb{Z}_2$ topological invariant.

Surface spin-polarized currents in 3D TIs generated by an electric field applied along the surface, including at room temperature [292], can be effectively used to remagnetize contacting ferromagnetic nano-objects due to the spin-orbit torque effect [54—56]. Spin-polarized currents can also be generated using circularly polarized laser radiation in magnetically doped TIs [293] and in Rashba systems with helical spin texture (BiTeI) [294]. The possibility of efficient generation of spin-polarized current in TI using circularly and linearly polarized laser and synchrotron radiation was shown in the works [293—303].

Another important effect that can be utilized in spintronics is the photovoltaic effect (PVE), which is related to the laser-generated surface photoelectricity in TIs [202; 203; 304—312]. A time-resolved laser pump-probe experiment [202; 203; 305—309; 311; 312] is commonly used to study this effect lately. The PVE in such experiments manifests itself as ultrafast photodoping of the electronic structure of TI by laser pulses [202; 305—309] and is proposed to be used as a source for generation of pulsed spin-polarized currents [295—298; 310; 313] and a tool for ultrafast control of them [202; 305—312; 314]. In magnetically-doped TIs, such laser pulses generating spin-polarized currents are expected to be accompanied by the corresponding induced magnetization.

Unfortunately, it is still not clear whether the laser-generated PVE in TI is predominantly a bulk effect or a surface effect? Is it a separate effect related to the choice of a particular material or a general phenomenon for similar systems? How

can PVE lead to the generation of a surface spin-polarized current? PVE has been previously observed in GaAs, Si, graphene [315—318] and some kinds of TIs [319; 320] with a significant change in the generated photo-EMF from a few meV to 100 meV [202; 306—309; 312] depending on the position of the Dirac point relative to the conduction band and valence band. At present, several types of PVEs are known [315], including those generated by bulk separation of electrons and holes or by a shift of the electrochemical potential compared to the ground state potential. The latter is due to the ultrafast accumulation of photoexcited electrons on unoccupied states [202; 305—309]. However, the question of the dependence of the PVE on the position of the Dirac point relative to the fundamental band gap and the Fermi level requires additional studies.

4.1 Giant two-dimensional laser-induced photovoltaic effect in magnetically doped topological insulators

In this section, we consider a two-dimensional photovoltaic effect detected for the first time on the surface of magnetically doped TI. It will be shown that this effect is associated with the surface accumulation of photoexcited electrons and is accompanied by spin-polarized currents with zero bias flowing along the surface beyond the localization of the laser spot. The studies of the PVE of various TIs have allowed us to determine the dependence of the effect strength on the electronic structure (the position of the Dirac point and the degree of filling of the upper Dirac cone).

Vanadium-doped TIs with stoichiometry $Bi_{1.97}V_{0.03}Te_{2.4}Se_{0.6}$ and $Bi_{1.31}V_{0.03}Sb_{0.66}Te_3$ and a significantly different position of the Fermi level and Dirac point relative to the conduction band and valence band edges were used for the experiment. The investigated TIs are characterized by a bulk Curie temperature of about 2.5 K (which is typical for magnetically doped TIs with a similar concentration of magnetic impurity [321—328]) and a significantly higher surface Curie temperature [329]. This can be evidenced by the discovery of the band gap at the Dirac point in surface-sensitive photoemission spectra (see, e.g., [322; 323]). Thus, the investigated TIs at 11 K can be considered as materials with paramagnetic volume

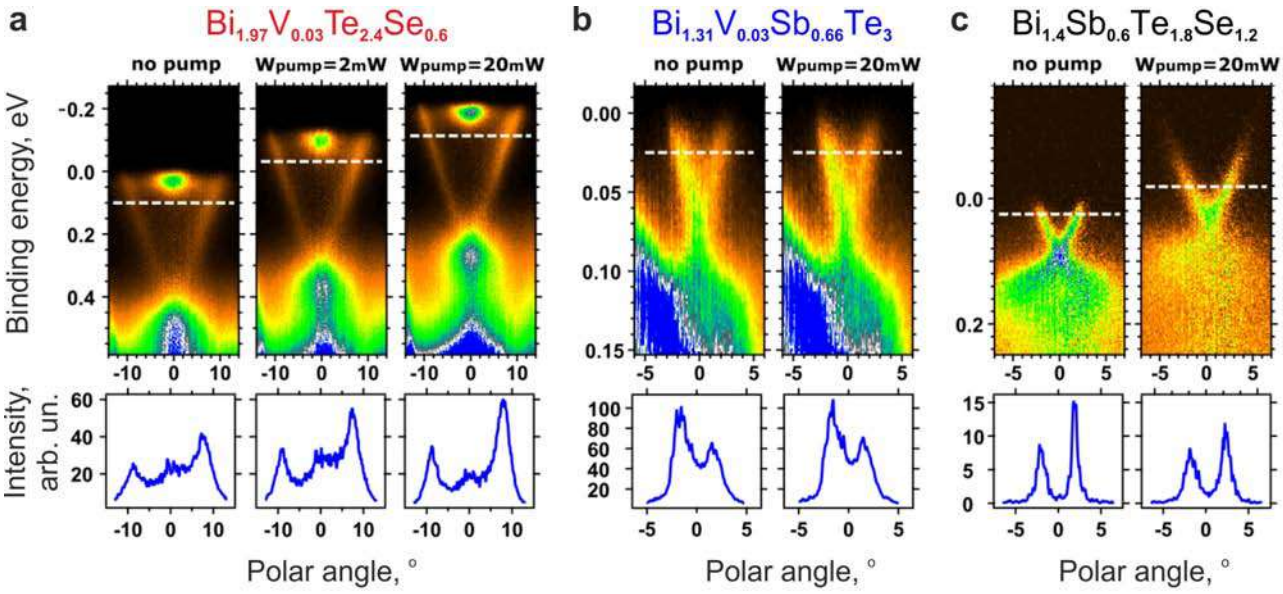

Figure 4.1 — Intensity maps with corresponding TSS dispersion dependences measured by time-resolved ARPES with pump and probe pulses at 11 K for $Bi_{1.97}V_{0.03}Te_{2.4}Se_{0.6}$ - (a), for $Bi_{1.31}V_{0.03}Sb_{0.66}Te_3$ - (b) and $Bi_{1.4}Sb_{0.6}Te_{1.8}Se_{1.2}$ - (c) at different pump pulse power (2 and 20 mW) and their energy shift relative to the dispersion maps measured for the initial "no pump" spectra. The zero-energy positions in the presented ARPES intensity maps correspond to the initial positions of the Fermi level in the maps "no pump". The corresponding TSS intensity profiles at the cutoff energies indicated by the white dashed line are presented below each ARPES intensity map.

and two-dimensional surface magnetic layer. Additionally, for comparison, pure TI with stoichiometry $Bi_{1.4}Sb_{0.6}Te_{1.8}Se_{1.2}$, similar to those presented in the literature on the study of PVE, was investigated under the same experimental conditions.

The results of the PVE experiment using the pump-probe method are shown in Fig. 4.1 for the above-mentioned TIs, pure and vanadium-doped ($Bi_{1.97}V_{0.03}Te_{2.4}Se_{0.6}$ – (a), $Bi_{1.31}V_{0.03}Sb_{0.66}Te_3$ – (b), and $Bi_{1.4}Sb_{0.6}Te_{1.8}Se_{1.2}$ – (c)). The presented ARPES intensity maps show the energy shifts in the electronic structure of TI induced by the pump pulse. To show the PVE magnitude more clearly, Fig. 4.1 shows the ARPES intensity maps measured under excitation with a probe pulse (the so-called "no-pump" spectra) and under pump-probe pulse excitation with the maximum pump pulse power (20 mW). For $Bi_{1.97}V_{0.03}Te_{2.4}Se_{0.6}$, the ARPES intensity map measured at a pump pulse power of 2 mW is also shown for comparison. The detailed energy shift dependences of the Dirac point position and Fermi level estimated from the

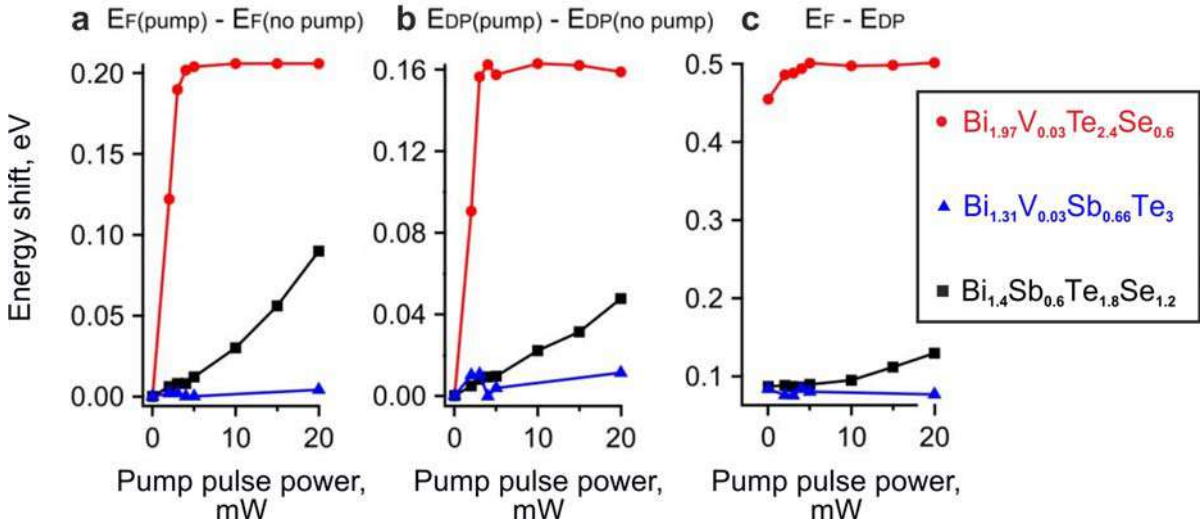

Figure 4.2 — Changes in the energy positions of the Fermi level – (a) and Dirac point – (b) in photoelectron spectroscopy spectra relative to those observed for the initial "no pump" spectra, as well as the energy distance between the Fermi level and the Dirac point position – (c), during the pump-probe experiment measured at a sample temperature of 11 K and with a pump pulse power variation from 2 to 20 mW.

measured dispersion dependences in the ARPES intensity maps for all pump pulse power values from 2 mW to 20 mW are shown in Fig. 4.2 for the investigated TIs.

From the analysis of the dispersion dependence on the ARPES intensity maps ("no pump" spectra), we can see that the topological surface states (TSSs) for $Bi_{1.97}V_{0.03}Te_{2.4}Se_{0.6}$ (Fig. 4.1 (a)) have a metal-like character with the location of the Fermi level in energy above the bottom of the conduction band. The conduction band states appear as a pronounced feature near the Fermi level located at the center of the Brillouin zone ($k_{||} = 0$). The Dirac point is located inside the fundamental band gap, with the TSSs above the Dirac point (upper Dirac cone) almost completely occupied. For the second sample with stoichiometry $Bi_{1.31}V_{0.03}Sb_{0.66}Te_3$ (Fig. 4.1 (b)), the Fermi level is located already inside the fundamental band gap, rather close to the upper edge of the valence band. At the same time, the Dirac point for this sample is located slightly below the upper edge of the valence band. The states of the upper Dirac cone are only partially occupied, i.e., the TSSs are largely unoccupied. The electronic structure of pure TI $Bi_{1.4}Sb_{0.6}Te_{1.8}Se_{1.2}$ (Fig. 4.1 (c)) is somewhat similar to that for $Bi_{1.31}V_{0.03}Sb_{0.66}Te_3$, only with the Dirac point located inside the fundamental band gap and outside the valence band.

It is important to note that the maximum PVE is observed for vanadium-doped Ti with stoichiometry $Bi_{1.97}V_{0.03}Te_{2.4}Se_{0.6}$ (see Fig. 4.2), which is characterized by almost completely filled TSSs and localization of the Dirac point inside

the fundamental band gap. An anomalously large energy shift of the dispersion dependences (up to 210 meV in the kinetic energy scale of photoelectrons) in the ARPES intensity maps and the corresponding Fermi level (compared to the "no-pump" maps) can be distinguished. This shift increases with increasing pump pulse power (see Fig. 4.2) up to a power of 4 – 5 mW, after which it practically reaches a constant level without significant change up to the maximum used power of 20 mW. It should be noted that the energy shift of the ARPES intensity map (PVE magnitude) measured for this type of TI is significantly higher than that reported in the literature for other types of TI [202; 312].

Interestingly, for the second kind of magnetically doped TI $Bi_{1.31}V_{0.03}Sb_{0.66}Te_3$ (Fig. 4.2) with a Dirac point located inside the upper part of the valence band and practically unoccupied states of the upper Dirac cone, the observed magnitude of the PVE is close to zero. In other words, the energy shift for this sample is not observed at any pump pulse power up to 20 mW. At the same time, for TI $Bi_{1.4}Sb_{0.6}Te_{1.8}Se_{1.2}$ the shift of the Dirac point position reaches a value of about 50 meV with a simultaneous shift of the Fermi edge of about 90 meV. This difference is determined by an additional shift of the non-stationary electrochemical potential caused by the ultrafast population of states above the initial Fermi level due to scattered photoexcited electrons, as in [202; 305–309].

From the analysis of the presented results, we can conclude that, when the Dirac point is located inside the fundamental band gap, the PVE magnitude is mainly determined by the degree of occupation of the upper Dirac cone of TI. The laser-generated photo-EMF correlates with the initial value of the energy distance between the Fermi level and the position of the Dirac point in the electronic structure of TI. On the other hand, when the Dirac point is located inside the valence band, the PVE magnitude decreases significantly. For $Bi_{1.97}V_{0.03}Te_{2.4}Se_{0.6}$ with a high filling of TSSs $(E_F^0 - E_D^0) \sim 450$ meV (see the original spectrum "no pump" in Fig. 4.1), the magnitude of the PVE reaches a value of about 210 meV. The localization of the Fermi level inside the conduction band does not play an essential role for the magnitude of the observed PVE. On the contrary, for $Bi_{1.31}V_{0.03}Sb_{0.66}Te_3$ with low TSSs filling $(E_F^0 - E_D^0) \sim 80$ meV and localization of the Dirac point inside the valence band, the observed PVE magnitude is close to zero.

Main factors responsible for the giant photovoltaic effect

Let us analyze the main factors leading to the observation of a giant PVE. First of all, it can be seen that the ARPES intensity map for $Bi_{1.97}V_{0.03}Te_{2.4}Se_{0.6}$ shows an almost rigid shift of the kinetic energy scale upon excitation by the pump pulse. It can be assumed that the observed energy shift is determined by photoinduced local charging of the surface inside the spot of the laser beam, as well as by the fact that there is an accumulation of scattered photoexcited electrons directly near the surface with a subsequent band bending toward higher kinetic energies. It has previously been suggested [202; 305—309] that the PVE may be related to the accumulation of scattered photoexcited electrons on the lower unoccupied states of the conduction band or unoccupied TSSs. As a result, a time-dependent increase in the electrochemical potential was observed, clearly visible in the ARPES intensity maps as a shift in the position of the Fermi level [202; 305—309]. For $Bi_{1.97}V_{0.03}Te_{2.4}Se_{0.6}$, the presented ARPES intensity map fails to distinguish a well-observed population of states above the initial Fermi level position. At the same time, a slight increase in the energy distance $E_F - E_D$ by 30 – 50 meV can be observed in the spectra under pump pulse excitation (see Fig. 4.2). Nevertheless, this shift is much lower than the observed value of the laser-generated surface photo-EMF and cannot explain the observed PVE.

Note that for pure TI $Bi_{1.4}Sb_{0.6}Te_{1.8}Se_{1.2}$, the increase in the energy distance ($E_F - E_D$) associated with the change in the electrochemical potential with increasing pump pulse power is already more pronounced (Fig. 4.2). At the same time, one can also distinguish rigid energy shifts of the positions of the Dirac point and the Fermi level around 40 meV, similar to the local charging effect. This value is much lower than the value of the rigid shift observed for the first sample. This implies that for $Bi_{1.4}Sb_{0.6}Te_{1.8}Se_{1.2}$ the PVE is largely determined by the growth of the quasi-static electrochemical potential, which occurs due to the filling of the TSSs upon laser excitation and subsequent relaxation, as in [202; 305—309].

To clarify the role of relaxation processes, a separate time-resolved pump-probe experiment was performed. A pump pulse power of 19 mW was used for this experiment. Figure 4.3 demonstrates the time-resolved relaxation dynamics of photoexcited electrons observed for magnetically doped TIs $Bi_{1.97}V_{0.03}Te_{2.4}Se_{0.6}$ – (a) and $Bi_{1.31}V_{0.03}Sb_{0.66}Te_3$ – (b) and for pure TI $Bi_{1.4}Sb_{0.6}Te_{1.8}Se_{1.2}$ – (c), which shows significantly different relaxation times in these materials. It can be seen that

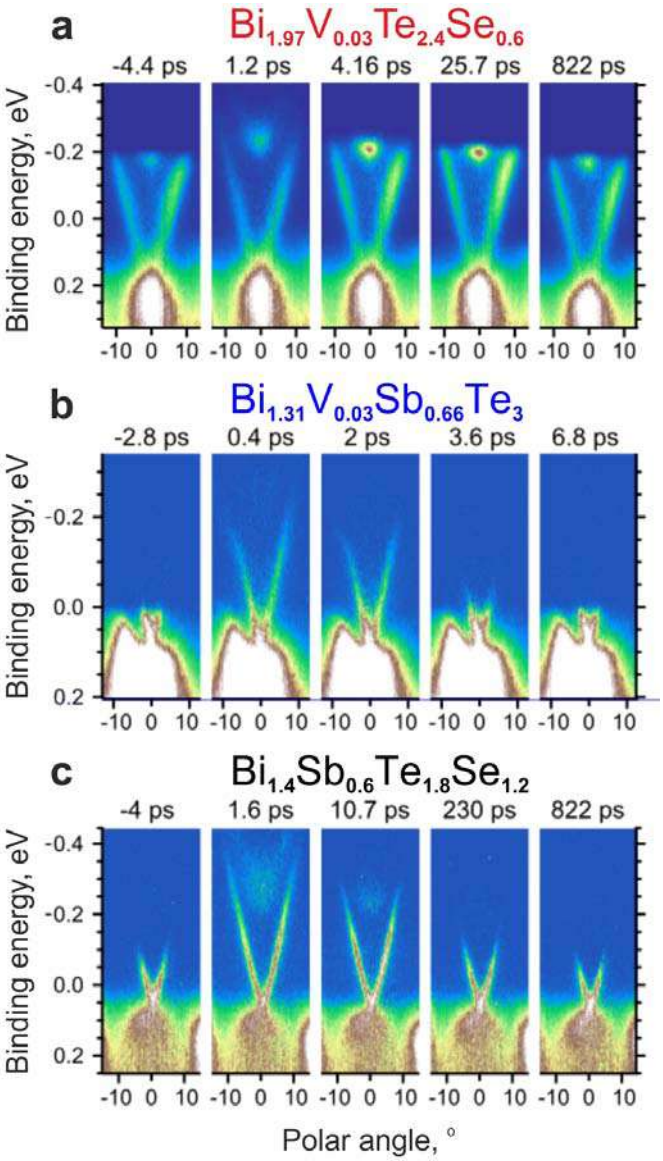

Figure 4.3 — Modification of the ARPES intensity maps as a function of the delay time during the laser pump and time-resolved probe experiment, measured at 11 K using a p polarization probe pulse (hν = 5.9 eV) and s polarization pump pulse (hν = 1.48 eV) for $Bi_{1.97}V_{0.03}Te_{2.4}Se_{0.6}$ – (a), for $Bi_{1.31}V_{0.03}Sb_{0.66}Te_3$ – (b) and $Bi_{1.4}Sb_{0.6}Te_{1.8}Se_{1.2}$ – (c). The delay times between pump and probe pulses are shown above each ARPES map. The zero-energy positions correspond to the initial positions of the Fermi level in the "no-pump" spectra in Fig. 4.1.

for both V-doped TIs, the relaxation of photoexcited electrons through the unoccupied conduction band states is completed rather quickly: for $Bi_{1.97}V_{0.03}Te_{2.4}Se_{0.6}$ – after a delay of about 50 ps; for $Bi_{1.31}V_{0.03}Sb_{0.66}Te_3$ the relaxation process is almost completed in 3 ps. In contrast, for pure TI $Bi_{1.4}Sb_{0.6}Te_{1.8}Se_{1.2}$, the relaxation time increases to 250 – 300 ps. This means that the observed giant PVE does not correlate with the presented relaxation processes.

However, it is important to note that for $Bi_{1.97}V_{0.03}Te_{2.4}Se_{0.6}$, the long-time laser-generated photo-EMF does not decrease practically even up to the next pump pulse generation, i.e., within 4 μs. This can be clearly seen by comparing the energy shift between the "no-pump" spectra in Fig. 4.1 and and the ARPES intensity map just before the next laser pump pulse (-4.4 ps) in Fig. 4.3, presented on the same energy scale. This means that the relaxation time of the generated photo-EMF is significantly longer and cannot be described from the positions analyzed in [305–308; 311; 312].

Two-dimensional relaxation due to the generated spin-polarized current

It is quite probable that the main factor responsible for the generation of giant PVE in $Bi_{1.97}V_{0.03}Te_{2.4}Se_{0.6}$ is the continuous accumulation of photoexcited electrons on the TSSs due to the reduced electron-phonon interaction on the TI surface compared to the bulk [202; 309]. This significantly reduces the relaxation rate of photoexcited electrons through the band gap. As a result, the two-dimensional relaxation through the TSSs with drift of the accumulated charge outside the laser beam spot begins to play a predominant role. The drift time for this kind of two-dimensional relaxation process [202; 330] is estimated to be $\sim$ 30 μs [202]. The two-dimensional relaxation rate through the TSSs depends on the degree of filling of the upper Dirac cone states and is largely determined by "a bottle neck" effect associated with electron scattering through the Dirac point (see, e.g., [306; 311; 331]). Due to the finite relaxation rate, there is an accumulation of scattered photoexcited electrons on the surface (on the TSSs), which leads to the generation of photo-EMF on the surface. This accumulation can be confirmed by the increase in the quasi-static electrochemical potential, as evidenced by the increase in the value of $(E_F - E_D)$

due to the filling of unoccupied TSSs (Fig. 4.2). This can also be evidenced by the increase in the intensity of occupied TSSs under pulsed laser excitation (pump-probe), shown in the TSS intensity profiles at the bottom of Fig. 4.1, compared to the “no pump” profile (excitation by probe pulses).

It is intriguing that for $Bi_{1.31}V_{0.03}Sb_{0.66}Te_3$ when the Dirac point is located inside the valence band, the role of “a bottle neck” effect is reduced due to the opening of a new relaxation channel from the TSSs directly to the valence band bypassing the Dirac point. In this case, the accumulation of electrons at the TSSs does not occur. The TSS intensities on the profile in Fig. 4.1 for laser excitation without and with a pump pulse are practically equal, and the PVE magnitude tends to zero. This proves that the observed giant PVE is actually related to the accumulation of photoexcited electrons on the TSSs. The accumulation of electrons on the surface is accompanied by local charging of the surface inside the laser beam spot, which cannot be effectively eliminated through the fundamental band gap. This charging inside the laser beam spot increases until it begins to be balanced by a zero bias surface electron current through the TSSs flowing to the nearest neighboring surface areas to compensate for this charging. This means that, on the one hand, the PVE is determined by the local surface charging and the generated surface compensating currents. On the other hand, since these compensating currents flow through the TSSs, they must be spin polarized. Consequently, the laser-generated surface photo-EMF can be considered as a generator of surface spin-polarized current.

In the case of photoexcitation asymmetry of Dirac states with opposite momentum and spin orientation, the compensating currents flowing in opposite directions will be unequal. As a result, a non-zero spin-polarized current will be generated along the direction determined by the asymmetry of the TSS intensity. This spin-polarized current, in turn, can induce a magnetic field in the plane of the surface due to the spin-orbit torque effect, similar to how spin-polarized current generated by an applied electric field changes the magnetization of contacting magnetic layers or magnetically doped TI [54–56]. Importantly, spin-polarized current in TI can be obtained even at room temperature [292]. For the studied magnetically doped TI $Bi_{1.97}V_{0.03}Te_{2.4}Se_{0.6}$, an intensity asymmetry is indeed observed in the photoexcitation of opposite dispersion branches of Dirac cone states (see Fig. 4.1), which suggests the possibility of generating the nonzero spin-polarized current and induced magnetization of magnetic impurities (V) via the spin-orbit torque effect, e.g., as in [293; 294].

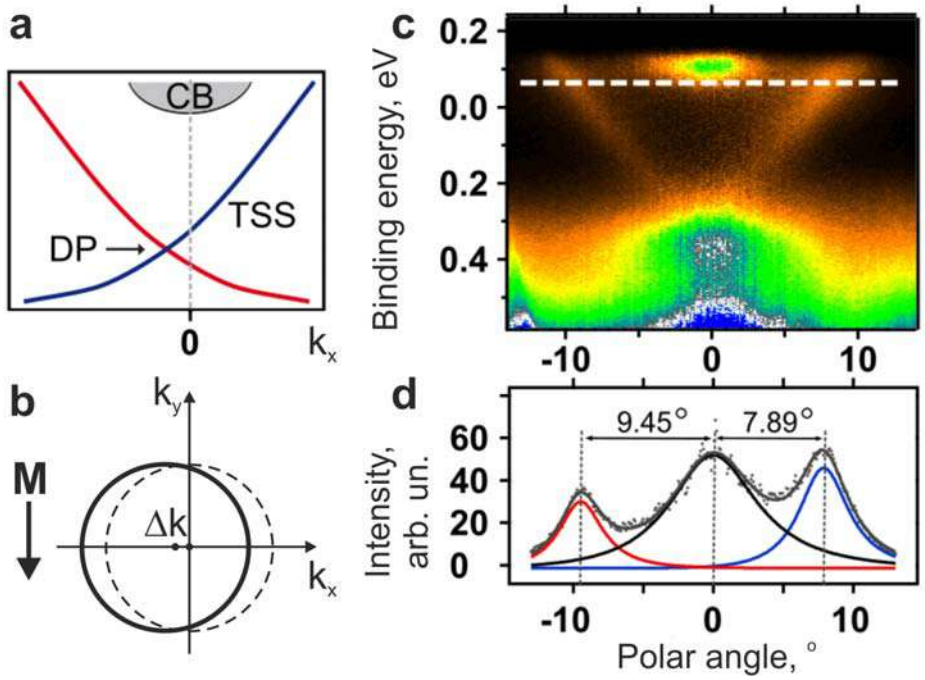

Figure 4.4 — Schematic drawing of the $k_{||}$-shift of the Dirac cone states relative to the unpolarized lower states of the conduction band (a) and the corresponding view of the shift of the upper Dirac state under the induced planar magnetic field M (b). Experimentally observed $k_{||}$-shift of the ARPES dispersion map (in units of polar angle) with respect to the conduction band states (c). The intensity profile of the states on a cut of the ARPES intensity map at the energy marked by the white dashed line is shown at the bottom. The measurements were performed within the pump-probe experiment at a pump pulse power of 2 mW.

It is known that a magnetic field in the surface plane can cause a $k_{||}$-shift of the spin-polarized states of the Dirac cone relative to the non-spin-polarized states of the conduction band centered at $k_{||} = 0$ [296; 310]. Figure 4.4 (a,b) schematically shows such a k_x-shift of the Dirac cone states relative to the lower edge of the conduction band under the action of a magnetic field in the surface plane oriented along the k_y direction. Figure 4.4 (b) shows the direction of the in-plane magnetic field that can be induced due to the asymmetry of the TSS intensity with opposite quasi-wave vectors, taking into account the helical spin texture of the TSSs. The domination of Dirac cone states with a certain direction of the quasi-wave vector (k_x) during photoexcitation is accompanied by the generation of an uncompensated spin-polarized zero-bias current with spin orientation perpendicular to the current direction. The current in turn leads to the appearance of a planar magnetic field, followed by a $k_{||}$-shift of the states, shown in Fig. 4.4 (a). Figure 4.4 (c) shows the experimental ARPES intensity map for the Dirac cone states of the magnetically doped TI $Bi_{1.97}V_{0.03}Te_{2.4}Se_{0.6}$, showing the

asymmetry of the TSS photoexcitation from opposite branches of the Dirac cone. At the bottom of Fig. 4.4 (d) is the intensity profile of the Dirac cone states with opposite quasi-wave vectors relative to the lower conduction band states located at the Fermi level in the center of the Brillouin zone (at $k_{\|} = 0$). The $k_{\|}$-shift of the maxima of the opposite branches of the TSSs relative to the conduction band states (in units of polar angle from the normal to the surface) is clearly distinguishable. This behavior can be well described by the above-mentioned induced planar magnetization. This result may be a good example of the magnetization induced by the spin-polarized zero-bias current generated as a result of the two-dimensional PVE in magnetically doped TIs. On the other hand, it indirectly confirms the generation of the spin-polarized current itself in the magnetically doped TI $Bi_{1.97}V_{0.03}Te_{2.4}Se_{0.6}$ with occupied upper states of the Dirac cone and localization of the Dirac point inside the fundamental band gap.

As a result of our studies, a new type of surface PVE generated in magnetically doped TIs of fractional stoichiometry $Bi_{2-x}V_xTe_{3-y}Se_y$ (e.g., $Bi_{1.97}V_{0.03}Te_{2.4}Se_{0.6}$), which are characterized by a broad fundamental band gap, the position of the Dirac point inside it, and a high degree of filling of the upper cone of Dirac states. In a time-resolved pump-probe experiment, we observe anomalously large photo-EMF for magnetically doped TIs, up to 210 meV. At the same time, for other types of TI characterized by a low degree of filling of the upper cone of Dirac states and localization of the Dirac point inside the valence band (e.g., $Bi_{1.31}V_{0.03}Sb_{0.66}Te_3$), the generated photo-EMF decrease to almost zero. It is shown that the giant PVE is determined by the accumulation of photoexcited electrons on the surface with a long-term surface relaxation by means of compensating currents flowing through the TSSs from the laser beam localization. In the case of asymmetry of photoexcitation of Dirac cone states with opposite momentum there is generation of a non-zero surface spin-polarized current, the direction of which is determined by the asymmetry of photoexcitation of the TSSs. The generation of this spin-polarized current was experimentally confirmed by the $k_{\|}$-shift of the Dirac cone states relative to the lower states of the conduction band in the direction perpendicular to the current-induced planar magnetization. Thus, magnetically doped TIs with a high degree of filling of the upper cone of Dirac states and localization of the Dirac point inside the fundamental band gap can be regarded as effective quasi-two-dimensional materials providing laser-induced generation of spin-polarized current on the surface with zero bias and local surface magnetization.

4.2 Study of the electronic and magnetic structure of BiTeI(0001) with increasing magnetic doping

Materials and systems that combine the properties of two-dimensional electron gas with strong spin-orbit interaction and intrinsic ferromagnetism represent one of the most promising platforms for the future development of spintronics and quantum computing [332; 333]. One such material is the polar semiconductor BiTeI doped with magnetic metal atoms. Pure BiTeI has a layered crystal structure formed by three-layer Te-Bi-I blocks separated by van der Waals spacings [334–337]. The electronic structure of this material in the vicinity of the Fermi level is characterized by two parabolic-type energy bands displaced along the $k_{\|}$ from the $\overline{\Gamma}$ point due to the Rashba effect ($E_{\pm}(k) \sim \frac{\hbar^2}{2m^*}k^2 \pm \alpha_R k$) . The Rashba parameter in BiTeI ($\alpha_R = 3.85$ eV·Å) is one of the largest measured experimentally for various quasi-two-dimensional materials. As a result, the parabolic bands are significantly spin-split [334–339]. However, the spin degeneracy is preserved at the intersection point of the parabolas, i.e., the Kramers point, due to the invariance of the time reversal symmetry. Doping BiTeI with magnetic atoms leads to the removal of spin degeneracy and the opening of the band gap at the Kramers point (at the $\overline{\Gamma}$ point for $k_{\|}$=0) [161]. As was shown in Paragraph 1.1.3, the band gap opens only in the case of out-of-plane magnetization of the sample (perpendicular to the surface). The spin structure of states in the vicinity of the Kramers point takes the form of a “hedgehog”, and the electronic structure contains a single circular contour at the Fermi level when it is located in the local band gap [161]. A similar removal of spin degeneracy can be observed for topological surface states in magnetic topological insulators [340–344] or for Rashba-type states [345].

Magnetically doped BiTeI systems can be used for high-efficient generation and control of spin currents [333; 346–350]. Therefore, they can be used as part of spin filters, high-speed spin valves of memory elements, Hall effect devices, etc. Moreover, states with opposite quasi-wave vectors and hence spin orientations can be coupled through the proximity effect to the superconductor. This can lead to the formation of a topologically nontrivial superconducting phase [332] and, as a consequence, to the appearance of Majorana fermionic modes with zero energy [48; 351]. The aforementioned effects in magnetically doped BiTeI can significantly advance the

technology of quantum computing and its solid-state realization [332; 352–354]. In earlier works [161; 355] devoted to the experimental and theoretical study of BiTeI doped with V atoms, it was shown that the band gap at the Kramers point reaches a value of $\sim$ 90 meV at 2% V concentration. However, first principles calculations show that the band gap in this case does not exceed 34 meV [161]. This inconsistency may be due to unaccounted Bi vacancies in the vicinity of the V impurity, which can affect the magnetic moments of the nearest Te atoms and increase the value of the band gap. A band gap up to 100 meV was also observed in the ferroelectric semiconductor GeTe doped with Mn atoms to a concentration of 15%, which becomes a Rashba-Zeeman system below the Curie temperature [356; 357]. Despite these studies, the reasons for the opening of the band gap at the Kramers point and its characteristic features are still poorly understood in magnetically doped Rashba systems.

This section presents the results of the study of the electronic structure and magnetic properties of BiTeI doped with magnetic metal atoms (V, Mn) with varying concentrations from 0.5% to 6%. The electronic structure modification in the region of the Kramers point, corresponding to the crossing of the parabolic dispersion dependences of the BiTeI valence states characterized by opposite spin orientations, has been investigated in detail, and the opening of an anomalously large energy band gap in the Kramers point, up to 130 – 140 meV, the value of which depends on the concentration of the magnetic metal impurity, has been shown. An increase in the impurity concentration V from 0.5% to 3% is accompanied by an increase in the energy band gap up to 130 – 140 meV. However, at the transition from 3% to 6% concentration of V atoms, the band gap decreases to 105 – 125 meV.

The electronic structure of the valence band states was measured by ARPES method. Figure 4.5 shows the dispersion dependences of the valence states in the form of N(E) and $\mathrm{d}^2\mathrm{N}/\mathrm{dE}^2$ measured for the BiTeI surface doped with V atoms of different concentrations: 0.5%, 2%, 3%, and 6%. To accurately determine the value of the band gap at the Kramers point, Fig. 4.5 (c) shows the corresponding N(E) spectra measured directly at the $\bar{\bar{\Gamma}}$ point, with decomposition into spectral components. The decomposition into components in Fig. 4.5 (a) was performed using the dispersion relation within the Rashba model and the massive Dirac fermion model [356], the latter of which gives the better match with experiment. The blue and violet peaks show the energy positions of the states at the edges of the band gap. It can be seen that the size of the band gap increases from 100 meV to 130 – 135 meV with increasing V concentration from 0.5% to 3%. However, further increase of V concentration up

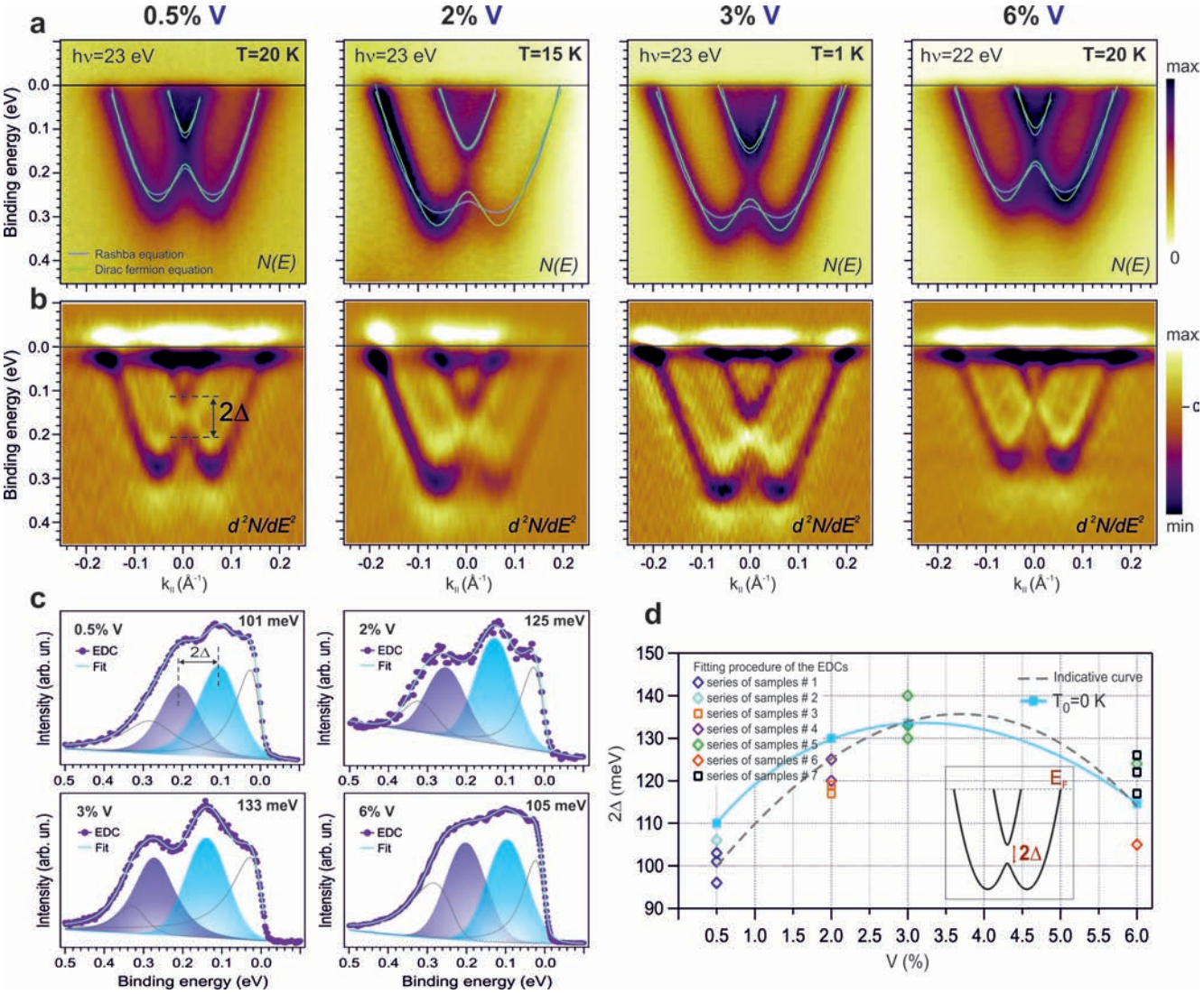

Figure 4.5 — (a,b) Dispersion dependences of the Rashba valence band states for BiTeI doped with V at different concentrations (0.5%, 2%, 3%, and 6%) in the N(E) and d^2N/dE^2 representation. (c) Energy profiles measured directly at the $\bar{\Gamma}$ point, with decomposition into spectral components (shown in blue and violet) and indication of the value of the band gap at the Kramers point. (d) Dependence of the value of the band gap on different concentrations of V doping obtained from the analysis of the energy profiles of Rashba states at the $\bar{\Gamma}$ point. The dotted line shows the non-monotonic dependence of the band gap value at the Kramers point, averaged over the set of measurements for clarity. The solid blue line shows the dependence of the band gap value in terms of temperature T = 0 K, estimated by the power law $\Delta E_{exp} = E_{T=0}(1 - T/T_C)^{1/2}$ assuming the surface Curie temperature T_C = 130 K.

to 6% leads to its decrease to 105 meV. The overall change of the band gap value (2Δ) for all measured spectra as a function of V concentration (i.e., at concentrations of 0.5%, 2%, 3%, and 6%) is represented by the set of dots and the dashed curve in Fig. 4.5 (d). In order to compare the results of the band gap measurement at the Dirac point for different temperatures, a temperature correction of the value of the band gap was performed assuming its power dependence on temperature. The presented data show a non-monotonic character of the change of its value with increasing concentration of V atoms.

The magnetic properties of V-doped BiTeI and their possible modulation at different concentrations of V were investigated by SQUID magnetometry. Figure 4.6 shows the isothermal magnetization curves M(H) for selected concentrations of V (2%, 3%, and 6%) measured at temperatures from 2 K to 30 K. The external magnetic field was applied perpendicular to the surface plane, i.e., along the *c*-axis. It is well evident that the saturation magnetization tends to increase with increasing V concentration up to 3%. In contrast, when the concentration of V is further increased from 3% to 6%, the saturation magnetization decreases. This trend is observed for measurements at both 2 K and 4 K (Fig. 4.6 (d,e)). This behavior correlates with the non-monotonic dependence of the change in the band gap value at the Dirac point as a function of the doping concentration of V atoms, shown in Fig. 4.5.

The decrease in the band gap value with increasing concentration of impurity magnetic metal atoms above 3% can be explained by the fact that some of the magnetic atoms begin to form dimers with antiferromagnetic type of bonds between themselves, which leads to a decrease in the effective magnetic moment and a corresponding decrease in the value of the band gap opened at the Dirac point. The fraction of such antiferromagnetic bond dimers increases with increasing concentration of magnetic metal, which is accompanied by a decrease in the fraction of unbound magnetic impurities.

To analyze the change in the band gap value with increasing temperature, as well as its dependence with increasing concentration of impurity magnetic atoms, taking into account the formation of dimeric antiferromagnetic bonds between impurity magnetic atoms, a theoretical analysis was carried out, the results of which are presented in Fig. 4.7. The presented results of the theoretical calculations correlate well with the experimental data.

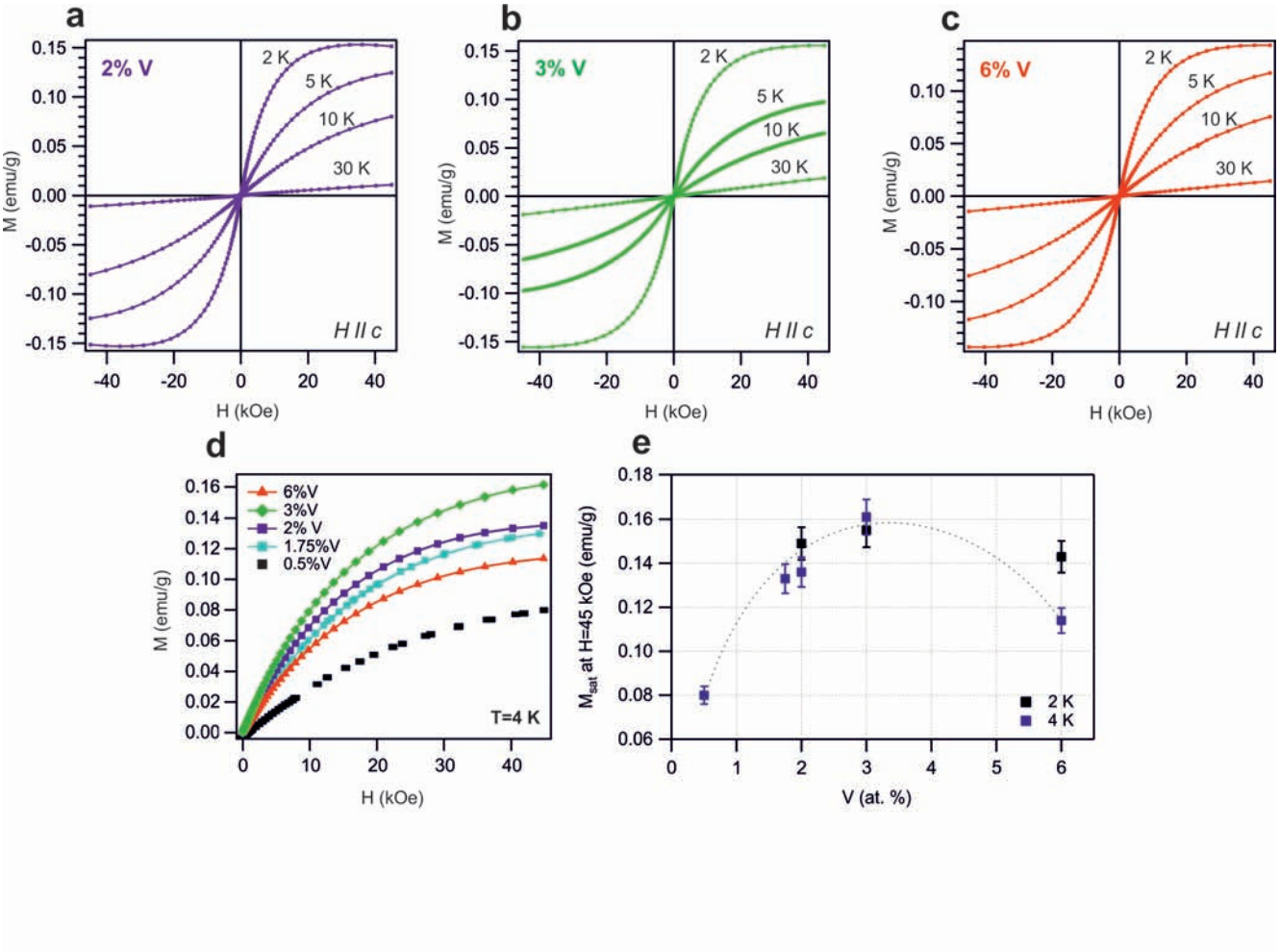

Figure 4.6 — Comparative magnetization measurements of V-doped BiTeI samples using SQUID magnetometry. (a-c) Isothermal magnetization dependences M(H) measured for BiTeI with doping concentrations of 2% V, 3% V, and 6% V at different temperatures when the external magnetic field is applied perpendicular to the surface plane (along the c-axis). (d) Comparative analysis of the magnetization curves M(H) measured for concentrations of 0.5% V, 1.75% V, 2% V, 3% V, and 6% V at 4 K temperature. (e) Dependence of the maximum magnetization value M_{sat} achieved in a 45 kOe magnetic field as a function of the atomic concentration V. The dotted line is presented for measurements at 4 K for clarity.

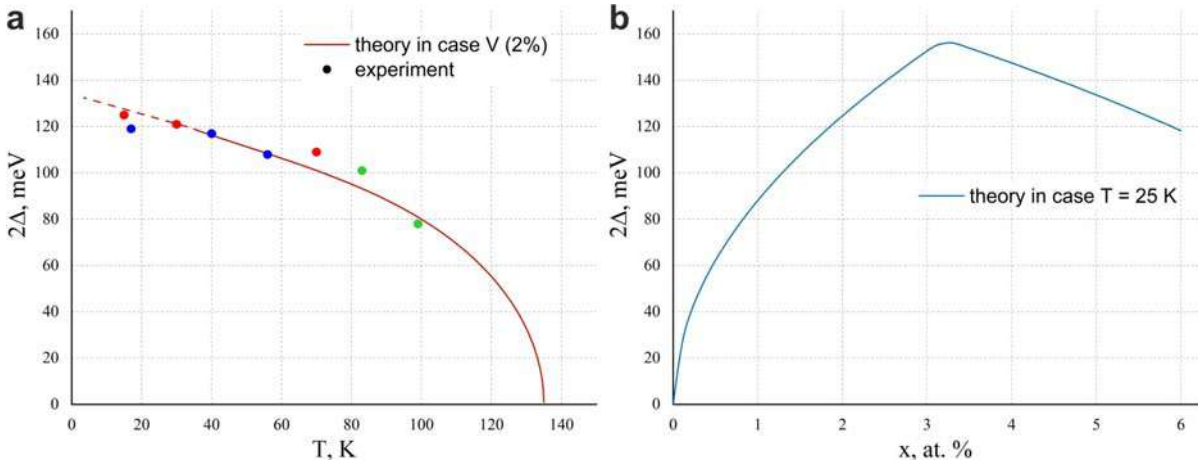

Figure 4.7 — (a) Theoretical temperature dependence of the band gap (2Δ) width versus experimental data for doping of 2% V (blue and red dots for different samples) and 2.5% Mn (green dots). (b) Theoretical dependence of the band gap width on the concentration of magnetic metal impurities, taking into account possible pairing. The figure is taken from the article [19], the calculations were performed in the group of Prof. A. K. Zvezdin.

Characterization of the surface of V-doped BiTeI by STM method

Large area STM images show an approximate 1:1 ratio of Te and I surface terminations (the boundary of the different terminations is shown by solid and dashed white lines in Fig. 4.8 (a-c)). This is in good agreement with a previous STM/STS study of the pure BiTeI surface [358]. It should be noted that it is the Te termination that contributes to the ARPES intensity map in the form of split parabolic dispersions [339]. Moreover, the Te and I terminations, which are characterized by a step height of about 1.8 Å, may be accompanied by an additional step height of about 7.2 Å (see Fig. 4.8 (b,c)), indicating the BiTeI unit cell step. Since the two possible surface terminations are characterized by different electron band energy shifts, the surface termination can be well identified by STS measurements (dI/dV curves) [358; 359]. Figure 4.8 (d-f) shows the different terminations with atomic resolution, indicating the good quality of the investigated V-doped samples. Panel (f) was measured at a different tunneling current and scale than panel (e) to obtain better atomic resolution. Bright and dark colored defects are often found on the I termination surface, which can be attributed to defects in the underlying Bi and Te layers [359]. Such atomic defects are marked by white circles in Fig. 4.8 (e); they differ in shape from those for the pure BiTeI surface, but are similar to Ag substitution defects in

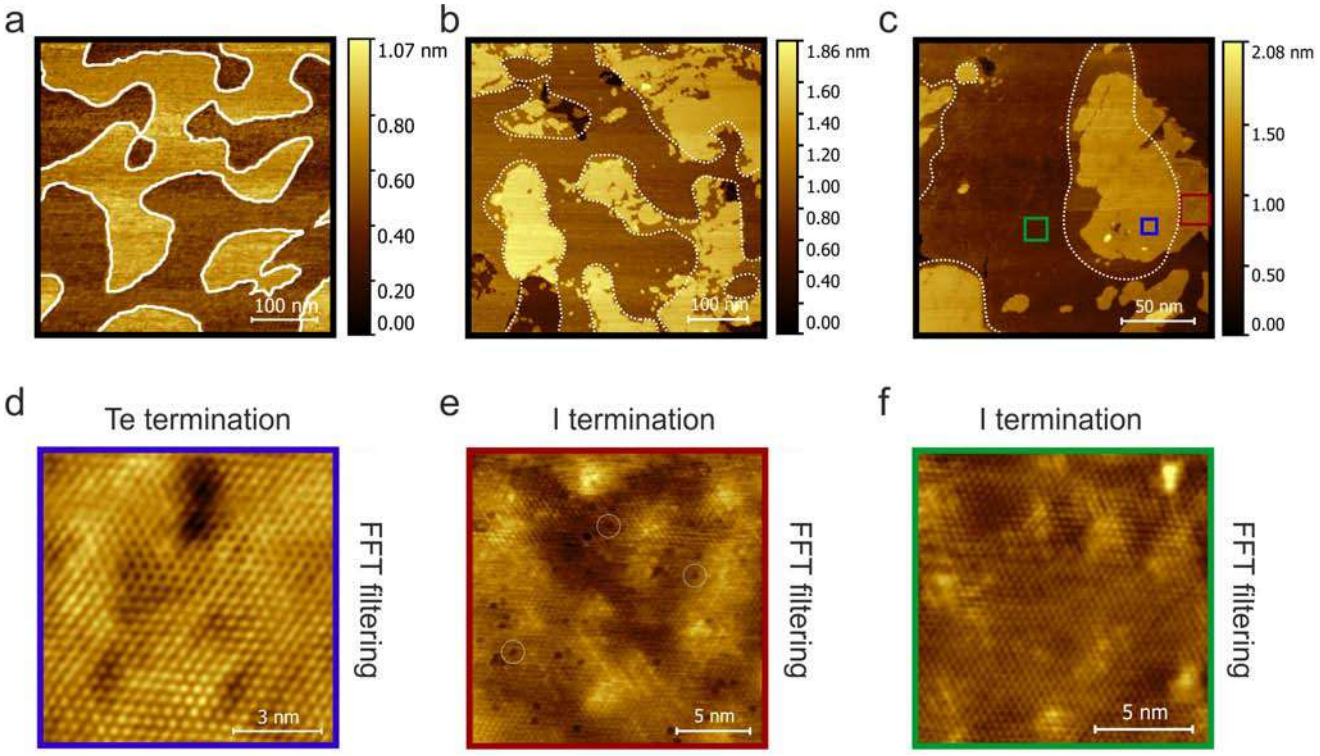

Figure 4.8 — STM images of BiTeI with 3% concentration of V: large area images obtained at bias voltage V_t = 0.5 V and tunneling current I_t = 0.1 nA (a), V_t = 1.46 V, I_t = 0.01 nA (b) V_t = 1 V, I_t = 0.1 nA (c) with colored squares, on which STM images of Te and I surface terminations were obtained with atomic resolution at V_t = 0.66 V and I_t = 0.3 nA (d), V_t = 1 V, I_t = 0.15 nA (e), and V_t = 1 V, I_t = 0.1 nA (f). The STM data in panels (d-f) were analyzed and filtered using 2D fast Fourier transform (FFT) to reduce noise and improve the visibility of periodic features.

the Bi layer [359]. The defect density (about 1.5 defects per 10 nm^2) is consistent with the density of Bi atoms substituted with V atoms at 3% concentration of V with respect to Bi.

4.3 Findings

In this chapter, magnetically doped BiTeI samples with concentrations of 0.5%, 2%, 3%, 6% for V and 2.5% for Mn are investigated by ARPES, STM, and SQUID magnetometry. STM studies confirm the homogeneity and concentration of magnetic impurities on the sample surface. From the electronic structure analysis, it follows that the band gap value at the Kramers point behaves non-monotonically with

increasing doping concentration. Indeed, the band gap increases first up to 130 – 135 meV at 3% V impurity. Then its value enters saturation and decreases with further increase of V concentration up to 6%. Theoretical estimates show that such a non-monotonic change in the value of the band gap is associated with the appearance of antiferromagnetically bound dimers of magnetic impurity at concentrations above 3%. Consequently, a decrease in the effective magnetic moment per magnetic impurity atom is accompanied by a decrease in the value of the band gap.

The studies have contributed to the understanding of the mechanisms of formation of intrinsic magnetic ordering and the associated band gap in magnetically doped semiconductors of the Rashba type. The obtained results on modulation of the band gap value at the Kramers point with variation of doping concentration by magnetic metal atoms can be useful in the development of models of highly efficient spin current generators in spintronics. In further studies of magnetically doped BiTeI by time-resolved ARPES (pump-probe experiment) [360], it was shown that bulk electron-phonon interactions predominate in the dynamics of unoccupied states, in particular, phonon “bottle neck”, leading to a very long time to establish equilibrium between the hot electron subsystem and the lattice.

Time-resolved studies of magnetically doped topological insulators by the ARPES method have revealed a new kind of two-dimensional photovoltaic effect with generation of anomalously large surface photo-EMF up to 210 meV. The photovoltaic effect has maximum efficiency for TIs with high filling of the upper Dirac cone states and the Dirac point located inside the fundamental band gap. For TIs with low filling of the upper Dirac cone states and Dirac point located inside the valence band, the generated surface photo-EMF decrease significantly. It was shown that the observed giant PVE is related to the accumulation of photoexcited electrons on the surface. This effect is accompanied by a two-dimensional relaxation process with the generation of spin-polarized zero-bias currents flowing through topological surface states outside the laser beam spot. As a result, the spin-polarized current generates an effective planar magnetic field, which is experimentally confirmed by the $k_{||}$-shift of TSSs relative to the lower spin-unpolarized states of the conduction band. The realized 2D PVE can be considered as a source of generation of surface spin-polarized currents with zero bias and laser-induced local surface magnetization occurring in materials with TSSs.

5. Synthesis and study of electronic and atomic structures of nanosystems based on ultrathin metal layers and quasi-freestanding graphene

Graphene remains one of the most promising materials in modern condensed matter physics. The linear dispersion dependence of $E(k)$ provides unusually high electron conductivity due to ballistic transport and many other unique electronic properties [81; 84; 139; 140; 361—367]. As a non-magnetic material with weak spin-orbit interaction, graphene cannot be considered as an active element of spintronics. However, the giant spin splitting of electronic states observed in graphene when in contact with heavy and magnetic metals offers great prospects for use in spintronics devices, particularly in the field of information storage and quantum computing. One of the most expected realizations of graphene in spintronics is magneto-spin-orbit graphene, which consists of well-ordered graphene in contact with a strong ferromagnetic element (cobalt) and a heavy metal (gold or platinum). As will be shown later in Chapter 7, when interacting with cobalt and gold, graphene not only retains its unique characteristics, but also partially adopts the properties of these metals – magnetism and spin-orbit interaction. For successful application of graphene in device elements it is necessary to use insulating substrates. Silicon carbide (SiC) is one of the most promising semiconductor substrates for the formation of thin nanosystems based on epitaxial graphene [368; 369]. In this regard, the realization of magneto-spin-orbit graphene on SiC substrate is an actual task.

In order to endow graphene with the required electronic properties, intercalation of magnetic or heavy atoms under graphene on SiC is usually used. However, it should be noted that there is an additional interface carbon layer, the zero-layer graphene (ZLG), between the graphene and the SiC substrate. Therefore, in many cases, intercalation of foreign atoms occurs both below and between these carbon layers [370—373]. Hence, in order to obtain only single-layer graphene as a result of intercalation, it is necessary to intercalate magnetic and/or heavy element atoms under ZLG on SiC substrate. The study of ZLG functionalization techniques is an important direction, as it will allow the creation of graphene-based layered structures on top of a semiconductor substrate and provide it with unique properties. Intercalation under the zero-layer graphene on SiC has been previously investigated for Sb [374], Ge [375],

Bi [376], Cu [377], and Si [378]. In these works, the transformation of ZLG into graphene was observed. Moreover, Co intercalation under ZLG was studied in [379], reporting the formation of a self-limiting silicide followed by Co intercalation between graphene and silicide.

This work attempts to explain the process occurring at the initial stage of Co intercalation, since the question of the modification of the electronic structure of graphene during the intercalation of a ultrathin Co layer is still unexplored. It should be noted that ARPES studies in the works on Co intercalation under ZLG on SiC have not been previously reported and the formation of quasi-freestanding graphene has also not been considered. Moreover, the study of graphene properties on magnetic ultrathin silicide layer is of considerable interest, since it is known that cobalt silicides exhibit different magnetic properties: from antiferromagnetic and ferromagnetic to paramagnetic, depending on the stoichiometry, quality of crystal structure and synthesis temperature [380; 381]. Various Hall effects due to spin-orbit and magnetic exchange interactions, such as quantum anomalous Hall effect (QAEH), valley-polarized QAEH, quantum valley Hall effect (QVHE), and circular dichroism Hall effect [88; 93], have been predicted in graphene. The use of promising semiconductor substrates such as silicon carbide to form thin nanosystems based on epitaxial graphene will allow the realization of these effects for use in industrially fabricated devices.

5.1 Synthesis of zero-layer graphene on 6H-SiC(0001) single crystal

A well-established approach to graphene synthesis is thermal graphitization of SiC surfaces under ultrahigh vacuum conditions [369; 382–387]. Prior to the graphitization process (obtaining the first and more graphene monolayers), several atomic reconstructions of the SiC surface are formed depending on the annealing temperature: (3×3), $(\sqrt{3} \times \sqrt{3})\mathrm{R30}^\circ$ and $(6\sqrt{3} \times 6\sqrt{3})\mathrm{R30}^\circ$. To synthesize a monolayer of intercalated graphene on SiC, it is more appropriate to use a carbon-rich $(6\sqrt{3} \times 6\sqrt{3})\mathrm{R30}^\circ$ reconstruction of SiC, called the zero-layer graphene. It is a carbon layer with a graphene-like hexagonal lattice in which about $1/3$ of

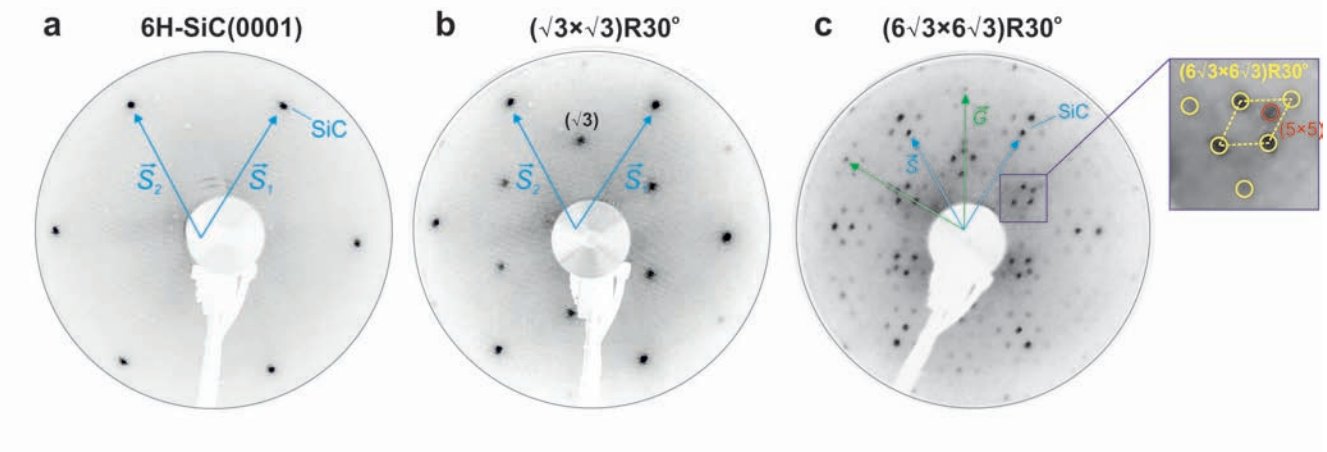

Figure 5.1 — LEED patterns of the initial 6*H*-SiC(0001) surface, E_p = 50 eV (a), $(\sqrt{3}\times\sqrt{3})$R30° reconstruction of the SiC surface after annealing at 950 °C, E_p = 57 eV (b), $(6\sqrt{3}\times 6\sqrt{3})$R30° reconstruction of the SiC surface after annealing at 1150 °C, E_p = 89 eV (c).

carbon atoms are covalently bonded to the silicon atoms of the SiC substrate [382; 383; 386]. As a result, the electronic structure of ZLG lacks the linear dispersion of the π band characteristic of the graphene Dirac cone. Intercalation of various metals is a widely used method to transform ZLG into a quasi-freestanding graphene monolayer [388–391].

A high-temperature surface annealing method of 6*H*-SiC(0001) was used to synthesize the ZLG [387]. The first step is to anneal the sample in ultrahigh vacuum at a temperature of about 600 °C. Each annealing step was limited to 15 min. Figure 5.1 (a) shows the bright LEED patterns of the (1 × 1) structure with reciprocal lattice vectors $(\vec{S}_1,\vec{S}_2)$ for pure SiC(0001) surface. Similar LEED images are observed after annealing at temperatures below 900 °C. The next annealing step at 950 °C leads to the formation of the $(\sqrt{3}\times\sqrt{3})$R30° SiC structure (see the diffraction pattern in Fig. 5.1 (b)). Further, annealing at T = 1150 – 1170 °C leads to the formation of the $(6\sqrt{3}\times 6\sqrt{3})$R30° (ZLG) structure. A typical LEED pattern from ZLG on SiC is shown in Figure 5.1 (c) [369; 382–387], and it is homogeneous throughout the sample. One of the distinctive features of the LEED patterns measured after annealing at different temperatures is the evolution with increasing temperature of the reflexes within the rhombus, marked by the yellow dashed line in Fig. 5.1(c) [383–385; 387]. After annealing at T = 1130 – 1150 °C, two diffraction reflexes from the "$(\sqrt{3})$" and "$(6\sqrt{3})$" structures are present inside the rhombus, i.e., they coexist on the surface of the system. The first reflex (in the lower half of the rhombus) corresponds to the $(\sqrt{3}\times\sqrt{3})$R30° structure, and the second (in the upper half of the rhombus) – the

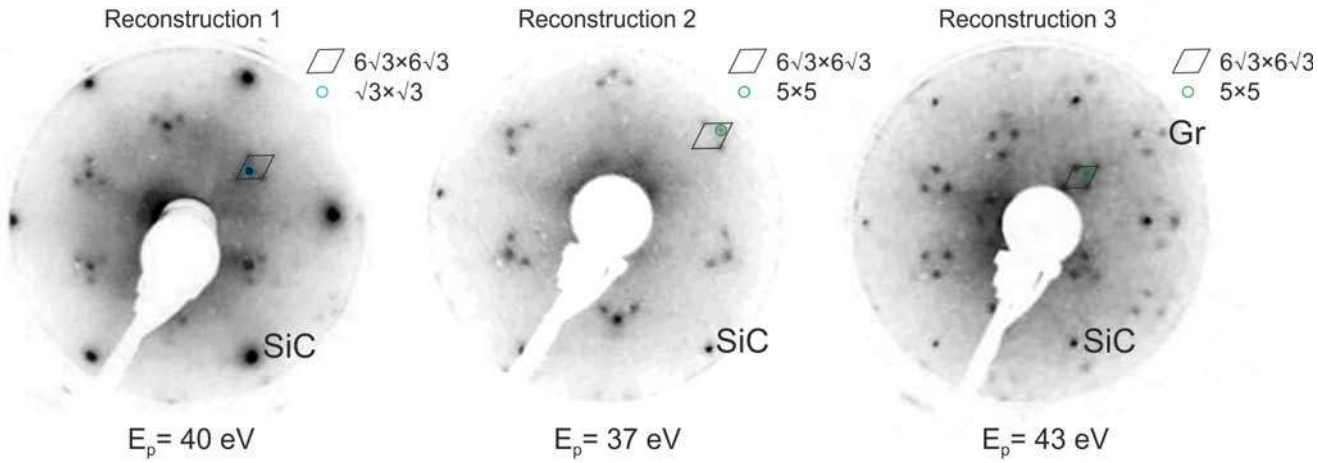

Figure 5.2 — LEED images of ZLG/SiC for different surface reconstructions.

quasi-(5×5) structure associated with the $(6\sqrt{3} \times 6\sqrt{3})$R30° reconstruction [385]. After annealing at T = 1150 – 1170 °C, only one bright reflex remains in the upper half of the rhombus (Fig. 5.1(c)), which corresponds to the formation of ZLG across the entire surface [383; 385]. Stepwise high-temperature annealing in an ultrahigh vacuum chamber allows us to determine the exact parameters to achieve high-quality ZLG on SiC by analyzing the *in situ* data obtained by LEED, XPS and ARPES methods. After finding the most appropriate parameters, the ZLG synthesis was carried out by one-step high-temperature annealing at 1150 °C with pre-degassing of the sample.

A more detailed study of the transition from "$(\sqrt{3})$" to "$(6\sqrt{3})$" reconstruction and further to graphene is shown in Fig. 5.2. From the LEED patterns, we can distinguish three different reconstructions on the surface: $(\sqrt{3} \times \sqrt{3})R30°+(6\sqrt{3} \times 6\sqrt{3})$R30° (reconstruction No. 1) and $(6\sqrt{3} \times 6\sqrt{3})$R30°+$(5 \times 5)$ (reconstruction No. 2) and $(6\sqrt{3} \times 6\sqrt{3})$R30°+$(5 \times 5) + 0.1$ ML of graphene (reconstruction No. 3). These reconstructions can be synthesized one after another with sequential increase in annealing temperature but the same annealing time (15 min). The 6H-SiC(0001) single crystal was temperature annealed at 1050 °C to obtain the zero-layer graphene with reconstruction No. 1, at 1150 °C – with reconstruction No. 2, and at 1170 °C – with reconstruction No. 3. It should be noted that reflexes from the reconstructions $(\sqrt{3} \times \sqrt{3})$R30° and (5×5)R0° are observed in addition to the main reflexes of the substrate (SiC) and "$(6\sqrt{3})$" (ZLG). Moreover, the reconstruction $(\sqrt{3} \times \sqrt{3})$R30° is replaced by the reconstruction (5×5) when the annealing temperature and/or annealing time are increased. The reconstruction (5×5) is associated with the formation of defects on the surface and is usually accompanied by the formation of graphene in the surface region with this reconstruction [385]. It is assumed that graphene domains

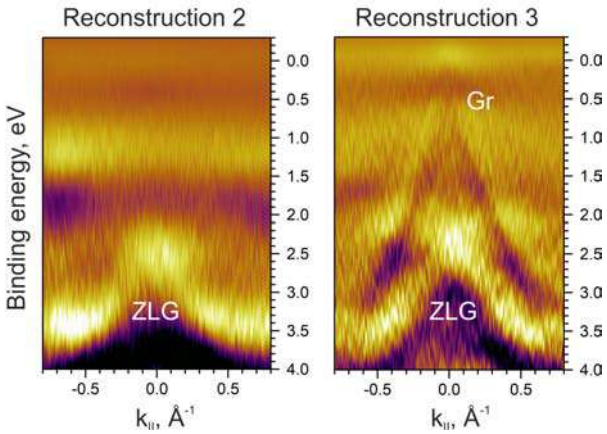

Figure 5.3 — ARPES intensity maps of the ZLG/SiC surface for different reconstructions measured in the region of the $\bar{\mathrm{K}}$ point of the surface Brillouin zone. For better visualization, the data are presented as the second derivative of the intensity with respect to energy. The photon energy is 40.8 eV.

begin to form between (5×5) domains. A distinguishing feature of reconstruction No. 3 from reconstruction No. 2 is the presence of a small amount of graphene on the surface of the system. Figure 5.3 demonstrates the ARPES intensity maps in the vicinity of the graphene $\bar{\mathrm{K}}$ point for these surface reconstructions. As can be seen in the Figure 5.3, reconstruction No. 3 is accompanied by the presence of a graphene cone near the Fermi level. Thus, the ARPES method together with the XPS method are highly sensitive methods to control the process of graphene formation on the system surface. Further in this work we will use the reconstruction $(6\sqrt{3}\times 6\sqrt{3})\mathrm{R}30^{\circ}+(5\times 5)$ (reconstruction No. 2), which is a precursor to further formation of quasi-freestanding graphene with increasing annealing temperature.

The valence band of the synthesized ZLG on SiC has been measured by ARPES mapping over a wide range of binding energies and quasi-wave vector values. Figures 5.4 (a-e) show the electronic structure of ZLG on 6*H*-SiC(0001) measured along and perpendicular to the $\overline{\Gamma\mathrm{K}}$ direction of the surface Brillouin zone. The π states typical of quasi-freestanding graphene are not observed in the measured electronic structure, while graphene-like σ states are easily resolved. At binding energies higher than 3 eV, a strong hybridization of the electronic states of the ZLG with those of the SiC substrate can be distinguished, which leads to avoided-crossing effect of the dispersion dependences and energy band gaps at the points of expected crossing. Other distinguishing features of ZLG are two localized states $g1$ and $g2$ at binding energies of 0.4 and 1.6 eV, which are observed near the Fermi level [378; 382; 386; 392]. To interpret the ARPES data measured at photon energies of 40.8 eV,

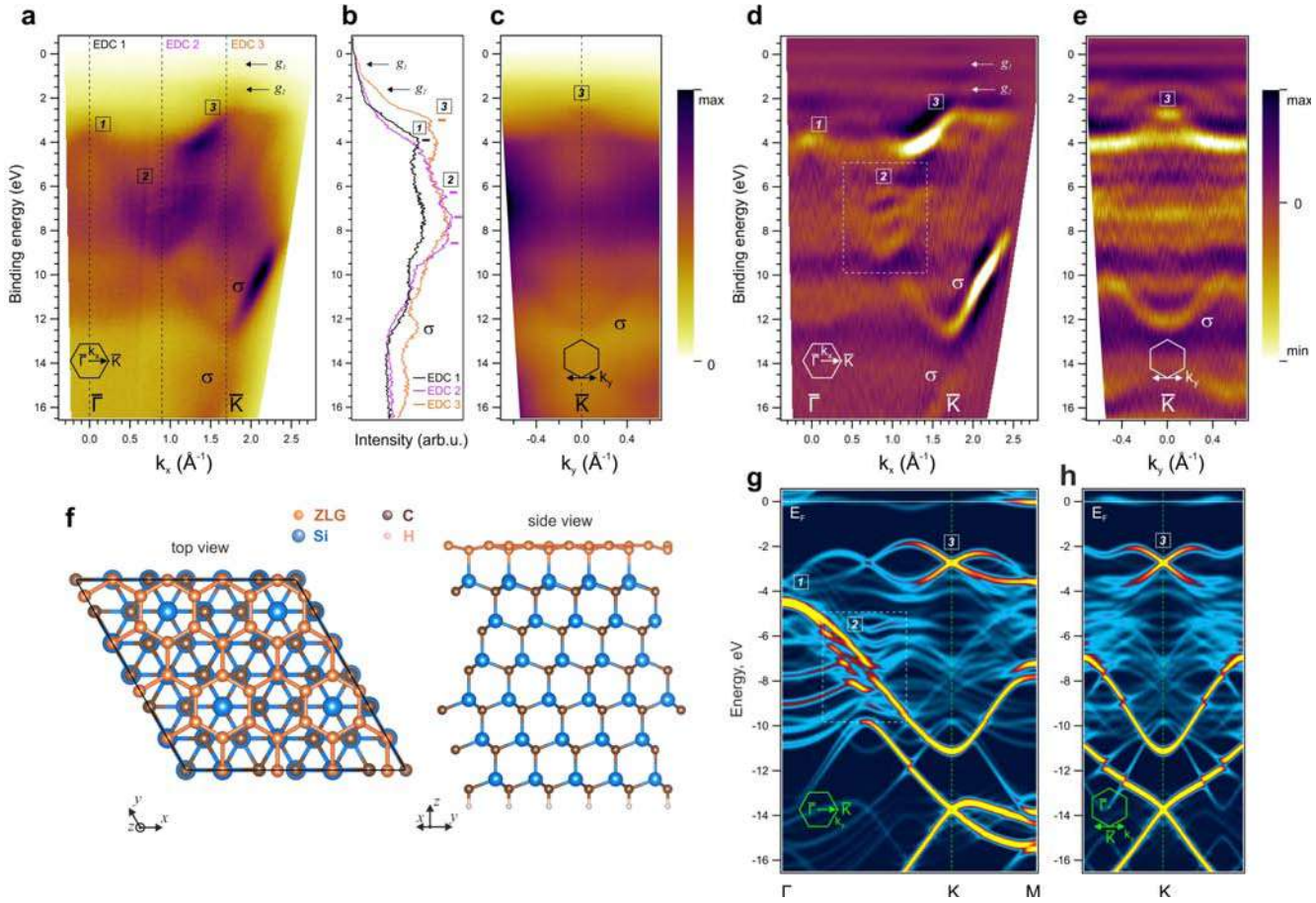

Figure 5.4 — (a), (c) ARPES intensity maps of ZLG on 6*H*-SiC(0001) measured along and orthogonal to the $\overline{\Gamma K}$ direction of graphene, photon energy is 40.8 eV (HeIIα). (b) Energy distribution curves (EDC) for quasi-wavelength vectors along the slices shown in (a). (d), (e) ARPES data presented as the second energy derivative to visualize the main features. (f) Ball-and-stick model of the ZLG on top of the 6*H*-SiC(0001) substrate. (g), (h) Calculated band structure of ZLG on 6*H*-SiC(0001) in the along and orthogonal to the $\overline{\Gamma K}$ direction in the same energy range.

first-principles calculations were perfomed within the DFT method for a structurally optimized unit cell (Fig. 5.4 (f-h)). Although similar calculations have been published previously [393; 394], the band structure calculated for a wide energy range of 0 – 17 eV is presented for the first time. The calculation results show that the characteristic band dispersion for the Dirac cone of graphene is indeed absent, a large band gap of 1.5 eV and an n-doped state are formed due to the strong covalent bonding between the ZLG and the Si atoms of the SiC substrate. The flat band just below the Fermi level is due to unsaturated broken Si bonds at the interface [393]. For ease of comparison between the ARPES data and the calculated band structure (Fig. 5.4 (g,h)), the main features that have a clear coincidence are labeled as 1, 2, 3. Of particular interest is the presence of band gaps in the intersection region

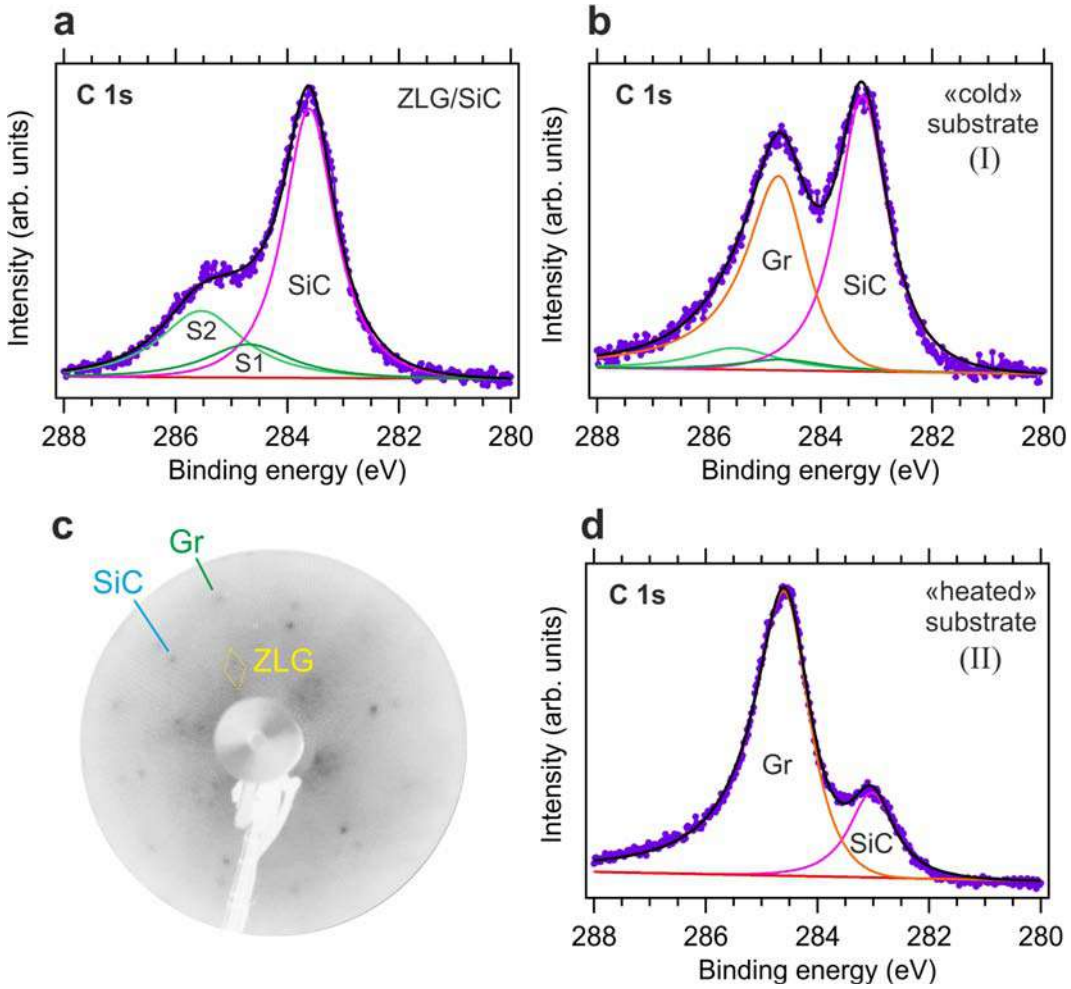

Figure 5.5 — XPS of the C 1*s* core level for (a) – ZLG on 6*H*-SiC(0001), (b) – after intercalation of 10 Å Co by deposition on a substrate at room temperature followed by annealing (step I), (d) – after intercalation of 14 Å Co by deposition on a heated substrate (step II). The photon energy is equal to 1486.6 eV. All spectra are normalized by the intensity maximum. (c) LEED pattern after step I, E_p = 93 eV.

of graphene σ and substrate states at energies of 6 – 10 eV both in theory and in experiment, which indicates the interaction between them (the region is indicated by a dashed rectangle in Fig. 5.4 (d,g)).

The analysis of the XPS data also confirms the conclusion about the successful ZLG synthesis. Figure 5.5 (a) shows the C 1*s* XPS spectrum for ZLG on SiC(0001), whose characteristic shape is explained by the presence of three components: a peak at 283.6 eV corresponds to carbon atoms in SiC, and two components S1 (284.7 eV) and S2 (285.5 eV) – carbon atoms in the ZLG [379; 382; 383]. The S2 component is due to the bonds formed in the plane of the reconstructed layer, and the S1 component is due to the bonds of the reconstructed layer with the uppermost Si atoms of the SiC substrate.

5.1.1 Adsorption of Co atoms on SiC substrate at different temperatures

The intercalation of Co under ZLG on SiC was carried out in two ways in order to find the most optimal regime. In the first step (I), 10 Å of cobalt were adsorbed onto the substrate at room temperature followed by annealing (for 3 h at 550 °C). Since ZLG intercalation was incomplete under these conditions, in the second step (II), 14 Å Co was adsorbed for $\sim$ 1.5 h onto a substrate heated to 450 °C. Figure 5.5 (b,d) shows the photoelectron spectra of C $1s$ measured after two intercalation steps. As a result of Co intercalation under ZLG, the spectral components of S1, S2, and SiC decrease in intensity. A new peak (Gr) appears in the spectra at a binding energy of 284.6 – 284.8 eV, which is characteristic of graphene formation [372; 382; 383]. The intensity of the graphene component is significantly higher after additional intercalation on the heated substrate. This indicates that a large surface area is covered by the graphene monolayer (Fig. 5.5 (d)), while for step (I) (Fig. 5.5 (b)), the ZLG and graphene phases coexist on the surface, and the complete conversion of ZLG to graphene cannot be achieved. The coexistence of the phases (ZLG and graphene reflexes) is confirmed by the LEED pattern taken after step (I) (Fig. 5.5 (c)). Moreover, the intensities of graphene and the S1 and S2 components were analyzed after deposition of 10 Å Co and intercalation by the two described methods on different samples. It was found that the ratio of intensities for the two methods $\frac{\text{Gr/S1(or S2)}^{(\text{II})}}{\text{Gr/S1(or S2)}^{(\text{I})}}$ is $\sim$ 1.4. Thus, it can be concluded that the conversion of ZLG to graphene is $\sim$ 1.4 times more efficient in the case of cobalt adsorption onto a heated substrate than in the case of cobalt adsorption onto a substrate at room temperature followed by annealing. The efficiency of intercalation during metal deposition on the heated substrate was previously shown for the graphene/SiC system [395], but for intercalation under ZLG was investigated for the first time.

5.1.2 Quasi-freestanding graphene by Co intercalation

Based on the results of the previous paragraph, the method of cobalt intercalation on heated substrate was chosen for further synthesis. For this purpose, 20 Å Co was deposited for 1 h on an ZLG/SiC substrate heated to 450 °C. Under these conditions, the intercalation of Co occurred directly during the deposition of metal atoms.

Analysis of XPS data

Figure 5.6 shows the decomposition of the photoelectron spectra into components using the approximation procedure. The C 1s spectrum of ZLG on SiC has the characteristic shape as in the previous figure, with three components: two components S1 (284.60 eV) and S2 (285.45 eV) corresponding to the carbon in the ZLG, and a carbon component in the SiC bulk (283.69 eV). The Si $2p$ spectrum (Fig. 5.6 (b)) presents a single broad peak at a binding energy of 101.66 eV with a full width at half maximum (FWHM) equal to 1.4 eV, which is in agreement with previous results [379; 383; 385; 387; 392; 396; 397]. However, the spin-orbit doublet of Si ($2p_{1/2}$ and $2p_{3/2}$) is not resolved when an X-ray tube with Al anode is used (without a monochromator), so a single asymmetric peak is recorded in the spectrum. The asymmetry parameter and the width of the Si $2p$ bulk component were fixed for all approximation procedures.

The shape of the C $1s$ and Si $2p$ spectra in Fig. 5.6 changes after the intercalation of 20 Å Co at a sample temperature of 450 °C. The S1 and S2 components are no longer observed in the C $1s$ spectrum, but an intense component corresponding to graphene at a binding energy of 284.4 eV appears [372; 382; 383]. The shape of the Si $2p$ spectrum gives important information about the processes involved. After cobalt intercalation, the Si $2p$ spectrum already has a complex multicomponent shape. In addition to the main bulk component, two new components appear in the Si $2p$ spectrum to the right and left of the main peak. The (A) component at a binding energy of 102 eV is located at a higher binding energy than the bulk

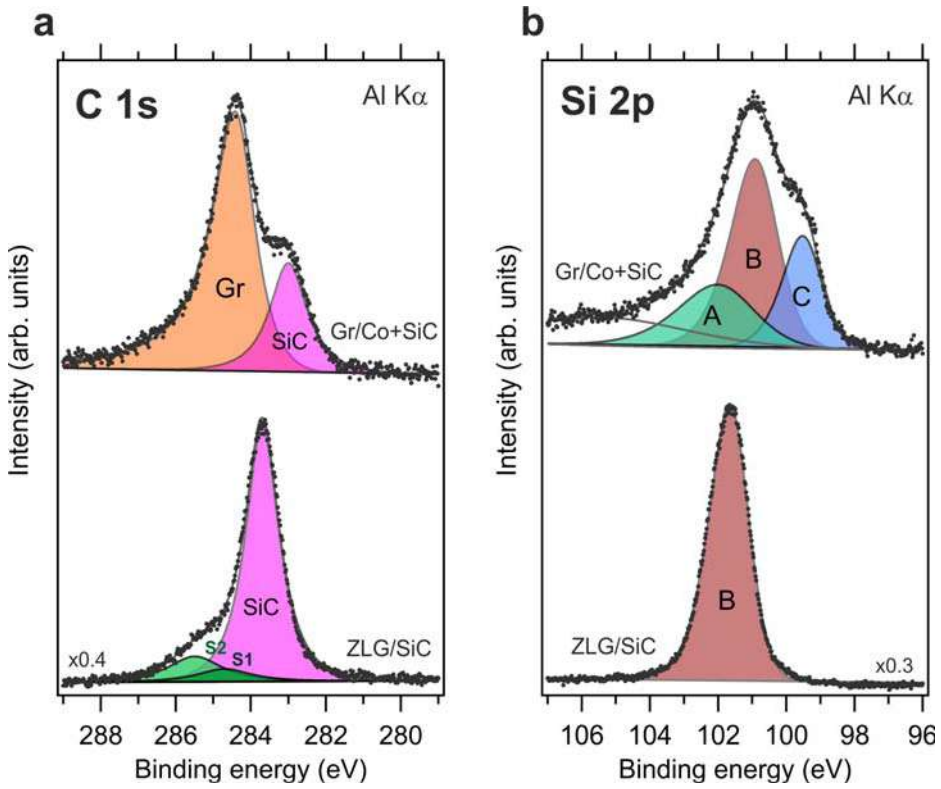

Figure 5.6 — XPS spectra of C $1s$ (a) and Si $2p$ (b) core levels measured for ZLG/SiC – bottom row, and after intercalation of 20 Å Co under ZLG on SiC – top row. The photon energy is 1486.6 eV.

component and may be related to the formation of the CoSi compound. The presence of a high-energy component relative to the bulk component in the Si $2p$ spectrum corresponding to the CoSi compound was also noted in [372; 398]. The low-energy component (C) with a binding energy of 99.5 eV can be attributed to the $CoSi_2$ compound with a lower concentration of Co [398]. There are significant contradictions in the published works regarding the energy position of the Si $2p$-component in Co-Si compounds [372; 397–400]. This is primarily due to the sensitivity of Co-Si compounds to the synthesis conditions: the amount of cobalt, reaction temperature, and crystal structure of the substrate surface. Therefore, several experimental methods, including angle-resolved XPS and Raman spectroscopy, were used to interpret the Si $2p$ components, and the consistency of the data with literature sources was verified. The spectral components corresponding to Si and C atoms in the SiC bulk (labeled as (B) and (SiC) in Fig. 5.6) are shifted by 0.7 eV toward lower binding energies. This effect can be explained by the different bending of the surface bands before and after cobalt silicide formation on the SiC surface [401]. Thus, based on the XPS data, it can be concluded that cobalt atoms interact with the substrate during

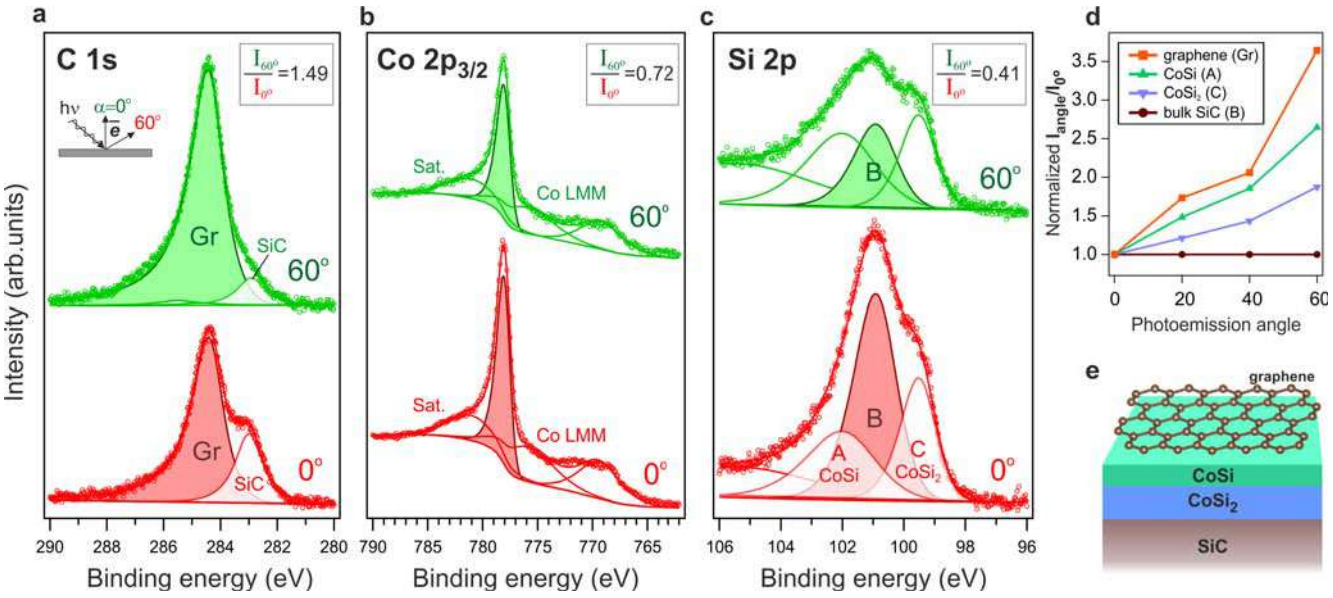

Figure 5.7 — Angle-resolved XPS spectra measured at emission angles of 0° and 60° relative to the surface normal for (a) – C 1s, (b) – Co 2p, (c) – Si 2p core levels, after Co intercalation under ZLG on SiC. The photon energy is 1486.6 eV. (d) Intensity ratios $I_{angle}/I_{0°}$ of individual spectral components normalized by the Si 2p bulk component as a function of the photoemission angle. (e) Structural model of the near-surface layers after Co intercalation based on the analysis of angle-resolved XPS spectra, is illustrated out of scale.

the intercalation process and two Co-Si surface compounds close in stoichiometry to CoSi and $CoSi_2$ are formed.

However, in order to study the localization of underlying layers, it is necessary to perform additional analysis of angle-resolved XPS data, in which photoelectron spectra are taken at different emission angles. By analyzing the angular dependences of the intensities of the element core levels, it is possible to determine the mutual location of layers by depth (see Paragraph 2.2.1 for more details).

The experimental angle-resolved XPS data are shown in Fig. 5.7 (a-c): changes in the spectra of C 1s, Co 2p, and Si 2p for two photoelectron emission angles 0° and 60° relative to the surface normal. The intensity ratios of the individual components for these two angles give us an idea of relative depth. A larger emission angle provides a more surface-sensitive spectrum. Therefore, by comparing the intensity ratios $I_{60°}/I_{0°}$ for the graphene component C 1s, the bulk component Co 2$p_{3/2}$, and the bulk component Si 2p (the numerical values of the ratios are shown in Fig. 5.7 (a-c) in insets), we can conclude that graphene is located above the cobalt silicides,

with the latter localized between the graphene and the SiC substrate. This proves the intercalation of Co under the ZLG on SiC.

Figure 5.7 (d) shows the values of intensity ratios I_{angle}/I_{0° for more angles and for all components of the Si $2p$ spectrum. To avoid changing the X-ray flux density in the analysis region when the photoelectron emission angle changes, the intensity of all components at a given angle was normalized by the intensity of the bulk component of Si $2p$ at the same angle. The intensity of the bulk component remains constant for all angles after normalization, with the fastest growing component belonging to the overlying layer and the slowest growing component belonging to the underlying layer. It is well seen that Co intercalation leads to the formation of near-surface Co-Si alloys. According to the work [402], the formation of CoSi alloy on the Si(100) surface occurs after annealing at 450 °C, and then as the annealing temperature increases, the $CoSi_2$ phase is formed at the triple points of two CoSi grains and the silicon surface. This agrees well with the presented experimental data, which shows that the CoSi compound is directly below the graphene and the $CoSi_2$ compound is lower. Figure 5.7 (e) shows a schematic model of the structure of the underlying layers after Co intercalation, assuming that they are flat and have a homogeneous composition. Nevertheless, this model gives us information about the process of cobalt intercalation and the formed Co-Si compounds.

High-resolution transmission electron microscopy studies

To obtain detailed information on the crystal structure of CoSi and $CoSi_2$ layers, high-resolution transmission electron microscopy (HRTEM) and high-angle annular dark-field scanning transmission electron microscopy (HAADF-STEM) measurements were performed using an energy dispersive X-ray spectroscopy (EDX) detector. An accelerating voltage of 200 kV was set for the measurements. Sample preparation was performed using the lift-out technique in a Zeiss Auriga Laser focused ion beam scanning electron microscope (FIB-SEM). Amorphous PtC protective material was deposited to prevent surface damage during FIB processing.

Figure 5.8 (a,b) shows the Z-contrast of the surface cross section cut. The intermediate layer between the SiC substrate and the PtC protective layer has a

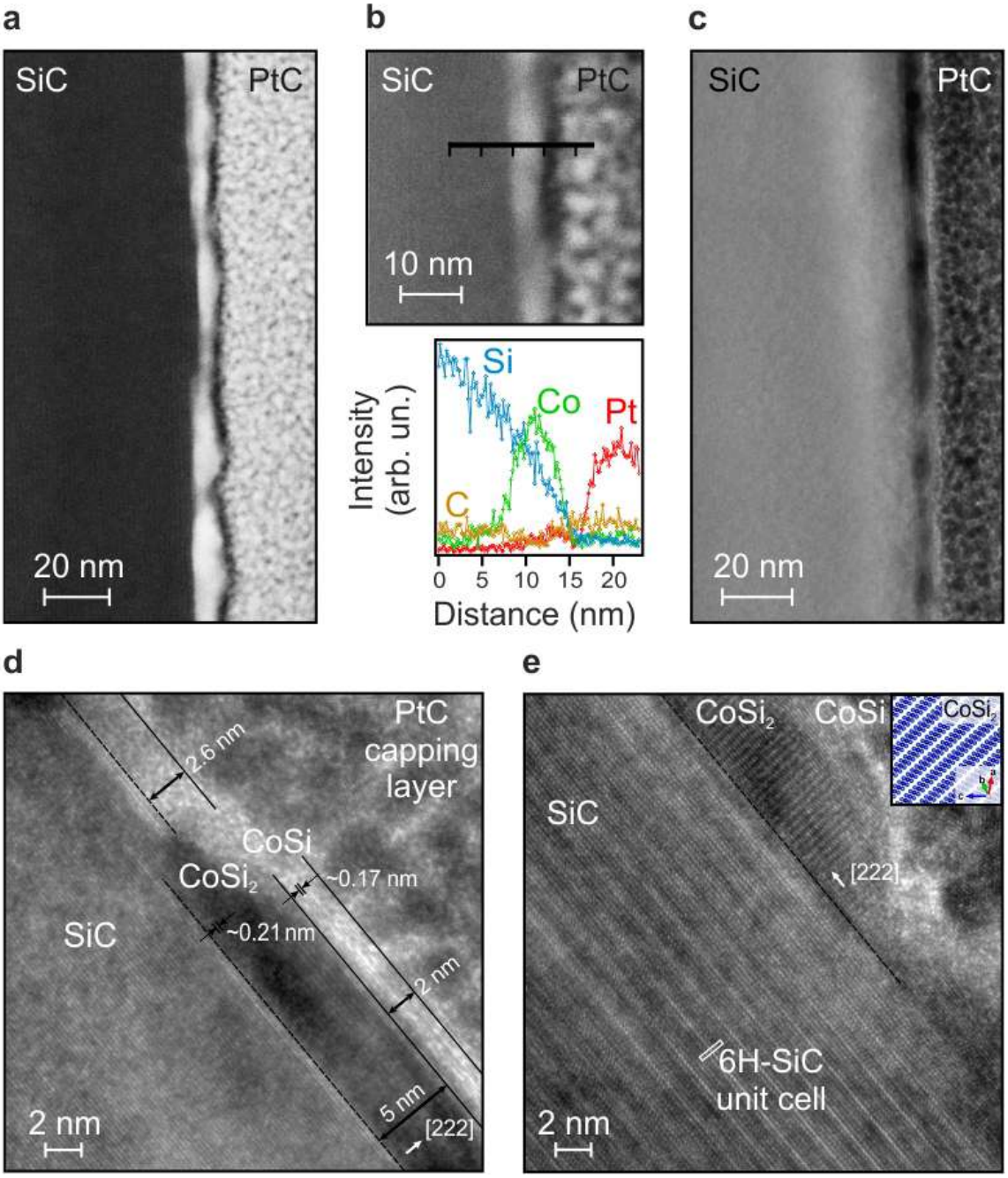

Figure 5.8 — (a,b) HAADF-STEM cross-sectional images with EDX profile measured along the black line shown in panel (b); (c) TEM cross-sectional image, (d) and (e) HRTEM cross-sectional images measured for two different rotation angles around the surface normal (0° and 15°, respectively). The inset in panel (e) shows a slice of the $CoSi_2$ single-crystal structure for reference.

thickness ranging from $\sim$ 4 nm to $\sim$ 10 nm. The EDX profile confirms the presence of Co atoms in this layer and the decreasing concentration of Si atoms from the SiC substrate to the protective layer. The TEM images (Fig. 5.8 (c-e)) have an inverse contrast compared to the HAADF-STEM images. A magnified image of the layered structure is shown in Fig. 5.8 (d). The nanometer-scale steps between the different lateral structures are well resolved. The smallest interlayer distance observed in the HRTEM images is $\sim$ 1.7 Å , which coincides with the measured height of each CoSi layer by the STM method [403], while the structure below it has a larger interlayer distance $\sim$ 2.1 Å. Searching for the zone axis in the range of sample rotation angles around the normal of 40° allows us to find the second zone axis, which is 15° away from the first one. For the second zone axis (Fig. 5.8 (e)), the SiC unit cell is well resolved and the cluster structure below the surface of the system is reproduced by the $CoSi_2$ single crystal structure. The clusters formed at the interface are $CoSi_2$ clusters covered by a residual CoSi layer. The growth mechanism has the same behavior as the high-temperature formation of $CoSi_2$ on Si(100) substrate, where $CoSi_2$ starts to form at the interface between CoSi and Si [402; 404; 405]. Notably, the orientation of the $CoSi_2$ clusters relative to the substrate differs in panels (d) and (e) of Fig. 5.8 by a rotation of 90° (see the rotation of the $CoSi_2$ vector [222] shown in the figure). This means that different growth directions of $CoSi_2$ nanocrystals are possible. The atomic structure of the CoSi layer is poorly resolved in HRTEM, and together with the absence of diffraction spots in the LEED pattern indicates a lateral misorientation of the CoSi atomic layers.

The study of the sample surface topography by atomic force microscopy method was performed by S.O. Filnov (Fig. 7 in the joint work [18]). It was shown that Co intercalation leads to the formation of terraces of different heights with the inclusion of triangular clusters of about 5 – 10 nm in size. In [403] it was reported that Co deposition on the Si(111) surface leads to the formation of triangular-shaped $CoSi_x$ islands ($x = 1,2$). Based on the experimental data obtained, the formation of triangular-shaped clusters with a layered $CoSi_x$ structure can also be suggested.

ARPES study

The ARPES study of ZLG on SiC after Co intercalation shows that ZLG transforms into graphene with the formation of a linear Dirac cone in the vicinity of the $\overline{\mathrm{K}}$ point of the surface Brillouin zone (Fig. 5.9 (a,b)). The Dirac point is located at a binding energy of 0.35 eV below the Fermi level. A similar electronic structure of quasi-freestanding graphene was observed after intercalation of Si under graphene on Co or Ni substrates [406; 407]. Nevertheless, we observe hybridization of the π state of graphene with a state at a binding energy of ~ 2.8 eV. This state can be attributed to the CoSi compound according to the calculation of the bulk density of states [408] and experimental results using ultraviolet photoelectron spectroscopy [409]. In the Figure 5.9 (c), the LEED pattern of ZLG after Co intercalation corresponds to the (1×1) crystal structure of graphene. Theoretical DFT calculations show that quasi-freestanding graphene with a linear Dirac cone is possible only in the case of graphene arrangement on the CoSi surface (see Fig. 5.10). Meanwhile, in the case of graphene arrangement on $CoSi_2$, the almost ideal Dirac cone is destroyed. This rules out the possibility of a significant contribution from the planar domains of CoSi and $CoSi_2$ within the same layer under the graphene.

According to the work [403] it is energetically favorable to form both $CoSi_2$ layers and CoSi/$CoSi_2$ layers on the surface. Figure 5.10 shows the structural relaxation of the model Gr/CoSi/$CoSi_2$/Gr system with two surfaces. While the structure of the CoSi surface is almost unchanged, the $CoSi_2$ surface, on the contrary, experiences strong deformation with the squeezing of cobalt atoms onto the surface (Figure 5.10 (b)). This causes the graphene to bind to the top cobalt atoms and its π states lose the linear dispersion character near the $\overline{\mathrm{K}}$ point (Fig. 5.10 (d)). At the same time, the graphene on the CoSi surface remains rather free, although it experiences some corrugation leading to the formation of a band gap. For the used period of the graphene cell (4×4 with respect to the unit cell of $CoSi_2$), graphene experiences a stretching by 2%, which for the real system can be much smaller, and, in turn, should lead to a decrease in the value of corrugation and the corresponding band gap. The same drawback of the model may explain the large electron doping of graphene (0.6 eV compared to the experimental value of 0.4 eV). However, the conclusion about the linear character of the dispersion of graphene π states is valid only for the CoSi surface.

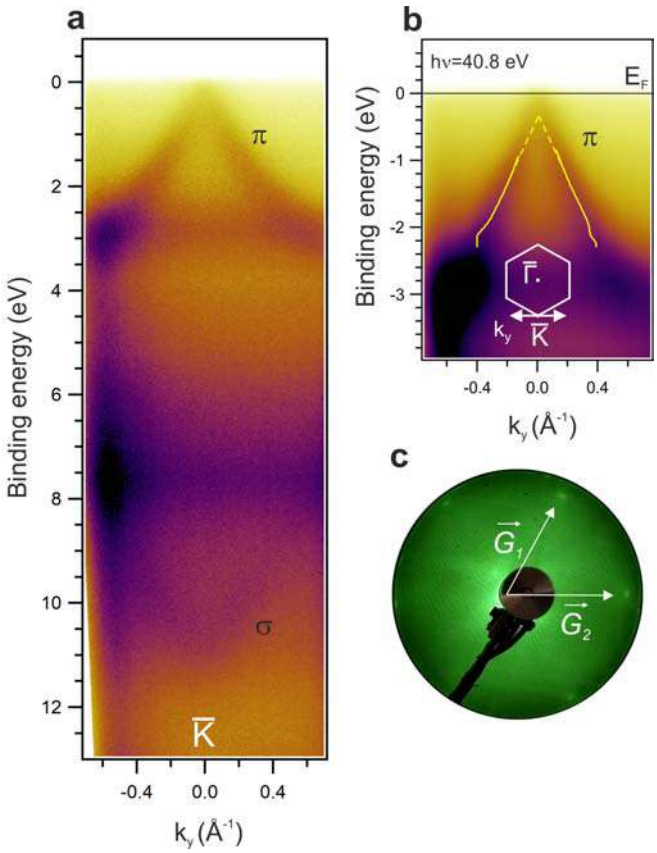

Figure 5.9 — (a) ARPES intensity map for the σ and π bands of Co-intercalated graphene measured in the direction orthogonal to $\overline{\Gamma K}$. The ARPES data were measured at a photon energy of 40.8 eV (HeIIα) and room temperature of the sample. (b) Dirac cone of quasi-freestanding graphene after Co intercalation. The solid yellow lines show the result of approximation of the momentum distribution curves by two Lorentzian peaks. (c) LEED pattern of graphene intercalated with Co, E_p = 60 eV.

Analysis of Raman spectroscopy data provides information on the composition and crystal structure of the sample. Raman spectra were measured in two different regions of the sample: in the center region, in which the growth of ZLG and Co intercalation occurred, and in the region that was covered by the metal mounting part. The spectra were measured and analyzed by I. A. Eliseev (Fig. 9 in the joint work [18]). The above presented XPS data (Fig. 5.7) indicate the presence of CoSi and $CoSi_2$ layers under graphene. It is known that the $CoSi_2$ layer does not give a noticeable contribution to the Raman spectra, but the CoSi layer is characterized by a rather strong line at 204 cm^{-1} and a weaker one at 224 cm^{-1} [410–412]. Thus, the appearance of an additional line at 204 cm^{-1} in the spectrum from the center region of the sample can be attributed to CoSi. The Raman spectroscopy data confirm the conclusions drawn from the XPS data about the presence of cobalt silicides under graphene.

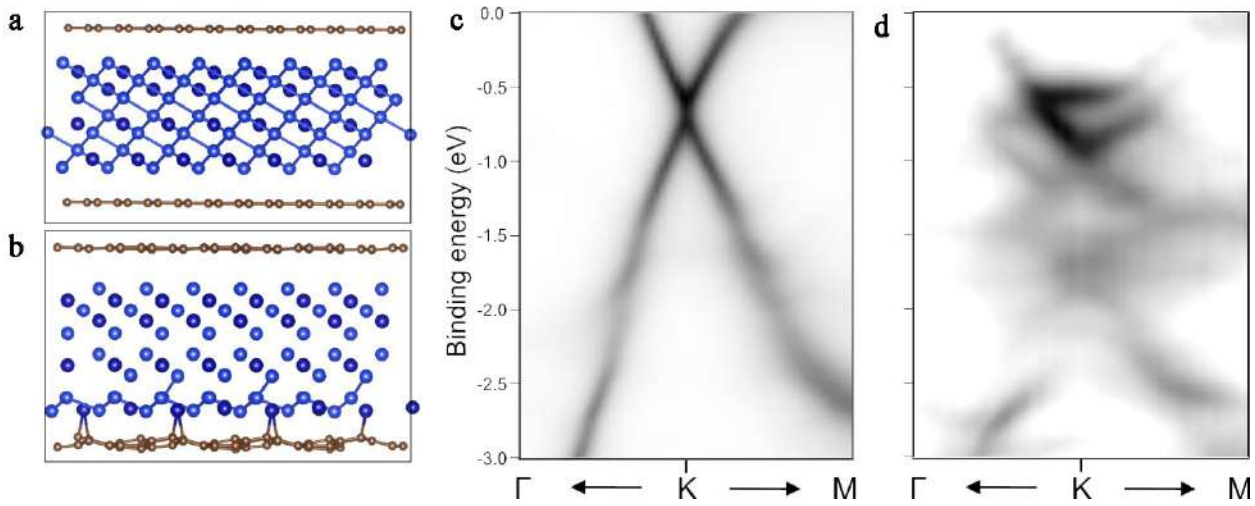

Figure 5.10 — The unit cell of Gr/CoSi/$CoSi_2$/Gr system before (a) and after (b) the atomic force minimization procedure. Contribution of graphene weight to the band structure for CoSi – (c) and $CoSi_2$ – (d) surfaces. Cobalt atoms are shown in dark blue, silicon – in blue, and graphene – in brown. The calculations were performed by A. V. Tarasov.

Study of magnetic properties

To investigate the magnetic properties of the sample, measurements were carried out using a SQUID magnetometer by applying a magnetic field parallel to the surface ($\perp$ axis c), in the sweep mode by temperature and magnetic field. It is known that for cobalt silicides on Si(100), the easy magnetization axis lies in the plane of the surface, and it is quite difficult to magnetize them along the surface normal [381]. The CoSi compound, which is a diamagnetic in the bulk [413], exhibits magnetic properties in nanoforms due to the uncompensated spins on the surface Co atoms [414]. At the same time, $CoSi_2$ does not exhibit strong magnetic properties in thin films a few nanometers thick [415].

Figure 5.11 (a,b) shows the magnetization curves $M(H)$ of Co-intercalated ZLG/SiC sample measured in an external magnetic field in the surface plane at different temperatures. Figure 5.11 (c) shows the variation of the hysteresis loop and coercivity in the temperature range of 2 – 100 K. The maximum value of coercivity is 180 Oe at 2 K. This value decreases with increasing temperature, and the hysteresis loop is practically closed at room temperature. At the same time, the magnitude of saturation magnetization decreases with increasing temperature (Fig. 5.11 (a)). It is found that the magnetization saturates at an applied magnetic field of 40 kOe and

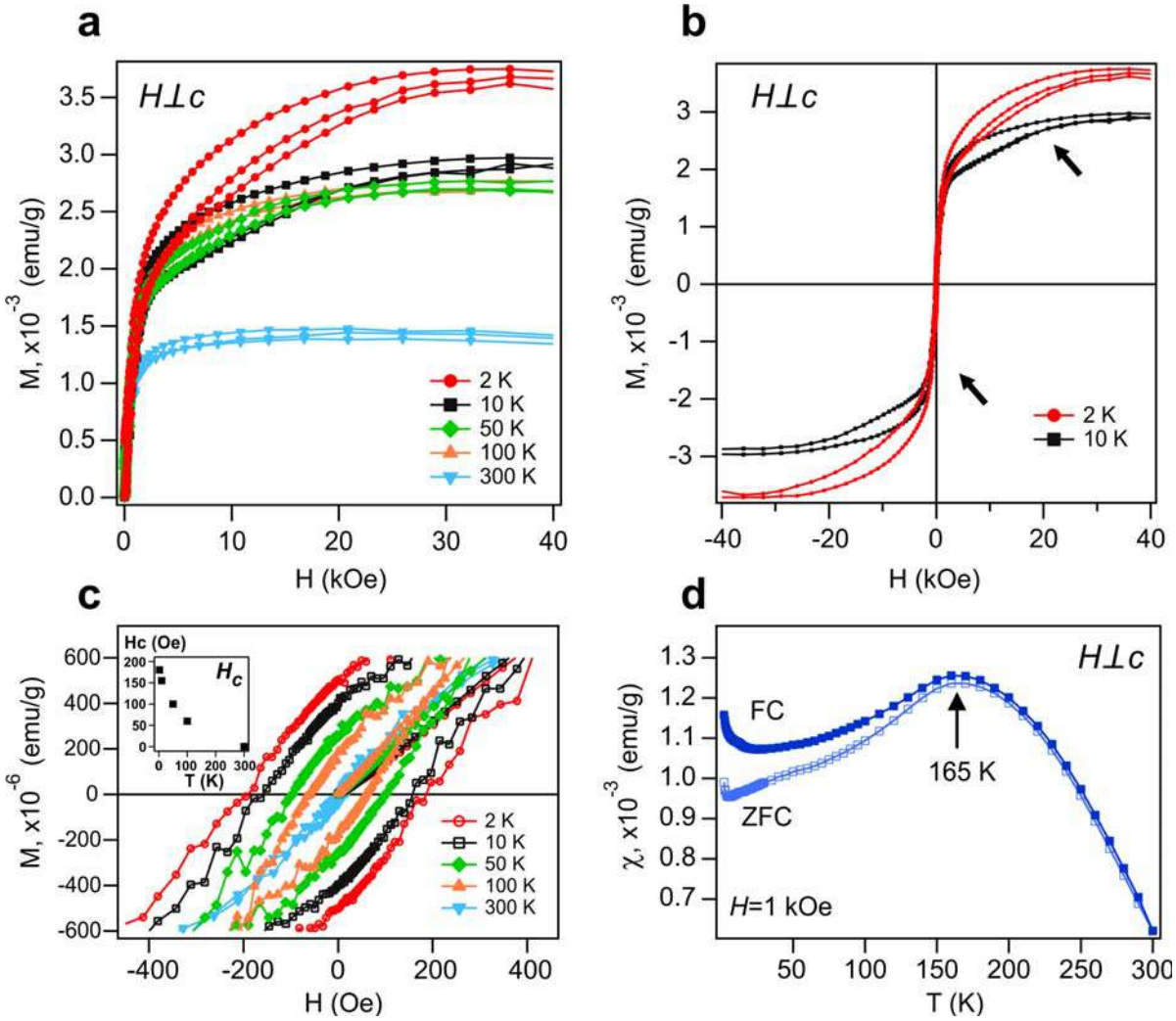

Figure 5.11 — (a) Isothermal magnetization curves $M(H)$ of Co-intercalated ZLG/SiC sample at different temperatures. (b) Two $M(H)$ curves at 2 K and 10 K over the whole range of applied field to demonstrate the double jump process on the hysteresis loop. (c) Modification of the hysteresis loops at different temperatures obtained from the $M(H)$ curves. Inset – plot of the temperature dependence of the coercive field (H_C). (d) Temperature dependence of the magnetic susceptibility $\chi(T)$ measured in a field H = 1 kOe. The zero field cooling curve (ZFC) is indicated by open symbols, the field cooling curve (FC) by shaded symbols.

at all temperatures. This indicates that all spins are ordered and aligned along the field direction at this value.

Interestingly, the magnetization curves (Fig. 5.11 (b)) have a loop shape with two jumps [415–417]. This behavior is characteristic of epitaxial ferromagnetic thin films with planar uniaxial anisotropy affecting cubic magnetocrystalline anisotropy. In this case, the magnetization change strongly depends on the orientation of the applied field. If the field is not co-directed with one of the cubic easy axes and is slightly tilted away from the hard axis, the magnetization is hampered and a two-jump process can be observed. The jumps are marked in Fig. 5.11 (b) by black arrows on the curve when the field is cycling between negative and positive values. The shape of the loop with two jumps is reproduced on the reverse cycle of field change.

The temperature dependences of the magnetic susceptibility $\chi(T)$ with zero field cooling (ZFC) and constant field cooling (FC) are shown in Fig. 5.11 (d). The magnetic susceptibility $\chi(T)$ in both ZFC and FC curves has a broad maximum at temperature $\sim$ 165 K. This can be related to superparamagnetism, as previously shown on cobalt ferrite or iron-palladium alloy nanoparticles [418–420]. The ZFC and FC curves diverge markedly below 165 K, and a slight divergence of the curves persists above this temperature up to 300 K. A similar behavior of magnetic susceptibility curves with the presence of hysteresis loop was found in the study of CoSi nanowires [414]. The magnitude of magnetic susceptibility increases for the ZFC and FC curves when the temperature reaches values below 5 K. This correlates with the increase in saturation magnetization of the $M(H)$ curve at 2 K (Fig. 5.11 (a)). The saturation magnetization changes slightly in the temperature range of 10 – 100 K, but the coercive field decreases gradually with increasing temperature (Fig. 5.11 (c)). Thus, the graphene/CoSi/$CoSi_2$/SiC system possesses ferromagnetic properties in the surface plane, presumably due to the CoSi nanothin layer.

5.1.3 Findings

In the present work, the synthesis parameters of the zero-layer graphene on 6*H*-SiC(0001) have been determined. It is found that the synthesis of ZLG is possible by one-step high-temperature annealing of SiC at 1150 °C with pre-degassing of the

sample. The results of LEED, XPS and ARPES studies prove the formation of ZLG with typical photoelectron spectra and diffraction pattern. The electronic structure of ZLG on SiC was investigated by the ARPES method over a wide range of binding energies and quasi-wave vectors. The band structure calculated by the DFT method agrees with the ARPES intensity maps.

Two methods of Co intercalation under ZLG on SiC have been investigated: Co deposition on a heated substrate and Co deposition on a substrate at room temperature followed by annealing. Both methods lead to the intercalation of Co and the transformation of ZLG into graphene. At the same time, Co deposition on heated substrate is more effective for the intercalation process and the transformation of ZLG into graphene.

The synthesized graphene on ultrathin $CoSi/CoSi_2$ layers has a quasi-freestanding character. The results of HRTEM study provided detailed information on the crystal structure of CoSi and $CoSi_2$ layers. Based on the magnetic measurements, it can be concluded that the graphene/$CoSi/CoSi_2$/SiC structure possesses ferromagnetic properties with an appropriate hysteresis loop and a coercivity value of 180 Oe at 2 K. Thus, a new method for the synthesis of quasi-freestanding graphene with a Dirac cone structure in contact with a magnetic substrate has been discovered. The obtained results are the basis for further realization of magneto-spin-orbit graphene on semiconductor substrate and are important for future application of such graphene in spintronics.

5.2 High-temperature synthesis of graphene by chemical vapor deposition on single-crystal metal substrates

The chemical vapor deposition (CVD) method is widely used to synthesize graphene on single-crystal transition metal substrates. It is known that graphene synthesized by CVD at a synthesis temperature of $\sim$ 560 °C is characterized by a low-energy electron diffraction pattern with arc-shaped reflexes [16]. This is due to the presence of prevalent misoriented domains, the existence of which has been established by other studies [421–423]. The STM data obtained for such a system are consistent with the LEED results: a well-known moiré pattern, characteristic

of the mismatched interface between graphene and a single-crystal cobalt film, is observed. Moreover, contributions from other rotational domains are observed in the ARPES intensity maps near the $\overline{\mathrm{K}}$ point of the surface Brillouin zone of the Co(0001) and (1×1) graphene domain [421—423], which significantly complicates the interpretation of the experimental data. In [424] it was shown that in the case of graphene synthesis on Ni(111), the quality of graphene increases with the synthesis temperature. At low-temperature synthesis (400 – 500 °C), a highly defective film is formed with small ordered graphene domains and disordered domains consisting of Stone-Wales type defects [425]. Graphene grown at 650 °C have a small number of defects that broke epitaxy (1×1), but excellent long-range order in the rest of the surface. The improvement in the structural perfection of graphene with increasing synthesis temperature may be related to the achievement of better crystallization of the transition metal thin film, the absorption/segregation kinetics of carbon atoms on the substrate surface, and the defect healing and recrystallization processes of graphene [426].

5.2.1 Graphene synthesis on Co(0001) ultrathin film on W(110) single crystal

Studies of the structural properties of graphene grown by the CVD method on an ultrathin Co(0001) layer have shown that well-ordered graphene perfectly oriented relative to the substrate can be grown only in a certain temperature range. As an example, Fig. 5.12 shows LEED patterns for a Co(0001) layer and two graphene samples on Co(0001) obtained at temperatures of 560 °C and 660 °C. The latter temperature is quite high and close to the graphene decomposition temperature of 670 – 700 °C (see Section 6.3). From the comparison of LEED patterns, it can be seen that the graphene synthesized at lower temperature (560 °C) is characterized by arc-shaped reflexes, while at higher temperature (660 °C) – is well oriented and commensurate with the Co(0001) surface. The ARPES intensity map taken near the $\overline{\mathrm{K}}$ point of the surface Brillouin zone of well-oriented graphene on Co(0001) shows the result of hybridization of π states of graphene with d states of cobalt (see Fig. 5.12 (a)). The most striking features of this system at the $\overline{\mathrm{K}}$ point, which distinguish it from graphene

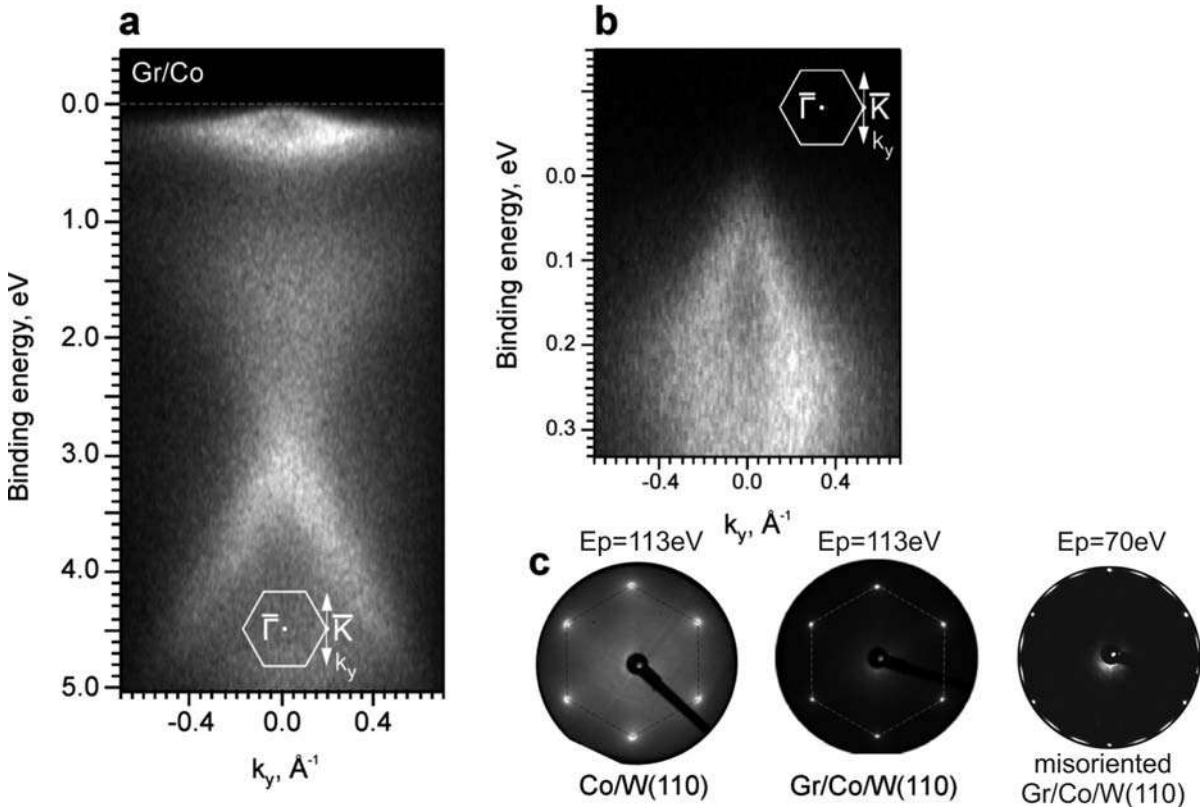

Figure 5.12 — (a) ARPES data obtained for well-oriented graphene on Co(0001) at room temperature. (b) Mini-cone of graphene at the Fermi level. hν = 40.8 eV in both cases. The arrows in the insets schematically indicate the direction of measurements in momentum space. (c) LEED patterns of Co(0001)/W(110) substrate (left) and well-oriented graphene on Co(0001)/W(110) (center) and misoriented graphene on Co(0001)/W(110) (right).

grown on other substrates, are the mini-cone of π state just below the Fermi level with spin polarization like that of minority Co (the enlarged image of the mini-cone is shown in Fig. 5.12 (b)) and the π state with spin polarization like that of minority Co at a binding energy of about 2.8 eV. The origin of these features in well-oriented graphene on Co(0001) is discussed in detail in [16].

Figure 5.13 shows the ARPES intensity maps for semi- and fully intercalated graphene. The semi-intercalated graphene shows a superposition of ARPES intensity maps from Gr/Co and Gr/Au/Co domains (mini Dirac cone and Dirac cone characteristic of quasi-freestanding graphene). A comparison of the quasi-wave vector values for the Dirac points of these two domains, indicated by the vertical dashed lines in Fig. 5.13 (a), gives an estimate of the stretching of the graphene lattice $\sim 2\%$ on the Co(0001) surface relative to quasi-freestanding graphene, which is consistent with the mismatch between the graphene lattice and the close-packed Co surface. It is well seen that increasing the amount of gold under graphene leads to a change in the n-doping

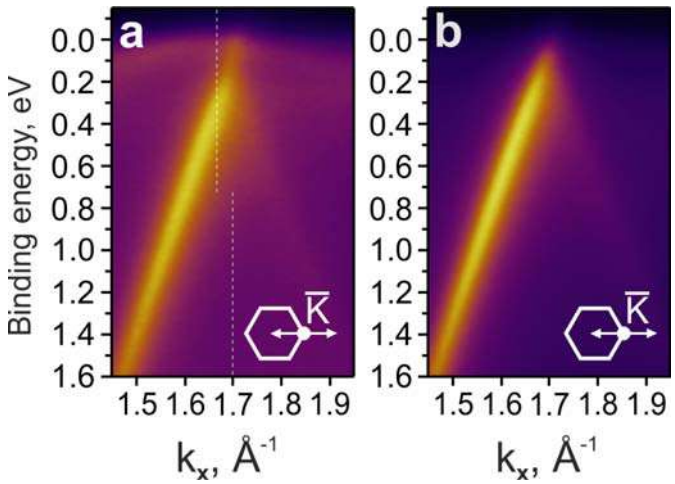

Figure 5.13 — LEED intensity maps for semi- (a) and fully (b) intercalated graphene measured along $\bar{\Gamma}\bar{K}$ at p-polarized radiation and 34 eV photon energy.

of graphene with a shift of the Dirac point closer to the Fermi level. This dependence is also confirmed by DFT calculations in [427]. It should be noted that no ARPES intensity from the Gr/Co domain was observed for fully intercalated graphene.

5.2.2 Graphene synthesis on Pt(111) single crystal

It is known that preparation of a pure Pt surface and subsequent CVD synthesis of graphene at 1200 K often yields a two-domain structure (with $0°$ and $30°$ rotational domains relative to the base Pt(111) substrate) [221]. Sometimes additional rotated domains with angles close to $0°$ and $30°$ can be formed, which significantly complicates the acquisition of ARPES data from the $0°$ and $30°$ main domains and the interpretation of experimental data after further synthesis, such as metal adsorption and intercalation. Analyzing the electronic structure of the Gr/Pt(111) system and the influence of Pt vacancies or bulk dissolved carbon on the electronic structure of graphene has so far remained an open question [217; 220; 223; 381].

As a result of the study of graphene synthesis by CVD method on Pt(111) single crystal, which is not subject to strong carbon contamination after multiple syntheses, it was found that when the synthesis temperature is increased to 1200 K, it is possible to obtain single-domain graphene whose unit cell is rotated by $30°$ relative to the unit cell of the substrate. The results of the study of such single-domain graphene are presented in [15]. However, in further syntheses of graphene on

the same single crystal it was more and more difficult to obtain the 30° domain; it was necessary to repeat the synthesis many times with the conventional procedures of etching with Ar^+ ions and temperature annealing, including in the atmosphere of O_2, otherwise multi-domain graphene was formed, as in the above publications. By means of XPS and STM studies it was found that segregation of carbon on the surface and formation of nanoclusters occurs when Pt(111) is heated to the synthesis temperature (without adding propylene). Apparently, these clusters are the nucleus of multidomain graphene. In order to remove carbon contamination from the surface of the Pt(111) single crystal, the surface cleaning procedure outlined in Paragraph 2.3.2 was prepared. The results of the study of graphene on Pt(111) prepared by this procedure are as follows.

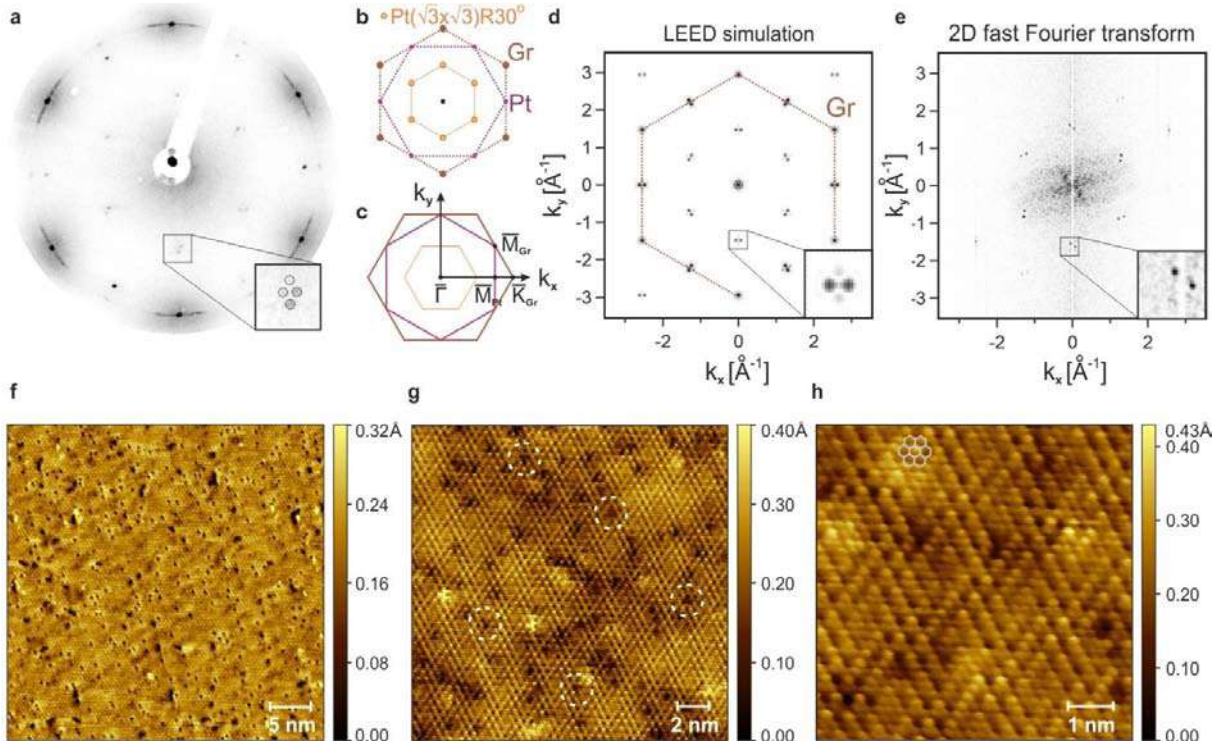

Figure 5.14 — Study of graphene/Pt(111) by LEED and STM methods: (a) LEED pattern at $E_p = 80$ eV with its schematic representation on panel (b); (c) mutual arrangement of the surface Brillouin zones of graphene and Pt(111) ; (d) modelling of the LEED pattern on panel (a) by single scattering; (e) 2D FFT of the STM image on panel (f); STM images measured at $V_s = 3$ mV, $I_t = 0.7$ nA (f) and $I_t = 2.6$ nA (g, h). The hexagonal lattice of graphene is shown in gray in panel (h).

The LEED pattern in Fig. 5.14 (a) clearly shows that reflexes from the rotational domains are present together with the reflexes from the 30° rotational domains of graphene, which form a superstructure close to $(\sqrt{3} \times \sqrt{3})$R30° relative to Pt(111). However, as will be shown in Fig. 5.16, these domains have a negligible

contribution to the ARPES intensity maps. A comparison of the diffraction spots of the main domain with the modelled ones, indicated by the dashed circles, is shown in the inset to Fig. 5.14 (a). The diffraction pattern was simulated in LEEDLab 2018 [428] with multiple scattering on graphene and Pt structures up to second order. It is well seen that additional reflexes appear near the expected positions of the Pt($\sqrt{3} \times \sqrt{3}$)R30° superstructure reflexes due to the incommensurability of Pt and R30° graphene domains. In addition, qualitative agreement is found with the single-scattering calculation of the LEED intensity (Fig. 5.14 (d)) for a free corrugated graphene cluster with an amplitude span of 0.3 Å and for an electron kinetic energy of 80 eV, which was used in the LEED measurement. The symmetry and corrugation period were set according to the unit cell of the Pt(111) single crystal surface. Remarkably, the STM measurements revealed a superstructure with a corrugation of about 0.2 – 0.3 Å, which agrees well with the value reported in Ref. [217]. The two-dimensional fast Fourier transform (2D FFT) of the large-area STM image (Fig. 5.14 (e)) also revealed reflex splitting associated with the presence of superstructure. Thus, the observation of superstructure in the LEED pattern is clear evidence of a well-oriented 30° graphene domain.

Moreover, non-periodic triangular-shaped defects were detected in the STM images (Fig. 5.14 (g-h)). Some of them are marked by dashed circles in Fig. 5.14 (g). It should be noted that these defects were absent from the STM images of other rotated domains, which make a minor contribution to the LEED and ARPES data. A commensurate surface structure Gr(2×2)/Pt($\sqrt{3} \times \sqrt{3}$)R30°, consisting of an ordered array of single Pt vacancies formed in the uppermost Pt layer and covered by graphene, was proposed by G. Otero et al. [217]. First-principles calculations of this vacancy superstructure confirm the strong covalent bonding between graphene and Pt [217; 381]. On the other hand, experimental studies of graphene on Pt(111) surface using ARPES [15; 220; 223; 429] show that graphene has a quasi-freestanding character. It has been suggested that the growth mechanism plays a crucial role in the hybridization and p-doping of the electronic structure of graphene on the Pt substrate [220]. It is shown that graphene grown by the carbon segregation method instead of the CVD method is characterized by a stronger p-doping and a lack of noticeable hybridization between graphene and Pt states, which is possibly due to the complex morphology of the Pt substrate surface as a result of carbon segregation [220].

To determine the influence of the surface concentration of Pt vacancies and the possible presence of carbon atoms in the vacancies on the interaction of graphene with the Pt substrate, three structures of graphene on Pt(111) were calculated by DFT method. To reveal the distinctive features of the different structures at the atomic level, STM images (Fig. 5.15) were modelled in the Tersoff-Hamann approximation [430]. The simulated images show a constant local density of states (LDOS) surface near the Fermi level. Gr(2×2)/Pt($\sqrt{3}\times\sqrt{3}$)R30° structure features are found in all images, but characteristic triangular-shaped features are only found for two structures with Pt vacancies. These structures without/with additional carbon atoms, shown at the top of Fig. 5.15 (b,c), have almost identical graphene bands because the equilibrium positions of the carbon atoms placed in the vacancies are close to the second Pt layer. Graphene – Pt distances of $\sim$ 3.9 Å and $\sim$ 3.7 – 3.8 Å were obtained for the structures without and with additional carbon atoms, respectively. In contrast, C. Wang et al. obtained the graphene – Pt distance for the same arrangement of graphene relative to the vacancy substrate to be $\sim$ 2.35 Å [381]. And at the same time, the distance of 3.36 Å for the structure without vacancies (Fig. 5.15 (a)) agrees well with previous calculations (3.29 Å) [381]). The difference in the graphene – Pt distances for the structures with vacancies can be explained by the different defect densities in the unit cells. The defect density in the presented (4×4) unit cell is equal to one vacancy per twelve atomic positions of the Pt surface. This is much smaller than in previous calculations with the (2×2) unit cell (one vacancy per three atomic positions of the Pt surface) [381]. Moreover, the band structure calculations show strong hybridization of graphene and Pt(111) in the (2×2) structure with vacancies and very weak in the case of (4×4).

Comparing the band structures of graphene in different model systems (Fig. 5.15), we can see that graphene in the vacancy-free structure is less p-doped and its π band is more hybridized with Pt states, as evidenced by the hybridization kinks shown by the dashed circles in Fig. 5.15 (a). This structure shows the best agreement with the ARPES data (Figs. 5.16 (a,e) and 5.17 (b)), which have a pronounced kink in the π band dispersion at a binding energy of $\sim$ 0.6 eV. This fact can be explained by the lower density of vacancies in the investigated sample and their non-periodic distribution according to STM measurements.

Figures 5.16 (a-e) and 5.17 (a,b) show the electronic structure of the π band near the Dirac point for graphene synthesized on Pt(111). Since the intensity of the Pt bands strongly depends on the photon energy, ARPES data were measured at

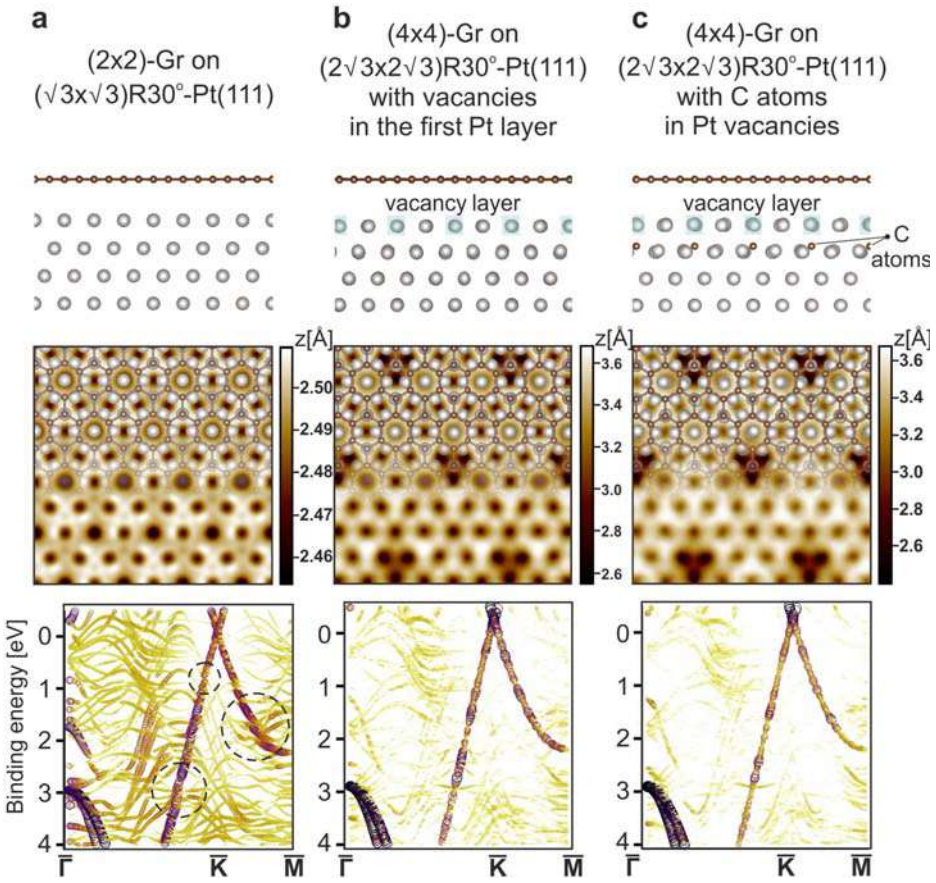

Figure 5.15 — Relaxed Gr/Pt(111) half-slabs without and with various vacancy defects, shown together with LDOS isosurfaces and DFT-calculated unfolded bands along the $\bar{\Gamma}\bar{\mathrm{K}}\bar{\mathrm{M}}$ direction of the surface Brillouin zone of graphene. The isosurface images are of size 20 Å × 20 Å, and in the upper parts they are superimposed with the corresponding relaxed structures. The size of the symbols and the "yellow-orange-violet" color palette indicate the Bloch spectral weight for the unfolded band structure.

different photon energies, namely at 40 eV (for a larger contribution of the graphene bands relative to the Pt $5d$ states) and 62 eV (for better visibility of the Pt states). The dispersion relations were measured in two orthogonal directions of the surface Brillouin zone: along and perpendicular to $\bar{\Gamma}\bar{\mathrm{K}}$. It is found that for graphene on Pt(111), the Dirac point is located above the Fermi level at a binding energy of about 150 meV. The kinks in the π band of graphene, detected by ARPES in the binding energy range of 0.6 – 1.5 eV, are formed due to hybridization between the π states of graphene and Pt. The latter are clearly visible using s polarization of radiation (Fig. 5.16 (d)), which provides lower intensity of graphene π states. According to *ab initio* calculations of the band structure (shown in Fig. 5.16 (f) in the same Brillouin zone direction as the ARPES measurements), we can conclude that the π states of

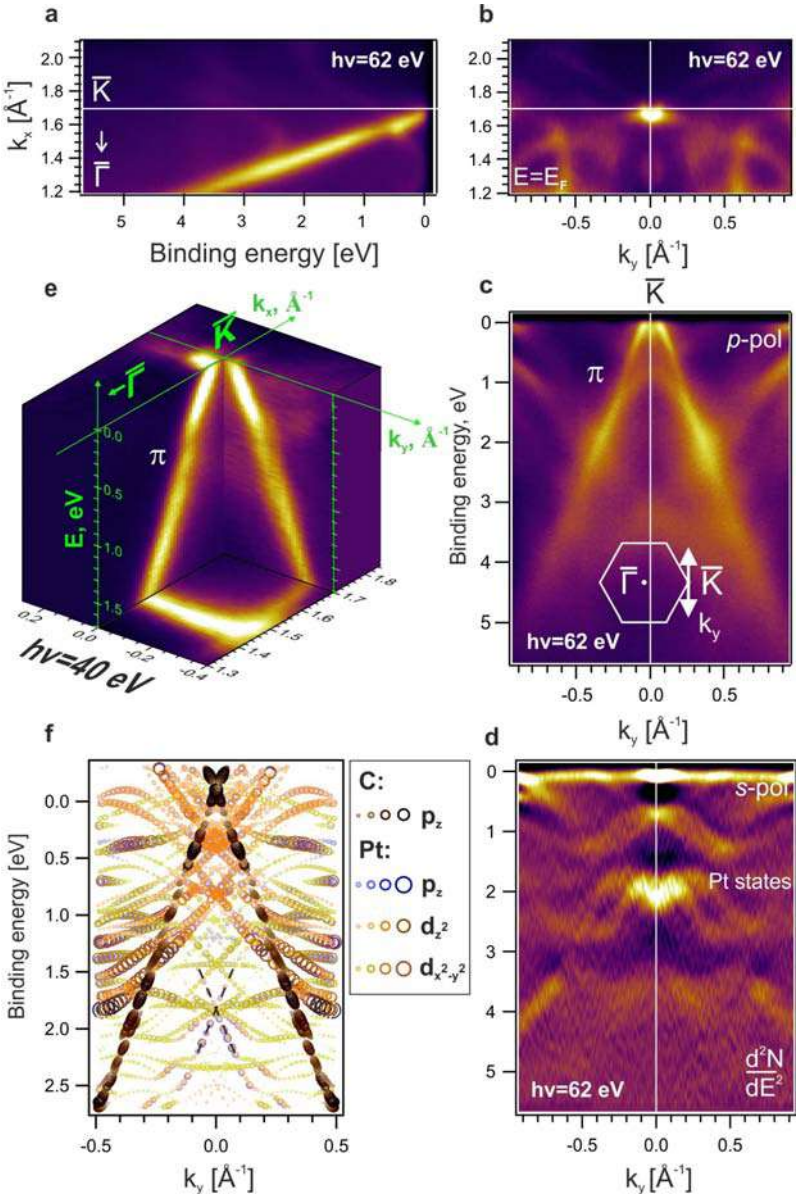

Figure 5.16 — ARPES study of the Gr/Pt(111) system: (a), (c) energy distribution maps (EDM) for the π band of graphene measured in directions along and orthogonal to $\bar{\Gamma}\bar{\mathrm{K}}$, respectively; (b) constant energy map of k_x, k_y at the Fermi level; (d) the same EDM as in panel (c), but for s polarization and as the second derivative of the intensity with respect to energy; (e) an overview of the Dirac cone dispersion maps in both k_x and k_y directions. The ARPES data were measured at 62 eV photon energy and at room temperature of the sample, except (e) – at 40 eV photon energy and 30 K temperature. (f) Calculated Gr/Pt band structure without vacancies as in Fig. 5.15 (a), but in $\bar{\mathrm{K}}' - \bar{\mathrm{K}} - \bar{\mathrm{K}}''$ direction perpendicular to $\bar{\Gamma}\bar{\mathrm{K}}$. The contributions of carbon atoms (p_z orbital character) and atoms of the first layer of Pt (main contributions $p_z, d_{z^2}, d_{x^2-y^2}$ orbital characters of Pt) are shown by circles of different sizes.

graphene and the Pt d states strongly interact to form hybridization band gaps at the supposed intersection points of their dispersions (the avoided-crossing effect).

Interestingly, a Dirac cone-like Pt state (marked by dashed lines in Fig. 5.16 (f)) was found in the calculation at a binding energy of 1.84 eV with almost equal contributions of d_{z^2} and p_z characters. This state was shown to be spin-polarized and hybridized with the π state of graphene [15]. Similar surface states of d character with a Dirac cone have been reported by R. Requist et al. for Ag(111) and Au(111) [290].

5.2.3 Findings

The use of high-temperature regimes of CVD synthesis of graphene on single-crystal metal substrates resulted in graphene of high structural quality. A number of surface-sensitive methods (LEED, XPS, ARPES, STM) and *ab initio* calculations were employed to characterize the structural and electronic properties of low-dimensional systems. It is shown that the ARPES intensity maps contain a contribution from only one graphene domain. The procedures for the synthesis of single-domain graphene (without rotational domains in the surface plane) created a basis for further studies, including those on the functionalization of graphene on these substrates (N-graphene, B-graphene, graphene/O, etc.). This improved the quality of the results obtained, and in the case of the Gr/Co(0001) system, new spin-polarized states at the Fermi level (mini-cone states) were discovered, which can be used to generate spin-polarized currents on the surface. For the Gr/Pt(111) system, it is found that Pt vacancies are chaotically distributed on the surface of the Gr/Pt(111) system, and their low surface concentration, compared to previously published values, allows the synthesis of quasi-freestanding graphene. The developed procedure for graphene synthesis facilitated further studies on the intercalation of Gd atoms under graphene, presented in the next section.

5.3 A new method for the synthesis of nanothin Pt_5Gd alloy for use in heterogeneous catalysis

Platinum lanthanide alloys have been intensively studied to enhance the oxygen reduction reaction (ORR) kinetics and reduce the amount of Pt in fuel cell cathodes with membrane polymer electrolyte [431–436]. These alloys have enhanced ORR activity relative to pure Pt because a compressive strain is applied to the top Pt layer, reducing the adsorption energy ΔE_{OH} [431; 435; 437]. It has already been shown that Pt_xGd nanoparticles exhibit outstanding activity in liquid half-cells [433; 434]. Moreover, the most platinum-rich and stable phase Pt_5Gd was found to exhibit residual catalytic activity 5 times higher than pure Pt after accelerated stability tests [435]. The enhanced ORR activity was demonstrated on Pt surface obtained by various methods: formation of Pt layers on bulk alloys of platinum and rare earth elements by acid leaching [435] and preparation of thin alloy with Pt surface termination by deposition of Gd on the surface of Pt(111) single crystal followed by annealing [436].

Another possible way to increase the catalytic activity and reduce the platinum load is to use graphene and its derivatives as electrocatalysts [438–441]. It has been shown that graphene on the surface of Pt(111) single crystal acts as a two-dimensional confined nanoreactor and promotes CO oxidation with lower activation energy [438; 439]. Thus, the formation of graphene-coated Pt lanthanide alloys is of interest for further catalytic activity studies. Based on these studies, an approach to synthesize such a system by intercalating Gd under graphene is proposed. A range of techniques such as LEED, ARPES, XPS, STM and DFT were used to investigate the electronic and atomic structures of the synthesized systems in detail. The stepwise synthesis of the nanothin alloy Pt_5Gd under graphene (after Gd deposition and intercalation to a thickness of $\sim$ 16 Å) will be studied, and theoretical and experimental data for the final synthesis step – formation of graphene on epitaxial nanothin Pt_5Gd alloy – will be presented in the context of electronic and atomic structure. Thus, this research has found a new way to synthesize a well-ordered nanothin Pt_5Gd alloy layer under graphene, thereby combining graphene and alloy within a single epitaxial system. Moreover, graphene retains its quasi-freestanding character and can serve as a chemical nanoreactor. It is expected to protect the alloy from acidic solutions.

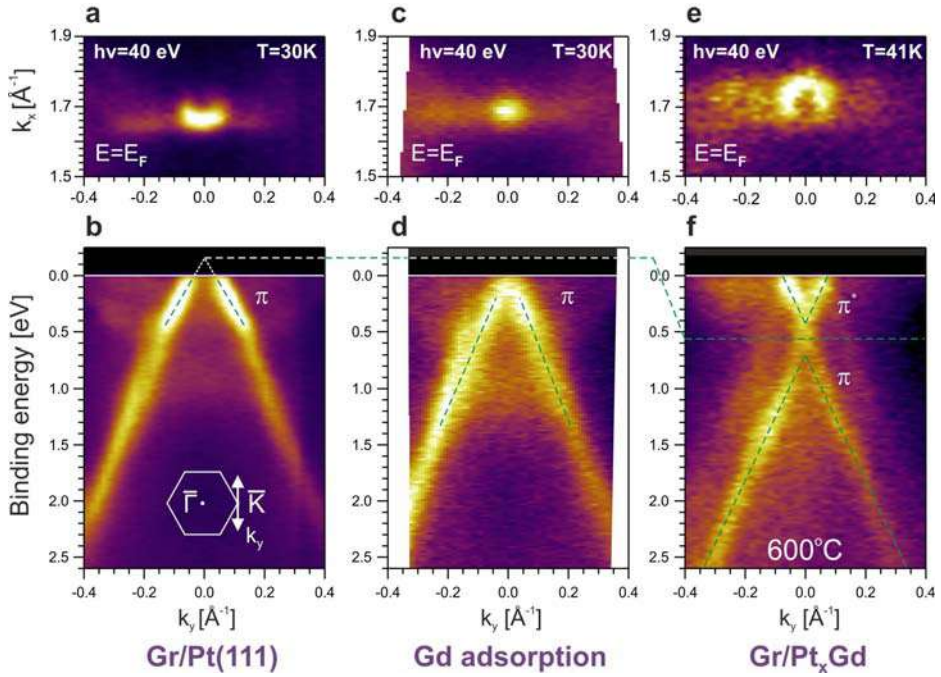

Figure 5.17 — Comparison of ARPES data at $\bar{K}$ point of graphene for Gr/Pt(111) (a,b), after Gd deposition (c,d) and annealing at 600 °C (e,f).

5.3.1 Adsorption and intercalation of Gd under graphene

Adsorption of 1 Å Gd onto Gr/Pt(111) surface is accompanied by a shift of the π band energy toward higher binding energies (Fig. 5.17 (c,d)). Hybridization with $5d$ states of Pt after Gd deposition is still observed as a kink in the graphene dispersion at a binding energy of $\sim$ 0.6 eV. A similar n-doping of graphene with an energy shift of the Dirac point through the Fermi level is observed upon adsorption of Gd onto quasi-freestanding graphene on Au, which will be shown in the next chapter. After additional deposition of Gd (total thickness for both depositions – 4 Å) followed by annealing of the system for 5 min at 600 °C, a shift of the Dirac point below the Fermi level is observed and the π^* conduction band becomes clearly visible (Fig. 5.17 (e,f)). A similar shift of the Dirac point was observed for Gd intercalated graphene on Ir and SiC substrates in [442; 443]. Moreover, a $\sim$ 0.25 eV band gap at the Dirac point is observed (see Fig. 5.17 (f)). According to the reference [444], the opening of the band gap is probably due to the corrugation of graphene on the intercalated Gd/$\mathrm{Pt_xGd}$ alloy. In other words, depositing Gd on top of Gr/Pt(111) and annealing the system at 600 °C leads to efficient n-doping of the electronic structure of graphene with a energy shift of the Dirac point below the Fermi level and with the opening of the fundamental band gap. Obviously, the amount of intercalated Gd and the stoichiometric composition of

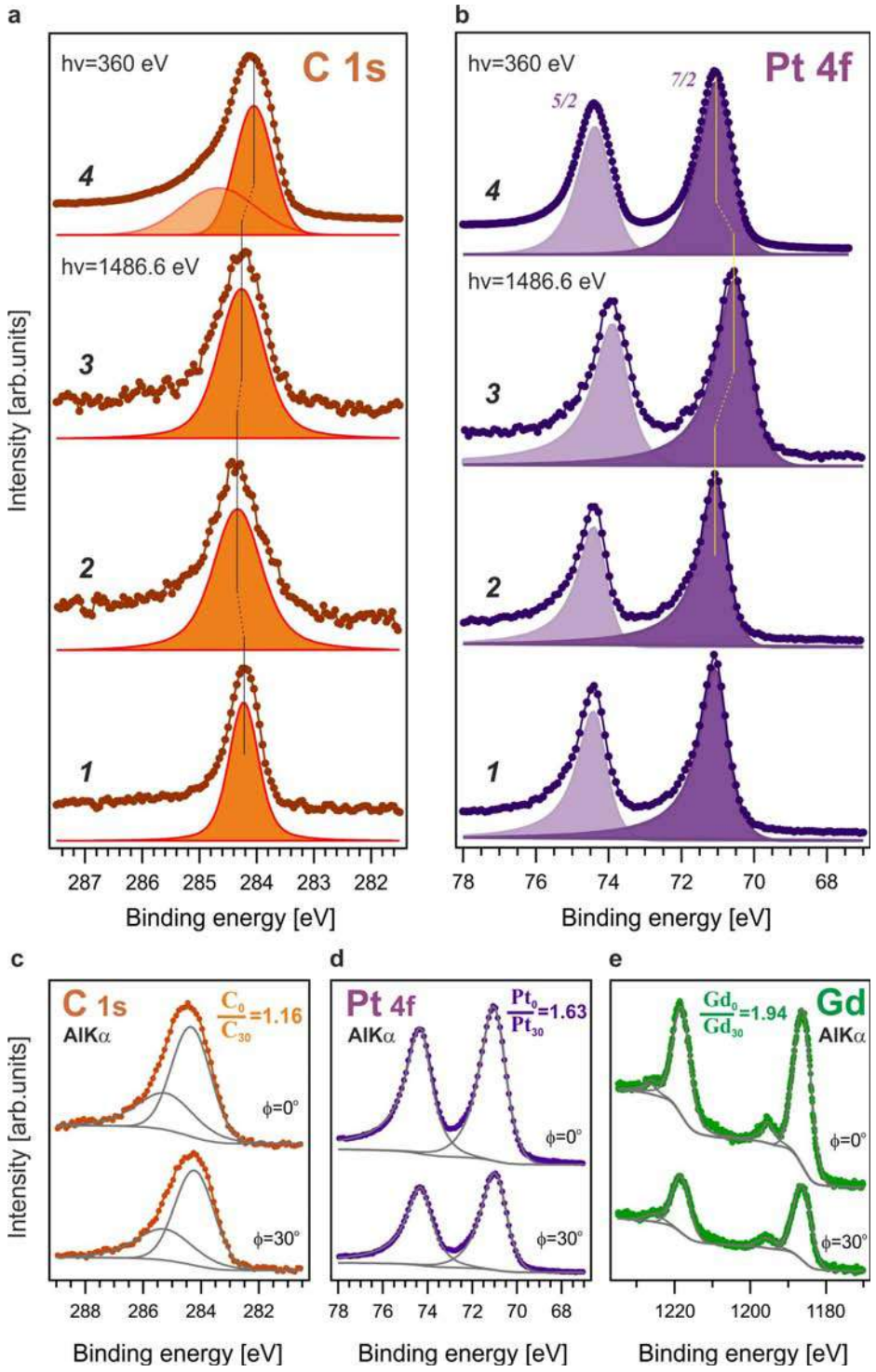

Figure 5.18 — (a,b) XPS study of the Gr/Pt(111) system after Gd deposition and annealing at different temperatures (photon energies of 1486.6 eV and 360 eV): 1 – Gr/Pt(111), 2 – Gd deposition (4 Å), 3 – annealing at 600 °C, and 4 – additional Gd deposition (5 Å) and annealing at 1080 °C. (c-e) XPS with angular resolution of the Gr/Pt_5Gd/ Pt(111) system after annealing at 1080 °C for emission angles of 0° and 30° (photon energy 1486.6 eV).

the alloy can be controlled, and hence the position of the Dirac point near the Fermi level. The control of graphene doping and the position of the Dirac point can be utilized in the development of advanced electronics [445].

If we refer to the XPS data measured at different synthesis steps, we find chemical shifts of the C $1s$ and Pt $4f$ peaks after Gd intercalation (see Fig. 5.18 (a,b)). These chemical shifts are associated with the formation of alloys in the near-surface region. Upon adsorption of Gd, the C $1s$ peak shifts toward higher binding energies by 0.1 eV. The inverse chemical shift of C $1s$ toward lower binding energies with increasing annealing temperature indicates the formation of $\mathrm{Pt_xGd}$ alloy under graphene. In contrast, the binding energy of the Pt $4f$ level does not change upon deposition of Gd and experiences a large shift in energy $\sim$ 0.5 eV after the intercalation of Gd at an annealing temperature of 600 °C. It shifts to the initial binding energy with increasing annealing temperature and the amount of Pt in the $\mathrm{Pt_xGd}$ alloy. In the next section, we consider the formation of a stoichiometric $\mathrm{Pt_5Gd}$ alloy in the final annealing step.

5.3.2 Formation of quasi-freestanding graphene on $\mathrm{Pt_5Gd}$ alloy

According to the publications of E.T. Ulrikkeholm et al. [436; 446], the most stable and platinum-rich alloy is formed after deposition of thin layers of Gd ($\sim$ 200 Å) on Pt(111) single crystal and annealing at 800 °C. The alloy $\mathrm{Pt_5Gd}$ is shown to have a p(1.9×1.9) structure with respect to the Pt(111) substrate [436; 446]. To synthesize a well-ordered $\mathrm{Pt_5Gd}$ alloy under graphene, an additional deposition of Gd (5 Å) on the Gd-intercalated system Gr/Pt(111) described in the previous section was performed, followed by annealing at 1080 °C for 5 min. The synthesis method used has two distinctive features: 1) according to the LEED pattern (Fig. 5.19 (a)), the alloy has a p(2×2) structure relative to graphene, which is rotated by 30° relative to Pt(111); 2) a well-ordered alloy is formed under the graphene after annealing at a higher temperature than that used in the works [436; 446].

According to the XPS measurements of the C $1s$, Pt $4f$, and Gd $3d$ core levels with angular resolution shown in Fig. 5.18 (c-e), it was found that both Pt and Gd atoms are located under the graphene, with the Gd atoms located deeper. In addition,

the calculated XPS intensities for a model layered structure with Pt termination of the alloy under graphene of the following type Gr-Pt-[Pt_2Gd-Pt]-[Pt_2Gd-Pt]-...-Pt(bulk) had the best agreement with the XPS data for the Pt_5Gd alloy with an estimated alloy thickness of about 3 nm.

It can be seen that the core level peak C $1s$ has an asymmetric shape (Fig. 5.18 (a)). Decomposition of the peak into two components gives the high-energy component at 284.67 eV and the main component at 284.05 eV. It is well known that the high-energy component of the C $1s$ peak for strongly doped graphene is associated with energy loss due to plasmons excitation [443; 447; 448]. This shake-up effect is theoretically described in [447] and experimentally observed in [443; 448] after intercalation of rare earth and alkali metals under graphene. In our case, the intense plasmon loss component of the C $1s$ peak is observed after the formation of a well-ordered stoichiometric alloy. This recovers the quasi-freestanding character of graphene with a shift of the binding energy of the C $1s$ core level to 284.05 eV (ΔE = -0,17 эВ relative to Gr/Pt(111)) and, as will be shown later, with a shift of the Dirac point to a binding energy $\sim$ -0.27 eV ($\Delta E_D \approx$ -0.12 eV relative to Gr/Pt(111)). These comparable energy shifts are consistent with a rigid band model (due to charge transfer) [448].

The LEED and STM data (Fig. 5.19 (a-d)) show the coexistence of the alloy structure (2×2) and a large-scale moiré structure with a periodicity of about 2 – 3 nm. The surface unit cell of the alloy is shown by the small white rhombus in Fig. 5.19 (c,d) with STM data and the black rhombus in Fig. 5.19 (e) with the Gr/Pt_5Gd structure model. Its side size from STM data is 5.2 $\pm$ 0.3 Å, which agrees well with the experimental values in other studies of the alloy Pt_5Gd [431; 435; 446]. The moiré structure cell is shown in Fig. 5.19 (c) by a large white rhombus with side size $\sim$ 2.8 nm and rotated by 90° relative to the graphene and alloy unit cells.

The observed large-scale moiré pattern can be easily modelled if a Pt alloy layer with “kagome” structure is placed on top of a Pt(111) substrate (see Fig. 5.19 (c) and (f) for comparison). Thus, the moiré pattern can be explained by the mismatch between the lattices of the alloy and the underlying Pt(111) single crystal, since only their surface unit cells have a 30° difference in lateral orientation.

As shown by STM modelling, graphene is poorly visible due to the large contribution to the tunnelling current from the alloy states and a sharp change in the LDOS isosurface in the region of Gd atoms location. Nevertheless, the presence of geometric corrugation of the alloy and the possibility of graphene arrangement in

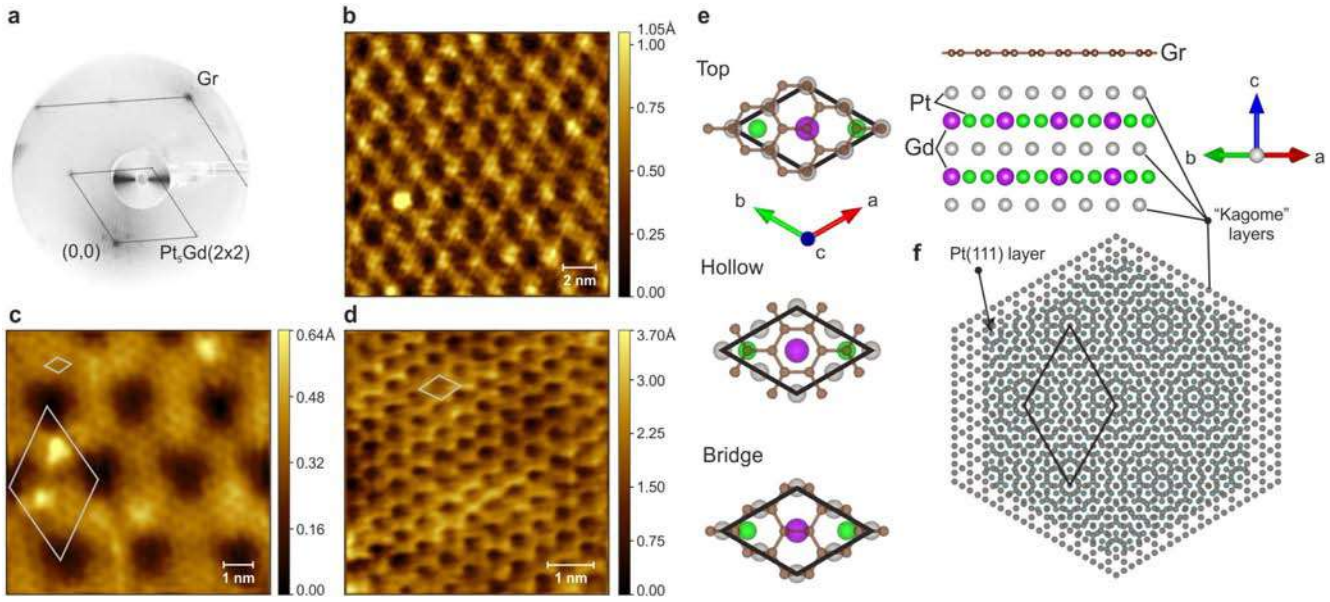

Figure 5.19 — Study of Gr/Pt_5Gd/Pt(111) by LEED and STM methods: (a) LEED pattern at E_p = 65 eV; STM images measured with V_s = 350 mV, I_t = 0.6 nA (b), V_s = 200 mV, I_t = 0.5 nA (c), and V_s = 40 mV, I_t = 0.63 nA (d). Panel (e) shows ball-and-stick models of the possible arrangement of graphene on the alloy surface. In panel (f), a moiré pattern between the alloy layer with "kagome" structure and the Pt(111) layer is included.

different configurations shown in Fig. 5.19 (e) cannot be excluded. Therefore, band structure calculations by DFT method were performed for three possible arrangements of graphene on the alloy, but the results for the "top" configuration are presented, since similar results were obtained for the others.

The results of ARPES examination of the system at the final stage of synthesis (annealing at 1080 °C) are shown in Fig. 5.20. The linear dispersion of π states indicates a quasi-freestanding character of graphene, with p-doping of graphene observed (the energy position of the Dirac point ∼ -0.27 eV as estimated in Fig. 5.20 (a)). However, by considering the second energy derivative of the ARPES intensity (Fig. 5.20 (b,c)), the presence of hybridization band gaps in the graphene π band and weakly dispersing substrate states can be observed.

To explain the experimental features of the electronic structure, *ab initio* calculations of the Gr/Pt_5Gd system (with van der Waals distance ∼ 3.2 – 3.4 Å between graphene and the alloy) have been performed and are additionally included in Fig. 5.20 (b,c). They are presented as follows: the unfolded band structure of graphene is shown together with the orbital contributions (orbital characters) of the

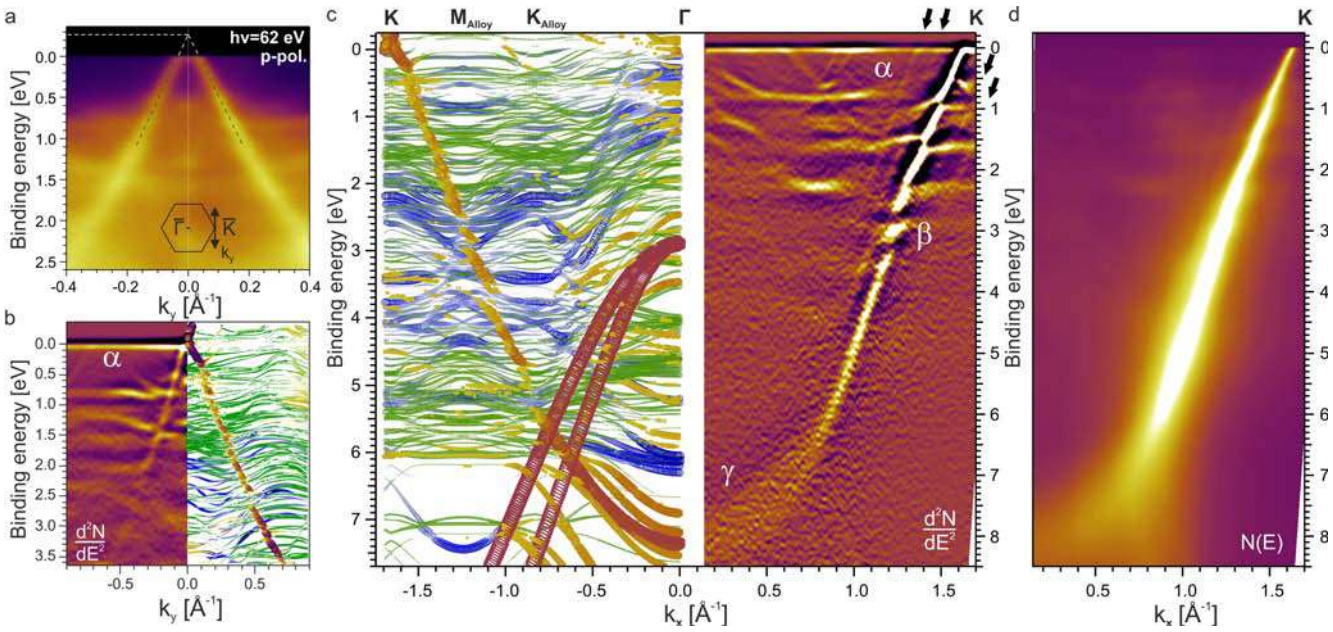

Figure 5.20 — ARPES study of the Gr/Pt_5Gd/Pt(111) system: dispersion map of the graphene π band measured in the direction orthogonal to $\bar{\Gamma}\bar{K}$ (a) and along $\bar{\Gamma}\bar{K}$ (d); (b) and (c) the second energy derivative of the ARPES intensity presented in (a) and (d), respectively. The photon energy is 62 eV. All ARPES data were measured at a sample temperature of 60 K. *Ab initio* calculation results are additionally included in panels (b) and (c) for comparison with experimental data. The size of the symbols and the color palette indicate the Bloch spectral weight for the unfolded band structure or the orbital characters of the alloy layers for the folded band structure: sandy brown – unfolded band structure, blue – second Pt layer with "kagome" structure, and green – Pt in the third Pt_2Gd alloy layer.

alloy layers for the (2×2) folded band structure in one figure, since the (2×2) cell is the smallest for the alloy structure.

When comparing experimental and theoretical data, several features can be found: the π state of graphene hybridizes with *d* Pt states of different localization in the alloy layers – in the underlying second "kagome" layer and in the third Pt_2Gd layer (the location of the atomic layers is shown in the unit cell cross-section in Fig. 5.19 (e)). Hybridization of the π state with *d* states of Pt strongly localized in the third layer (marked with α in Fig. 5.20 (b,c)) occurs in the binding energy range 0.2 – 1.0 eV below the Fermi level. And hybridization with *d* states of Pt localized in the second layer gives obviously large band gaps (marked β in Fig. 5.20 (c), right). Thus, the dispersion of the graphene π band has more pronounced gaps at binding energies ∼ 2.8 and ∼ 3.3 eV in experiment. In addition, we can detect hybridization states close to the $\bar{\Gamma}$ point in the region of binding energies 7.5 – 8.5 eV with a large

contribution of Pt s,d orbital characters (marked γ in Fig. 5.20 (c), right). This leads to a broadening of the peak π state in energy near the $\bar{\Gamma}$ point. The moiré pattern resulting from the superposition of the Pt_5Gd and Pt(111) alloy lattices imposes a periodic superlattice potential leading to the Dirac cone replicas marked by arrows in Fig. 5.20 (c), right.

It can be stated that the π electronic states of graphene formed on the Pt_5Gd alloy, in contrast to Pt(111), are more strongly hybridized with the Pt d character states, but still retain a linear dispersion dependence near the Fermi level. Charge transfer to graphene is observed at comparable energy shifts of the C $1s$ core level and the Dirac point (relative to Gr/Pt(111)). The electronic structure of graphene exhibits p-doping up to $\sim$ 0.3 eV above the Fermi level, which is essential for heterogeneous catalysis, since an increase in the density of states near the Fermi energy typically enhances the catalytic activity of the material.

5.3.3 Findings

In dissertation work, nanothin epitaxial Pt_xGd alloys on the surface of Pt(111) single crystal initially coated with well-oriented graphene have been synthesized and their electronic and atomic structures at different synthesis steps have been investigated. The variable stoichiometric composition of the alloy can be used to control the doping of the electronic structure of graphene in the development of advanced electronics. The data of low-energy electron diffraction, photoelectron spectroscopy, and scanning tunneling microscopy show that adsorption of Gd onto the graphene/Pt(111) system and its subsequent intercalation at 1080 °C lead to the formation of a nanothin Pt_5Gd alloy coated with quasi-freestanding graphene. The atomically flat surface of the alloy is terminated by an atomic layer of Pt with a “kagome” structure. According to the ARPES data and DFT calculation, the graphene on the Pt_5Gd alloy surface is p-doped and exhibits hybridization with the alloy even at van der Waals distances. Nevertheless, the linear dispersion of π states near the Fermi level is conserved.

Graphene plays an important role in the synthesis of nanothin epitaxial alloy Pt_5Gd. The surface unit cell of the alloy corresponds to the lateral orientation of the

graphene unit cell, but is rotated by 30° relative to the surface unit cell of Pt(111), and an interface between the alloy and the Pt(111) single crystal with a moiré pattern is formed. The results suggest that the growth of thin layers of platinum by magnetron sputtering with its crystallization [449] and subsequent synthesis of graphene on nanothin alloy $\mathrm{Pt_5Gd}$ offers great opportunities for cheaper production of catalysts.

6. Giant Rashba effect in graphene

Induced spin-orbit interaction in graphene is still actively investigated, since it opens the way to the realization of the quantum Hall effect in graphene without an external magnetic field [86; 87; 450—452]. It is known that strong spin-orbit interaction is a prerequisite for the observation of effects such as the spin Hall effect [85—87], quantum anomalous Hall effect [87; 91; 93; 450; 453], spin-galvanic effect [454], Rashba-Edelstein effect [455], giant Rashba effect [12; 14], spin-transfer and spin-orbit torque effects [18; 85; 456—458], magnetoresistance and spin-filtering [82; 84; 459], spin interference effects, etc. Various approaches can be used to enhance the spin-orbit interaction in graphene and graphene-like materials. Recently, it has been reported that the curvature-induced spin-orbit interaction in corrugated graphene structures offers great potential for applications in graphene-based spintronics nanodevices [460]. Other ways to control the spin-orbit interaction are the so-called proximity effect with adatoms or substrate [14; 134; 461; 462] and symmetry breaking in 2D Janus materials [463—465].

6.1 Giant Rashba effect in graphene on intercalated Au monolayer

The giant Rashba effect in graphene was considered in Paragraph 1.1.3. This effect has been published in several experimental papers on the thesis topic [4; 6; 12—14]. Let us note the most important, characteristic features of this effect. It was shown that hybridization of π states of graphene with $5d$ states of Au is responsible for the appearance of giant spin-orbit splitting in the π band of graphene. In the region of binding energies, where π states of graphene cross $5d$ states of Au, their interaction with each other for the same spin orientations occurs, leading to spin splitting of π states up to 0.6 – 0.7 eV. Outside the band crossing region, in the region where the π band dispersion is linear, the spin splitting of π states is constant and has a value of $\sim$ 100 meV. Despite the experimental evidence of giant Rashba splitting in graphene, the work [12] was only able to obtain comparable splitting values for closer distances

between graphene and the gold monolayer than at the equilibrium distance between them. On the other hand, the giant splitting was confirmed by DFT calculations for the Gr/Ni system with intercalated Au clusters [466] and by tight binding calculations of graphene on a gold monolayer in a hollow configuration [467]. Giant spin splitting was also observed for graphene intercalated by Au on SiC substrate [468], but the authors concluded that spin splitting becomes giant ($\sim$ 100 meV) only near the band gap formed due to the avoided-crossing effect.

In this dissertation work, an attempt was made to resolve the contradictions between theory and experiment accumulated over several years. For this purpose, a new system with a sub-monolayer amount of intercalated Pt atoms under graphene on SiC(0001) substrate was synthesized. It was assumed that the rarefied layer of Pt atoms would be a non-planar layer, and this would lead to a reduction in the equilibrium distance between graphene and the Pt layer, and, accordingly, to the manifestation of giant Rashba splitting even for a low concentration of intercalated heavy metal atoms.

6.2 Origin of the giant Rashba effect in graphene on Pt/SiC(0001)

Graphene on metal substrates cannot be directly applied in future electronics or spintronics. In this respect, graphene systems on semiconductor substrates, such as graphene on silicon carbide (SiC) with intercalated metal [391; 469–474], are more promising for applications. The possibility of intercalation of noble metals under graphene on SiC, such as Au and Pt, was shown in [388; 468; 470; 471].

At the same time, platinum is the most commonly used non-magnetic metal in spintronics because it is characterized by spin-polarized $5d$ states at the Fermi level, which leads to a strong intrinsic spin Hall effect [475]. Furthermore, it has been shown that graphene on Pt(111) surface [15] or on Ir(111) surface with an intercalated Pt monolayer in between [476] has a pronounced spin-polarized Dirac cone structure of π states. In the next section, it will be shown that the magnetization of ferromagnetic nanodots on the surface of the Pt/graphene/Au/SiC(0001) system can be reversibly controlled by passing a surface current through graphene due to the spin-orbit torque effect.

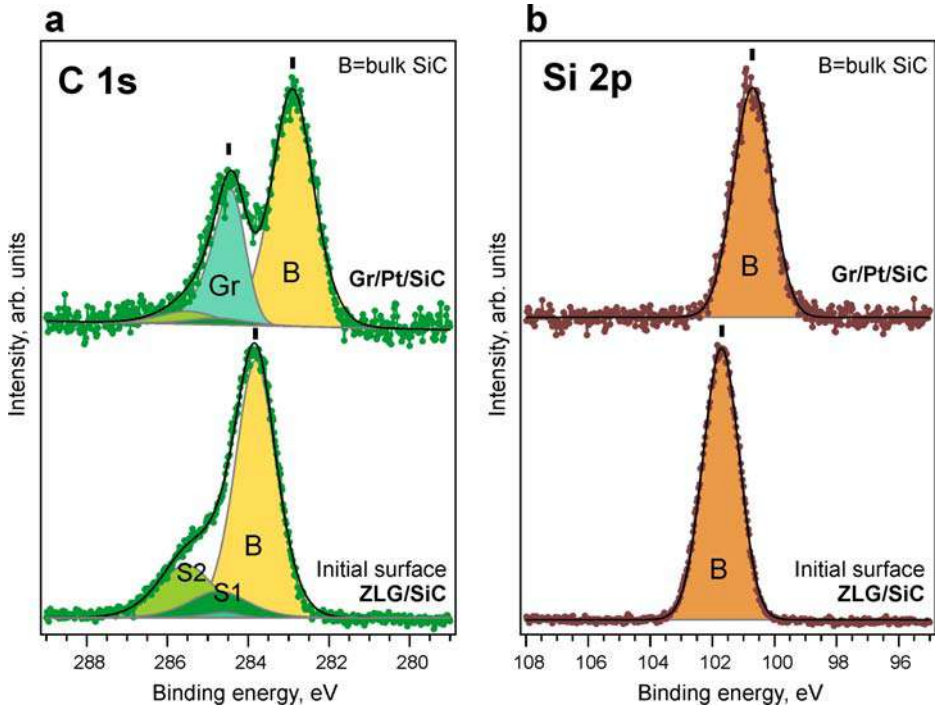

Figure 6.1 — XPS spectra of the C $1s$ (a) and Si $2p$ (b) core levels measured for ZLG on SiC – bottom row, and after intercalation of 1.5 Å Pt under ZLG on SiC – top row. The photon energy is 1486.6 eV.

We consider the investigation results of a system consisting of graphene on a SiC substrate with an intercalated Pt submonolayer to evaluate the effect of corrugation at the nanoscale on the induced spin-orbit interaction in graphene. The system was synthesized by intercalating Pt atoms under ZLG on 6H-SiC(0001). In contrast to graphene with an intercalated Au submonolayer (0.5 ML) [466], a single ordered graphene phase was found in graphene on the intercalated Pt submonolayer. For such a single-phase system it was possible to explain the results obtained by different methods and to discuss the nature of the giant Rashba effect.

Initially, a zero layer of graphene on SiC(0001) was synthesized with a surface reconstruction of $(6\sqrt{3} \times 6\sqrt{3})\mathrm{R}30^\circ + (5 \times 5)$. Figure 6.1 shows the spectra of the C $1s$ and Si $2p$ core levels before and after Pt intercalation. A decomposition of the photoelectron spectra into spectral components by the curve fitting method is presented. The line shapes of the Si $2p$ and C $1s$ spectra were determined using the Gauss/Lorenz product formula with mixing parameters of 0 and 0.5, respectively [477]. The asymmetry parameter of the graphene peak was 0.12 when approximating the C $1s$ spectra with curves. The measured data are shown in the figures with circles along with the best fit curves, corresponding components and background. The C $1s$ spectrum of ZLG (Fig. 6.1 (a)) has a characteristic shape with

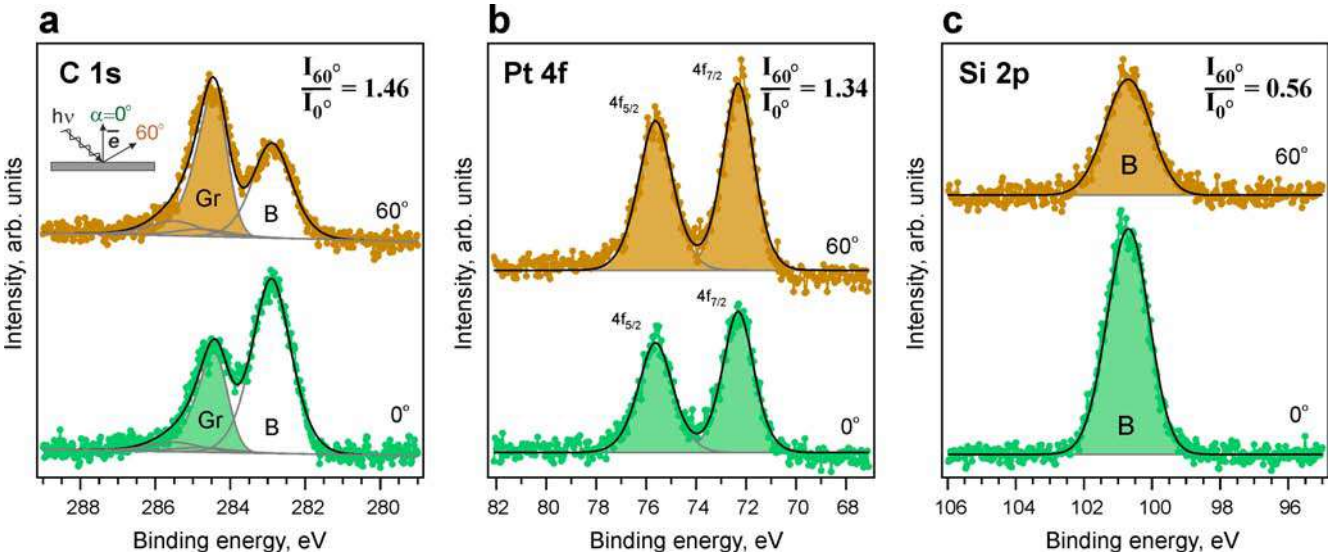

Figure 6.2 — Angle-resolved XPS spectra measured at emission angles of 0° and 60° relative to the surface normal for (a) – C $1s$, (b) – Pt $4f$, and (c) – Si $2p$ core levels, after Pt intercalation under ZLG on SiC. The photon energy is equal to 1486.6 eV.

three components: two components S1 (284.7 eV) and S2 (285.5 eV) corresponding to the carbon in ZLG, and a bulk carbon component (labeled (B)) in the SiC compound (283.8 eV). The Si $2p$ spectrum (Fig. 6.1 (b)) presents a single broad peak at a binding energy of 101.7 eV, which is consistent with previous results [383; 385; 392]. However, the Si spin-orbit doublet ($2p_1/2$ and $2p_3/2$) is not resolved, so a single asymmetric peak is obtained during the fitting procedure. It should be noted that a small amount of graphene monolayer was present for the initial ZLG (see the low intensity component at 284.6 eV in Fig. 6.1 (a)). However, as will be shown later, this part of the surface is inert to the intercalation process.

Changes in the XPS spectra are observed after adsorption of 1.5 Å Pt onto the zero-layer graphene surface on SiC(0001) and subsequent annealing at T = 1100 °C for 1 h. First, there is a decrease in the ZLG and bulk components of carbon atoms in SiC and an increase in the graphene component at a binding energy of 284.4 eV. This implies the conversion of ZLG to graphene as a result of the intercalation process. Second, the spectral components corresponding to Si and C atoms in bulk SiC were found to be shifted by 0.9 eV toward lower binding energies. This effect can be explained by the influence of Pt atoms on the surface bend bending of the system [401].

Additional measurements of photoelectron spectra at different emission angles were carried out to determine the depth of the near-surface layers. It is possible to determine the location of the layers in depth relative to each other by

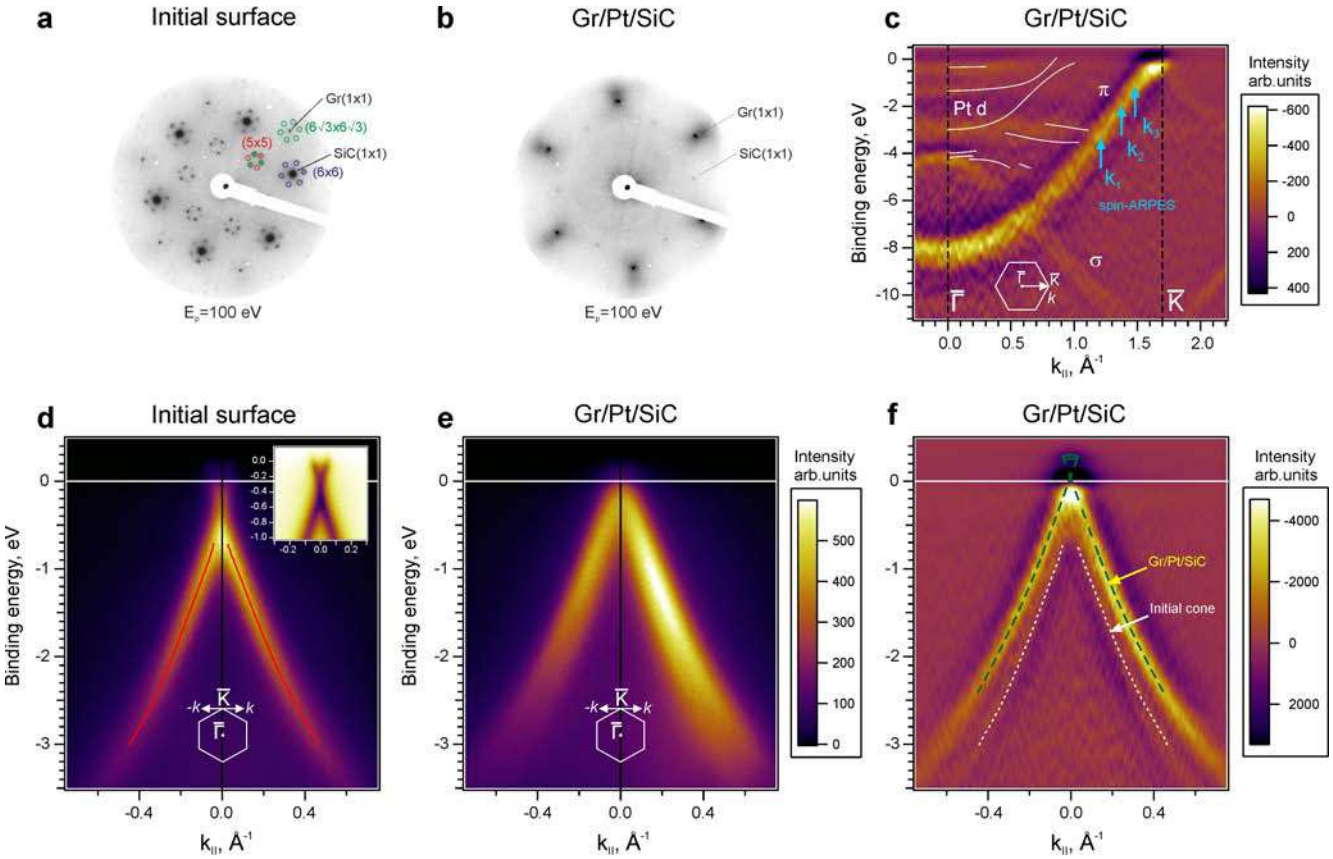

Figure 6.3 — (a,b) LEED patterns of the initial SiC surface with a zero-layer graphene $(6\sqrt{3} \times 6\sqrt{3})\mathrm{R30°}+(5 \times 5)$ and a small amount of graphene monolayer and after intercalation of 1.5 Å Pt, E_p = 100 eV. (c) ARPES intensity maps after Pt intercalation measured along the $\overline{\Gamma\mathrm{K}}$ direction of the surface Brillouin zone and presented as the second derivative of the intensity with respect to energy. (d,e) ARPES intensity maps of the initial surface and after Pt intercalation, measured in the direction orthogonal to $\overline{\Gamma\mathrm{K}}$. The solid red lines show the fitting result of the momentum distribution curves by two peaks with Lorentz functions. An enlarged view of the Dirac cone for the initial surface is shown in the inset with inverted palette. (f) ARPES data from (e), presented as the second derivative of intensity with respect to energy to distinguish the main features more clearly. The photon energy is 40.8 eV (He IIα).

studying the angular dependences of the intensities of the elements core levels (see Paragraph 2.2.1). The spectra of C $1s$, Pt $4f$, and Si $2p$ measured at photoelectron emission angles of 0° and 60° relative to the surface normal are shown in Fig. 6.2. Comparing the intensity ratios $I_{60°}/I_{0°}$ of the graphene component C $1s$, Pt $4f$ and the bulk component Si $2p$ (the numerical values of the ratios are shown in Fig. 6.2), we can conclude that the graphene is located above the Pt submonolayer, with the latter located between the graphene and the SiC substrate. This proves the successful intercalation of Pt between ZLG and SiC.

The LEED image in Figure 6.3 (a) shows the formation of ZLG on SiC with reconstructions of $(6\sqrt{3} \times 6\sqrt{3})$R30° and (5×5) [384]. The bright SiC reflexes are clearly observed together with very pale graphene reflexes and a set of diffraction reflexes characteristic of $6\sqrt{3}$ or ZLG reconstruction. It is known that the diffraction reflexes corresponding to the graphene inverse lattice slightly increase in intensity when the first layer of graphene is formed [382]. Indeed, we observe such an increase in intensity after Pt intercalation together with the appearance of fuzzy diffraction reflexes of the moiré pattern (Fig. 6.3 (b)). The diffraction reflexes of the ZLG reconstruction are now not visible, which proves the successful intercalation of Pt atoms between ZLG and SiC substrate. The observation of (1×1) SiC reflexes up to high kinetic energies ($\sim$ 200 eV) indicates the good crystalline quality of the substrate after intercalation. Notably, the superstructure period $\sim (5 \times 5)$ measured by STM ($\sim$ 1.2 nm $\times$ 1.2 nm) is in a good agreement with that predicted for the 0° rotation angle between the graphene and the Pt layer [219].

The ARPES intensity maps were measured before and after Pt intercalation (Fig. 6.3 (c-f)) to analyze the changes in the electronic structure of the system. Due to the fact that the electronic structure of ZLG does not have intense electronic states near the Fermi level, even a small amount of graphene will contribute to the signal in the ARPES maps. Thus, the initial surface was characterized by the presence of a Dirac cone, typical of n-doped graphene on SiC, and the energy position of the Dirac point about 0.42 eV below the Fermi level (see Fig. 6.3 (d)) [383]. However, according to the analysis of the XPS data, the coverage of graphene was much smaller than that of ZLG.

A new Dirac cone is clearly visible in the ARPES intensity maps in Fig. 6.3 (e,f) after Pt intercalation. This cone is associated with the intercalated graphene formed by ZLG transformation. The Dirac point is above the Fermi level (p-doping) due to the intercalation of Pt. At the same time, the initial Dirac cone remains unchanged. The band structure in the $\overline{\Gamma \mathrm{K}}$ direction is shown in Fig. 6.3 (c). Dispersions of graphene π and σ states are observed, and d bands of Pt are visible near the Fermi level. At the $\bar{\Gamma}$, the π state has a binding energy of 8.2 eV, which is in agreement with the results for graphene on Pt(111) presented in [15]. The Pt surface states observed in [15; 476] are shown in white solid lines and coincide with the intense features of the ARPES map. The dispersions of Pt d states may be less intense and resolved to a worse degree due to the smaller amount of intercalated Pt compared to the investigation of the Gr/Pt/Ir(111) system [476] and the formation of atomic chains and 2D Pt clusters

under graphene. The quantization of Pt bands will be crucial in this case, as was shown in the electronic structure study of pentacene molecules on the Ni(110) surface [478].

6.2.1 Electron spin structure

The electronic spin structure of the graphene/Pt/SiC system was measured using the spin-ARPES method at $k_{||}$ values indicated by the blue arrows in Fig. 6.3 (c). The spin-ARPES spectra for the Rashba spin component (S_y) are shown in Figure 6.4. The spin-resolved data were analyzed using a standard procedure (see Paragraph 2.2.3). The spin polarization is shown in Fig 6.4 (b). The slope of the polarization curve and the change in its sign in the energy localization region of the peak of π states indicate the presence of spin splitting of this peak [479]. Next, the spin-resolved spectra in Fig. 6.4 (a) were obtained using the polarization curve. The calculated data points are shown together with the best approximation curves in Fig. 6.4 (a). In addition,

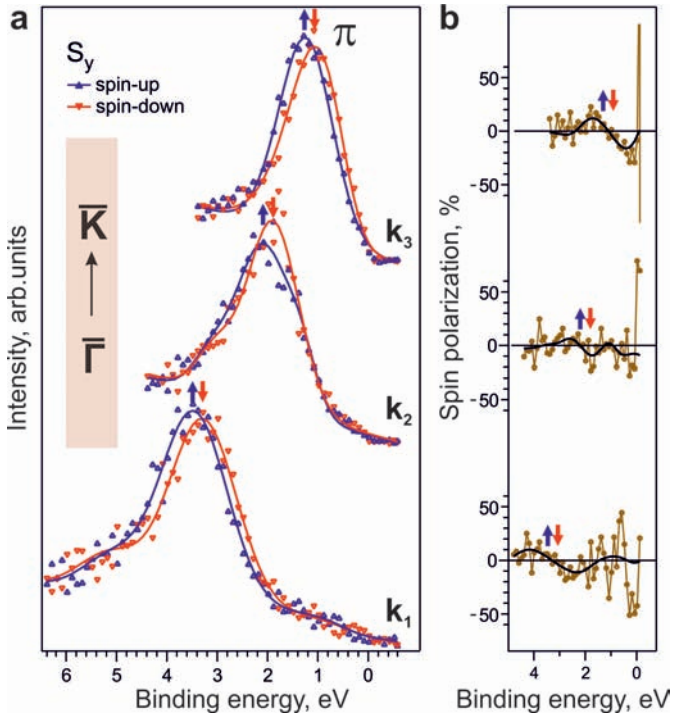

Figure 6.4 — Spin-ARPES spectra with spin polarization (a,b) of the Gr/Pt/SiC(0001) system measured at the quasi-wave vectors k_1, k_2, and k_3 marked in Fig. 6.3 (c). In (a), the projections of the electron spin of different sign on the axis lying in the plane of the surface and directed perpendicular to the quasi-wave vector are indicated in blue and red colors. The photon energy is 40.8 eV (He IIα).

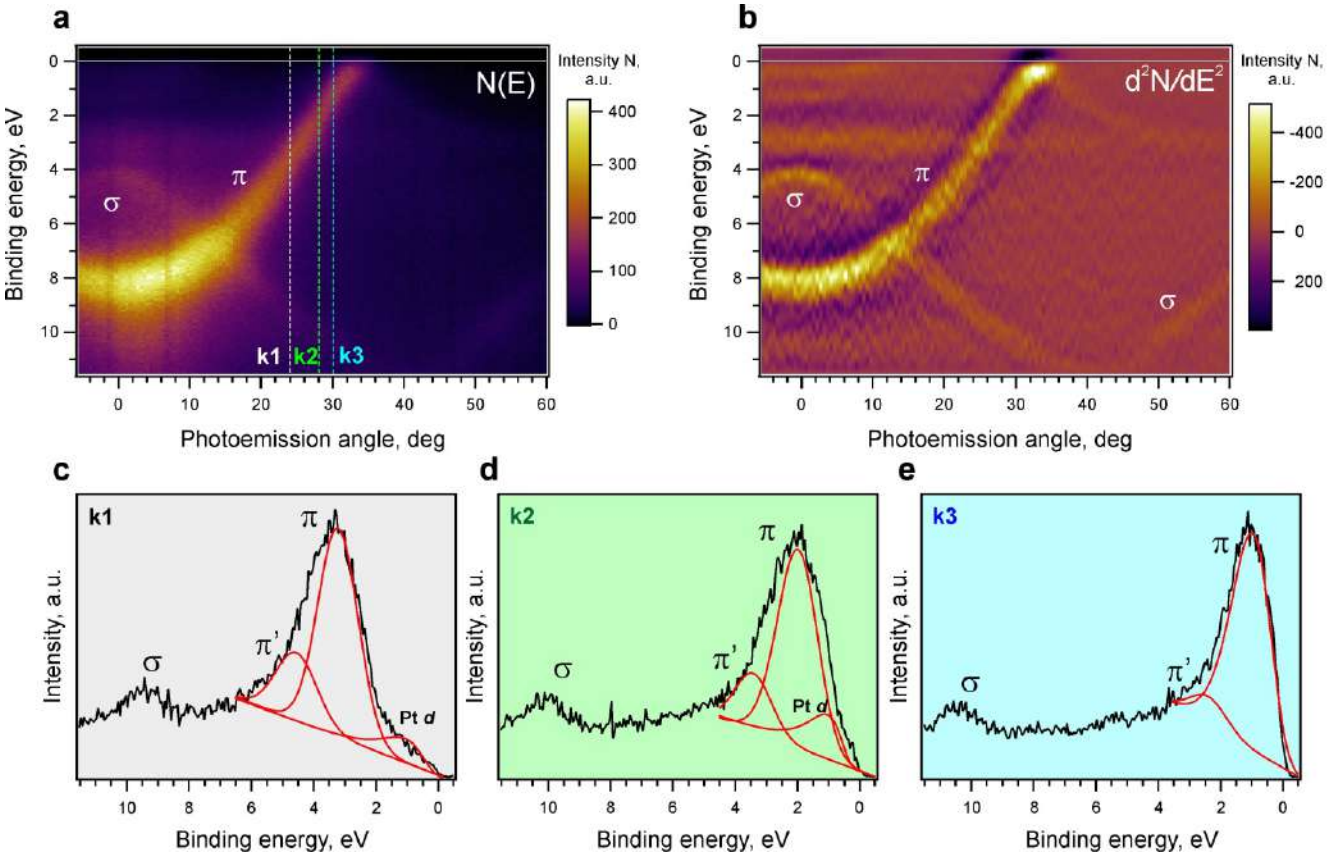

Figure 6.5 — (a) ARPES intensity map of Pt-intercalated graphene measured along the $\overline{\Gamma K}$ direction of the surface Brillouin zone. (b) The same ARPES intensity map presented as the second energy derivative. (c-e) EDC profiles taken from the ARPES intensity map in panel (a) at different values of emission angles ($k_{\parallel}$).

the polarization curves calculated inversely from the approximation curves of the spin-resolved spectra are shown with solid lines in Fig. 6.4 (b). The procedure for the approximation of the spin-ARPES data and the estimation of the spin splitting will be described below.

Figure 6.5 (a) shows the ARPES intensity map of Pt-intercalated graphene on SiC substrate similar to the map presented in Fig. 6.3 (c), but without differentiating the data. The energy distribution curves (EDC) taken from the ARPES intensity map are shown in Fig. 6.5 (c-e) to visualize the change in the shape of the spectra with increasing binding energy of π states (or the corresponding angle/quasi-wave vector). Note that in addition to the main peak (labeled as π), there are low-intensity peaks on the left and right. One of them corresponds to a branch of the original Dirac cone detected before Pt intercalation (denoted as π′), and the second one can be related to the *d* states of Pt according to the article [15]. As a result, the shape of the spectrum becomes more complicated, and the its peculiarities were taken into account when analyzing the spin-resolved data.

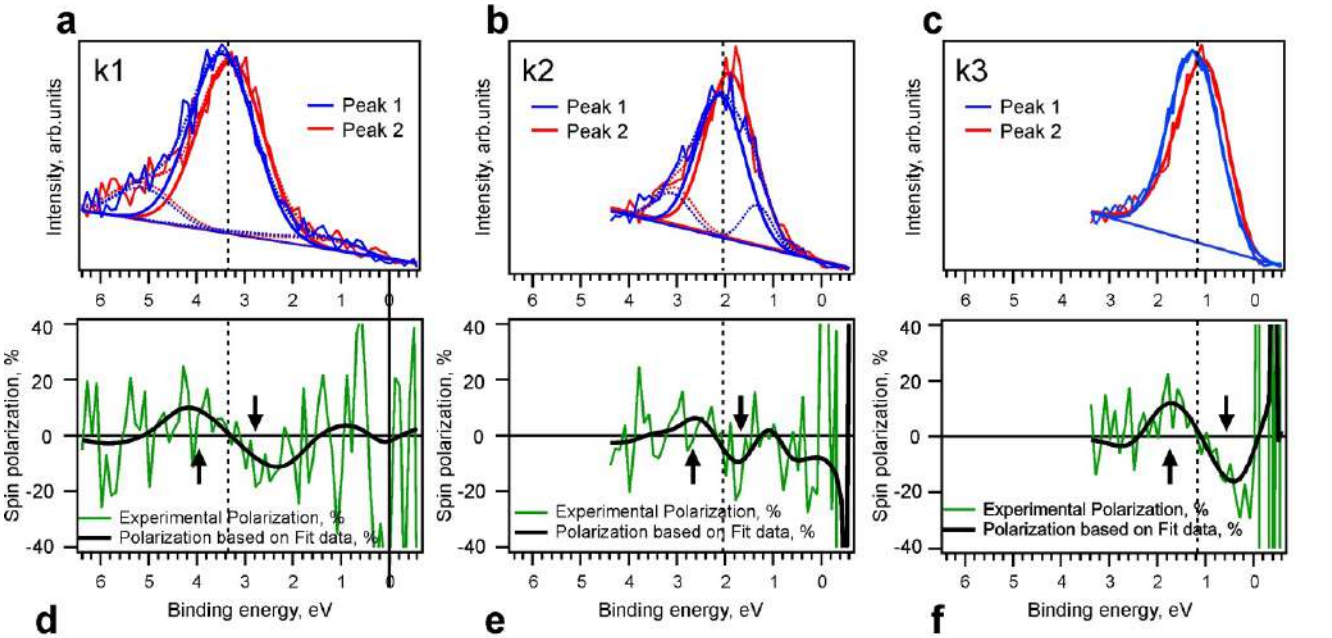

d

k1	Energy of Peak 1 Spin up, eV	Energy of Peak 2 Spin down, eV	Δ SO splitting, eV
Fit resuls	3.48	3.30	0.180

e

k2	Energy of Peak 1 Spin up, eV	Energy of Peak 2 Spin down, eV	Δ SO splitting, eV
Fit resuls	2.11	1.91	0.200

f

k3	Energy of Peak 1 Spin up, eV	Energy of Peak 2 Spin down, eV	Δ SO splitting, eV
Fit resuls	1.26	1.06	0.200

Figure 6.6 — (a-c) Spin-ARPES spectra of Pt-intercalated graphene measured at different emission angles ($k_{\parallel}$) along the $\overline{\Gamma K}$ direction of the surface Brillouin zone – the spectra are presented together with the best approximation results. The original spin polarization curves and the curves calculated inversely from the approximated spectra are presented below the spin-resolved spectra. Blue and red colors denote electron spin projections of different sign. (d-f) Tables of the binding energies of π states and spin splitting values obtained from the approximation procedure.

Figure 6.6 shows the spin-ARPES spectra measured at different emission angles ($k_{\parallel}$). To determine the spin splitting of π states of graphene, the spin-resolved curves were approximated by several Gaussian peaks and a linear background. The results of the best approximation for different $k_{\parallel}$ profiles are also shown in Fig. 6.6. The original polarization curves are shown below the spin-resolved data. Additionally, the polarization curves were calculated inversely from the approximated spectra using the following expression:

$$P^{fit} = \frac{I_{up}^{fit} - I_{down}^{fit}}{I_{up}^{fit} + I_{down}^{fit}}, \tag{6.1}$$

where I_{up}^{fit} and I_{down}^{fit} are the best-fit curves of the corresponding initial spectra. It is worth noting that the original polarization curves have a strong deviation near the Fermi energy because it arises from the division of small values $(I_L - I_R)$ and

($I_L + I_R$) due to the low intensity of the photoelectron emission signal near the Fermi level (division by a value close to zero gives a large uncertainty).

Figure 6.6 (d-f) shows the energy positions of π states with spin-$\uparrow$ and spin-$\downarrow$ obtained by the approximation procedure. The spin splitting values are consistent with those determined from the maxima of the spin-ARPES spectra because of the high intensity of the π states compared to the additional states. Thus, a spin splitting of 200 meV ($\pm$ 50 meV) is observed for all measured spectra over a wide range of binding energies. The experimentally detected magnitude of the spin splitting is unprecedentedly large for both freestanding graphene and previously studied experimental graphene-based systems.

6.2.2 Surface atomic structure

STM measurements were performed to obtain additional information on the surface atomic structure. Only one well-ordered structure on large nanometer scales was resolved, namely, the structure of periodic triangular-shaped defects (Fig. 6.7). The periodicity of the superstructure is $\sim (5 \times 5)$ with respect to the graphene lattice. The two-dimensional fast Fourier transform (2D FFT) image shown in inset of panel (b) also contains reflexes from the superstructure. It should be noted that the corrugation of the surface topography is about 0.2 – 0.3 Å, which agrees well with a previously measured value for graphene on a Pt(111) surface with vacancies in the top layer (see Paragraph 5.2.2). The observation of a corrugation of comparable magnitude after intercalation of an incomplete Pt monolayer indicates the formation of a rarefied platinum layer with vacancies beneath the graphene. To show the presence of corrugated graphene lattice, 2D FFT filtering of the image was performed and the result is presented in a 3D view with illumination by a light source. The 2D FFT image shows six reflexes corresponding to the superstructure, while the 3D image shows the structure of graphene (see Fig. 6.7 (c)). The enlarged image, marked by the white square, shows the curved lattice of graphene due to corrugation. The atomic resolution of graphene is degraded in some regions due to the simultaneous contribution to the tunneling current of the signal from different atoms of the corrugated surface, even with a sharp tip achieving atomic resolution on a graphite surface.

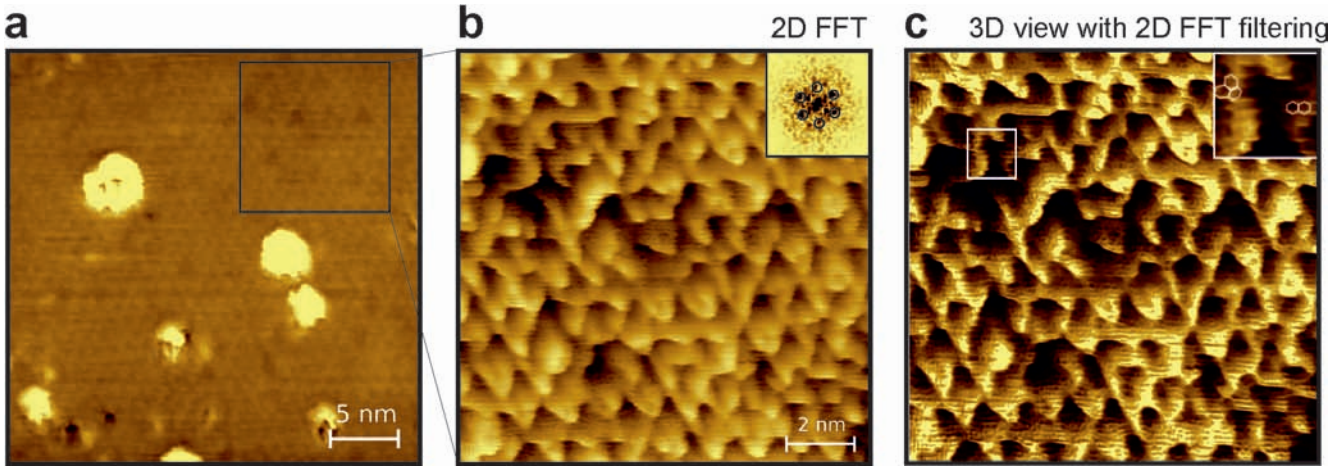

Figure 6.7 — STM images of the graphene/Pt/SiC system after annealing at temperature T = 1100 °C. The image dimensions and measurement parameters are as follows: (a) 30× 30 nm, V_s = −0.4 V, I_t = 0.5 nA, (b) 11×11 nm, V_s = −0.5 V, I_t = 0.5 nA. The 2D FFT of the STM image is shown in the inset in panel (b). (c) 3D view of the image with 2D FFT filtering to visualize the graphene lattice. The enlarged region is shown in the inset.

6.2.3 Comparison of experimental and theoretical results

To analyze the experimental data obtained and to understand the origin of the giant spin-orbit Rashba interaction, DFT calculations were performed. It should be noted that any published data on experimental spin-orbit splitting in graphene with the magnitude higher than 100 meV could not be found. Similar experimental values of splitting were obtained earlier, but only due to exchange and spin-orbit interactions [6]. Moreover, the DFT calculations had significant differences from the experimental results either in the magnitude of spin-orbit splitting or in the atomic structure of graphene and the underlying layer. Because of the impossibility to take into account in the calculations all the features of the structure of the real system and the need to achieve experimental values of spin splitting, unrealistic surface models are usually used. In our case of a single-phase system it was possible to perform calculations of rather realistic simple unit cells, which could shed some light on the complex nature of the observed giant Rashba effect. Having a single-phase system with a rarefied Pt layer with voids, one can theoretically simplify the system as if it were composed of single Pt atoms.

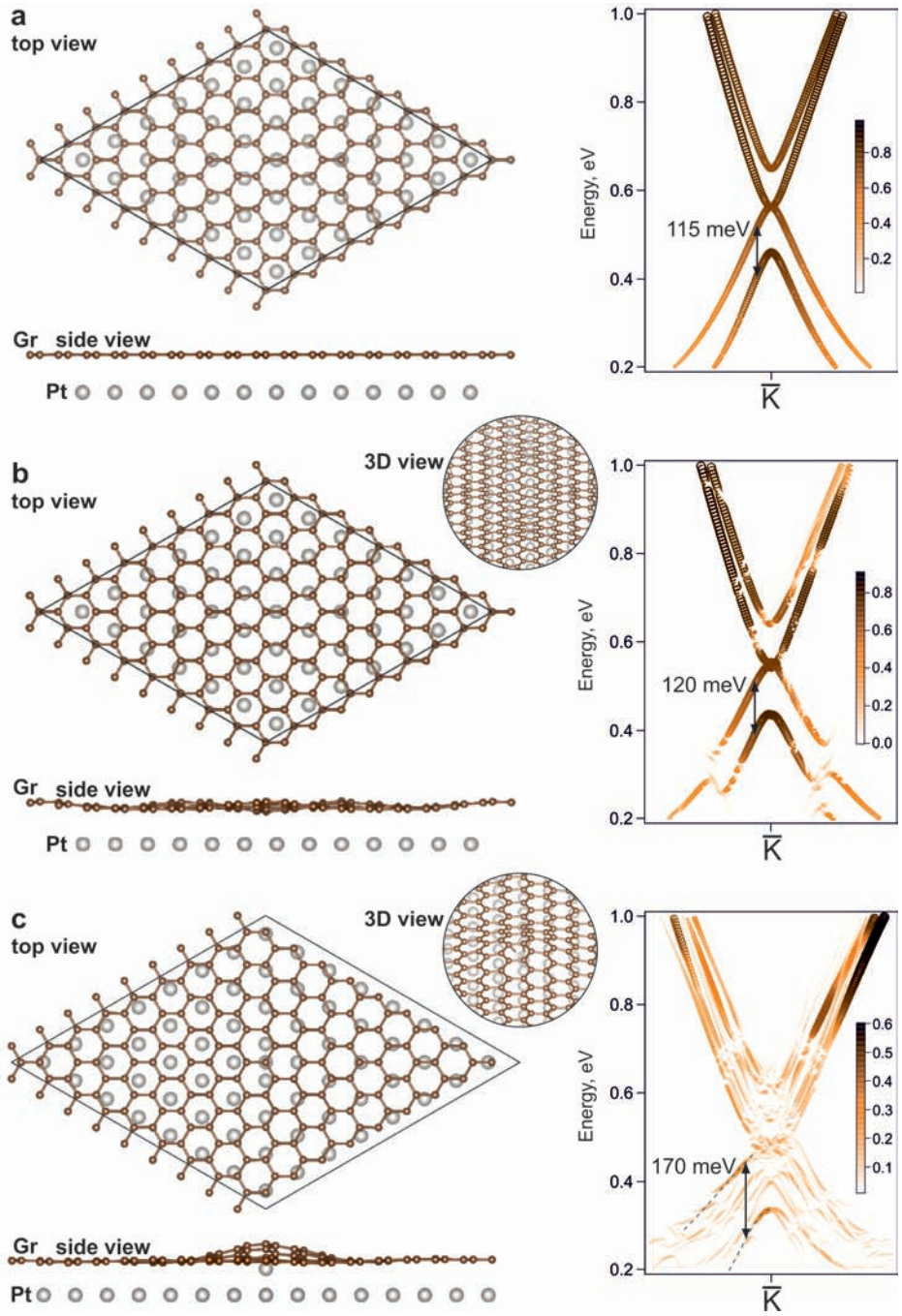

Figure 6.8 — Gr/Pt interface model systems in the form of slabs: (8 × 8) with flat graphene and Pt layer (a), (8 × 8) with large-scale corrugation of graphene (b), and (9 × 9) with Pt atom-induced corrugation of graphene (c). The corresponding unfolded bands calculated by the DFT method near $\overline{\mathrm{K}}$ points along the $\overline{\Gamma\mathrm{KM}}$ direction of the Brillouin zone of graphene are shown on the right. The size of the symbols and the color palette denote the Bloch spectral weight of the carbon atoms for the unfolded band structure.

The first model in Fig. 6.8 (a) presents the Gr/Pt interface with flat layers. A splitting close to 100 meV was obtained at a distance of $\sim$ 2.8 Å, which is smaller than the equilibrium distance for the Gr/Pt(111) system ($\sim$ 3.3 – 3.4 Å according to Paragraph 5.2.2). Nevertheless, even this close distance is not sufficient to obtain a splitting value comparable to the experimental one. It is worth considering that further reduction of the distance between graphene and the Pt layer leads not only to an increase in the splitting, but also to the destruction of the Dirac cone due to strong hybridization with $5d$ states of Pt. In the second model, the effect of corrugation of graphene near the average Gr – Pt distance $\sim$ 2.8 Å was verified. Corrugation was obtained after optimizing the Gr(8×8)/Pt interface structure with an equilibrium distance $\sim$ 3.3 Å. Since the splitting has slightly increased compared to the previous case, and the carbon atoms now have different distances to the Pt layer, we can conclude that the average distance between the graphene and the Pt layer plays a major role in the Rashba effect. In order to reduce this average distance without bringing graphene and platinum closer together, a point defect in the form of an additional Pt atom under graphene was constructed and structural optimization of the system was carried out. At the same time, due to the formation of a “hat-like” graphene structure above the additional Pt atom, some carbon atoms have a small distance to the nearest platinum atom ($\sim$ 2.3 Å), which should increase the spin-orbit interaction induced in graphene. It should also be noted that the structural optimization resulted in flat regions even closer to the Pt layer ($\sim$ 2.5 Å). As it turned out, such a defect enhances the splitting up to $\sim$ 170 meV. At the same time, the Dirac cone dispersion of graphene is not destroyed. Within the experimental resolution, we have good agreement between this model and experiment. Thus, the essential features revealed for the first time in the calculations are the possibility of corrugation of graphene in a large-scale unit cell with a flat substrate and the effect of graphene convergence in the case of point defects in the form of Pt single atoms under graphene.

Without any doubt, the unit cells used in the calculations have too small lateral parameters, and the model of the system based on STM data should have a unit cell of minimum size (15×15) with a periodic arrangement of voids and quasi-periodic arrangement of Pt atoms between each other. For this reason, the performed DFT calculations cannot fully account for the complex structure of the real surface, and it is necessary to solve the difficult problem of calculating large unit cells in order to finally establish the role of nanometer-scale unit cells in the giant Rashba effect. However, despite the described limitations, the performed calculations of model unit

cells give a fairly good idea of the possible cause of the giant Rashba splitting in the considered system, which consists in the decrease of the average distance between carbon and platinum atoms due to the appearance of an ordered grid of platinum clusters and voids under the graphene.

6.2.4 Findings

Intercalation of noble metals leads to giant Rashba-type spin-orbit splittings of electronic states in graphene. Spin-orbit splitting greater than 100 meV has not been previously achieved in graphene on metal or semiconductor substrates. For p-doped graphene obtained by intercalation of a Pt underneath zero-layer graphene on a SiC substrate, a spin splitting of $\sim$ 200 meV is observed over a wide range of binding energies. Based on the analysis and comparison of the results of theoretical studies of various models with the results of experimental studies by spin-ARPES, XPS, and STM methods, it is concluded that not only a relatively close distance between graphene and the Pt layer, but also the presence of corrugation of graphene caused by the nonplanar Pt layer is necessary to obtain giant spin-orbit splitting. This allows a compromise between strong hybridization and enhanced spin-orbit interaction. In our case, the Pt submonolayer possesses nanometer-scale lateral ordering underneath the graphene in the form of a rarefied Pt layer with triangular-shaped voids. A theoretical model with additional platinum atoms under the graphene shows a decrease in the distance between the graphene and the Pt layer atoms due to the convergence effect under graphene corrugation at point defect sites. A more complex boundary between graphene and the intercalated noble metal layer is assumed to underlie the giant Rashba effect. Nevertheless, the synthesized system is a good candidate for measuring the spin Hall effect because it is grown on a silicon carbide substrate and the intercalation of an incomplete Pt monolayer minimizes the electrical shunting of graphene by metal atoms.

6.3 Advanced graphene recording device for magnetoresistive memory based on spin-orbit torque effect

Spin-orbit torque magnetoresistive RAM (SOT-MRAM) is a promising technology to be realized in near-future computers because it has several advantages such as non-volatile, high storage density, and scalability. Next, we consider a graphene-based recording element model for a SOT-MRAM unit cell consisting of quasi-freestanding graphene intercalated with Au and an ultrathin Pt layer located between the graphene and the magnetic tunnel junction (MTJ). The graphene-based recording element will result in faster memory operation and lower power consumption when writing information by reducing the electric current required for the writing. The efficiency of graphene-based recording element has been confirmed by experimental results and theoretical calculations.

Modern development of computing and data storage systems requires miniaturization of memory devices, increased performance and energy efficiency. Magnetoresistive RAM (MRAM) has a number of advantages over other widely used memory types in modern computers (DRAM, FLASH, SRAM). The most important advantage of MRAM is the non-volatile behavior of its memory elements, due to which information is stored not due to electric charge, but due to the magnetic state of matter. In addition, MRAM has a higher speed of operation than DRAM or FLASH. The memory element used in MRAM consists of two ferromagnetic layers: a “fixed” layer (hereinafter referred to as the fixed layer) with constant magnetization and a “free” layer (hereinafter referred to as the free layer) with changing magnetization, separated by a thin insulating layer, and operating on the basis of MTJ [480–483]. The read process in MRAM is realized by measuring the electrical resistance of the cell. The write process is a change in the magnetization orientation of the free layer using a write element (or write line).

There are various methods to write data to a memory cell. The classical method uses a pair of lines to write [484; 485]. An electric current is passed through them, which induces a magnetic field at the junction, followed by a change in the orientation of the magnetization of the free layer. Unfortunately, the described MRAM design requires high power consumption, and the use of induced external magnetic field

makes it difficult to reduce the size of the unit cell at the desired high density of data storage.

A more efficient way to write information into an MRAM unit cell is based on the spin transfer torque effect (STT-MRAM) [485; 486] or spin-orbit torque effect (SOT-MRAM) [45; 485; 487; 488]. The fundamental difference between STT-MRAM and SOT-MRAM is the control of tunnel junction. Writing and reading information into the STT-MRAM unit cell occurs when currents are flowing perpendicular to the tunnel junction. This causes the cell to wear out during the write and read process, although the read currents are much smaller than the write currents. A SOT-MRAM tunnel junction cell is written by passing current along the plane of the MTJ rather than through all layers of the unit cell (Fig. 6.9 (b)). The switching of the magnetization of the free layer occurs by a spin-polarized current due to the transfer of orbital angular momentum from the lattice to the spin system. The geometric change of the method of passing currents significantly reduces the wear of the cell and increases the switching rate of the free layer [485; 487; 489]. In [487; 489; 490], it is shown that the magnitude of the write current for a cell based on the spin-orbit torque (SOT) effect is reduced compared to that for a cell based on spin-transfer torque (STT). The results show that magnetization switching in the SOT device requires less energy than that in the STT-driven device. Advanced magnetic memory based on the SOT effect is an excellent candidate for a versatile non-volatile memory that solves the problems of MRAM and promises reduced write current, low power consumption, high performance and high memory density. Therefore, finding suitable materials and systems based on them in which the spin-orbit torque effect can be realized is an urgent task. Devices based on the SOT effect can be used not only in memory cells but also in spintronics logic elements.

The control of magnetization in nanomagnets using the spin-orbit torque effect induced by currents has led to a growing interest in MRAM and the realization of SOT-MRAM [457; 491; 492]. In some previous works, the idea of in-plane injection of spin-polarized currents in non-magnetic materials such as topological insulators [492] and Pt thin films [491] has been used to induce magnetization in ferromagnetic layers on top of them due to the spin-orbit torque phenomenon. This effect results in electron spin transfer from the bottom layer of topological insulator or Pt to the ferromagnetic layer. Layers of Fe, Ni, Co, or permalloy have been used as ferromagnetic. In the work [492], an insulating layer (e.g., MgO or AlO_x) was used between the topological insulator and the ferromagnetic layer to preserve the

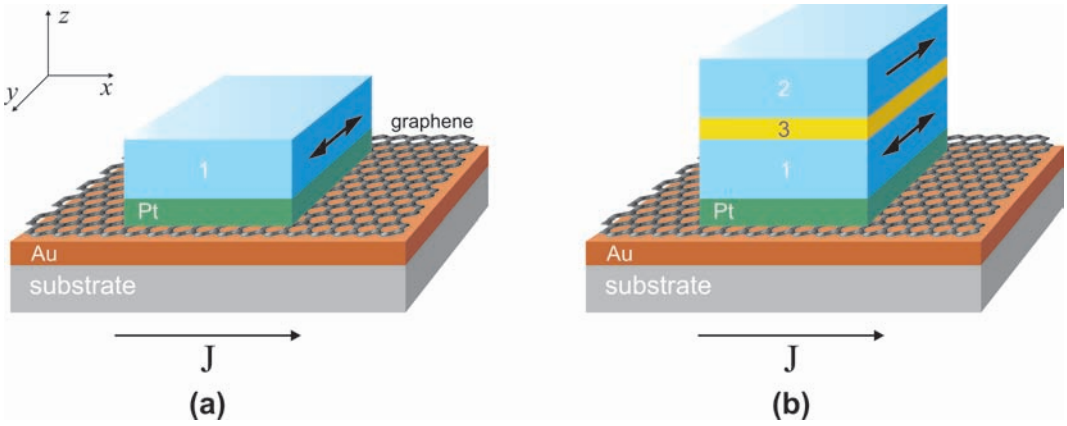

Figure 6.9 — (a) Model of graphene recording element. (b) A SOT-MRAM-type magnetic memory cell using a graphene recording element. The layer designations in the figure are as follows: substrate (gray layer), Au (brown layer), graphene, Pt (green layer), free magnetic layer (1), dielectric layer (3), fixed magnetic layer (2). Parts (1), (2), and (3) form the MTJ of the memory cell. The in-plane electric current direction along the surface (J) is perpendicular to the magnetization orientation of the magnetic layers.

electronic structure of the topological Dirac cone states, which plays a major role in the formation of spin-polarized current. On the other hand, the use of Pt is very promising since its contact with the ferromagnetic Co is known to exhibit high spin transfer efficiency [491; 493—496]. An alternative way to switch the magnetization in quasi-two-dimensional systems with strong spin-orbit interaction is the spin moment induced by the spin Hall effect [497]. However, in this case, the directions of the applied electric current and spin current do not coincide.

The application of graphene on nonmagnetic Ir and Ru substrates has been proposed for magnetization switching in SOT-MRAM cell [498]. Graphene is a preferred candidate for two-dimensional spintronics because of its long spin relaxation length and efficient spin transport at room temperature [122—124]. Moreover, graphene can be considered as a promising device element because it can withstand very high current density [124; 499]. The unique properties of graphene provided by its Dirac cone electronic structure promise to reduce power consumption and speed up the operation of the memory cell [124; 500]. At the same time, graphene has a weak intrinsic spin-orbit interaction, making it difficult to use in spintronics [501]. However, various approaches [12; 502—505] have been taken to enhance the spin-orbit interaction in graphene. The induced giant Rashba spin-orbit interaction in graphene in contact with some heavy metals (Au, Pt) discovered in this work increases the

efficiency of spin-polarized current generation, which also improves the recording properties. However, it should be noted that the use of graphene formed on substrates of ferromagnetic metals (Ni, Co) or some transition metals (Ru, Re) is inefficient, because the contact of graphene with the above metals leads to the destruction of the linear dispersion of π states, as was experimentally confirmed [14; 16; 108; 506; 507]. Near the $\overline{K}$ points of the Brillouin zone, the π state of graphene is significantly modified due to hybridization with the substrate states. This is accompanied by the loss of the unique transport properties of graphene and the impossibility of spin moment transfer from the graphene layer to the free ferromagnetic layer of the memory device. Thus, the contact of graphene with Ni, Co, Re and Ru cannot be used as a basis for a recording element. To overcome this limitation, we consider induced spin-orbit interaction in graphene on a ferromagnetic substrate followed by Au intercalation for use in a memory cell. The advantages of using graphene in a SOT-MRAM recording element will be discussed based on the experimental and theoretical results obtained.

6.3.1 Device description

The proposed model of the graphene recording element is shown in Fig. 6.9 (a). The present device consists of a free magnetic layer and a recording element that changes the magnetization of the free layer in two opposite directions. The recording element is based on the spin-orbit torque effect and consists of graphene lying on an insulating substrate, with an intercalated thin gold layer underneath and an ultrathin platinum layer located between the graphene and the free magnetic layer. The free magnetic layer is made of a ferromagnetic metal such as Ni, Co, Fe, or an alloy of the mentioned metals, and the dimensions of the free magnetic layer and the ultrathin platinum layer are about 50 – 200 nm in plane and 2 – 10 nm in height. Silicon carbide SiC(0001) can be used as a substrate, on whose surface a graphene monolayer can be synthesized. The width of graphene on the substrate is limited by the size of the free magnetic layer, and the length exceeds the length of the free magnetic layer by 2-3 times. One monolayer of gold atoms is incorporated between the graphene and the substrate.

Figure 6.9 (b) shows the realization of a SOT-MRAM magnetic memory cell using the proposed graphene writing element. The magnetic memory cell consists of a recording element described in Figure 6.9 (a) and a reading element above. The reading element includes an insulating layer and a second fixed magnetic layer for operating the MTJ. The magnetization of the free and fixed layers is located in the surface plane. Information is read by measuring the electrical resistance of the cell.

Let us return to the consideration of the claimed recording device (Fig. 6.9 (a)). The model uses a well-ordered epitaxial graphene monolayer synthesized on a SiC(0001) substrate. However, it is known that the spin-orbit splitting of π states in graphene on a silicon carbide substrate is very small, which makes it difficult to use graphene as an active element of spintronics devices [468]. In contrast, intercalation of various metals results in the separation of the zero-layer graphene and the formation of quasi-freestanding graphene (Chapter 5 and [388; 508—512]). Au intercalation leads not only to the formation of quasi-freestanding graphene, but also to induced spin-orbit interaction in graphene and spin splitting of π states of graphene [512]. Spin splitting of π states of graphene with magnitudes up to 100 – 200 meV was observed when Au was intercalated under graphene on Ni(111) and Co(0001) (see Section 6.1 and Chapter 7). Thus, the use of Au-intercalated graphene will achieve a high spin polarization efficiency for current flow through the planar graphene/Au/substrate system.

When an electric current passes through the system graphene/Au/substrate, a spin-polarized current (spin current) is created along the electric current direction with spin orientation perpendicular to the current. When a reverse current is applied, the spin orientation is also reversed. In this case, the silicon carbide substrate does not shunt the spin current in graphene, which leads to an increase in device efficiency and simplifies the implementation of the element in the design of a spintronics device. The spin current can induce magnetization of the free magnetic layer of SOT-MRAM cell due to the spin-orbit torque effect. In this case, changing the direction of the spin current will switch the orientation of induced magnetization in the free layer.

An ultrathin Pt layer (1-2 monolayers) is placed between the graphene/Au/-substrate contact and the free magnetic layer. On the one hand, the ultrathin Pt layer will prevent the Dirac cone states of graphene from destruction upon contact with the magnetic metal of the free layer, since the contact of graphene with Pt allows the formation of quasi-freestanding graphene [15]. On the other hand, strong magnetic anisotropy and spin moment transfer were found for Co and Pt multilayer structures

[493]. The use of Co/Pt nanostructures to create induced magnetization in them while generating spin current along the graphene surface improves the performance. The publication [513] concluded that the closer in energy the d zone of noble metal to the d zone of cobalt, the stronger spin-orbit torque effect observed in the system. Thus, the use of Pt or its alloy with gold $\mathrm{Au}_{0.15}\mathrm{Pt}_{0.85}$ is more appropriate to observe the effect.

Only annealing and metal atom adsorption cycles (without cleavage, etching, etc.) are required to form the described system, which can be accomplished on an industrial scale, making the proposed device commercially attractive for realization.

6.3.2 Experimental results

A distinctive feature of the above model of the recording element is the utilization of the unique characteristics of graphene and the induced spin-orbit interaction in contact with Au. Figure 6.10 shows the dispersion dependences of the Dirac cone π states of graphene on Ni(111) – (a) and on Co(0001) – (b) intercalated with Au atoms, measured by the ARPES method in the vicinity of the $\overline{\mathrm{K}}$ point of the Brillouin zone. Graphene was synthesized by CVD on the surface of Ni(111)/W(110) or Co(0001)/W(110) substrates in order to obtain well-oriented graphene on the whole surface of single crystals. The thickness of the Ni or Co films was about 50 – 100 Å. The intercalation of Au monolayer was realized by adsorption of gold atoms onto graphene followed by annealing at temperatures of 450 – 600 °C. After Au intercalation, quasi-freestanding graphene with a small p-doping (the Dirac point is located just above the Fermi level) is formed. The linear character of the dispersion of π states determines the unique physicochemical properties of graphene. Spin-resolved ARPES data are presented in Fig. 6.10 (c,d). Hybridization of π states of graphene and d states of gold reveals induced spin-orbit splitting of π states. In the case of graphene on intercalated Au on Ni(111), the magnitude of spin splitting is about 100 meV, and in the case of graphene/Au/Co(0001), the magnitude of spin splitting reaches a giant value of 150 – 200 meV near the $\overline{\mathrm{K}}$ point of the Brillouin zone. Figure 6.10 (e) shows the spin-split spectra of π states of graphene for the graphene/Au/Co system. It can be seen that a giant Rashba splitting of the π states of graphene is observed up to 1.5 eV below the Fermi level.

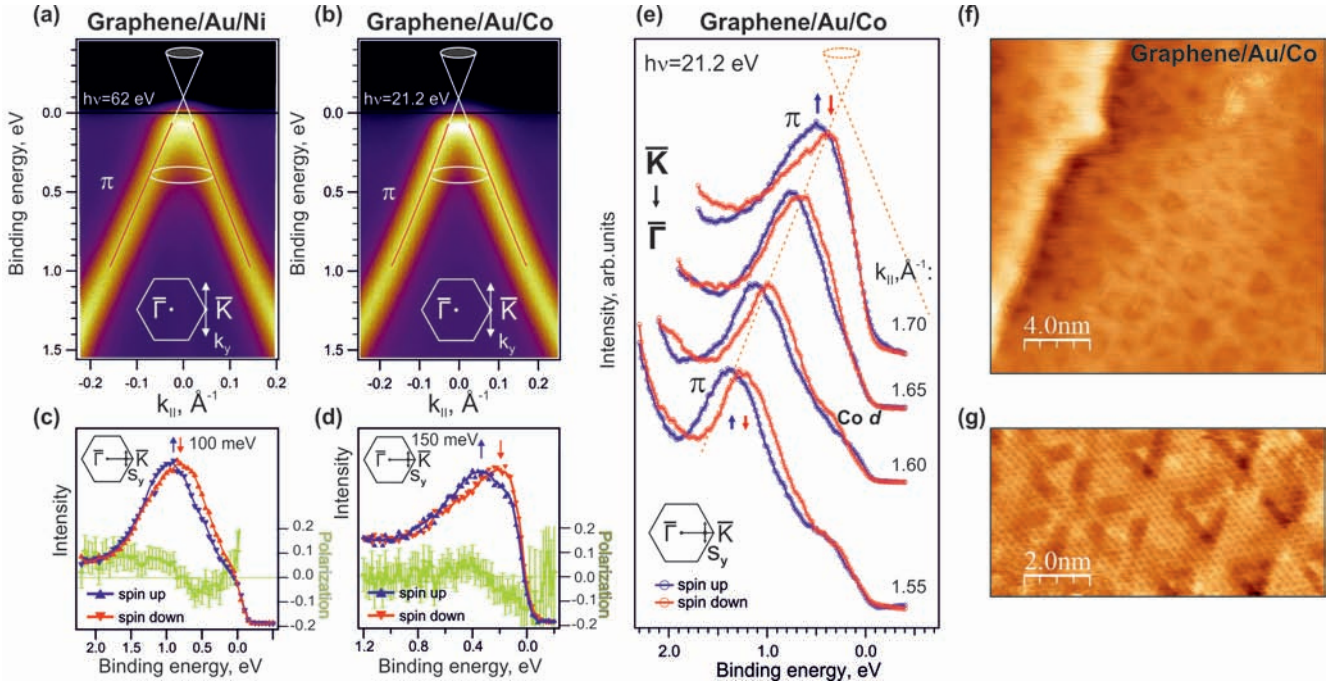

Figure 6.10 — (a) Dispersion of π states of Gr/Au/Ni(111) near the $\overline{\mathrm{K}}$ point measured along the k_y direction ($\perp \overline{\Gamma\mathrm{K}}$) using a photon energy of 62 eV. (b) Dispersion of π states of Gr/Au/Co(0001) measured as in (a) but using a photon energy of 21.2 eV. The solid red lines show the result of approximation of the quasi-wave vector distribution curves by two peaks with Lorentz shape. (c, d) Spin-ARPES spectra of π states in the vicinity of $\overline{\mathrm{K}}$ points for Gr/Au/Ni(111) and Gr/Au/Co(0001), respectively. The green curves below the spectra show the corresponding spin polarizations. In panels (c, d), blue and red colors indicate opposite sign spin projections on the axis lying in-plane and directed perpendicular to the quasi-momentum. (e) Spin-ARPES spectra of π states of graphene measured along the $\overline{\Gamma\mathrm{K}}$ direction at several $k_{\|}$. (f) 20×20 nm^2 STM image of Gr/Au/Co obtained at tunnelling current $\mathrm{I_t}$ = 0.45 nA and bias voltage $\mathrm{V_t}$ = 3 mV and (g) 10×5 nm^2 STM image at $\mathrm{I_t}$ = 0.4 nA and $\mathrm{V_t}$ = 10 mV.

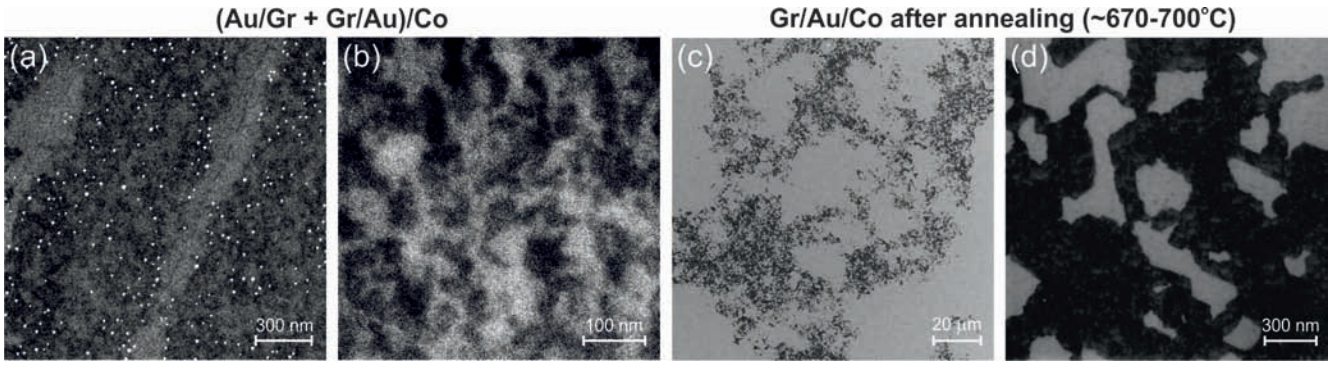

Figure 6.11 — (a,b) SEM images of Gr/Co with deposited and partially intercalated 0.5 ML Au and (c,d) - overheated Gr/1ML Au/Co system at about 670 – 700 °C for 2 hours. The EHT voltage is 10 kV for (a) and (c), 4 kV for (b) and 0.5 kV for (d).

The origin of the giant spin splitting can be explained by the combination of strong magnetism and strong spin-orbit interaction in the system. In the next chapter, it will be shown that the strong exchange interaction induced by the Co substrate and the spin-orbit interaction induced by Au are perfectly achievable in graphene all at once. A kind of interface rearrangement between the Au and Co(0001) monolayer is responsible for the transfer of the exchange interaction to graphene, resulting in the realization of a "magneto-spin-orbit" version of graphene. Figure 6.10 (f,g) shows the results of STM measurements for the Gr/Au/Co(0001) surface. First of all, a well-ordered Au-intercalated graphene layer is formed on top of the Co(0001) substrate. The results of STM measurements depend on the used bias voltage V_t. When the bias voltage is lower (e.g., $V_t = 2$ mV), a moiré structure is observed. And when the bias voltage is increased to $V_t = 10$ mV (Fig. 6.10 (f,g)), a triangular shaped periodic feature pattern starts to appear. In the next chapter, it will be shown that these structural features (loop dislocations) can induce magnetic exchange interaction in graphene, which allows us to increase the spin splitting of π states up to 150 – 200 meV (Fig.6.10 (d)).

The electron spin structure of Au-intercalated graphene on SiC(0001) has been studied in detail in [388; 468; 511; 512]. The formation of quasi-freestanding graphene after Au intercalation under graphene on SiC is shown. The induced spin-orbit splitting in graphene on Au/SiC(0001) is found to reach a value of $\sim$ 70 meV near the Dirac point [512].

To better understand the Au intercalation process and the thermal stability of the graphene/Au/Co system, additional studies were performed: formation of a semi-intercalated system and thermal destruction of fully intercalated graphene.

SEM images (Fig. 6.11 (a,b)) of the system annealed at 550°C for 20 min after adsorption of 0.5 ML Au show intercalated regions of graphene in the light tone and non-intercalated regions in the dark tone. Residual clusters are also visible, as full intercalation requires higher temperatures up to $600\ ^{\circ}$C and longer annealing times (up to 2 hours). The figure 6.11 (a) clearly shows that intercalation occurs more efficiently at the step edges. Annealing the system at $670 - 700\ ^{\circ}$C leads to graphene destruction, as only a small part of the surface is covered by graphene islands after annealing, shown in Fig. 6.11 (c,d). This is accompanied by the absence of signal from π states of graphene in ARPES, and only Au and Co states contribute to the valence band spectra. Nevertheless, we observe a bright LEED pattern (Fig. 6.12 (b))

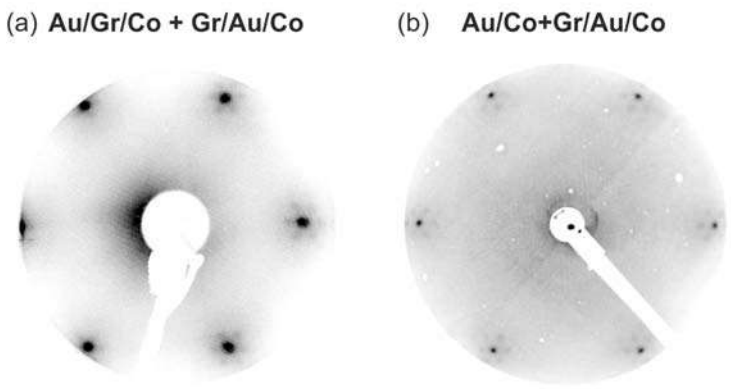

Figure 6.12 — (a) LEED image at $E_p = 63$ eV for the Au/Gr/Co+Gr/Au/Co system shown in Fig. 6.11 (a,b). (b) LEED image at $E_p = 65$ eV for the overheated Gr/Au/Co system shown in Fig. 6.11 (c,d).

of the reconstructed Au/Co surface with dislocation loops, which has less intense graphene/Co reflections compared to the semi-intercalated system.

To test the electronic structure at the Dirac point of n-doped graphene, Gd adsorption onto the surface of the system was carried out. It was found that graphene dispersion does not change upon Gd adsorption, except for a gradual shift of the Dirac point below the Fermi level (Fig. 6.13 (a)) with increasing amount of adsorbed Gd (up to 1 ML). At the same time, the Rashba spin splitting of $\sim 80 - 100$ meV is observed for the non-magnetized sample (Fig. 6.13 (b)), which is the same for the graphene/Au/Ni system. Moreover, there are no obvious signs of the opening of the band gap at the Dirac point (value below the detection limit ~ 20 meV).

The observation of giant spin splitting in graphene at room temperature allows us to design a device that works under realistic conditions. The effect of induced spin-orbit splitting in graphene will be observed even after heating to temperatures of $600 - 650$ °C, providing the thermal stability of a real device, which is a standard requirement for complementary metal-oxide-semiconductor back end of line (CMOS BEOL) [490]. Adsorption of Gd atoms on graphene leads to a controlled change in the position of the Dirac point depending on the amount of Gd. Graphene is promising as an active element in devices because it can withstand very high current densities, is mechanically robust and chemically inert [124; 499]. The experimental study of graphene-based systems is expected to be useful for further device design as well as for the control and management of memory cells.

The spin accumulation at the Gr/Au interface induced by the Rashba effect can be regarded as an effective internal magnetic field capable of magnetizing or

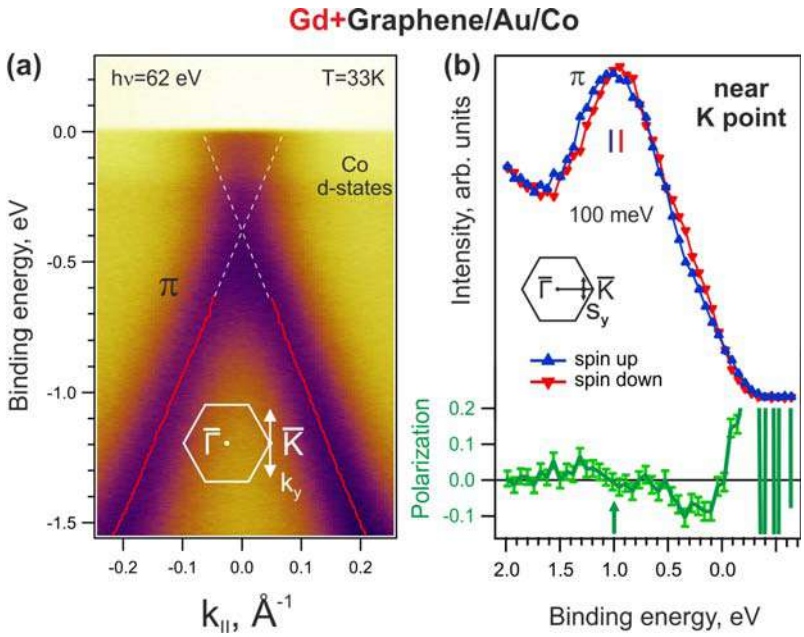

Figure 6.13 — (a) Dispersion of π states of Gr/Au/Co with adsorbed Gd atoms near the $\overline{\mathrm{K}}$ point measured along the k_y direction using 62 eV photon energy. The solid red lines show the result of the approximation of the quasi-wave vector distribution curves by two peaks with Lorentz functions. (b) Spin-ARPES spectrum of π state in the vicinity of the $\overline{\mathrm{K}}$ point for Gd/Gr/Au/Co system. The green curve below the spin-resolved spectrum shows the spin polarization. Blue and red colors indicate the spin projections of different sign on the axis lying in the plane and directed perpendicular to the quasi-wave vector.

remagnetizing the free layer of SOT-MRAM magnetic cell. This effective magnetic field induced by the spin current in graphene leads to the magnetization of the free magnetic layer. The effective magnetic field creates a torque acting on the magnetization in the layer (e.g., Ni-Fe) defined by the expression [45; 488]:

$$\vec{T}_{SO} = \left[\vec{M} \times \vec{B}_{SO}\right] \tag{6.2}$$

In our case, the spin polarization vector is in-plane, so the most promising MRAM cell design is an in-plane cell. Usually in this case, the free magnetic layer does not have perpendicular anisotropy, but has some in-plane anisotropy due to material properties or shape anisotropy. The hysteresis loops of the free layer of size $50 \times 50 \times 2$ nm^3 are shown in Fig. 6.14 (a) for different values of the magnetic anisotropy constant. At the same time, the most popular design of a planar memory cell is an elliptical quantum dot made of permalloy. In this case, the magnetostatic interaction admits two equilibrium states along the large semi-axes of the ellipse. Consider an elliptical free layer of size $100 \times 160 \times 4$ nm^3. The time dependence of the

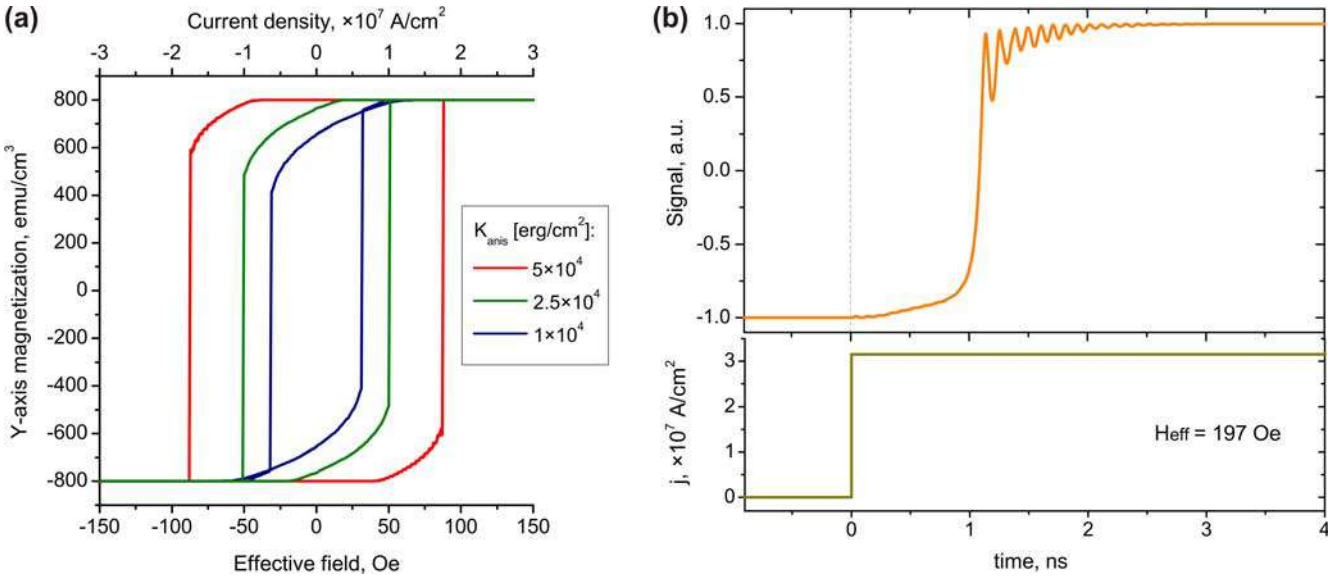

Figure 6.14 — (a) Calculated hysteresis loops of the free layer for different values of the magnetic anisotropy constant. (b) The switching process in the case of an elliptical ($100 \times 160 \times 4$ nm^3) free layer. Taken from the article [18], calculations were performed in the group of Prof. A. K. Zvezdin.

tunneling magnetoresistance (TMR) signal obtained from micromagnetic modelling, which is the normalized scalar product of the magnetizations of the free and fixed layers, is shown in Fig. 6.14 (b). The total resistance of the MTJ is expressed as $R = R_0 + \Delta R * Signal/2$, where R_0 is the average resistance of the MTJ and ΔR is the difference between the antiparallel and parallel states of the MTJ. The critical effective magnetic field required to remagnetize such a device is about 100 – 200 Oe (corresponding to current densities up to $1.6-3.2\times10^7$ A/cm^2), as shown in Fig. 6.14.

6.3.3 Findings

Based on the conducted studies, a model of a graphene recording element for a SOT-MRAM unit cell consisting of Au-intercalated quasi-freestanding graphene and an ultrathin Pt layer placed between the graphene and the free magnetic layer has been developed. A spin-polarized current is created when an electric current is passed through the graphene as a result of spin splitting of the electronic states of graphene at the Fermi level. The spin current has a spin orientation in the plane of the quasi-two-dimensional system and perpendicular to the current direction. This

induces magnetization in the free magnetic layer through the ultrathin platinum layer on top of the system graphene/Au/substrate due to the spin-orbit torque effect. In this case, changing the spin current direction will switch the orientation of the induced magnetization in the free layer.

The use of the proposed recording element model in SOT-MRAM magnetic memory devices will result in faster operation and lower power consumption when writing information: the increase in speed is due to the use of quasi-freestanding graphene, which has higher carrier mobility and higher electrical conductivity than its analogues; the highest efficiency for spin momentum transfer due to the use of magnetic layer contact with Pt; and lower energy consumption for information recording due to the fact that the contact of graphene with gold is used to create spin currents without the use of an external magnetic field.

7. Magnetic proximity effect in graphene

Magnetic proximity is a promising way to implement exchange splitting in material [87; 91; 150; 168; 170] that does not initially possess spin-polarized electronic states. If the time reversal symmetry is broken without an external magnetic field and the system still remains topologically nontrivial, the quantum anomalous Hall effect is realized. Haldane's model is the first example of a topological insulator with properties far beyond the quantum Hall effect [91]. It shows that if the topological index is not zero, all phenomena expected for a quantum Hall state will be observed, including quantized Hall conduction and the existence of edge states. Systems similar to the Haldane model are known as Chern insulators (characterized by a mean magnetic field equal to zero and a strong lattice potential). Their topological characteristics are well defined by the stability of single-directional edge states, non-zero Chern number and quantized conductivity. It is shown that contact of graphene with antiferromagnetic oxide leads to quantum anomalous and quantum valley Hall effects depending on the orientation of the magnetization, perpendicular or along the surface plane [93]. In the case of zero Chern numbers and opposite Berry curvatures for $\bar{K}$ and $\bar{K}'$ valleys, the circular dichroism Hall effect and the Dirac-Mott insulator state in antiferromagnetic superatomic graphene have been theoretically discovered [178].

The simplest way to make graphene magnetic is to synthesize it on magnetic substrates such as Ni(111) and Co(0001) [108; 421; 422; 514; 515]. However, there is a price to pay for this: the initial electronic band structure of freestanding graphene is strongly affected due to hybridization of the π state and surface states of the metal under the graphene [108; 421; 422; 514; 515]. Another alternative way is to use non-magnetic and relatively inert substrates, allowing to control the magnetization of graphene by creating isolated vacancies [175; 516–519] or by adsorption of light atoms [516; 520–522]. These methods have proven to be experimentally feasible, although they require precise control of the vacancy/adsorbate distribution, which seems to be a very challenging task. Despite all these efforts, significant spin splitting resulting from the combination of spin-orbit interaction and induced magnetization in graphene has not been measured.

7.1 Ferromagnetic graphene (p-graphene)

In this section, we present the first experimental evidence for the quasi-freestanding electronic structure of graphene characterized by the giant Rashba effect and magnetic exchange interaction (magneto-spin-orbit graphene). Depending on whether magneto-spin-orbit graphene is doped with holes or electrons, for simplicity we will call it p-graphene and n-graphene, respectively. The different doping of graphene is associated with different amounts of intercalated gold atoms. As we will show below, the two types of graphene are characterized by different spin-orbit interaction and different magnetic ordering on the carbon atoms.

Using angle- and spin-resolved photoelectron spectroscopy to study p-graphene intercalated with Au on Co(0001)/W(110), a giant spin splitting (up to 200 meV) of the Dirac states is found, the linear dispersion of which, however, is largely preserved. Based on density functional theory calculations, it was found that the splitting occurs as a result of the combined action of the exchange field due to the Co layer and the Rashba spin-orbit interaction induced by Au. A distinctive feature of this phenomenon is the strong asymmetry of the band structure relative to the center of the Brillouin zone. Further measurements using scanning tunnelling microscopy show that the transfer of the exchange field from the Co layer to graphene is facilitated by a peculiar reconstruction of the interface between Au and Co(0001). These results provide a striking example in which quasi-freestanding graphene simultaneously exhibits strong spin-orbit and magnetic effects without external fields, opening up promising possibilities for the implementation of graphene spintronics at temperatures above room temperature.

7.1.1 Spin splitting asymmetry

We begin with the structural characterization of graphene on Co(0001)/W(110) before and after the intercalation of gold atoms. The low-energy electron diffraction pattern obtained for the graphene grown by CVD on Co(0001) is a perfect hexagon with clear and bright reflexes (Fig. 7.1 (a)). It can be concluded that the synthesized

graphene has high structural quality and is commensurate with the Co(0001) surface in the structure (1×1) according to Section 5.2.1. It is known that graphene grows with position of one sublattice on top of the Co surface layer atoms ("top" position) and the other sublattice on top of the Co(0001) fcc hollow sites ("hollow" position) [174]. The bonds formed between the "top" graphene atoms and the underlying Co atoms stabilize a commensurate structure with a slight lattice mismatch. However, despite the chemical bonding between graphene and Co, it is still possible to intercalate the gold layer [422]. As can be seen in Fig. 7.1 (b) showing the LEED pattern after Au intercalation, an additional structure appears consisting of six reflexes surrounding each (1×1) reflex, which can be identified as a $\sim p(10 \times 10)$ superstructure. A similar $p(9 \times 9)$ periodicity was previously observed for gold intercalated graphene on Ni(111) [12; 149].

Another reliable evidence of successful gold intercalation is the analysis of ARPES spectra of the Gr/Co sample before and after intercalation. It is well known that the electronic structure of graphene is strongly modified when interacting with ferromagnetic $3d$ substrates [16; 149; 173; 422]. However, the intercalation of non-magnetic metal atoms helps to recover the graphene band structure close to that of freestanding graphene [12; 14; 523]. Indeed, in contrast to the Gr/Co case, the gold intercalated system is characterized by a good linear dispersion of π states up to binding energies of 2 eV, the Dirac point being $\sim$ 100 meV above the Fermi level E_{F} (Fig. 7.1 (c,d)). Important for the formation of the band structure of quasi-freestanding graphene is that the d states of gold are located in the region of binding energies 2 – 6 eV, where deviations from linear dispersion due to spin-dependent avoided-crossing effect are already observed (the region is marked by a large rectangle in Fig. 7.1 (d)) [12; 14]. The absence of photoelectron spectroscopy signal in the second Brillouin zone along the $\overline{\mathrm{KM}} \parallel k_x$ direction (see Fig. 7.2) indicates that the A – B symmetry of the sublattices after gold intercalation is no longer broken [524; 525], in contrast to the case of graphene/Co [16]. As further confirmed by STM measurements, the superstructure $p(10 \times 10)$ does not cause A – B symmetry breaking. Thus, the electronic structure of Au-intercalated graphene on Co(0001) appears to be much similar to that of freestanding graphene with conservation of its linear dispersion, with the p-doped Dirac cone and no clear sign of a band gap opening at the Dirac point. However, as we will show below, there is a fundamental difference from the case of freestanding graphene – a large spin splitting of the π band.

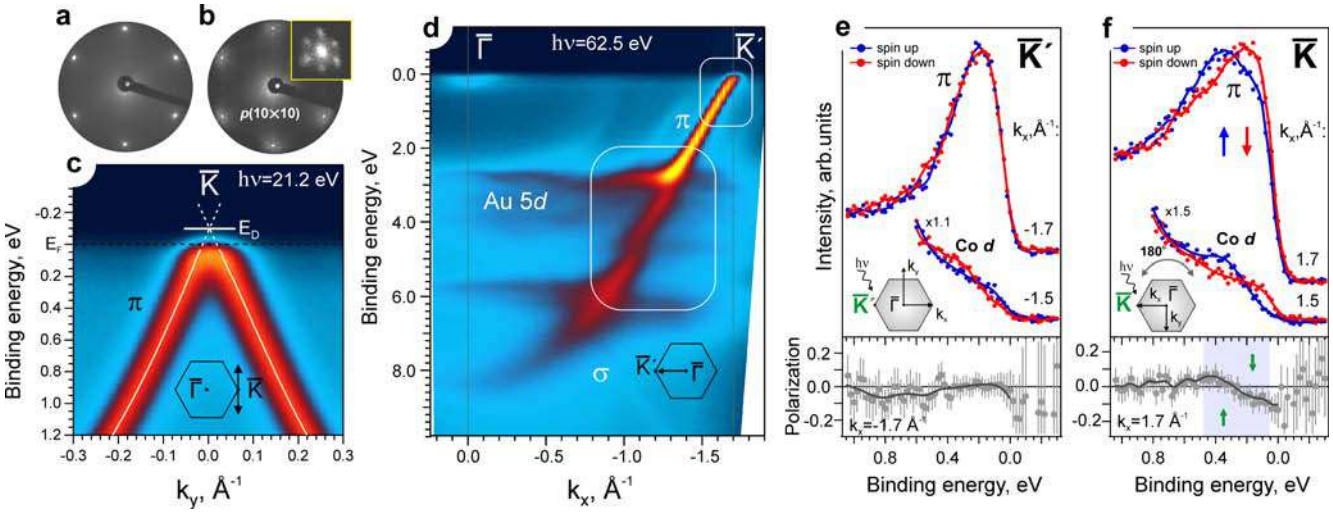

Figure 7.1 — LEED and spin-ARPES studies of the crystal, electronic and spin structure of Gr/Co before and after Au intercalation. (a,b) LEED patterns of Gr/Co(0001) and Gr/Au/Co(0001), respectively, obtained at energy $E_p = 113$ eV. Inset (b) shows the enlarged (1×1) reflex with six additional reflexes. (c) Dispersion of π states of Gr/Au/Co(0001) near the $\overline{K}$ point of the surface Brillouin zone measured along the k_y direction using a photon energy of 21.2 eV (solid white lines show the result of approximating the quasi-wave vector distribution curves by two peaks with Lorentz shape). (d) ARPES data for Gr/Au/Co(0001) measured in the $\overline{\Gamma K}'$ direction with a photon energy of 62.5 eV. (e,f) Spin-ARPES spectra measured in the valleys of the $\overline{K}'$ and $\overline{K}$ points, respectively ($h\nu = 62.5$ eV). The panels below the spin-resolved spectra show the corresponding spin polarizations. The data obtained at $k_{\|} = 1.7$ Å^{-1} correspond to a signal predominantly from the π band of graphene near the Fermi level, while Co d states are observed at $k_{\|} = 1.5$ Å^{-1} (states near the edges of the spin-polarized d bands and the local band gap). In panels (e,f), blue and red colors denote projections of different sign of the electron spin on the axis lying in plane and directed perpendicular to the quasi-momentum. Energy distribution curve (EDC) data with spin resolution without smoothing of the spin polarization function are shown by red and blue dots.

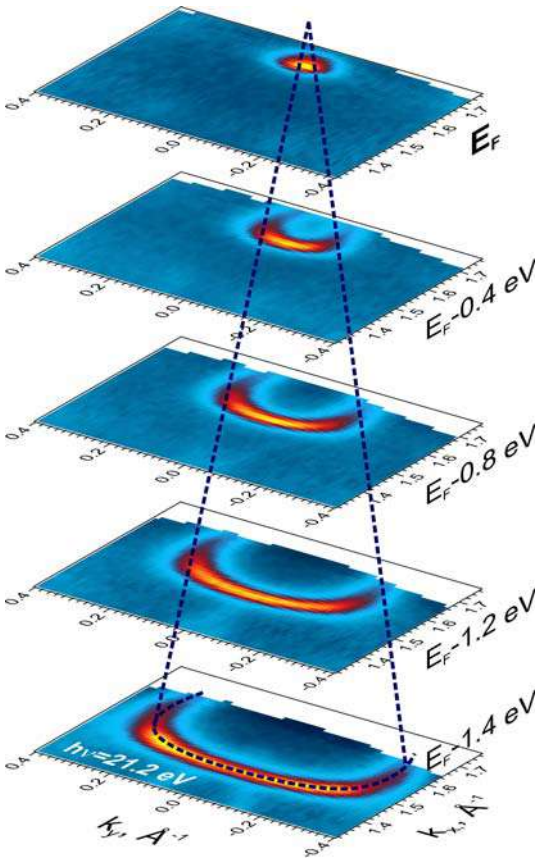

Figure 7.2 — ARPES intensity constant energy maps for graphene/Au/Co(0001) at the $\overline{\mathrm{K}}$ point.

Strong or even giant spin-orbit effects can be expected upon intercalation of such a heavy element as gold under graphene [12; 14; 135; 136]. To verify their presence in the Gr/Au/Co(0001) system, spin-ARPES measurements with spin resolution were performed. Surprisingly, no noticeable splitting of π states near the $\overline{\mathrm{K}}'$ point ($k_{\|}$ = -1.7 Å^{-1}) was detected within the experimental error of 20 meV, as can be seen in Fig. 7.1 (e), which shows the spin-resolved spectrum at the Dirac point of graphene. The spin-resolved spectrum at the $\overline{\mathrm{K}}$ point ($k_{\|}$ = 1.7 Å^{-1}) was then measured, and in contrast to the measurements for the opposite $\overline{\mathrm{K}}'$ point, a giant spin splitting of π states with magnitudes up to 150 $\pm$ 20 meV was detected (see Fig. 7.1 (f)). It should be noted that this measurement was performed after rotating the sample 180° around the normal axis (hereafter referred to as azimuthal rotation), as shown in the lower left corner of the figure. The reason for this transition between opposite $\overline{\mathrm{K}}$ points is to maintain the geometry of the photoelectron experiment during measurements, i.e., the photon incident angle and photoelectron emission. Measurements without azimuthal angle rotation were also performed and the result obtained is in good agreement with the results shown in Fig. 7.1 (e,f). The

asymmetry of spin splitting for $\pm k_{\|}$ directions in the surface Brillouin zone suggests that its mechanism goes beyond the simple Rashba model in graphene.

7.1.2 Combination of Rashba spin-orbit interaction and exchange field

The main reason for the asymmetry of the electronic structure in the $\pm k_{\|}$ directions is the violation of the time reversal symmetry. Considering the magnetic nature of the Co substrate, it can be assumed that its magnetization plays a role in the formation of the observed electron spin structure. In particular, this asymmetry can be caused by the joint Rashba effect and exchange interaction, which was first observed for rare-earth metal surfaces [106], but was later applied to graphene [108]. However, the effect requires the magnetization vector to lie in the surface plane, while it is well known that bulk Co in a hexagonal close packed structure has an easy magnetization axis along the (0001) direction, i.e., perpendicular to the basis plane [526]. In contrast, for a thin film system with the same surface, this axis lies in the plane of the surface due to surface anisotropy effects [527; 528]. This is exactly what happens in the Co(0001) layer grown on the W(110) substrate, for which the magnetization is known to be oriented along the W[$1\bar{1}0$] direction in films with thicknesses more than 3 and up to at least 50 monolayers [527; 528]. Since the thickness of the grown Co(0001) layer ($\sim$ 95 Å or 46 monolayers) is close to the mentioned upper limit, the easy axis direction was checked by spin-ARPES measurements. This was done by investigating the d states of Co both near the $\overline{\mathrm{K}}$ point ($k_{\|}$ = 1.5 Å^{-1} along k_x) and at the $\overline{\Gamma}$ point under normal emission. In the first case, the spin polarization along k_x was absent, while along k_y on the contrary was present (Fig. 7.1 (e,f)). Measurements with photon energy of 120 eV at the $\overline{\Gamma}$ point showed that the magnetization axis rotates with the sample, proving that the Co(0001) layer is magnetized in the surface plane along the [$01\bar{1}0$] axis (i.e., parallel to $-k_y$).

To confirm that it is the joint influence of spin-orbit and magnetic exchange interactions that leads to the spin splitting asymmetry effect, we performed spin-ARPES measurements after the application of an external magnetic field first in the [$01\bar{1}0$] direction and then in the opposite direction. We consider the spectra in normal

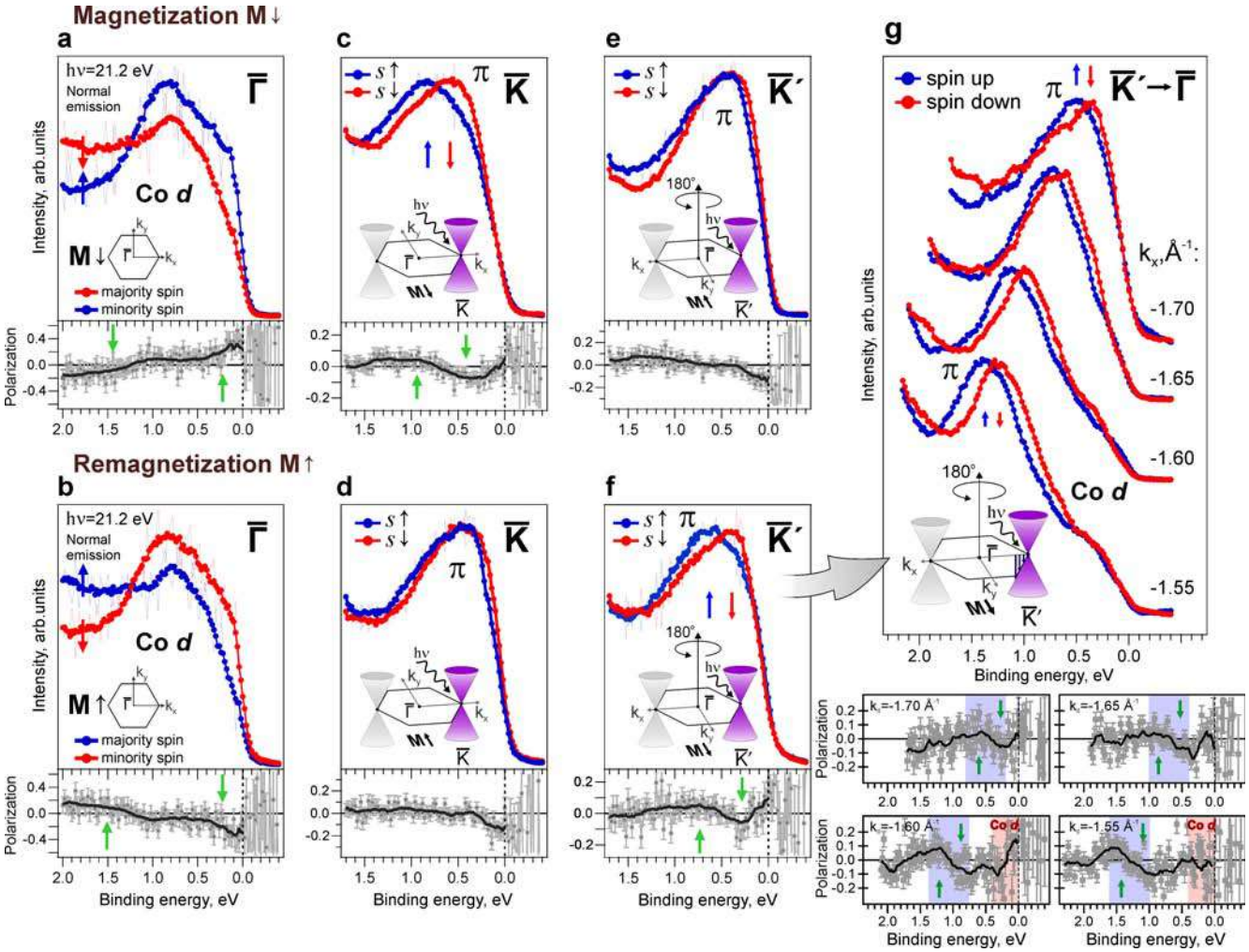

Figure 7.3 — Spin splittings in Gr/Au/Co(0001) after magnetization and remagnetization by an external field. (a,b) Spin-ARPES spectrum of the Co d band in normal emission geometry after application of an external magnetic field along the $[01\bar{1}0]$ (magnetization) and $[0\bar{1}10]$ (remagnetization) directions, respectively. The color designations are the same as in Fig. 7.1. (c-f) Spin-ARPES spectra of π states of graphene at the $\overline{\mathrm{K}}$ and $\overline{\mathrm{K}}'$ points after magnetization (c,e) and remagnetization (d,f). The $\overline{\mathrm{K}}'$ measurements were performed after rotating the previously magnetized (remagnetized) sample by 180° along the azimuthal angle R2. The spin-resolved EDC data without smoothing of the spin polarization function are shown as thin red and blue lines. (g) Spin-ARPES spectra of π states of graphene, measured along the $\overline{\mathrm{K}'\Gamma}$ direction for several values of the $k_{\|}$ quasi-wave vector after remagnetization. The panels below the spin-resolved spectra show the corresponding spin polarizations. All measurements were performed at a photon energy of 21.2 eV.

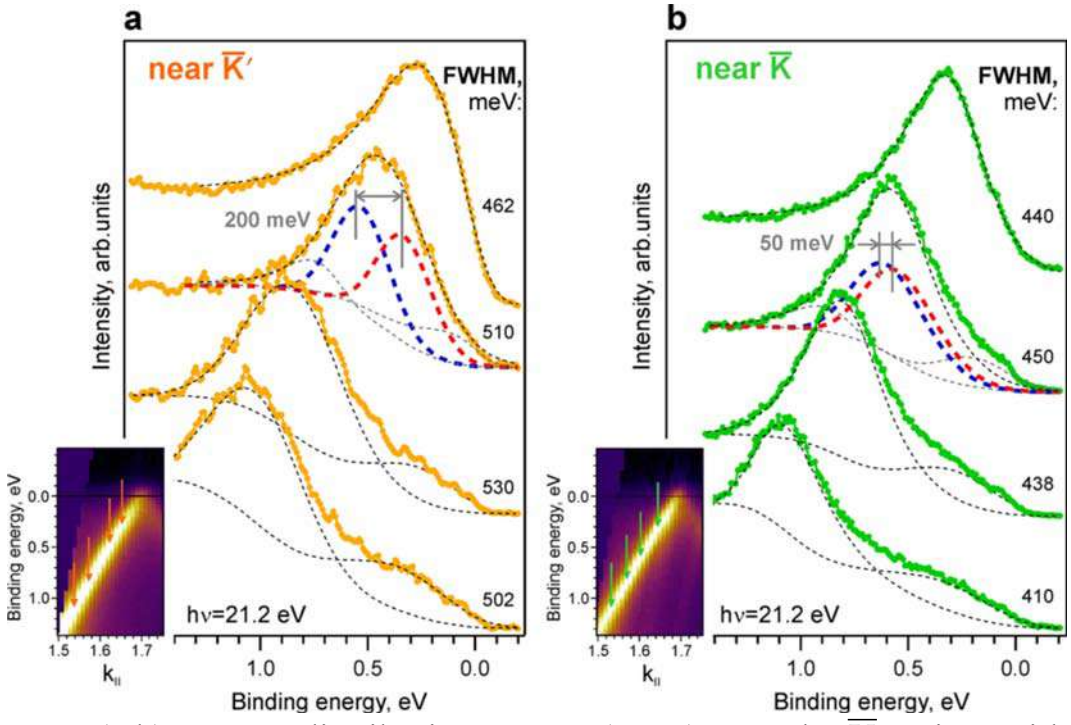

Figure 7.4 — (a,b) Energy distribution curves (EDC) near the $\overline{\mathrm{K}}$ points with ARPES intensity maps of E, k_x and approximation curves of the main peaks and background at $k_{\|} = \sim 1.6$ Å^{-1} along k_x. The topmost EDC in (a) has an asymmetric peak due to the large FWHM of π states in the $\overline{\mathrm{K}}'$ the valley, and the proximity of the Fermi level. A symmetric peak approximation can be achieved for the uppermost peak in (b) because the FWHM π states in the $\overline{\mathrm{K}}$ valley are smaller and the peak does not cross the Fermi level. The spectra were measured after applying an external magnetic field along $[0\bar{1}10]$ (M$\uparrow$ in Fig. 7.3).

emission geometry to determine the polarization of the d states of Co after application of a magnetic field. The results are shown in Fig. 7.3 (a,b). The photon energy of 21.2 eV was chosen deliberately for a clear comparison with the data in [528; 529], and there is indeed a good agreement. It is important to note that by comparing the two spectra shown in Fig. 7.3 (a,b), one can see a change in the spin polarization of Co $3d$ states, indicating the remagnetization of the sample.

The analysis of changes in the electronic structure of graphene accompanying the sample remagnetization shows the following. After applying a field in the $-k_y$ direction, we find a significantly increased spin splitting of 200 $\pm$ 40 meV at the $\overline{\mathrm{K}}$ point (Fig. 7.3 (c)) and a moderate splitting of 40 $\pm$ 40 meV at the $\overline{\mathrm{K}}'$ point (Fig. 7.3 (e)). To detect signatures of such asymmetry in the spin-integrated ARPES spectrum, we analyzed the EDC in the $\overline{\mathrm{K}}$ and $\overline{\mathrm{K}}'$ valleys. Figure 7.4 shows the spin-integrated EDCs near the $\overline{\mathrm{K}}'$ (panel a, gold color) and $\overline{\mathrm{K}}$ (panel b, green color) points.

Measurements were made along the $\overline{\Gamma K}$ and $\overline{\Gamma K}'$ directions for the magnetization directed along $+k_y$ ([0$\bar{1}$10]). At first glance, one can see that the peaks near the $\overline{K}'$ point are significantly wider than near the $\overline{K}$ (the full width at half maximum of $\sim$ 500 – 530 meV and $\sim$ 410 – 450 meV, respectively), which is consistent with the fact that the measured spin splitting in the $\overline{K}'$ valley is significantly larger than in the $\overline{K}$ valley. It should be noted that near the $\overline{K}'$ point the FWHM decreases sharply, which is due to the proximity of the Fermi level leading to a "truncated" shape of the π states peak (see the topmost EDC in Fig. 7.4 (a)). The approximation of the second peak from the top gives two main components (shown in red and blue), which have different energies of their maxima. These blue and red peaks can be easily identified as spin splitting states based on the spin-ARPES data shown in Fig. 7.3: the spin splitting near the $\overline{K}'$ point is gigantic (200 meV, Figs. 7.3 (f) and 7.4 (a)), while near the $\overline{K}$ point it is much smaller (40 – 50 meV, Figs. 7.3 (d) and 7.4 (b)). Note that according to the EDC analysis, the full width at half maximum of each of the two components of π states reaches a value of $\sim$ 380 meV (Fig. 7.4), which does not allow us to see spin splitting in the spin-integrated ARPES spectrum.

It should be noted that after magnetization (M$\downarrow$ in Fig. 7.3) the spin splitting near the $\overline{K}$ point significantly increases compared to the splitting shown in Fig. 7.1 for spontaneous magnetization, which can be explained by the growth of domains magnetized by the field in the [01$\bar{1}$0] direction. We emphasize that the observed spin splitting has a record value of 200 meV for graphene with conservation of the linear dispersion dependence and group velocity. Earlier it was found twice less spin splitting for gold intercalated graphene on Ni(111) [12], which is explained by a pure Rashba effect due to the 90° rotation of the easy magnetization axis at the transition from Co(0001) layers to Ni(111) layers of the same thickness (magnetization in the plane of the layer surface). Further, if we assume the mechanism of spin splitting as a result of a combination of the Rashba interaction and exchange interaction [106; 108], then after remagnetization of the sample, the electron spin structure should change symmetrically with respect to the center of the Brillouin zone, see Fig. 7.3 (d,f). Indeed, after remagnetization, the 200 meV giant spin splitting is now observed at the $\overline{K}'$ point, while the small splitting appears now at the $\overline{K}$ point. Moreover, as shown in Fig. 7.3 (g), the spin splitting of π states lies in the range 120 – 200 meV with an error of 40 meV along the $\overline{K'\Gamma}$, at least up to $k_{\|}$ = -1.55 Å^{-1}, which is in agreement with *ab initio* calculations.

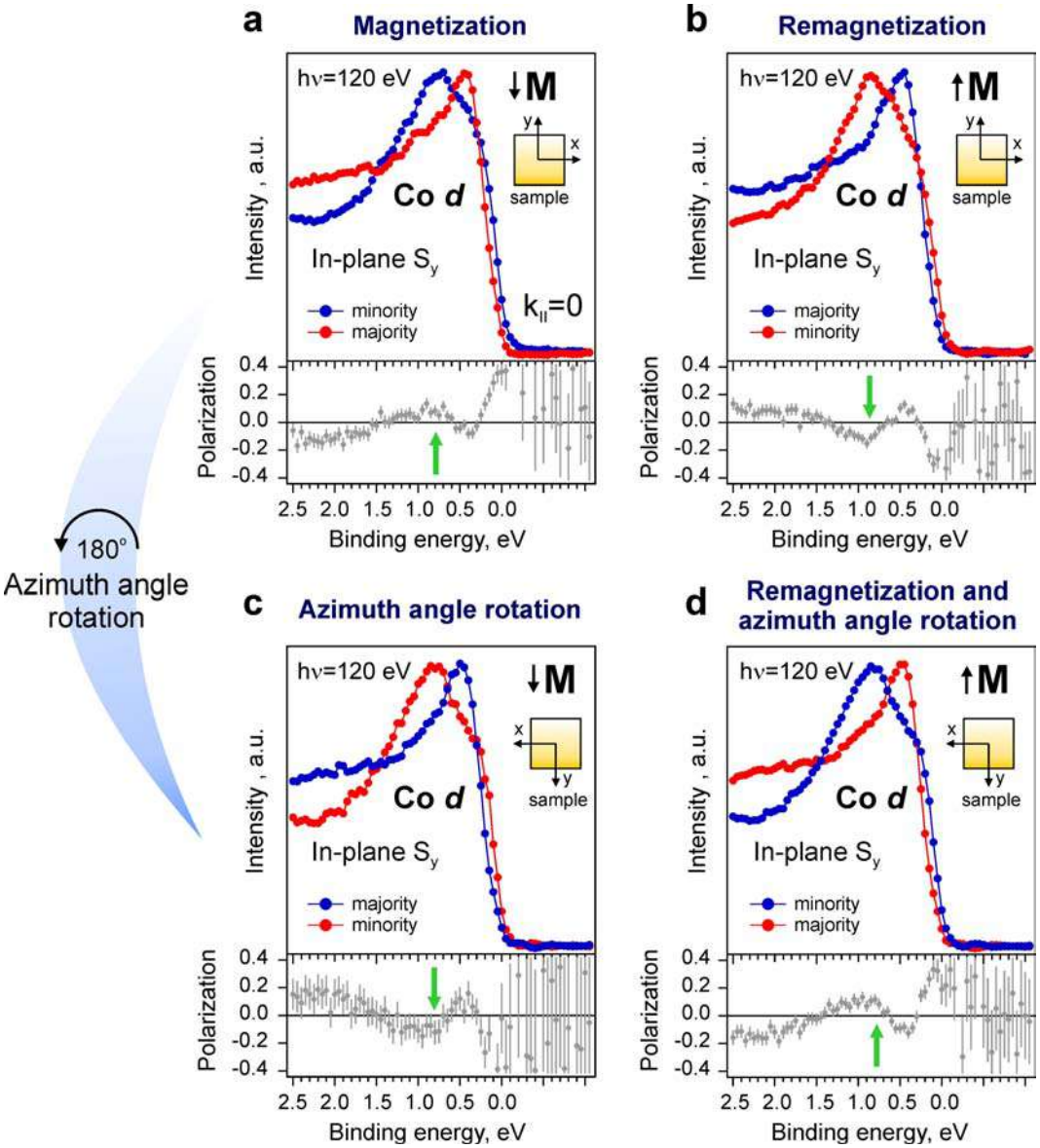

Figure 7.5 — Spin-ARPES spectra of the Co *d* band with spin resolution for two experimental geometries. (a, b) Co *d* band spectra in normal emission geometry for Gr/Au/Co(0001) after magnetization and remagnetization, respectively. (c, d) The same spectra but measured after rotating the sample by 180° in azimuthal angle. (a,c) are measured after M↓ magnetization, and (b,d) – after M↑ remagnetization. The photon energy is 120 eV.

We note once again that the measurements at the $\overline{\mathrm{K}}$ and $\overline{\mathrm{K}}'$ points of the Brillouin zone of graphene were carried out by rotating the azimuthal angle by 180°, as shown in the insets to Fig. 7.3 (c-g). The Co d band spectra at normal emission (see Fig. 7.5) show that a rotation of the azimuthal angle by 180° is equivalent to remagnetization. The majority and minority Co bands change places when the sample is remagnetized (see the transitions in Fig. 7.5 (a) $\rightarrow$ (b) and Fig. 7.5 (c) $\rightarrow$ (d)) in the same way as when the sample is rotated by an azimuthal angle of 180° (see the transitions in Fig. 7.5 (a) $\rightarrow$ (c) and Fig. 7.5 (b) $\rightarrow$ (d)).

In order to check that the observed effect of spin splitting asymmetry is not related to the summation of the signal in spin-ARPES data from spin-split states of graphene and spin-polarized Co states (at the points $\overline{\mathrm{K}}$ and $\overline{\mathrm{K}}'$, see Fig. 7.1 (e,f)), we simulated this situation. By summing the intensities of the spin-split states of graphene and the spin-polarized d states of Co, a certain degree of splitting asymmetry was found in the total intensity spectra, 70 and 120 meV for the $\overline{\mathrm{K}}'$ and $\overline{\mathrm{K}}$ points, respectively. However, this degree of asymmetry is very far from the measured values shown in both Figs. 7.1 (e,f) ($\sim$ 0 and 150 $\pm$ 20 meV) and 7.3 (40 and 200 $\pm$ 40 meV). Therefore, the asymmetric splitting cannot be explained by a simple summation of the signal from the Co and graphene states, and the coexistence of the Rashba effect and exchange splitting in graphene is necessary to explain this phenomenon.

7.1.3 Exchange field transfer mechanism

DFT calculations were performed to explain the experimental data of spin splitting asymmetry. If we neglect the formation of the Au-Co surface alloy at the interface, the joint effect of the combination of spin-orbit and exchange interactions turns out to be negligible. In fact, the inability of the theoretical flat-layer model to describe the induced spin-orbit and exchange interactions may indicate a more complex crystal structure of the synthesized sample. Therefore, prior to the theoretical analysis, additional atomic structure measurements by STM were performed. It was found that the STM images depend significantly on the bias voltage V_t. As shown in Fig. 7.6 (b), the well-known moiré structure of Au-intercalated graphene is observed

at V_t = 2 mV [12; 149; 523]. However, if the bias voltage is increased, for example, to 5 mV, a peculiar periodic pattern of triangular-shaped elements begins to appear (Fig. 7.6 (a)). Using an intermediate value of V_t equal to 3 mV, both moiré and triangular patterns can be obtained in the same image – the lower and upper parts of Fig. 7.6 (c). Figure 7.6 (d) shows a well-resolved STM image of the triangular-shaped element structure obtained at V_t = 10 mV and I_t = 0.4 nA. The period of the structure is $\sim$ 24 – 26 Å, as shown in the profile in Fig. 7.6 (e), which corresponds to the superstructure $p(10 \times 10)$ determined using the LEED method (Fig. 7.1 (a)). Such STM results were obtained at scales up to 100×100 nm^2. Note that a change in the applied bias voltage from 2 to 10 mV is accompanied by a large (up to 3.5 Å) change in the probe-sample distance s, which confirms the change in the structural appearance of the STM images shown in Fig. 7.6. Only when using sufficiently large values of s (i.e., sufficiently large values of V) a triangular network of dislocations is observed, although the exact threshold value of V_t for its observation is rather low, only a few mV. The physical explanation for these observations is that the Au/Co(0001) states close to the Fermi level have a larger spatial extent perpendicular to the surface than the graphene states, and hence only at sufficiently large distances between the probe and the sample the triangular dislocation network is best measured with minimal influence of the graphene states. Indeed, Fig. 7.6 (d) shows the best resolution for the triangular dislocation network of the Gr/Au/Co(0001) system in the STM image obtained at 10 mV, i.e., at the largest probe-sample distance, with a rather blurred graphene structure on top of the Au-Co structure. At $V_t = 5$ meV, enlarging the STM image between the triangles allows the hexagonal lattice of graphene to be resolved (Fig. 7.6 (f)).

Here it is worth noting that the observed moiré pattern indicates that the superstructure $p(10 \times 10)$ practically does not break the A – B symmetry of graphene, since the two sublattices are indistinguishable. This fact, together with the above-described absence of the ARPES signal from π states of graphene in the second Brillouin zone, indicates the absence of a band gap at the Dirac point of any origin. In this case, the Au-intercalated graphene on Co(0001) has a quasi-freestanding character.

To the best of our knowledge, triangular-shaped structural defects for Au-intercalated graphene have not been discussed in the literature so far. Similar structures have been previously detected by STM method for Au submonolayer on Ni(111) with periodicity $p(9.7 \times 9.7)$ and were named “loop mismatch

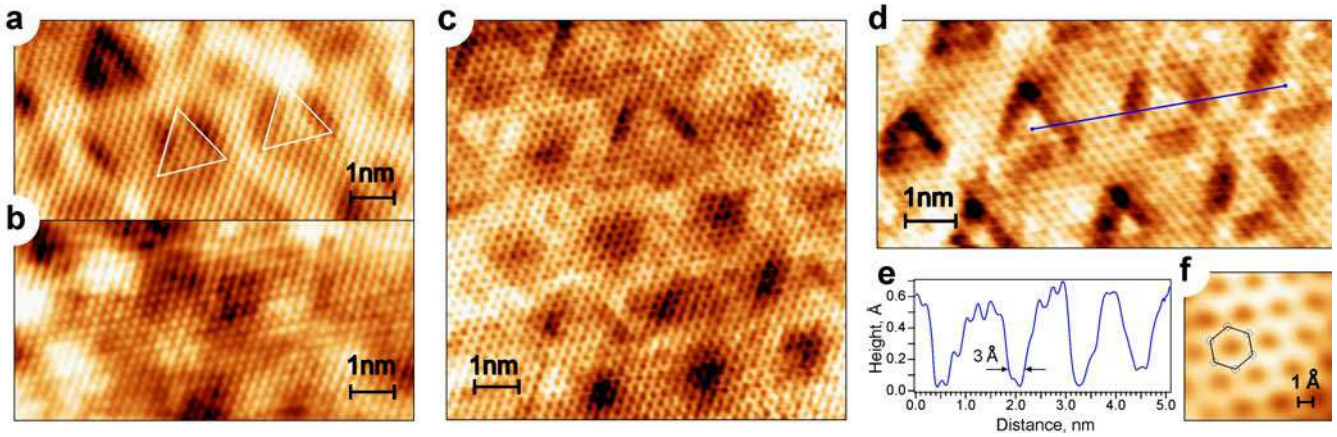

Figure 7.6 — STM studies of Gr/Au/Co(0001) atomic structure. (a,b) STM images of 9×4.5 nm^2 obtained for the same region using different bias voltages V_t: $V_t = 5$ mV, $I_t = 0.43$ nA (a) and $V_t = 2$ mV, $I_t = 0.43$ nA (b). (c) STM image of 9×9 nm^2 obtained at $V_t = 3$ mV and $I_t = 0.4$ nA. (d,e) STM image of 9.42×4.5 nm^2 periodic triangular structure ($V_t = 10$ mV and $I_t = 0.4$ nA) with profile taken along the blue line. (f) STM image of 1×1 nm^2 with atomic resolution ($V_t = 5$ mV and $I_t = 0.4$ nA).

dislocations' [530]. It was found that a periodic grid of triangles, reflecting the structure at the Au-Ni(111) interface, appears due to strain removal. In this case, the formation of each triangle requires the squeezing out of several atoms from the Ni interface layer, which appear to be incorporated into the upper Au layer, apparently either as isolated monomers or as clusters consisting of several atoms [530]. It was found that the number of Ni atoms removed from the surface layer to form underlying loop dislocations is equal to the number of Ni atoms incorporated into the Au layer. Returning to the graphene/Au/Co system, we find that it shares several similarities with the Au/Ni(111) system. First, the Co(0001) and Ni(111) surfaces have hexagonal structure and close lattice parameters. Second, as evidenced by STM, the periodicities of the superstructures are very close: $p(10 \times 10)$ and $p(9.7 \times 9.7)$, respectively. A similar periodic network of triangles is observed for both systems. Of course, there is a fundamental difference between these systems: the presence of a graphene layer on top of Au/Co(0001). Taken together, these facts indicate that the Au/Co(0001) interface under graphene is the same as the interface formed in Au/Ni(111) without graphene [530], which, in particular, means the presence of cobalt atoms incorporated in the Au layer. Unfortunately, the XPS analysis did not reveal any noticeable energy shift (more than 0.1 eV) of the Co $2p$ core level after Au intercalation. A similar situation at the Au/Co interface is described in [531; 532]. As for the valence band states, the d peak of Co measured at normal emission broadens

after Au intercalation, which can be explained by hybridization between the layers, while no observable energy shift of the peak is observed. Note that the absence of energy shifts of the Co core level and valence band states during Au intercalation (at least within the experimental resolution) does not exclude the presence of a certain number of Co atoms in the Au layer, as explained above using the example of the triangular mismatch dislocation model [530].

To confirm that such an asymmetry of the π state splitting can indeed be a consequence of the joint action of the exchange field and the Rashba spin-orbit interaction, a DFT calculation with magnetic moment constraints on carbon atoms was performed. Figure 7.7 (a,b) shows the calculated in $\overline{\mathrm{K}}$ and $\overline{\mathrm{K}}'$ valleys band structure of graphene with spin-orbit interaction only (i.e., for zero exchange field). In this case, a Rashba-type spin splitting is expectedly found for the Dirac cone [152], with the Rashba parameter λ_R equal to 57 meV. Then, if we introduce an exchange field parallel to the $+k_y$ direction, thereby fixing a magnetic moment $\sim$ 0.002 μ_B on each carbon atom (inside the Wigner-Seitz sphere), the exchange splitting of the Dirac cone is $\sim$ 140 meV, the asymmetric splitting is observed along the k_x direction in good agreement with experiment, reaching a giant value of 175 meV near $\overline{\mathrm{K}}'$ along $\overline{\Gamma}\,\overline{\mathrm{K}}'$ (Fig. 7.7 (c)), and only 53 meV near the $\overline{\mathrm{K}}$ point along the $\overline{\Gamma}\,\overline{\mathrm{K}}$ (Fig. 7.7 (d)). On the other hand, a giant (moderate) splitting along the $\overline{\Gamma}\,\overline{\mathrm{K}}$ ($\overline{\Gamma}\,\overline{\mathrm{K}}'$) direction is observed upon remagnetization (Fig. 7.7 (e,f)). The band dispersion of π states shown in Fig. 7.7 is in qualitative agreement with that obtained in the calculations within the model Hamiltonian [454]. Note that although the graphene dispersion has local band gaps at the $\overline{\mathrm{K}}$ and $\overline{\mathrm{K}}'$ points, the fundamental band gap between the π and π^* bands is absent.

It should also be noted that the choice of the graphene adsorption height of 2.65 Å and the magnetic moment value of 0.002 μ_B per C atom provides calculated splitting values that are in the best agreement with the experimental ones. This adsorption distance can be interpreted as the average graphene-Au distance considering the corrugation shown in Fig. 7.6 (d,e). It is expected to provide hybridization of Co $3d$ and C $2p$ states leading to magnetization of graphene. We would also like to note that a magnetic moment of only $\sim$ 0.002 μ_B per carbon atom is required to achieve a giant splitting of 175 meV. This value is an order of magnitude smaller than that induced on C atoms in graphene/Co (i.e., without Au). Taking into account that under the graphene is located intercalated Au layer, such magnetization value of carbon looks quite realistic, although at first glance suggests

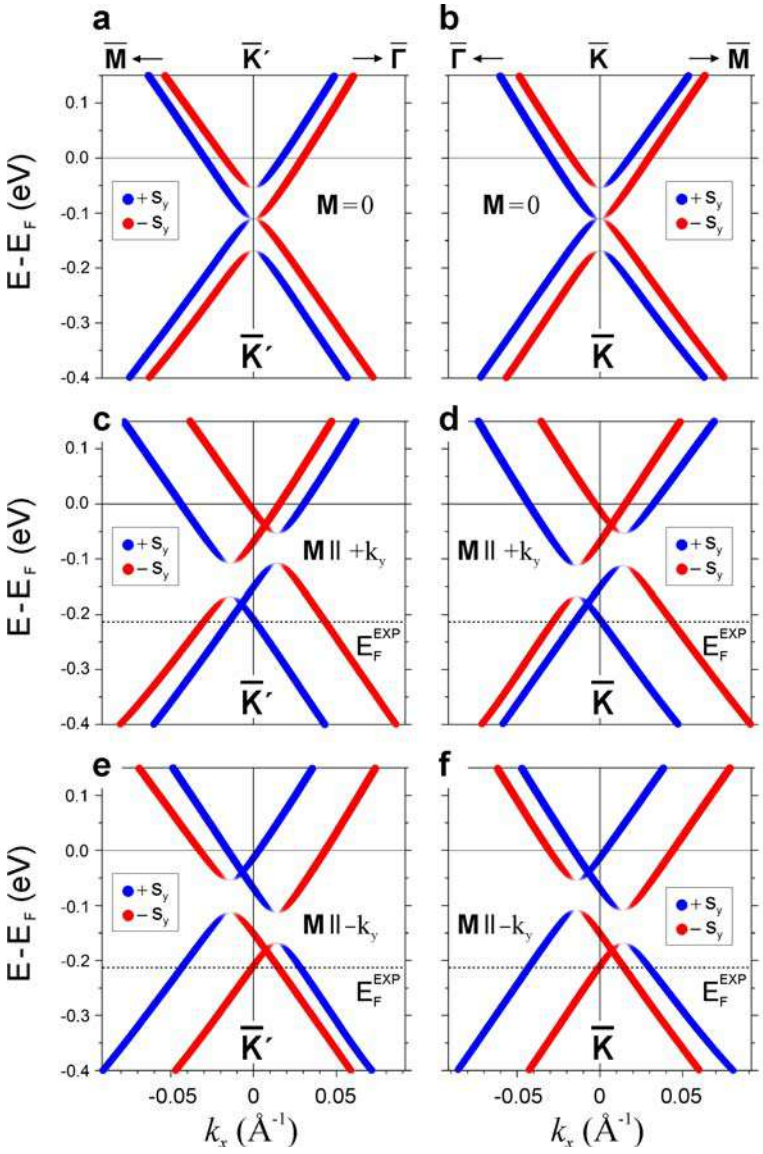

Figure 7.7 — First-principles characterization of π band graphene dispersions in the Gr/Au system in the presence of Rashba spin-orbit interaction and exchange field in the surface plane. (a-f) Spin- and valley-resolved band structure of graphene without (a,b) and with (c-f) confinement of magnetic moments on carbon atoms. The magnetization vector is directed along $+k_y$ ($-k_y$) on c,d (e,f). The left and right panels show the graphene bands in the $\overline{\mathrm{K}}'$ and $\overline{\mathrm{K}}$ valleys. The thickness of the colored lines and the degree of their transparency reflect the modulus of the $\pm s_y$ spin projections. Theoretical studies were carried out by M. M. Otrokov.

mainly ferromagnetic alignment of local moments of Co atoms included in the Au layer.

7.2 Ferrimagnetic graphene (n-graphene)

In the previous section, we detailed the electronic and atomic structures of magneto-spin-orbit graphene synthesized on Au/Co surface with loop dislocations. It was shown that the exchange interaction in graphene with giant Rashba splitting leads to asymmetry of spin splitting at opposite $\bar{\mathrm{K}}$ and $\bar{\mathrm{K}}'$ points of the Brillouin zone of graphene. The observation of giant Rashba splitting in Au/Co graphene agrees well with previous experiments [12; 14; 150], but contradicts DFT calculations, the results of which are presented in published articles [154—156]. On the other hand, the giant Rashba effect is confirmed by DFT calculations of the Gr/Ni system with intercalated Au clusters [466] and tight binding method calculations [467]. In [154—156] it was concluded that significant spin splittings become giant ($\sim$ 60 – 100 meV) only near the band gaps formed as a result of the avoided-crossing effect of dispersions. The authors of the work [156] state that the experimental values of spin splitting can be determined by the magnetic interaction with the metal surface rather than by the spin-orbit interaction. The reasons for the inconsistencies between the theoretical and experimental results may be structural differences in the synthesized and model systems and the additional influence of phonon oscillations on the spin-orbit interaction in graphene [112; 533].

In this section, we address the long-standing problem of giant spin-orbit and exchange splittings in graphene, related to the need for DFT calculations of large-scale structures (including mismatch dislocations) to correctly describe the magnetization of graphene and explain experimental data. Magneto-spin-orbit graphene has been investigated using DFT applied to large-dimensional unit cells and spin-ARPES to understand the mechanism of exchange field transfer to graphene at van der Waals distances. We will also discuss the role that loop dislocations would play in exchange field transfer and sublattice ferrimagnetism in a hexagonal lattice.

First, we turn to the experimental characterization of fully intercalated graphene using low-energy electron diffraction and spin-ARPES measurements. Figure 7.8 (b)

shows the LEED pattern with superstructure periodicity $\sim$ (9×9) and diffraction reflexes up to the second order. As we have found, the Au monolayer forms a surface alloy with Ni or Co to form loop dislocations with lateral periodicity (9-10)×(9-10) [534; 535]. Figure 7.8 (a,c) plots the ARPES intensity maps in the $\bar{\Gamma}\bar{\mathrm{K}}$ direction of the surface Brillouin zone. The following characteristic features were found: the opening of the band gap ($\mathrm{E_g}$) of 80 $\pm$ 25 meV (Fig. 7.8 (c,d)) and the asymmetric spin splitting of the π band near the $\bar{\mathrm{K}}$ point for opposite magnetization directions. The spin splitting is shown by the blue and red arrows in Fig. 7.8 (e) and is 40 $\pm$ 10 and 80 $\pm$ 10 meV for the "up" and "down" directions of cobalt magnetization, respectively. The magnetization is perpendicular to the $\bar{\Gamma}\bar{\mathrm{K}}$ direction (along the k_y axis). Changing the magnetization direction by rotating the sample by 180° around the surface normal is equivalent to remagnetizing the sample and hence measuring in opposite $\bar{\mathrm{K}}$ and $\bar{\mathrm{K}}'$ valleys. In this case, the magnetization of the cobalt layer remains constant, only its direction in the surface plane is reversed. The asymmetric picture of spin splitting with the same sign of spin polarization (Fig. 7.8 (e)) suggests that spin-orbit splitting dominates over exchange one [536]. Otherwise, the polarization curve would change sign for π states, as well as for Co d states with changing magnetization.

To explain the obtained asymmetry of spin splitting, DFT calculations were performed for a large unit cell Gr(9×9)/Au(8×8). Figure 7.9 shows the structural relaxation result of the unit cell with five missing atoms in the Co layer, which is consistent with the scanning tunnelling microscopy data shown in the inset to Fig. 7.9 (c). Structural relaxation results in the formation of a mismatch dislocation at the Au-Co boundary with displacement of Au atoms toward the Co layer at the corners of the triangular dislocation, as in the case of Au on Ni(111) [534; 535]. Band structure calculations for this relaxed unit cell, shown in Fig. 7.10 (a), reveal the formation of a band gap $\mathrm{E_g}$ around 60 meV at the Dirac point. Comparing the spin splitting near the $\bar{\mathrm{K}}$ and $\bar{\mathrm{K}}'$ points, we can see the asymmetry of the spin splitting (23 meV vs. 38 meV at a binding energy of 0.5 eV). However, it is smaller than that obtained in the experiment, indicating a smaller spin-orbit contribution to the spin splitting in the calculation. The value of spin-orbit splitting $\sim$ 7.5 meV estimated from the calculation results agrees with previously published values at the equilibrium distance between graphene and Au $\sim$ 3.3 – 3.5 Å [12; 154; 156]. In Fig. 7.8 (e), it can be observed that the spin polarization of π states is not reversed when the magnetization is changed in the experiment. In this case, the spin-orbit splitting is

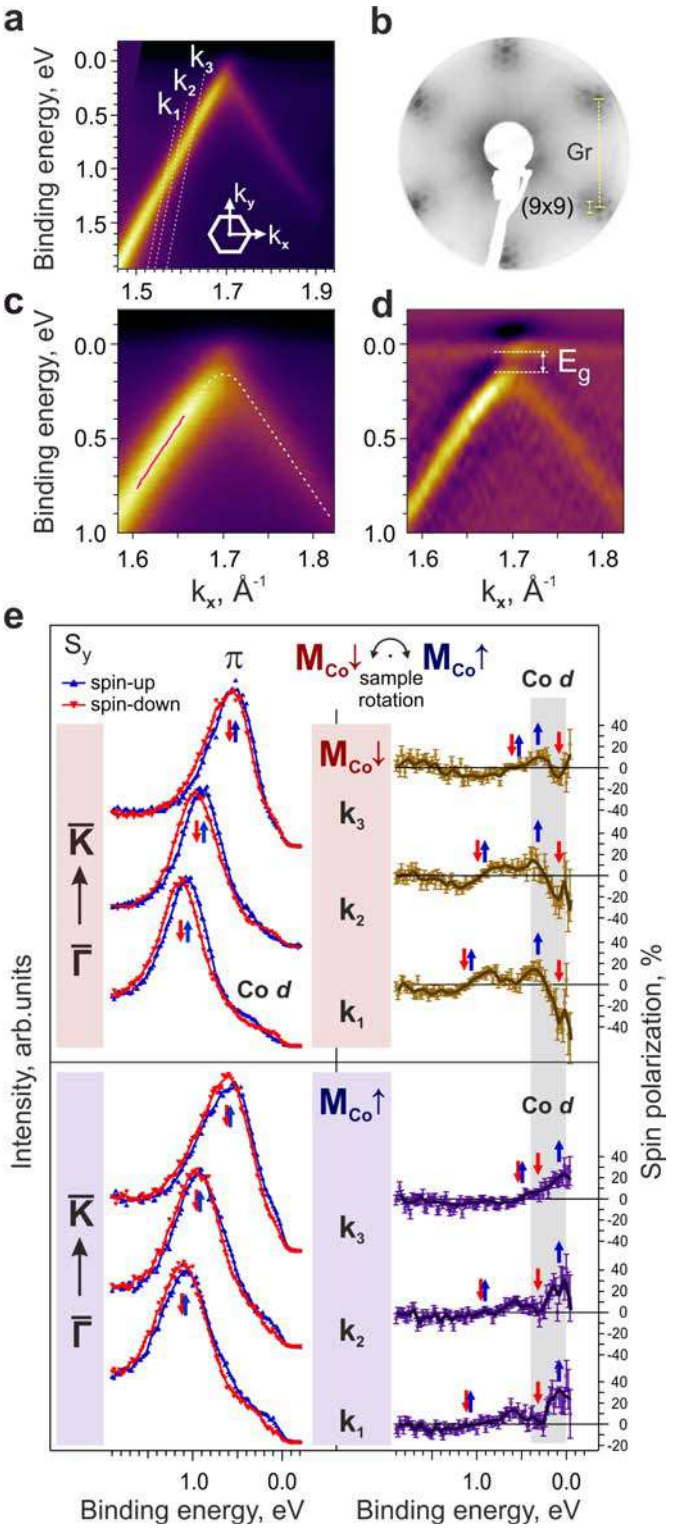

Figure 7.8 — (a) ARPES intensity map for the π band, including the enlarged map (c) and its second energy derivative (d). The solid red line shows the result of approximation of quasi-wave vector distribution curves by two peaks with Lorentz functions. (b) LEED pattern of the epitaxial graphene superlattice ∼ (9×9) formed at the Au/Co(0001) interface. (e) Spin-ARPES spectra (with spin polarization on the right) of Gr/Au/Co(0001)/W(110) system measured at k_1, k_2, and k_3 quasi-wave vector values marked in panel (a), and for opposite magnetization directions obtained by rotating the sample by 180°. The photon energy is 21.2 eV.

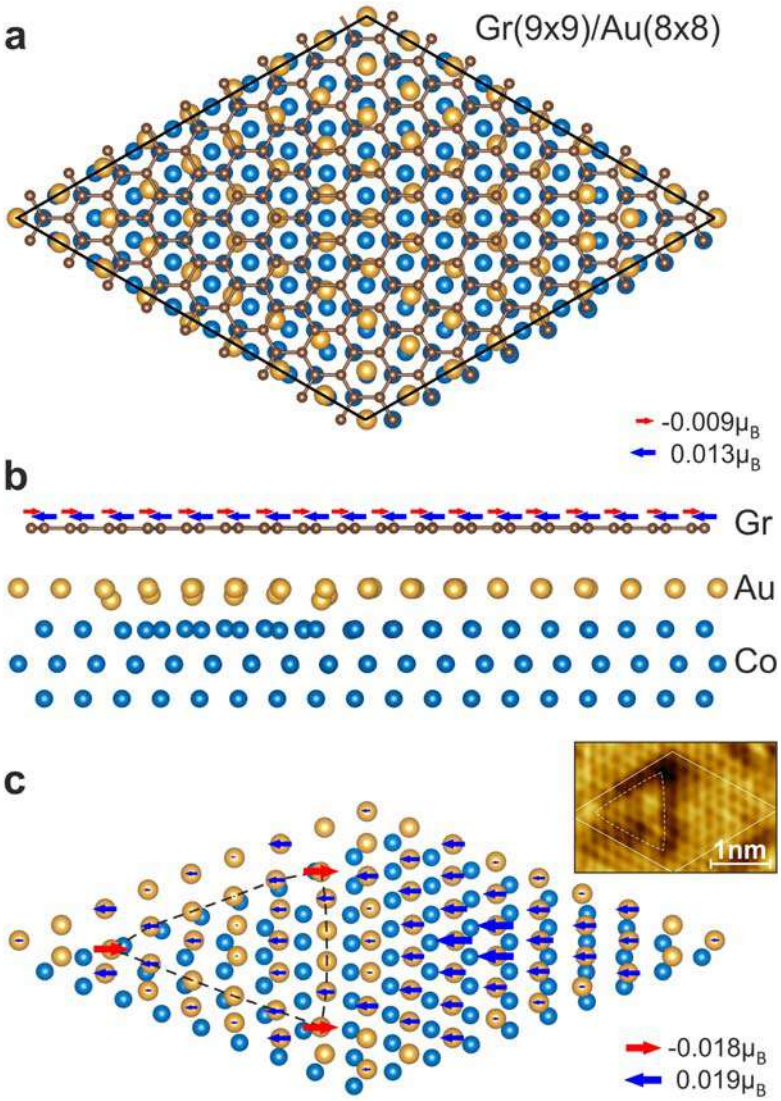

Figure 7.9 — Relaxed unit cell of Gr/Au/Co structure with loop dislocation: top view (a), side view (b) and isometric view of the Au-Co loop dislocation under graphene (c). The loop dislocation is marked with a dashed line in panel (c) and in the STM image in the inset. The sizes of the arrows are proportional to the values of the atomic magnetic moments on the gold and carbon atoms. The legends include arrows indicating the maximum magnetic moments in two opposite directions for graphene and the Au-Co loop dislocation. The direction of magnetization of the Co layer is to the right.

about 60 ± 10 meV and the exchange splitting is about 20 ± 10 meV. One of the reasons for the underestimation of spin-orbit splitting in the calculation results may be spin-orbit splitting due to electron-phonon interactions [112; 533].

Surprisingly, ferrimagnetic (FIM) ordering is observed in graphene and Au layers (the calculated atomic magnetic moments are shown by blue and red arrows

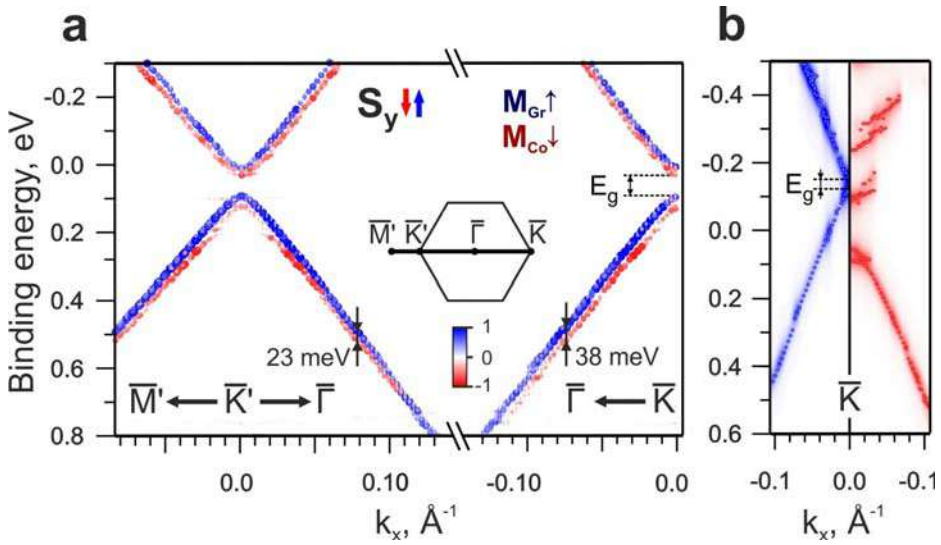

Figure 7.10 — (a) The unfolded (9×9) Gr/Au/Co band structure near the opposite $\bar{K}'$ and $\bar{K}$ points. The size and color of the symbols represent the Bloch spectral weight for the spin component S_y. (b) The unfolded (9×9) band structure of graphene/Au/Co without dislocation loop. Spectral weights were used for ARPES simulation in which the bands were broadened using a Lorentz function with a half-width of 0.02 eV. In both calculations, the cobalt layer was magnetized in a plane perpendicular to the $\bar{\Gamma}\bar{K}(\bar{K}')$ direction. M_{Gr} ↑ and M_{Co} ↓ denote the magnetization directions of the graphene and cobalt layers, respectively.

in Fig. 7.9). Despite the difference in the magnitude of the magnetic moments on the gold atoms, the atomic magnetic moments on the graphene sublattices have a uniform distribution with an accuracy of 0.001 μ_B.

To provide further evidence for the ferrimagnetic nature of the band gap and the relationship between FIM ordering and the dislocation loop structure, DFT calculations were performed for a unit cell (9×9) but without the dislocation loop (Fig. 7.10 (b)). The unit cell was constructed based on the original cell with a Gr-Au distance of 3.36 Å. In this case, the band gap at the Dirac point (see spin-↑ states of graphene) is about half of that for the structure with dislocation loops due to the suppression of sublattice ferrimagnetism (the magnetic moments on graphene atoms of A and B sublattices have the same sign and are close to 0.002 and 0.007 μ_B). At the same time, strong hybridization is observed for the states of graphene and cobalt with spin-↓ in the Dirac point region. Such hybridization between graphene and cobalt states was previously observed for the unit cell (2×2) of Gr/Au/Co [4]. The calculation of the band structure of graphene with the distance between graphene and gold monolayer reduced by 0.2 Å from the equilibrium distance also confirms

the magnetic nature of the band gap. In this case, the values of magnetic moments on graphene atoms decrease by two orders of magnitude and the band gap is closed.

In order to better understand the band structure of ferrimagnetic graphene, the antiferromagnetic (AFM), ferrimagnetic (FIM) and ferromagnetic (FM) states have been calculated with a tight binding model in graphene using DFT results. The effective Hamiltonian can be written in the form:

$$H = -t \sum_{\langle i,j\rangle\alpha} (\hat{c}^{\dagger}_{i\alpha}\hat{c}_{j\alpha} + h.c.) + U \sum_{i} (\hat{n}_{i\uparrow}n_{i\downarrow} + \hat{n}_{i\downarrow}n_{i\uparrow}) + \\ it_R \sum_{\langle i,j\rangle\alpha,\alpha'} (\hat{c}^{\dagger}_{i\alpha} \left[\boldsymbol{\sigma}^{s}_{\alpha,\alpha'} \times \tilde{\mathbf{d}}_{ij}\right]_z \hat{c}_{j\alpha'} - h.c.), \tag{7.1}$$

where *i, j* denote nearest neighbour sites in sublattice A(B), the fermionic operator $\hat{c}^{\dagger}_{i\alpha}$ ($\hat{c}_{i\alpha}$) creates (annihilates) electron at the *i* site with spin α ($\uparrow, \downarrow$), and the same for the *j* site, *t* is the hopping parameter, *U* is the repulsion force of electrons at the site simulating the exchange interaction with the substrate, $\hat{n}_{i\alpha}$ is the spin density operator ($\hat{n}_{i\alpha} = \hat{c}^{\dagger}_{i\alpha}\hat{c}_{i\alpha}$) and $n_{i\alpha}$ is the mean-field occupation number, t_R is the Rashba spin-orbit interaction constant, where $\mathbf{d}_{ij}$ is the lattice vector pointing from site j to site i ($\tilde{\mathbf{d}}_{ij}$ is the corresponding unit vector), and $\boldsymbol{\sigma}^{s}$ is the vector of Pauli matrices.

With the model Hamiltonian, three cases of graphene magnetization are possible, as shown in Fig. 7.11: AFM, FIM, and FM. Obviously, AFM ordering leads to the opening of the band gap. On the other hand, the presence of non-zero magnetization of graphene in the FIM phase leads to a decrease in the size of the gap, which is completely closed in the FM phase, but exchange splitting increases with increasing magnetization. The main difference between AFM and FIM phases with Rashba interaction is related to the absence or presence of spin splitting asymmetry near $\bar{\mathrm{K}}(\bar{\mathrm{K}}')$ points. Figure 7.11 (d) shows the results of the tight binding method calculations with weak and strong Rashba interactions, which are in best agreement with the DFT and experimental results. Thus, we have competing contributions from the Rashba interaction and the exchange interaction leading to an asymmetry of the spin splitting with respect to the $\bar{\Gamma}$ point.

Using the tight binding Hamiltonian with selected parameters, we calculated the Berry curvatures and Chern numbers for the magnetization in the surface plane to analyze the possibility of realizing the Hall effects [6]. Although the Chern numbers are zero, the Berry curvatures for all bands have a dipole structure and opposite signs for the valleys $\bar{\mathrm{K}}$ and $\bar{\mathrm{K}}'$. The calculation of the Hall conductivity (Fig. 7.11 (e)) taking into account the probability of optical transitions showed the presence of a

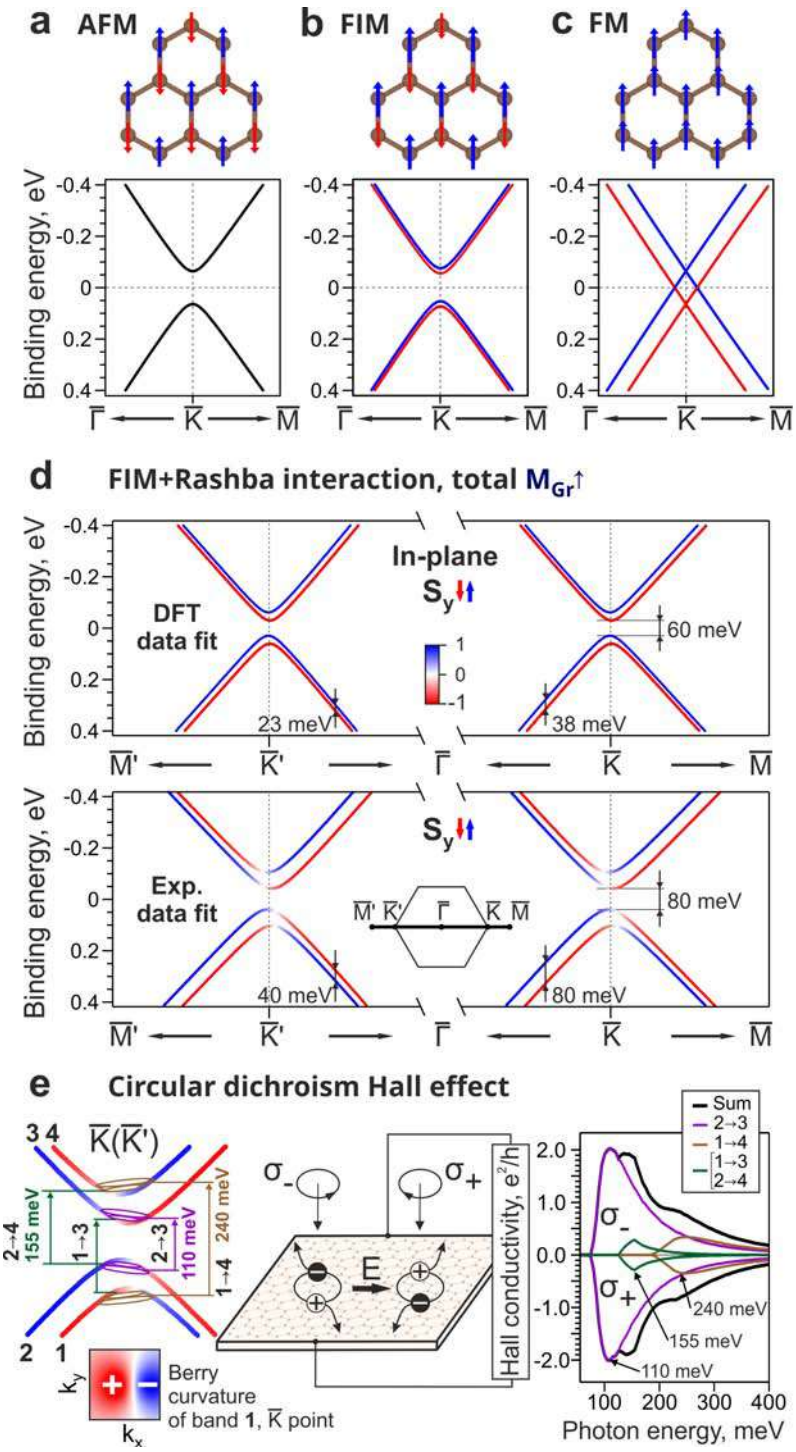

Figure 7.11 — Band structures calculated near $\bar{\mathrm{K}}$ ($\bar{\mathrm{K}}'$) points using the model Hamiltonian for different graphene magnetizations and without considering the spin-orbit interaction: AFM (a), FIM (b), and FM (c). Panel (d) shows the FIM case with Rashba interaction, corresponding to the DFT and experimental data. (e) Schematic illustration of the circular dichroism Hall effect with left (σ_-) and right ($\sigma+$) polarizations of light. The maxima on the Hall conductivity curve are observed due to the inclusion of new interband transitions with increasing photon energy. A rectangular shape with $\Delta E/\hbar\omega = 10\%$ was used for the model power spectral density curve. The calculations were performed by A.V. Eryzhenkov.

stable Hall effect when using light with circular polarization. This phenomenon is related to the presence of the dipole structure of Berry curvatures near the $\bar{\mathrm{K}}(\bar{\mathrm{K}}')$ points and non-equilibrium photoexcitation in these regions.

Thus, we have shown the existence of ferrimagnetic ordering in n-graphene on Au/Co surface with loop dislocations and with homogeneous magnetization on graphene sublattices. Such magnetic ordering of the system is found to lead to the appearance of a band gap in $\bar{\mathrm{K}}$ and $\bar{\mathrm{K}}'$ points of graphene and asymmetry of its spin structure. The results of tight binding calculations are in good agreement with the spin-ARPES data, showing that the circular dichroism Hall effect can be realized.

7.2.1 Role of loop dislocations in the formation of ferrimagnetism in graphene

This paragraph presents the study of the stability of ferrimagnetic ordering on graphene sublattices located on Au/Co(0001) in relation to possible structural changes in the real system: the formation of loop dislocations of different sizes under the graphene and the appearance of additional cobalt and gold atoms near the graphene. The necessity of investigating this subject is supported by the results of L. P. Nielsen dissertation work [537], which discusses the presence of nickel atoms on the surface alloy displaced from the top atomic layer of nickel during alloying and demonstrates the formation of loop dislocations of different sizes for a monolayer of Au on Ni(111). On the other hand, articles [18; 466] reported the presence of surface phases with gold clusters under graphene and residual gold clusters on the graphene surface after intercalation, which can affect the electronic structure of graphene. Thus, studying the role of structural differences of the synthesized system from the model system is an urgent task.

Figure 7.12 (a) shows the LEED pattern with periodicity of the superstructure $\sim (9 \times 9)$. It is well known that monolayers of noble metals (Ag, Au) alloy with transition metals (Ni, Co, Cu) to form triangular-shaped loop dislocations [4; 535; 537; 538]. The size of a single dislocation depends on the number of displaced atoms from the transition metal interface layer during its formation [535; 537]. As can be seen in Fig. 7.12 (b), the loop dislocations formed under graphene are periodic over fairly

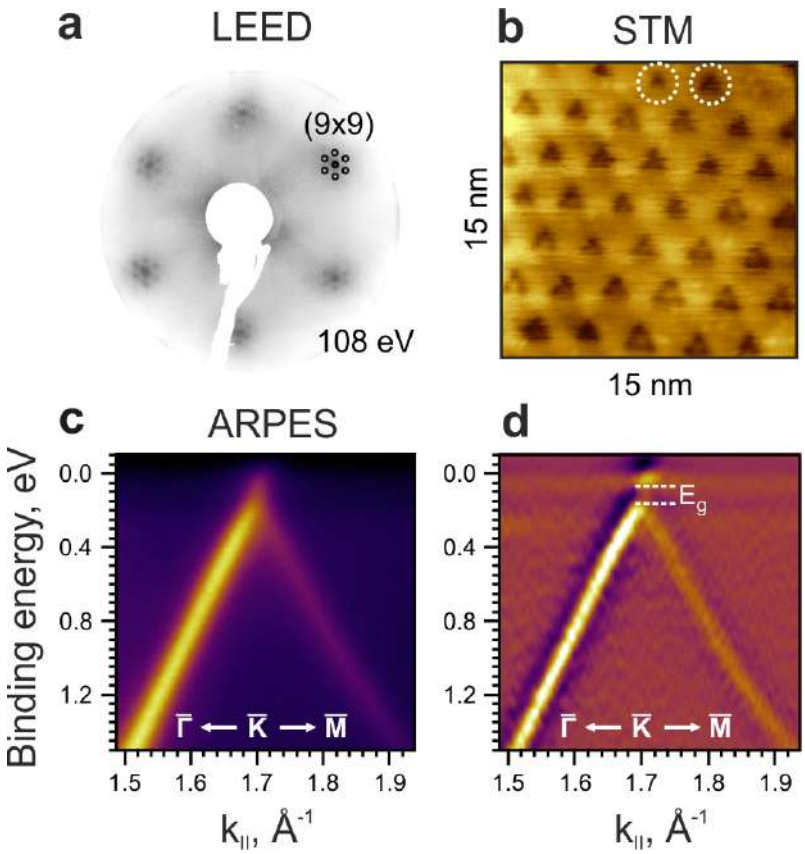

Figure 7.12 — (a) LEED pattern of the Gr/Au/Co/W(110) system. (b) Scanning tunnelling microscopy image of the surface. Loop dislocations of different sizes are marked by circles with dotted lines. (c) ARPES map in the $\bar{\Gamma}\bar{K}\bar{M}$ direction of the Brillouin zone and (d) its second derivative with respect to energy.

large areas of the sample, but can be of two sizes, with one and three gold atoms in the center of the loop dislocation. As in [537], loop dislocations with three gold atoms in their center are the most frequently observed dislocations on the surface. Figures 7.12 (c,d) show the ARPES intensity maps in the $\bar{\Gamma}\bar{K}$ direction of the surface Brillouin zone. It can be observed that E_g band gap is observed in the electronic structure of the Dirac cone of graphene. In order to investigate the electronic structure of graphene and analyze the magnitude of the band gap, theoretical calculations have been carried out.

DFT calculations of the electronic structure of the Gr/Au/Co(0001) system, with period (9×9) and containing loop dislocations, have shown that graphene is characterized by ferrimagnetic order on A and B sublattices. The computational results are presented in Fig. 7.13. During structural optimization, the node gold atoms in the dislocation are displaced closer to the cobalt layer, and their magnetic moments appear to be co-directed with the magnetization of the cobalt layer. Most of the remaining gold atoms around the perimeter of the cell and in its right part are magnetized against the magnetic moments of the cobalt atoms. In the cell without a loop dislocation,

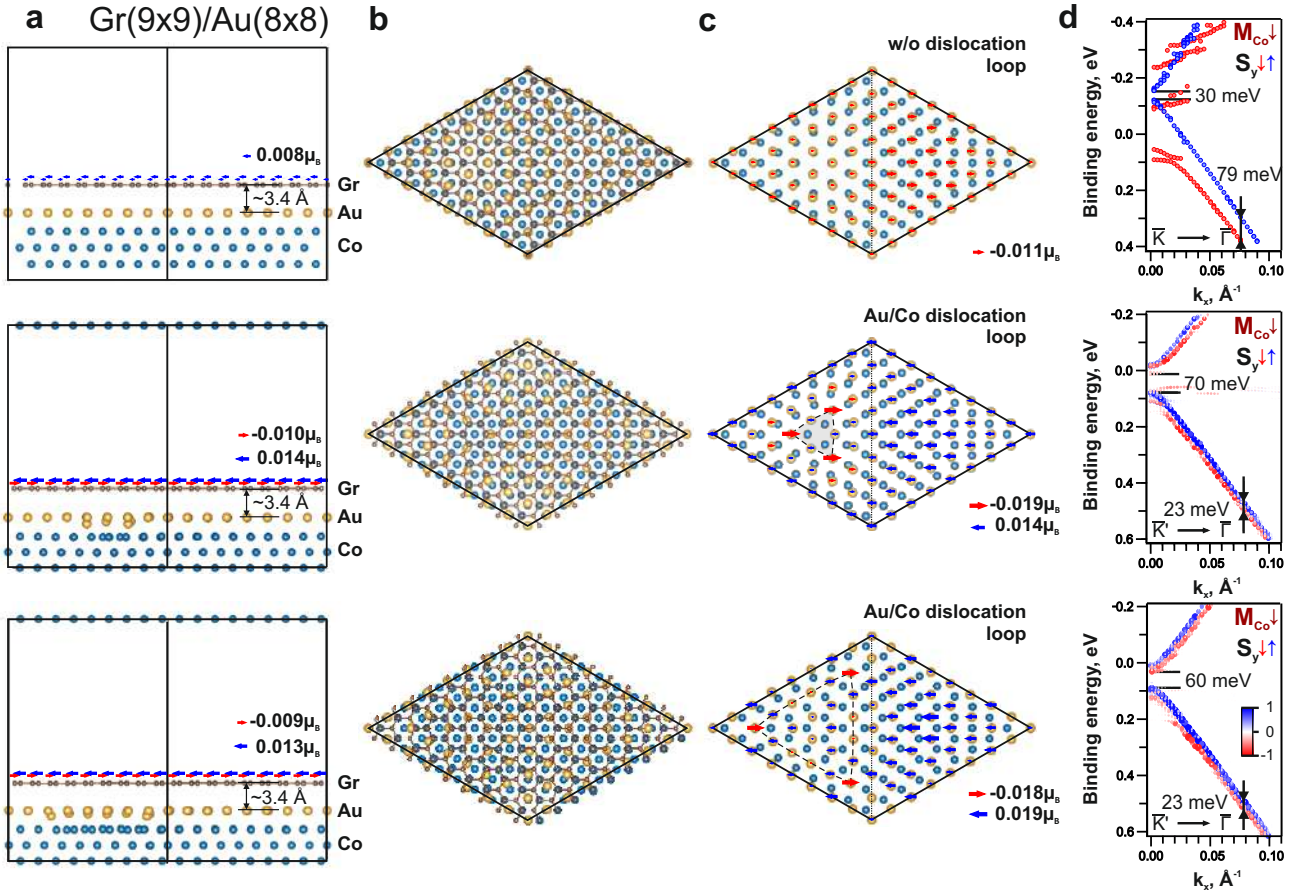

Figure 7.13 — Unit cells of the Gr(9×9)/Au(8×8)/Co(0001) system without loop dislocation and with loop dislocations of different sizes: (a) side view, (b) top view, and (c) view of the Au-Co interface under graphene. (d) The corresponding unfolded (9×9) electronic structure in the vicinity of $\bar{\mathrm{K}}$ and $\bar{\mathrm{K}}'$ points. The size and color of the symbols show the Bloch spectral weight for the S_y spin component.

based on a structurally optimized cell with a loop dislocation with Gr-Au distance of 3.4 Å, no ferrimagnetic ordering is observed in the gold layer (Fig. 7.13 (c)). In this case, all the gold atoms have magnetic moments co-directed with the magnetic moments in the cobalt layer. Now, if we consider the magnetic moments on the graphene atoms for the presented cells, we can observe that ferrimagnetic ordering in the graphene layer is present only in the cells with loop dislocations (Fig. 7.13 (a)). As can be seen in Fig. 7.13 (d), ferrimagnetic ordering in graphene leads to a band gap in $\bar{\mathrm{K}}$ points of graphene. In contrast, for the cell without loop dislocation, strong hybridization with d states of cobalt is observed and the band gap is at most 30 meV. The obtained theoretical results are confirmed by spin-ARPES data, according to which the magnitude of the band gap is 80 ± 25 meV (Figs. 7.12 (c) and (d)).

The interface (Au monolayer)/Co(0001) with periodic loop dislocations plays a key role in transferring the exchange interaction to graphene, since it is the presence

of dislocations in the model that fundamentally changes the picture of the electronic structure of graphene, creating a band gap in it due to Hubbard-type interaction and non-equivalence of A and B sublattices.

7.2.2 Model of a graphene-based infrared circularly polarized radiation detector

The problem of detecting circularly polarized radiation is an actual task due to the development of optical technologies, quantum computing and information processing. At the same time, conventional infrared detectors require additional use of polarizers to register polarized radiation, which complicates the design and increases the cost of the device. Therefore, a more efficient way is direct detection of circularly polarized radiation based on materials sensitive to this radiation. There are materials and heterostructures sensitive to radiation with circular polarization. Due to the features of the electronic structure of materials, the incident radiation leads to the occurrence of electrical effects and optoelectric conversion, the registration of which allows the detection of circularly polarized radiation. In this regard, the study and synthesis of such promising materials is of great importance for the purposes of optoelectronics and valleytronics. There are known works on the study of chiral heterostructures based on CoPt, $CuCl_4$, PbI_x perovskites sensitive to circularly polarized radiation in the visible range or near-infrared [539–541]. Also, it is known technical solution [542], in which it is proposed to use materials based on three-dimensional Weyl semimetals to generate photocurrent under circular-polarized irradiation. The disadvantage of using these materials is low sensitivity to radiation in the mid-infrared range.

The method of determining the sign of circular polarization of laser radiation [543] based on the phenomenon of surface circular photovoltaic effect in silver-palladium resistive film is known. This method allows to register the sign of circularly polarized radiation by measuring the photo-EMF in the operating range from ultraviolet (0.25 μm) to mid-infrared (5 μm). The disadvantage of this method is the use of thicker films of expensive precious metals and photosensitivity of

materials mainly in the ultraviolet and visible radiation ranges, poorly affecting the mid-infrared region.

The prospects for the use of two-dimensional material graphene in optoelectronic devices are due to the presence of unique electronic and optical properties. Graphene has high mobility of charge carriers, optical transparency, as well as flexibility, strength and environmental resistance. Because of this, applications of graphene in solar cells, light-emitting devices, touch screens, photodetectors, and ultrafast lasers have been developed to date [544; 545]. For the detection of circularly polarized radiation, a technical solution using graphene is known [546], in which it is proposed to use monolayers of graphene, which are almost transparent to incident radiation, due to which there is an increase in the efficiency of charge carrier transfer from the absorbing SiGe layer. It is also known that other quasi-two-dimensional materials such as black phosphorus (allotropic modification of phosphorus), monolayers of transition metal dichalcogenides of MX_2 type find wide application in mid-infrared optoelectronics [547]. However, the application of graphene as an active element in such devices has so far proved difficult.

Based on the results of the investigations, a device model of the infrared detector of circularly polarized radiation based on n-graphene is proposed. The essence of the proposed device model is illustrated in Fig. 7.11 (e). The theoretically calculated dependence of the transverse Hall conductivity on the photon energy of incident radiation with circular polarization is shown on the right. The upper curve corresponds to the incident radiation with negative circular polarization, and the lower curve corresponds to the incident radiation with positive circular polarization. A rectangular shape with $\delta E/\hbar\omega$ = 10% was chosen for the power spectral density of the incident radiation. The dependence was obtained as a result of calculations by the tight binding method with the choice of parameters to agree with the experimental data. The maxima on the Hall conductivity curve are observed due to the inclusion of new interband transitions with increasing photon energy. The total conductance curve has several extrema and allows the Hall voltage to be recorded over a wide range of mid-infrared radiation. In this case, the polarity of the Hall voltage determines the sign of the prevalent polarization of radiation. Thus, in the claimed device model it will be possible to register the middle range of infrared radiation with wavelengths from 15 μm to 3 μm (radiation energy from 80 meV to 400 meV).

7.2.3 Influence of cobalt and gold adatoms

To analyze the influence of possible structural inhomogeneities on the electronic and spin structure of graphene, DFT calculations were performed for the Gr/Au/Co system with different variants of additional atoms. Let us consider three main cases.

1) A cluster of three cobalt atoms under graphene, which can be formed by the formation of a loop dislocation of minimal size (see Fig. 7.14 (a)).

As can be seen from Fig. 7.14 (b), π states of graphene (marked by dashed lines) are strongly hybridized with d states of cobalt, the Dirac cone appears to be destroyed. At the same time, graphene is magnetized ferromagnetically with respect to the cobalt layer, with magnetic moments on carbon atoms $\sim 0.9\ \mu_B$.

2) Gold adatoms under graphene as a result of excessive intercalation (see Fig. 7.14 (c)).

The electronic structure of graphene for this case is presented in Fig. 7.14 (d). It is found that for this system ferrimagnetism is preserved in the graphene lattice with magnetic moments $\sim 0.010 \div 0.011\ \mu_B$ and $-(0.011 \div 0.012)\ \mu_B$ on the sublattices, an additional gold atom in the cell leads to an increase in the Rashba splitting in the Dirac cone region up to $\sim$ 20 meV. The band gap width is $\sim$ 60 meV and appears as a result of antiferromagnetic interaction in graphene.

It should be noted that the value of the Rashba splitting in this case ($\sim$ 20 meV) is still less than the experimental value ($\sim$ 60 meV). The corrugation of the gold layer under graphene and the contribution of phonon oscillations of graphene can play an important role in explaining the effect of giant Rashba splitting.

3) Gold adatoms on graphene remaining on the surface after intercalation (see Fig. 7.14 (e)).

In this case, no increase in the Rashba splitting near the Fermi level is observed and it is less than 7 meV. In contrast to the previous case, there is no spin inversion with respect to the $\bar{\Gamma}$ point, indicating a dominant contribution of exchange splitting up to $\sim$ 50 meV. At the same time, the ferrimagnetic order is conserved, but the fraction of antiferromagnetic interaction decreases, which leads to a decrease in the band gap width at the Dirac point to 40 meV. A similar decrease in the fraction of antiferromagnetic ordering is also observed for the case of graphene approached to the gold layer at 0.3 Å from the equilibrium state.

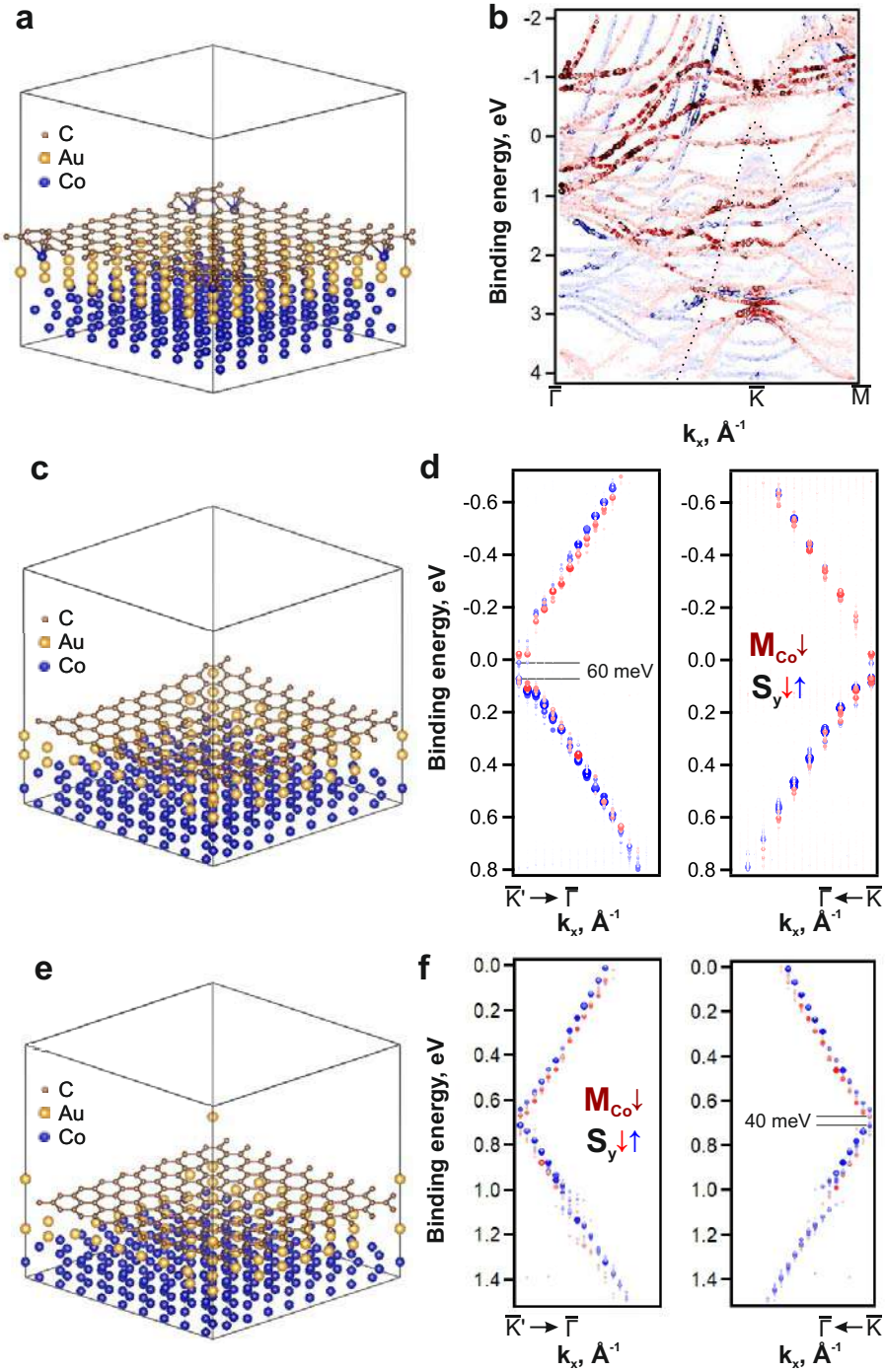

Figure 7.14 — Unit cells with additional atoms: cobalt under graphene (a), gold under graphene (c), and gold over graphene (e). (b), (d), and (f) The unfolded electronic structure in the vicinity of the $\bar{\mathrm{K}}$ and $\bar{\mathrm{K}}'$ points corresponding to the unit cells shown on the left. The graphene π band is marked by the dashed line in (b). The size and color of the symbols show the Bloch spectral weight for the S_y spin component.

Based on the performed investigations, it can be concluded that graphene on Au/Co loop dislocations of different sizes is characterized by ferrimagnetic ordering on its sublattices. The presence of additional gold adatoms under graphene enhances the induced spin-orbit Rashba interaction in graphene, but does not destroy its ferrimagnetic ordering. Controlling the number of gold atoms above/below the graphene can be used to find the optimal ratio between spin-orbit and exchange interactions for the observation of the quantum anomalous Hall effect.

7.3 Comparison of p-graphene and n-graphene

It is important to note that the properties of graphene depend markedly on the atomic density of the intercalated Au layer. To obtain n-graphene with the formation of an ordered (9×9) superstructure, a smaller amount of gold was adsorbed and intercalated under graphene than to obtain p-graphene. This led to the manifestation of completely new properties of graphene, namely ferrimagnetism on the A and B sublattices.

Let us emphasize the main differences between the two systems with p-graphene and n-graphene:

1. less amount of deposited and intercalated gold in the case of n-graphene. To obtain it, 3.1 Å Au was deposited instead of 3.6 Å, resulting in n-doping of graphene after intercalation, instead of p-doping. The strong dependence of the electronic structure of graphene on the amount of intercalated gold was also demonstrated in [12].
2. different periodicity and crystal quality of the superstructure. For n-graphene, the LEED pattern shows a periodicity of (9×9) instead of (10×10) for p-graphene with diffraction reflexes of the superstructure up to the second order, indicating better ordering compared to p-graphene, for which only the first-order reflexes were observed. In addition, for n-graphene, periodic loop dislocations are observed over rather large areas of the sample (see Fig. 7.15). The increase in the spectral weight of graphene Dirac cone with respect to the background is associated with a better crystalline perfection of the synthesized system and a smaller amount

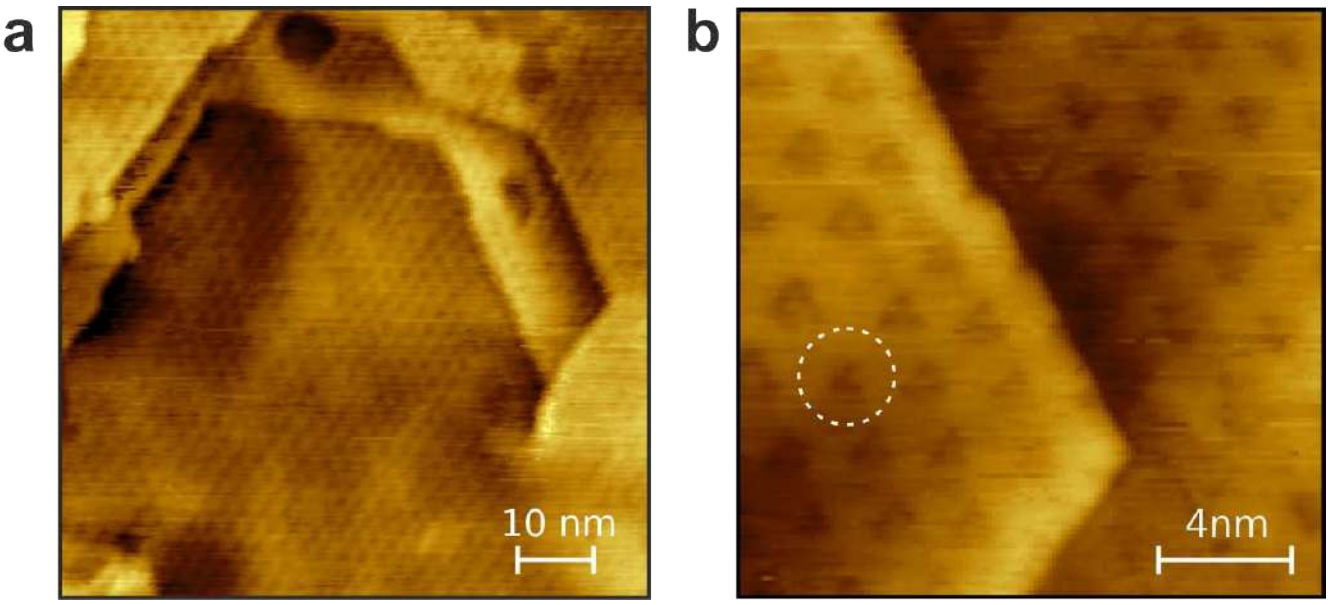

Figure 7.15 — STM images of the n-Gr/Au/Co(0001)/W(110) sample at different scales, scanning parameters $V_t = 3$ mV, $I_t = 4.5$ nA for (a), $V_t = 7$ mV, $I_t = 5$ nA for (b).

of deposited gold. The spectral weight of graphene Dirac cone in the case of p-graphene was smaller due to partial misorientation of graphene and a larger contribution of Au states to the background. Smaller amount of the intercalated gold and, consequently, the formation of periodic dislocation loop structure with well-defined dimensions allowed us to obtain a new system with ferrimagnetic properties.

3. different spin splitting asymmetry, induced by spin-orbit and exchange splittings.
4. the absence/presence of the ARPES signal in the second Brillouin zone along the $\overline{\mathrm{KM}}$ direction for p-/n-graphene shows that in the case of p-graphene the symmetry of A and B sublattices is not broken, and in the case of n-graphene the symmetry breaking indirectly confirms the sublattice ferrimagnetism.

Figure 7.16 shows a comparison of the data for p- and n-graphene. For p-graphene, a larger total magnetization of graphene and a larger Rashba splitting are revealed, which lead to an increase in the splitting asymmetry. If we restrict the tight binding parameters m_A and m_B to a maximum absolute value of 0.013 (obtained in the present work), we can approximate the experimental data presented in Fig. 7.16 (a) with the corresponding spin splitting asymmetry and only purely ferromagnetic phase without opening the antiferromagnetic gap ($E_g = 0$ meV). For larger values of the parameters m_A and m_B in modulus, a ferrimagnetic phase can be achieved in

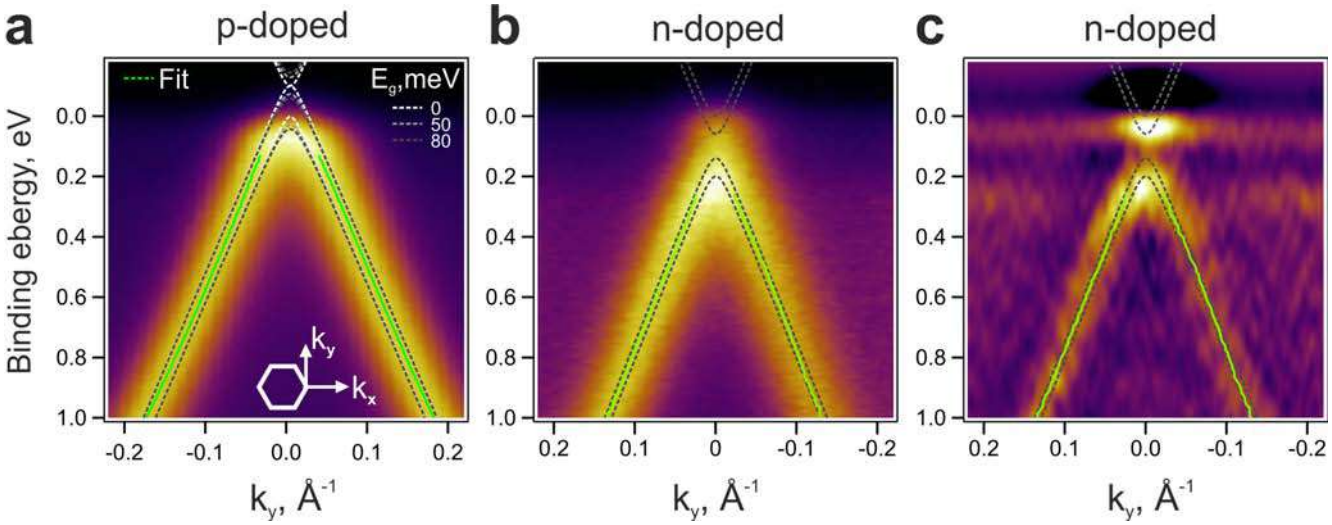

Figure 7.16 — ARPES data for p-graphene (a) and n-graphene (b) with tight binding calculation results for different values of the band gap E_g. The second energy derivative of the data of panel (b) is shown in (c) for better visualization. The solid green lines show the result of approximating the quasi-wave vector distribution curves by two peaks with Lorentz functions.

agreement with the spin-ARPES data ($m_A = -0.01797$ and $m_B = 0.00515$ for $E_g = 50$ meV, $m_A = -0.02078$ and $m_B = 0.00798$ for $E_g = 80$ meV). The results of the tight binding calculation for different E_g are presented on top of the ARPES data in Fig. 7.16 (a). Nevertheless, the ferrimagnetic phase with a significant increase of atomic magnetic moments on the carbon atoms of one of the sublattices is not confirmed by DFT calculations, including the reduced distance between graphene and Au monolayer. For this reason, we can assume that the ferromagnetic phase is the most probable for p-graphene.

7.4 Spectroscopic features of two-dimensional magnetism in graphene and underlying gold monolayer

Topological surface states (TSS) have attracted much interest in the condensed matter physics community in recent years. TSSs have been predicted and observed in 2D and 3D topological insulators, in which spin and quasi-momentum are coupled and form a helical spin texture in the Brillouin zone, similar to a Dirac cone. Another class of materials – topological crystal insulators or semiconductors – can contain one-dimensional topological protected states on defects such as step edges and dislocations that connect bulk Fermi points in momentum space [548—550]. Features such as high spin polarization, stability to magnetic perturbations and temperature make TSSs suitable for spintronics applications. Recently, it has been shown in semiconductors that the spin texture of one-dimensional topological states of a screw dislocation exhibits a much higher degree of spin coherence than the two-dimensional state of the Rashba/Dresselhaus spin-orbit interaction [548].

Metallic TSSs are observed on the surfaces of noble metals such as Au, Cu, Pt, and Pd, which were previously thought to be the prototype of Shockley surface states [551]. They exist in the bulk band gap due to the nontrivial $\mathbb{Z}_2$ volume index. Dirac cones of deep d orbital surface states have been observed in Ag(111) and Au(111) [290]. Since they possess spin polarization of the upper and lower Dirac cones, the topological character of the states was discussed with the possibility of existence of yet undiscovered topological invariants. In addition to noble metals, spin-polarized Dirac-like states have been found on the surface of single crystal W(110) (Chapter 3). The made assumption about topological metallic states was confirmed several years later in a theoretical article [263], despite further experimental investigation of trivial states near the $\bar{\Gamma}$ point [261; 262]. The existence of different fermionic states in the same topological metal is not contradictory and was found for Hf_2Te_2P with states characteristic of both strong and weak topological insulator [552].

Nowadays, the search and study of metal topological states is still an important task. Recently, a linear energy dispersion of the Au surface state in the form of a Dirac cone in 1ML-Au/Pt(111) has been reported [553]. This state is in the bulk continuum of the Pt substrate bands, which makes it difficult to detect. On the other hand, in the two-dimensional Fe/W(110) ferromagnet, a nontrivial topology of the

Fermi surface was found to arise from a complex interaction between the ferromagnet and the heavy metal with a strong spin-orbit interaction [102].

Graphene in contact with a quasi-two-dimensional layer composed of ferromagnetic and heavy metals will also acquire topological properties, and in the case of out-of-plane magnetization, the QAHE phase was theoretically predicted in [451].

In this section, we will study the features of Dirac-like states at the interface between Au and Co(0001) monolayer with loop dislocations, analyze their modification for different systems, and establish a connection with two-dimensional ferrimagnetism in graphene and the underlying Au monolayer. The existence of spin-polarized states near the $\bar{\Gamma}$ point, as well as the presence of an energy band gap in the local density of states in graphene is strong evidence of sublattice ferrimagnetism. An important confirmation of ferrimagnetism in graphene will be the comparison of experimental STS curves and theoretical local density of states (LDOS) curves for the magnetization perpendicular to the sample surface. It will be shown that only one graphene sublattice can be measured for ferrimagnetic graphene by STM method, and the presence of defects in the form of residual gold clusters does not affect the ferrimagnetic state of graphene.

It will be shown that the observed conical states remain stable in contact with graphene, but are not characteristic of the system without loop dislocations. The presented experimental and theoretical results allow us to consider them as metallic TSSs hosted in a surface alloy of Au and Co with a periodic loop dislocation structure.

7.4.1 Conical states at $\bar{\Gamma}$ point

An experimental study of the synthesized Gr/Au/Co(0001)/W(110) system revealed new features of the electronic structure at the $\bar{\Gamma}$ point of the surface Brillouin zone. Figure 7.17 shows the characterization of the synthesized system by experimental ARPES and spin-ARPES methods using synchrotron and laser radiation. Interface states with a linear cone at the $\bar{\Gamma}$ point of the surface Brillouin zone (labeled as “DC” in the figure) are found. According to the spin-resolved spectra, these conical states are spin-polarized with the same spin projection as the cobalt majority spin band

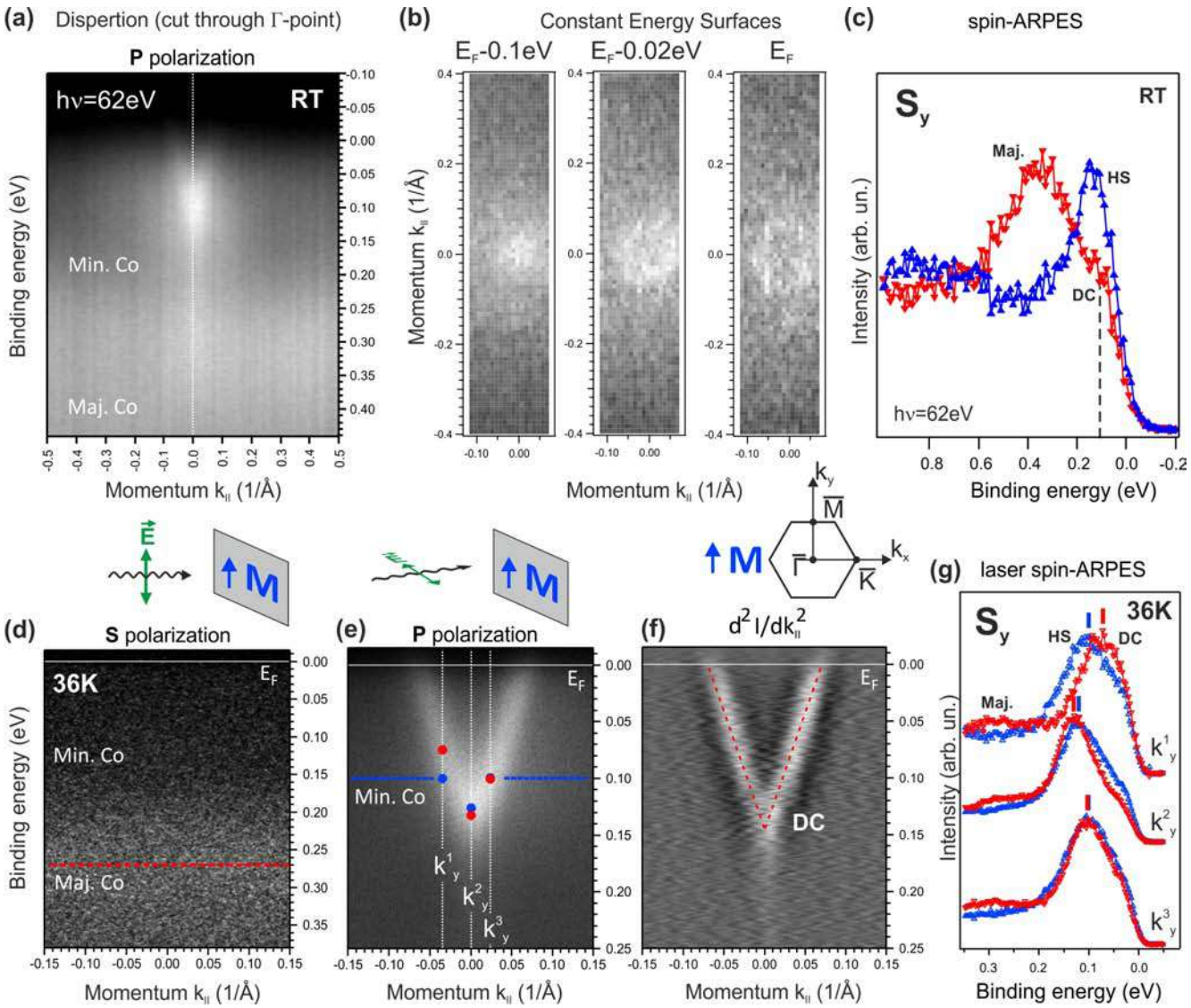

Figure 7.17 — Electronic structure of interface states at the $\bar{\Gamma}$ point in graphene/Au/Co measured with synchrotron (a-c) and laser (d-g) radiation. Spin-resolved spectra measured for specific emission angles are shown in (c) and (g). The photon energies are 62 eV (a-c), 6.3 eV (d), and 6.39 eV (e-g).

(layer magnetization in the surface plane), but are located in the localization region of the cobalt minority spin band. It should be noted that these states exhibit strong linear magnetic dichroism. As shown in insets (d) and (e) of Fig. 7.17, it is rather difficult to detect them in the ARPES intensity maps using s-polarization, while the states have the maximum intensity at p-polarization. In contrast, the intensity of the majority band is maximal at s-polarization and minimal at p-polarization. It was found that dichroism is directly related to the direction of magnetization of the system, which is determined by the magnetization of the cobalt layer and does not depend on the crystallographic orientation of the sample relative to the photoelectron emission plane. If the vector E of the incident photon is parallel to the direction of

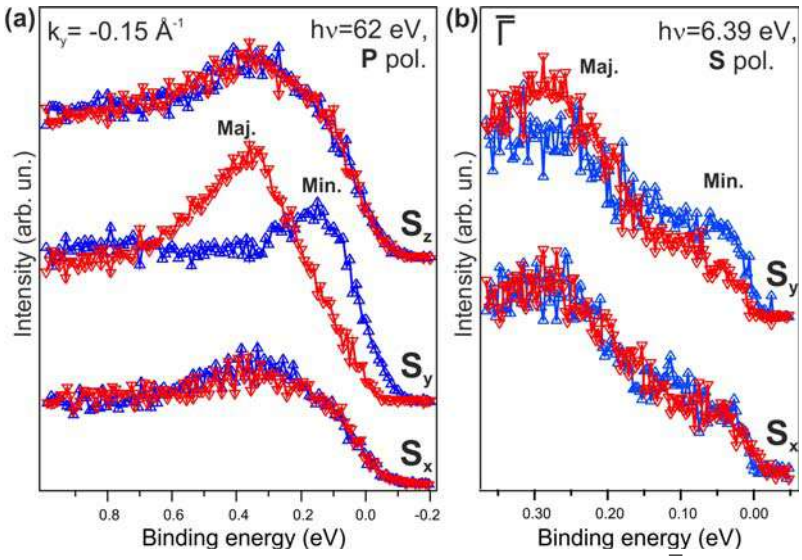

Figure 7.18 — Spin-resolved spectra of Co d states near the $\bar{\Gamma}$ point using synchrotron (a) and laser radiation (b).

magnetization of the cobalt layer, the Dirac-cone-like states have minimal, almost zero intensity, and if it is perpendicular, maximum intensity. It should be noted that in addition to the spin-polarized cone of electronic states, the spectra show a spin-polarized peak near the peak maximum of the cobalt minority band and with the same spin polarization (marked as “HS”). Its dispersion has a smaller slope and opposite spin polarization. In Fig. 7.18 we can see that this state is significantly weakened for large values of $k_{\|}$ outside the localization region of the conical states. The spin-resolved measurements of the cobalt states (see Fig. 7.18) clearly determine the direction of the cobalt layer magnetization, namely along the $\bar{\Gamma}\bar{\mathrm{M}}$ direction, along the $\vec{y}$ axis. Thus, these measurements establish a precise spatial relationship between the sample magnetization vector and the polarization vector of the incident radiation. Next, we consider DFT calculations of systems with loop dislocations to discuss the nature of the observed states.

The DFT calculations presented in Fig. 7.19 confirm the existence of Dirac-cone-like states in both Au/Co and Gr/Au/Co systems. In panels (d) and (e), in the region marked by a black rectangular box, states are observed that were not detected in the calculation of a thin cobalt layer without a monolayer of gold and graphene (solid lines in the figure, the boundary of the projected bulk cobalt bands is shown by the green line). Obviously, the states are formed as a result of hybridization of the d states of cobalt and sp states of gold. Due to the localization of the Dirac-like state with a minority spin in the band gap for bulk Au(111) and Co(0001), the state is a surface state with no dispersion with changing photon energy and a maximum

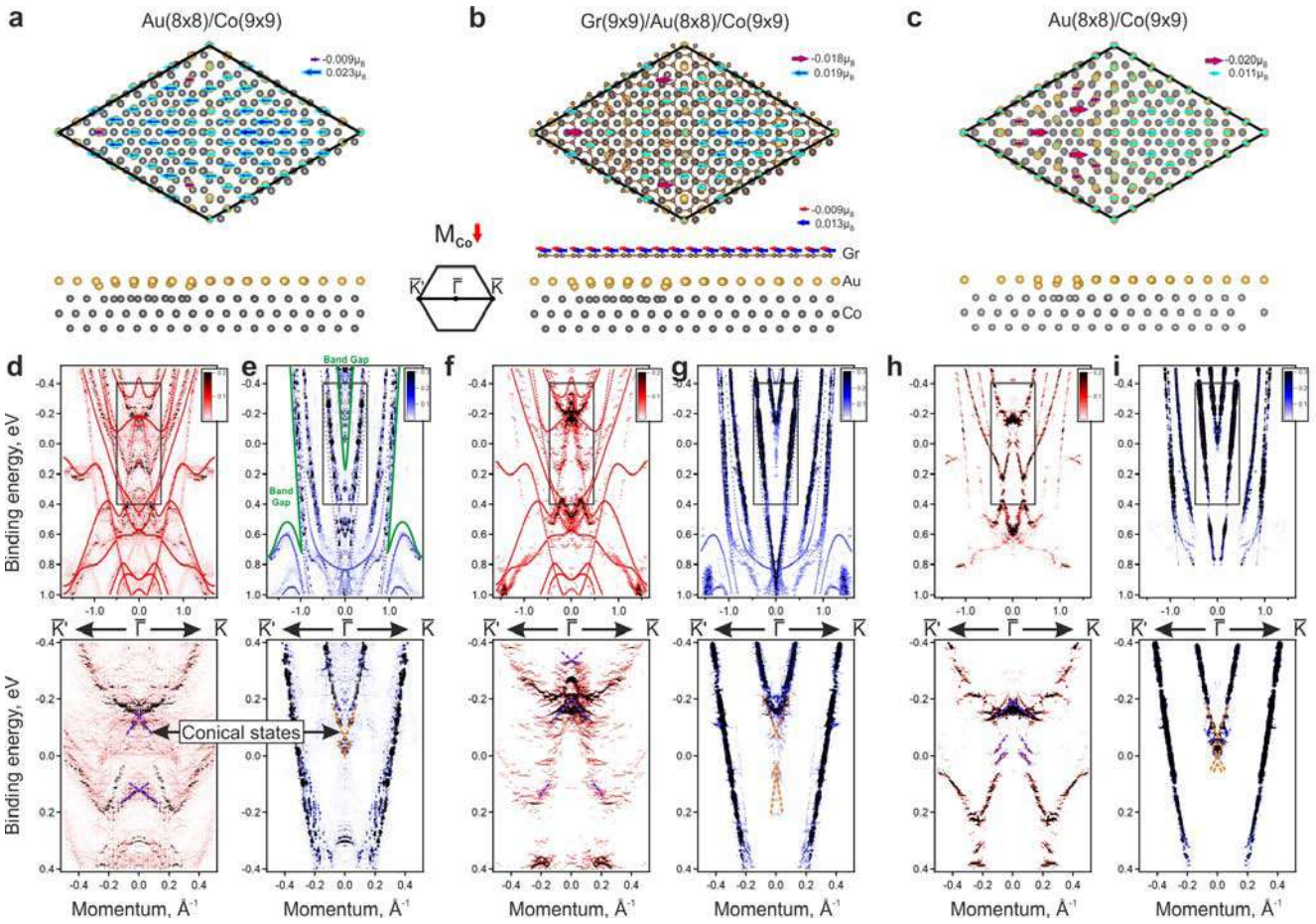

Figure 7.19 — Unit cells of the systems after structure optimization: Au/Co with dislocation loop surrounding the center of Au cluster of 6 atoms (a), the same cell with graphene on top (b) and Au/Co with dislocation loop surrounding Au cluster of zero size (c). The sizes of the arrows are proportional to the values of atomic magnetic moments on the gold and carbon atoms. The legends include arrows indicating the maximum magnetic moments in two opposite directions for graphene and the Au-Co dislocation loop. The direction of magnetization of the Co layer is to the right. The unit cell drawings were created using VESTA software [554]. (d-i) The unfolded band structures in the vicinity of the $\bar{\Gamma}$ point for the unit cells shown above. The size and color of the symbol represent the Bloch spectral weight for the components with spin-↑ and spin–↓ (shown in the white-blue-black and white-red-black palettes, respectively).

intensity relative to the intensity of the Co substrate states at about 60 eV. As can be seen from Fig. 7.20, the electronic structure of the system with a residual amount of adsorbed gold on the graphene surface after intercalation includes, in addition to Dirac-like states, the well-known Au(111) surface states with parabolic dispersion. It can be assumed that the appearance of Au(111) surface states is associated with the

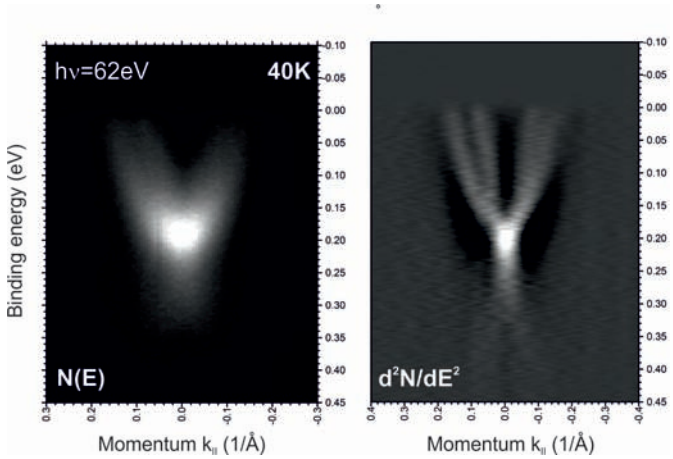

Figure 7.20 — Electronic structure of interface states at the $\bar{\Gamma}$ point in graphene/Au/Co after adsorption of 3.5 Å Au and intercalation under graphene.

formation of ordered Au(111) islands on graphene. It should be noted that the interface states are characteristic only for cells with loop dislocation and ferrimagnetic ordering in the Au layer. Calculation for the cell without dislocation (see Fig. 7.21) showed that ferrimagnetic ordering is changing to ferromagnetic ordering with non-uniform distribution of magnetic moments on gold atoms in the left and right parts of the cell due to a decrease in the distance between gold atoms and the nearest neighbor cobalt atoms. At the same time, states with linear dispersion near the Fermi level are absent. The shape of the state dispersion with minority spin projection becomes similar to that of the bulk Co states (see Fig. 7.19 (d)). The state with majority spin projection is shifted towards higher binding energies, which is consistent with the transition to the ferromagnetic Au state. Thus, the presence of Dirac-like states near the Fermi level confirms the ferrimagnetic ordering in the gold layer both with and without graphene.

To confirm the existence of interface states in Au/Co system without graphene, a separate experiment was performed, the results of which are presented in Fig. 7.22. 2,3 Å of gold was deposited on a 132 Å Co(0001) thin film on W(110) with subsequent annealing at 400 °C for 35 min. The diffraction pattern contains the superstructure $\sim (10 \times 10)$. It is known that adsorption of 0.8 ML Au on Ni(111) followed by annealing at temperatures above 150 °C should lead to the formation of $\sim (10 \times 10)$ loop dislocations. In the case of the Co(0001) substrate, we observe a similar periodicity. As can be seen from the ARPES intensity map, Dirac-like states were found in this system without graphene. Graphene is a protective layer for the Au-Co surface alloy when exposed to the atmosphere. The electronic structure, including interface states, can be recovered after degassing the sample in a chamber at temperatures $\sim 300 - 400$ °C.

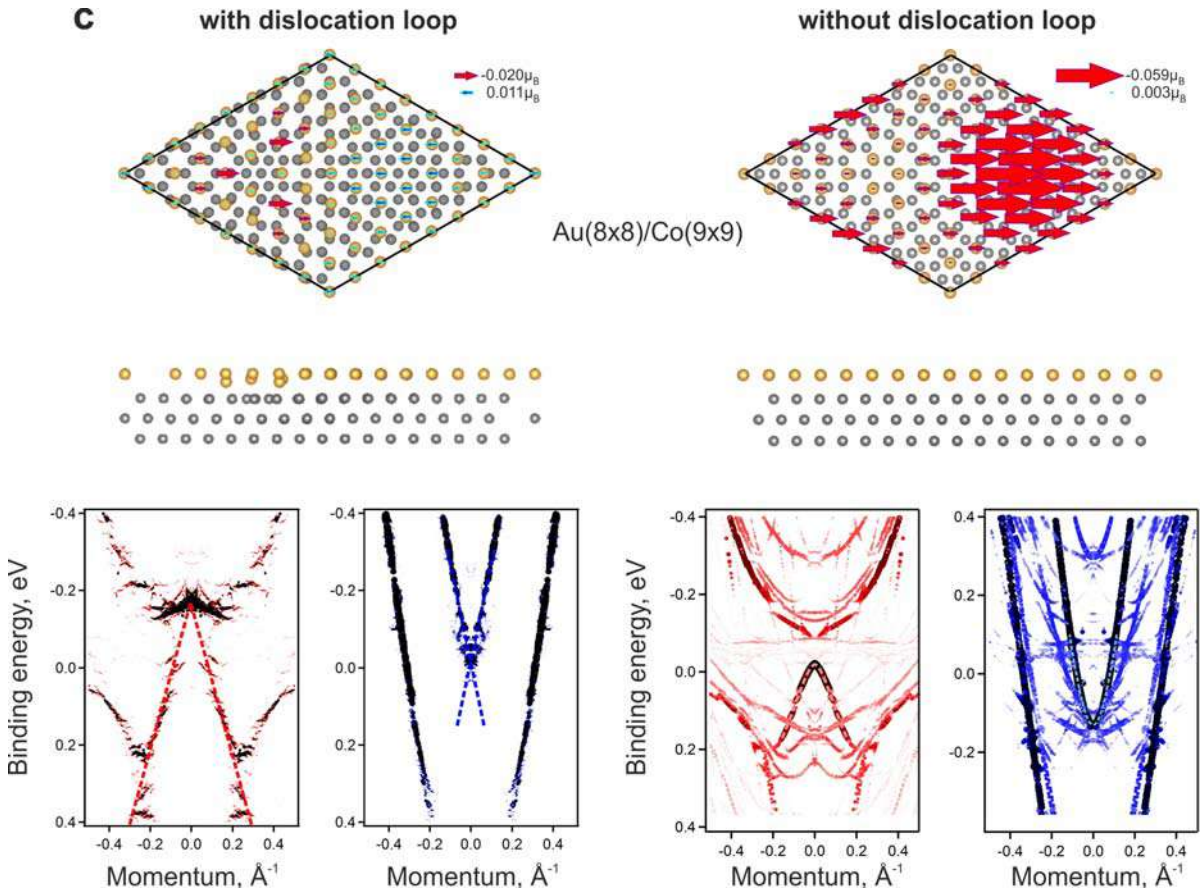

Figure 7.21 — Comparison of the electronic structure of Gr/Au/Co system near the $\bar{\Gamma}$ point for cases with and without a loop dislocation.

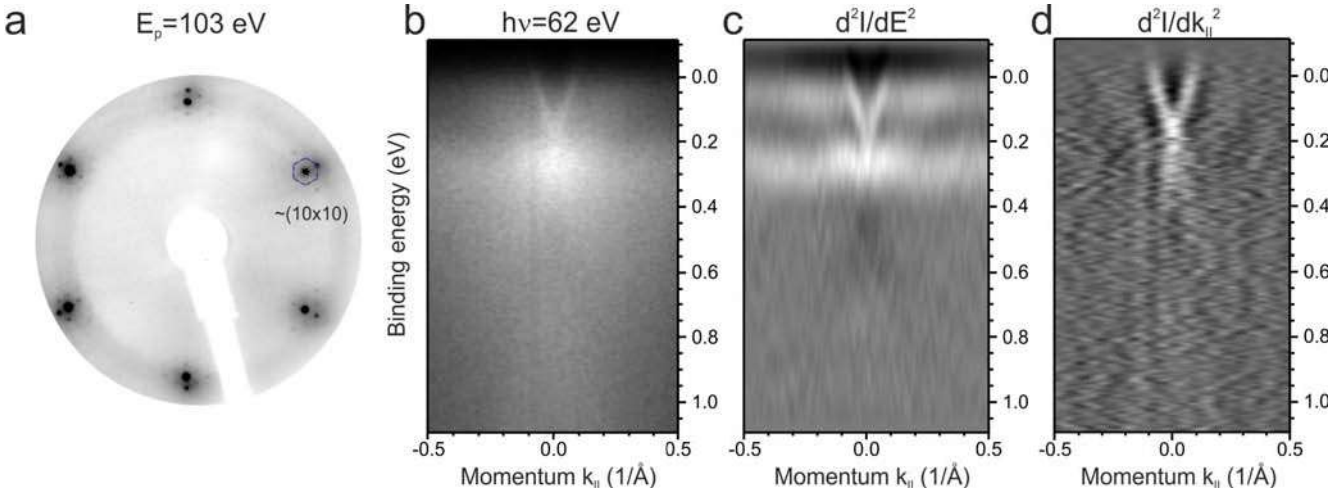

Figure 7.22 — Study of Au/Co(0001) system: (a) LEED pattern, (b) ARPES intensity map near the $\bar{\Gamma}$ point with second derivatives (c,d).

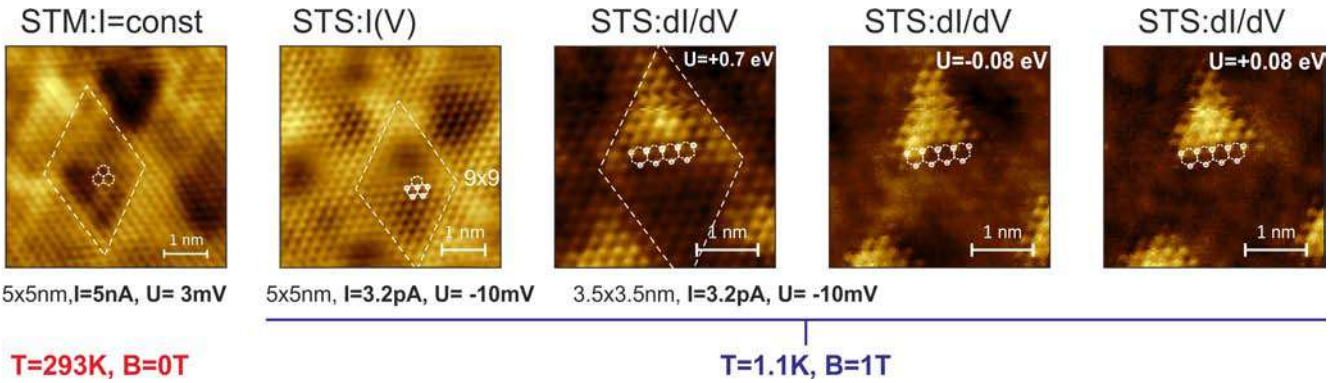

Figure 7.23 — STM images of Gr/Au/Co system measured at different sample temperatures and external out-of-plane magnetic field (perpendicular to the surface). Images obtained by mapping in the STS mode are shown for different values of the tunnelling voltage.

7.4.2 Dirac cone states at $\bar{\mathrm{K}}$ point

As previously shown, sublattice ferrimagnetism in graphene leads to the appearance of a band gap at the Dirac point. To study the local band gap and the homogeneity of ferrimagnetic ordering on the graphene surface, STM/STS methods were used. Figure 7.23 shows the measurements of the same system at room temperature of the sample and upon cooling using liquid helium and in an external magnetic field. In the STM image obtained at room temperature of the sample, two sublattices of graphene can be distinguished. In this case, the magnetization of the ultrathin Co layer (thickness 80 Å) is in the plane of the surface. Measurements at 1 K temperature in a 1 T magnetic field perpendicular to the surface show the presence of one graphene sublattice situated in fcc hollows and magnetized in the same direction as the Co layer. Although the DFT calculation shown in Fig. 7.24 confirms the ferrimagnetic state in graphene for the perpendicular magnetization of the system (the band gap value is $\sim$ 30 meV and the spin splitting near the $\overline{\mathrm{K}}$ point is $\sim$ 40 meV), we have a significant difference in the STM images. Mapping with measurement of STS spectra at each point with disabling feedback also showed only one sublattice on the cuts at different tunneling voltages. To explain the observed effect, we simulated the STS spectra with peak broadening by a Lorentz contour at the optimal distance $\sim$ 2.3 Å, at which a good agreement with the experimental spectrum was found. Figure 7.24 shows the comparison of the theoretical spin density curve with the total experimental curve over the whole STM image. The position

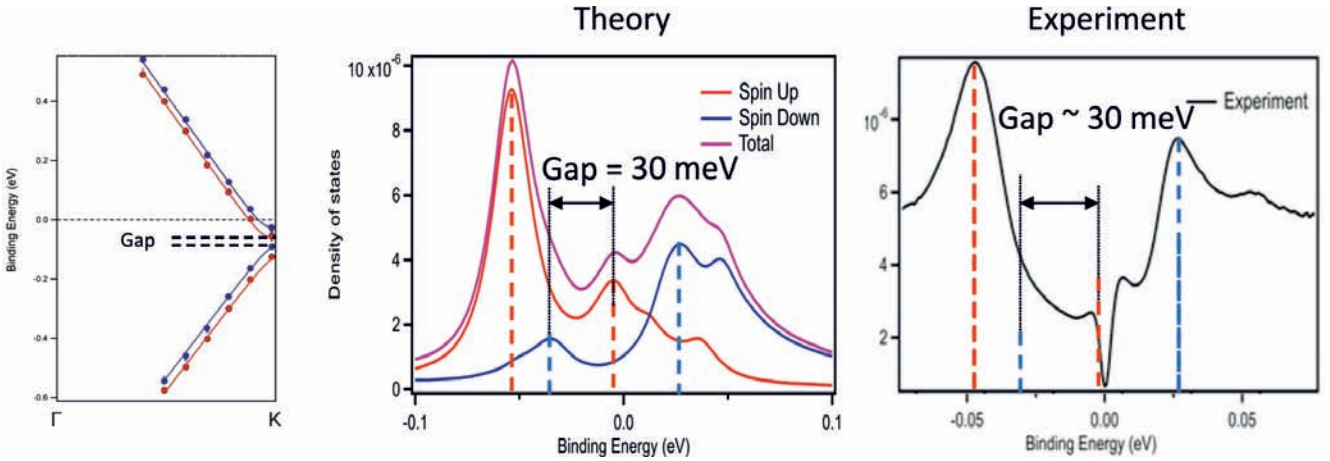

Figure 7.24 — STS spectra of Gr/Au/Co system in comparison with theoretical curves of the local density of electronic states. The electron density cut was taken at a height of $\sim$ 2.3 Å from graphene.

of the graphene peaks and the size of the band gap are in good agreement with each other. However, a band gap near zero energy is observed in the experimental spectrum, which is possibly related to the opening of the superconducting band gap in the system at $\sim$ 1 K. On the one hand, cobalt thin films on a pure W(110) surface are known to grow in hcp geometry, which is magnetic [555]. The magnetism of the cobalt film is also confirmed by the spin-resolved measurements of d states of cobalt presented above. On the other hand, only cobalt films in fcc geometry [556] can possess superconductivity. However, not only the material geometry but also the size factor affects the presence of superconductivity, as has been shown theoretically in the case of CoO_2 monolayer [557] and experimentally in the case of CoSb monolayer [558]. Moreover, it has been shown in recent works that the alloy of gold atoms with plumbene [559], as well as the gold film itself in contact with the superconductor [560], are superconducting. In our case, a near-surface Au-Co alloy is formed, the superconducting features of which cannot be ignored and require further investigation.

As it was shown earlier, gold clusters may be present on the surface after gold intercalation, and the formation of clusters under graphene is also possible. Theoretical studies have predicted the preservation of ferrimagnetic ordering in such cases as well. Figure 7.25 shows an STM image in the region of gold clusters. One of the clusters is intercalated under the graphene as the electron density varies continuously in the cluster region, the other is located on the graphene and was captured by a tip during STS map measurements at constant tunnelling current. As can be seen in Fig. 7.25, inset A, the cluster has been moved from its former location, but the visualization of

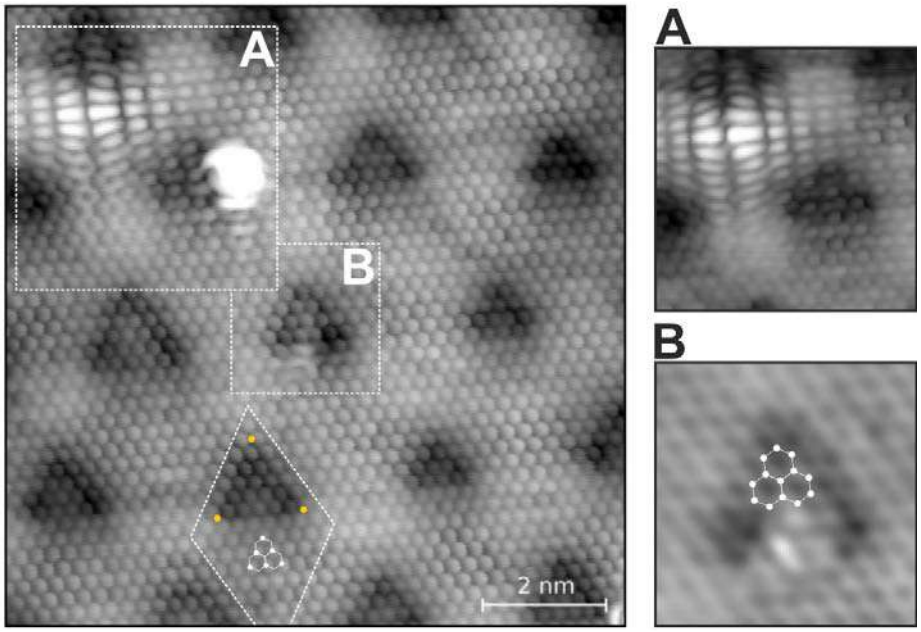

Figure 7.25 — STM image of Gr/Au/Co system with gold clusters under/over graphene measured at the following parameters: T = 1.2 K, B = 1.5 T, $U_t = -30$ mV, $I_t = 53$ pA. Inset A is measured after removing the cluster from the surface and at the same scanning parameters. Inset B is measured after reducing the tunneling current to $I_t = 4.2$ pA.

only one sublattice of the graphene has been preserved. Importantly, the homogeneous imaging of the electronic density of graphene is also found in the region of loop dislocations of different sizes, confirming the great potential to utilize magnetism in graphene even when the underlying interface is structurally imperfect. It should be noted that the reduction of the tunnelling current by more than an order of magnitude, which roughly corresponds to the tip withdrawal from the surface by ~ 1 Å leads to the visualization of two graphene sublattices in the image. Since the measurement was made on the same surface area with a small intercalated cluster (inset B), a comparison of the two images was made (graphene lattice shown in the images), confirming the measurement of only one sublattice at closer distances to the surface.

The following conclusions can be drawn on the basis of the conducted studies. Ferrimagnetism in graphene and the underlying Au layer manifests itself in the form of spectroscopic features observed by ARPES and STS methods. At the $\bar{\Gamma}$ point near the Fermi level, Dirac-like spin-polarized states are observed. These states are characteristic of ferrimagnetic ordering in the Au layer, which arises as a result of the formation of loop dislocations. In a strong magnetic field, a band gap in the electronic structure of graphene, characteristic of out-of-plane ferrimagnetic ordering, is detected. At the same time, only one sublattice of graphene is measured on STM

images at certain parameters. The presence of structural defects in the form of an intercalated gold cluster or gold cluster on the graphene surface does not affect the measurement of only one graphene sublattice in the defect region. This indicates the preservation of ferrimagnetic ordering in the region of structural defects as well. Thus, the presence of ferrimagnetic ordering in the layers can be confirmed not only by direct methods registering the magnetic properties of the system or the spin projection of electron states, but also on the basis of observations made by spectroscopic methods.

7.5 Findings

This chapter presents the realization of magneto-spin-orbit graphene on Au/Co(0001) substrate with loop dislocations. The results of spin-ARPES, STM and DFT studies show that the spin-orbit and magnetic exchange interactions induced in graphene lead to spin splitting asymmetry at opposite $\bar{\mathrm{K}}$ and $\bar{\mathrm{K}}'$ points. Intercalation of less gold under graphene leads to a shift of the Dirac point of graphene from the conduction band to the valence band, i.e., a transition from p-doped to n-doped graphene. The presence of loop dislocations under graphene is the main reason for the ferrimagnetic ordering of magnetic moments on the carbon atoms of the two sublattices of n-doped graphene and the opening of magnetic band gap in the electronic structure of graphene, which is observed in both ARPES and STS data. Additional evidence for intralayer ferrimagnetic ordering in graphene and gold monolayer is the detection of spin-polarized states with conical dispersion near the Fermi level. Due to the opposite sign of the Berry curvatures for the $\bar{\mathrm{K}}$ and $\bar{\mathrm{K}}'$ valleys, the synthesized system appears to be promising for the implementation of the circular dichroism Hall effect.

Conclusion

The dissertation presents the main results of the work on the development of fundamental principles and practical approaches for the formation of high-quality systems based on new quasi-two-dimensional materials (graphene, ultra-thin metal layers, topological insulators and other systems with surface electron states), in which unique properties that provide a joint enhancement of spin-orbit and magnetic exchange interactions are manifested to the maximum extent. Using a combination of integral photoelectron spectroscopy methods, local tunnelling microscopy/spectroscopy methods and theoretical methods of density functional theory and tight binding allowed us to establish the relationship between the atomic structure of the studied systems and their unique electronic and magnetic properties. On the basis of the developed approaches to the formation of high-quality systems and a comprehensive study of their electronic, magnetic and crystalline structures, effects suitable for practical use in spintronics devices have been discovered, such as the giant Rashba effect in graphene, the giant two-dimensional photovoltaic effect in topological insulators, the spin-dependent avoided-crossing effect in ultrathin metal layers, the magnetic proximity effect in quasi-freestanding graphene, and the linear magnetic dichroism effect in the Au/Co surface alloy, etc. Models of spin electronic devices using unique properties and corresponding effects – graphene spin filter, information recording device for magnetoresistive RAM (reversible spin current magnetization switch) and infrared detector of circularly polarized radiation have been developed. The inventions can be used in the field of spintronics and optoelectronics.

The following main points and conclusions of the work could be emphasized.

1. The electron energy and spin structure of W(110) and ultrathin Al and Au layers on W(110) have been investigated. It is found that the atomically pure surface of W(110) is characterized by spin polarization of surface d resonances in the pseudogap of tungsten opened as a result of spin-orbit interaction. The spin-polarized surface resonances of W(110) in the $\bar{\Gamma}\bar{\mathrm{S}}$ direction of the surface Brillouin zone exhibit linear dispersion and spin structure characteristic of topological surface states. For thin Al layers on W(110), spin-dependent hybridization effects between quantum well states and interface states at the boundary with the substrate lead to anomalously high spin splitting, which is not characteristic of freestanding Al layers. The

possibility of transferring the strong spin-orbit interaction in the substrate to quantum well states in an ultrathin Al layer up to 15 monolayers is shown.

2. A giant two-dimensional photovoltaic effect has been found in a magnetically doped topological insulator. The analysis of measurement results for topological insulators of different stoichiometric composition showed that the magnitude of the effect depends on the position of the Dirac point relative to the Fermi level and the edge of the valence band. It was found that the photovoltaic effect has maximum efficiency for topological insulators with high filling of the upper Dirac cone states and a Dirac point located inside the fundamental band gap.
3. The electronic structure and magnetic properties of BiTeI semiconductors doped with magnetic metals have been studied. A non-monotonic character of the change in the value of the energy band gap and the magnitude of saturation magnetization with increasing concentration of magnetic impurity atoms was found, which indicates the magnetic character of the observed band gap modulated by the pairwise interaction between doped magnetic metal atoms.
4. New methods of graphene formation at elevated temperatures by chemical vapor deposition have been developed, which leads to the formation of highly oriented graphene on Co(0001)/W(110) and on Pt(111), for which it became possible to measure ARPES intensity maps near the $\overline{\mathrm{K}}$ point of graphene without contribution from additional graphene rotation domains. The developed methods of graphene formation opened unique opportunities to study the joint influence of spin-orbit and exchange interactions on the electronic structure in the graphene/Au/Co(0001) system, to study the electronic structure of quasi-two-dimensional catalytically active systems based on graphene and platinum lanthanides, and to apply the graphene/Co interface with high spin polarization of states at the Fermi level in spintronics.
5. Intercalation of highly oriented graphene on Pt(111) single crystal by gadolinium atoms allowed to obtain a well-ordered nanothin epitaxial layer of $\mathrm{Pt_5Gd}$ alloy under graphene. In this case, the atomically flat surface of the alloy is terminated by an atomic layer of Pt with “kagome” structure. It is found that the surface unit cell of the alloy is rotated by 30° relative to the surface unit cell of Pt(111) and corresponds to the orientation of

graphene. Involvement of a set of methods for the investigation of the system (LEED, ARPES, XPS and STM) at each stage of intercalation allowed us to determine the optimal conditions for the synthesis of an alloy of high structural perfection and homogeneous composition. Changing the stoichiometry of the alloy $\mathrm{Pt_xGd}$ under graphene is a way to control the energy position of the Dirac point in graphene, and thus the concentration of charge carriers. The method of synthesizing nanothin epitaxial layers of $\mathrm{Pt_5Gd}$ terminated by an atomic layer of Pt with a "kagome" structure opens up great possibilities for cheaper production of catalysts.

6. Systematic studies of spin splitting of graphene electron states on ferromagnetics and nonmagnetic sp and d metals have been carried out. The effect of giant Rashba splitting in graphene on Au monolayer, on incomplete Pt monolayer and on Pt(111) substrate, which is absolutely inaccessible earlier in freestanding graphene, was found. It is shown that the contact of graphene with a metal with a high atomic number (Au, Pt) in contrast to metals with significantly lower atomic numbers (Co, Ni, Cu) leads to the effect of induced spin polarization of graphene states.
7. Quasi-freestanding graphene obtained by intercalation of an incomplete platinum monolayer under the zero-layer graphene on SiC(0001) is characterized by the giant Rashba spin-orbit splitting of π electron states, up to values of $\sim$ 200 meV. It is shown that the observation of the giant Rashba effect is related to the reduction of the distance between graphene and platinum atoms during corrugation of graphene.
8. Gold intercalation under highly oriented graphene on Co(0001)/W(110) leads to n- and p-doping of the electronic structure of quasi-freestanding graphene depending on the amount of intercalated gold. It is found that graphene is magneto-spin-orbit, i.e., it possesses strong induced spin-orbit and exchange interactions.
9. It is shown that quasi-freestanding graphene on Au/Co(0001)/W(110) substrate with p-type doping exhibits magnetism in the surface plane in the same direction as a thin Co(0001) film. The magnetization effect of graphene is observed in the form of asymmetric spin splitting of π electron states of graphene in opposite $\overline{\mathrm{K}}$ points of the Brillouin zone of graphene. Study of the surface by scanning tunnelling microscopy revealed the formation of loop

dislocations at the Au – Co interface, due to which the magnetic exchange interaction is transferred to graphene.

10. It is shown that quasi-freestanding graphene on Au/Co(0001)/W(110) substrate with n-type doping is characterized by homogeneous ferrimagnetic ordering on its sublattices, which allowed us to predict the possibility of observing the circular dichroism Hall effect in this system. The experimentally measured value of the band gap 80 $\pm$ 25 meV in the electronic structure of graphene is magnetic in nature and is related to the Hubbard-type electron-electron interaction and the non-equivalence of A and B sublattices.
11. In the electronic structure of Au/Co(0001)/W(110) and graphene/Au/-Co(0001)/W(110) systems near the Fermi level and $\overline{\Gamma}$ point, a spin-polarized interface state with conical dispersion is formed, which is a consequence of ferrimagnetic magnetization in the gold monolayer. The photoelectron spectroscopy spectra using laser radiation show a strong linear magnetic dichroism effect for this state.
12. The presence of ferrimagnetic ordering in graphene and intercalated gold layers can be confirmed by the results of measurements made by spectroscopic methods without spin resolution, such as ARPES and STS. The ferrimagnetic ordering is characterized by the appearance of a band gap in the electronic structure of graphene in the ARPES/STS measurement results and the observation of only one sublattice of graphene in the STM/STS results (at certain scanning parameters determining the distance from the STM tip to the surface).
13. Graphene on Au/Co loop dislocations of different sizes is characterized by ferrimagnetic ordering on its sublattices. The presence of additional gold adatoms under graphene enhances the induced spin-orbit Rashba interaction in graphene, but does not destroy its ferrimagnetic ordering. Controlling the number of gold atoms above/below the graphene can be used to find the optimal ratio between spin-orbit and exchange interactions for the observation of QAHE.
14. Graphene on the intercalated Au layer is thermally stable up to temperatures 600 – 650 °C. It has been established that graphene thermal destruction occurs during its long-term annealing at temperatures $\sim$ 670 – 700 °C, thus, on the surface remains a surface alloy of Au with underlying transition metal.

15. Step-by-step high-temperature annealing in an ultrahigh vacuum chamber enables us to determine the exact parameters for achieving a high-quality zero-layer graphene on SiC(0001) by analyzing the data obtained in situ by LEED, XPS and ARPES methods. It is shown that high-temperature annealing at 1150 – 1170 °C leads to the formation of a zero-layer graphene with a reconstruction of $(6\sqrt{3}\times 6\sqrt{3})\mathrm{R}30^\circ+(5\times 5)$, preceding further growth of the next graphene layer.
16. It is shown that intercalation of cobalt atoms under zero-layer graphene on SiC(0001) leads to its transformation into graphene of monolayer thickness, while ultrathin layers of CoSi and $CoSi_2$ silicides are formed under the graphene. Adsorption of Co onto the surface of heated sample leads to more efficient intercalation than in the case of adsorption onto the surface of the sample at room temperature followed by annealing. It is shown that the synthesized system possesses ferromagnetic ordering.

A significant result in the technical and methodical part of the work is the organization on the basis of the resource center "'Physical methods of surface investigation'" of an experimental research complex consisting of a number of setups, including the unique scientific setup Nanolab.

Finally, the author expresses his gratitude and great appreciation to his scientific advisor and supervisor, Prof. A. M. Shikin for support, assistance and discussion of the results over the years. I would also like to thank my colleagues, Dmitry Yu. Usachov, Anna A. Rybkina, Dmitry A. Pudikov, Mikhail M. Otrokov, Vladimir Yu. Voroshnin, Ilya I. Klimovskikh, Artem V. Tarasov, Oleg Yu. Vilkov, Anatoly E. Petukhov, Alexander V. Eryzhenkov, Evgeny V. Zhizhin, Sergey O. Filnov, Sergey V. Lebedev, laboratory head E. V. Chulkov and the entire staff, Laboratory of Electronic and Spin Structure of Nanosystems, Department of Solid State Electronics, Faculty of Physics, SPbU, and the SPbU Science Park for their help in obtaining and discussing the results. The author expresses special gratitude for the opportunity to carry out measurements at synchrotron radiation centers, for low-temperature STM measurements to V. S. Stolyarov (MIPT), for measurements by Raman spectroscopy to I. A. Eliseev and V. Yu. Davydov (Ioffe Institute of Physics and Technology, Russian Academy of Sciences), for calculations to E. E. Krasovskii (University of the Basque Country) and for micromagnetic modelling to the research group of prof. A. K. Zvezdin (Prokhorov General Physics Institute, Russian Academy of Sciences).

The dissertation work was performed within the framework of the SPbU state assignment project (project No. 95442847) and grants of the Russian Science Foundation (No. 23-12-00016 and No. 23-22-00112).

List of acronyms

AFM – antiferromagnetic;
ARPES – angle-resolved photoelectron spectroscopy;
CMOS BEOL – complementary metal-oxide-semiconductor back end of line;
CVD – chemical vapor deposition;
DOS – density of states;
DFT – density functional theory;
EDC – energy distribution curve;
EDM – energy distribution map;
EDX – energy-dispersive X-ray spectroscopy;
EHT – electron high tension;
EMF – electromotive force;
FC – field cooling;
fcc – face-centered cubic;
FIM – ferrimagnetic;
FM – ferromagnetic;
FFT – fast Fourier transform;
FWHM – full width at half maximum;
GGA – generalized gradient approximation;
Gr – graphene;
HAADF-STEM – high-angle annular dark-field scanning transmission electron microscopy;
hcp – hexagonal close-packed;
HRTEM – high-resolution transmission electron microscopy;
LDA – local density approximation;
LDOS – local density of states;
LEED – low-energy electron diffraction;
ML – monolayer;
MTJ – magnetic tunnel junction;
ORR – oxygen reduction reaction;
PAW – projector augmented wave method;
PVE – photovoltaic effect;
QAHE – quantum anomalous Hall effect;

QSHE – quantum spin Hall effect;
QVHE – quantum valley Hall effect;
QWS – quantum well state;
SEM – scanning electron microscopy;
SOT-MRAM – spin-orbit torque magnetoresistive random-access memory;
spin-ARPES – spin- and angle-resolved photoelectron spectroscopy;
SQUID – superconducting quantum interference device;
STM – scanning tunnelling microscopy;
STS – scanning tunnelling spectroscopy;
STT-MRAM – spin-transfer torque magnetoresistive random-access memory;
TEM – transmission electron microscopy;
TI – topological insulator;
TMR – tunnel magnetoresistance;
TSS – topological surface state;
VP-QAHE – valley-polarized quantum anomalous Hall effect;
XPS – X-ray photoelectron spectroscopy;
ZFC – zero field cooling;
ZLG – zero-layer graphene.

List of references

1. Large spin-orbit splitting in light quantum films: Al/W(110) / A. G. Rybkin [et al.] // Phys. Rev. B. — 2010. — Vol. 82, issue 23. — P. 233403. — URL: https://link.aps.org/doi/10.1103/PhysRevB.82.233403.
2. Spin-dependent avoided-crossing effect on quantum-well states in Al/W(110) / A. G. Rybkin [et al.] // Phys. Rev. B. — 2012. — Vol. 85, issue 4. — P. 045425. — URL: https://link.aps.org/doi/10.1103/PhysRevB.85.045425.
3. Topology of spin polarization of the $5d$ states on W(110) and Al/W(110) surfaces / A. G. Rybkin [et al.] // Phys. Rev. B. — 2012. — Vol. 86, issue 3. — P. 035117. — URL: https://link.aps.org/doi/10.1103/PhysRevB.86.035117.
4. Magneto-Spin–Orbit Graphene: Interplay between Exchange and Spin–Orbit Couplings / A. G. Rybkin [et al.] // Nano Letters. — 2018. — Vol. 18, no. 3. — P. 1564—1574. — URL: https://doi.org/10.1021/acs.nanolett.7b01548 ; PMID: 29365269.
5. A new approach for synthesis of epitaxial nano-thin Pt_5Gd alloy via intercalation underneath a graphene / A. G. Rybkin [et al.] // Applied Surface Science. — 2020. — Vol. 526. — P. 146687. — URL: https://www.sciencedirect.com/science/article/pii/S0169433220314446.
6. Sublattice Ferrimagnetism in Quasifreestanding Graphene / A. G. Rybkin [et al.] // Phys. Rev. Lett. — 2022. — Vol. 129, issue 22. — P. 226401. — URL: https://link.aps.org/doi/10.1103/PhysRevLett.129.226401.
7. Robust ferrimagnetism in quasi-freestanding graphene / A. G. Rybkin [et al.] // Pis'ma v ZHETF. — 2023. — Vol. 117, issue 8. — P. 626. — URL: http://jetpletters.ru/ps/2418/article_35652.shtml.
8. Quasi-freestanding graphene on SiC(0001) via cobalt intercalation of zero-layer graphene / A. A. Rybkina [et al.] // Phys. Rev. B. — 2021. — Vol. 104, issue 15. — P. 155423. — URL: https://link.aps.org/doi/10.1103/PhysRevB.104.155423.

9. Effect of gold intercalation on the electronic structure of graphene on Co-Si/SiC(0001) / A. A. Rybkina [et al.] // FTT (in Russian). — 2022. — Vol. 64, no. 8. — P. 1122. — URL: https://journals.ioffe.ru/articles/viewPDF/52716.

10. Origin of Giant Rashba Effect in Graphene on Pt/SiC / A. A. Rybkina [et al.] // Symmetry. — 2023. — Vol. 15, no. 11. — P. 2052. — URL: https://www.mdpi.com/2073-8994/15/11/2052.

11. Magnetic effects in the electronic structure of new quantum materials / A. M. Shikin [et al.] // Quantum structures for post-silicon electronics / ed. by A. V. Latyshev. — Novosibirsk, Parallel' : Minobrnauki Rossii; Institut fiziki poluprovodnikov im. A. V. Rzhanova SO RAN, 2023. — P. 111—128. — URL: https://www.isp.nsc.ru/nauka/izdaniya/kvantovye-struktury-dlya-postkremnievoj-elektroniki.

12. Giant Rashba splitting in graphene due to hybridization with gold / D. Marchenko [et al.] // Nature Communications. — 2012. — Vol. 3, no. 1. — P. 1232. — URL: https://doi.org/10.1038/ncomms2227.

13. The graphene/Au/Ni interface and its application in the construction of a graphene spin filter / A. A. Rybkina [et al.] // Nanotechnology. — 2013. — Vol. 24, no. 29. — P. 295201. — URL: https://doi.org/10.1088/0957-4484/24/29/295201.

14. Induced spin–orbit splitting in graphene: the role of atomic number of the intercalated metal and π–d hybridization / A. M. Shikin [et al.] // New Journal of Physics. — 2013. — Vol. 15, no. 1. — P. 013016. — URL: https://doi.org/10.1088/1367-2630/15/1/013016.

15. Nontrivial spin structure of graphene on Pt(111) at the Fermi level due to spin-dependent hybridization / I. I. Klimovskikh [et al.] // Phys. Rev. B. — 2014. — Vol. 90, issue 23. — P. 235431. — URL: https://link.aps.org/doi/10.1103/PhysRevB.90.235431.

16. Observation of Single-Spin Dirac Fermions at the Graphene/Ferromagnet Interface / D. Usachov [et al.] // Nano Letters. — 2015. — Vol. 15, no. 4. — P. 2396—2401. — URL: https://doi.org/10.1021/nl504693u ; PMID: 25734657.

17. Gigantic 2D laser-induced photovoltaic effect in magnetically doped topological insulators for surface zero-bias spin-polarized current generation / A. M. Shikin [et al.] // 2D Materials. — 2018. — Vol. 5, no. 1. — P. 015015. — URL: https://doi.org/10.1088/2053-1583/aa928a.

18. Advanced graphene recording device for spin–orbit torque magnetoresistive random access memory / A. A. Rybkina [et al.] // Nanotechnology. — 2020. — Vol. 31, no. 16. — P. 165201. — URL: https://doi.org/10.1088/1361-6528/ab6470.

19. Non-monotonic variation of the Kramers point band gap with increasing magnetic doping in BiTeI / A. M. Shikin [et al.] // Scientific Reports. — 2021. — Vol. 11, no. 1. — P. 23332. — URL: https://doi.org/10.1038/s41598-021-02493-8.

20. Graphene spin filter : patent RU 2585404 C1 : Int. Cl. G01R 33/05 / A. M. Shikin [et al.] ; applicant federalnoe gosudarstvennoe byudzhetnoe obrazovatelnoe uchrezhdenie vysshego obrazovaniya "Sankt-Peterburgskij gosudarstvennyj universitet" (SPbGU) ; patent attorney A. A. Matveev. — No. 2015113131/28 ; req. 04/09/2015 ; publ. 05/27/2016, bul. no. 15. — 11 p. : il.

21. Device for recording of information for magnetoresistive RAM : patent RU 2677564 C1 : Int. Cl. G11C 11/16 / A. M. Shikin [et al.] ; applicant federalnoe gosudarstvennoe byudzhetnoe obrazovatelnoe uchrezhdenie vysshego obrazovaniya "Sankt-Peterburgskij gosudarstvennyj universitet" (SPbGU) ; patent attorney A. A. Matveev. — No. 2017138165 ; req. 11/01/2017 ; publ. 01/17/2019, bul. no. 2. — 16 p. : il.

22. Infrared detector of circularly polarized radiation based on graphene : patent RU 2805784 C1 : Int. Cl. G01J 4/04 / A. G. Rybkin [et al.] ; applicant federalnoe gosudarstvennoe byudzhetnoe obrazovatelnoe uchrezhdenie vysshego obrazovaniya "Sankt-Peterburgskij gosudarstvennyj universitet" (SPbGU) ; patent attorneys A. A. Matveev, T. I. Matveeva, I. F. Leonov. — No. 2023109819 ; req. 04/17/2023 ; publ. 10/24/2023, bul. no. 30. — 11 p. : il.

23. Program for recording photoelectron spectra (XPS spectra) : certificate of state registration of the computer program 2020610365 / A. G. Rybkin [et al.] ; applicant federalnoe gosudarstvennoe byudzhetnoe obrazovatelnoe uchrezhdenie vysshego obrazovaniya "Sankt-Peterburgskij gosudarstvennyj universitet" (SPbGU). — No. 2019666984 ; req. 12/19/2019 ; publ. 01/13/2020.

24. *F. J. Himpsel J. E. Ortega, G. J. M.* Magnetic nanostructures / G. J. M. F. J. Himpsel J. E. Ortega, R. F. Willis // Advances in Physics. — 1998. — Vol. 47, no. 4. — P. 511—597. — URL: https://doi.org/10.1080/000187398243519.

25. Exchange split quantum well states of a noble metal film on a magnetic substrate / C. Carbone [et al.] // Phys. Rev. Lett. — 1993. — Oct. — Vol. 71, issue 17. — P. 2805—2808. — URL: https://link.aps.org/doi/10.1103/PhysRevLett.71.2805.

26. *Garrison, K.* Spin polarization of quantum well states in copper thin films deposited on a Co(001) substrate / K. Garrison, Y. Chang, P. D. Johnson // Phys. Rev. Lett. — 1993. — Oct. — Vol. 71, issue 17. — P. 2801—2804. — URL: https://link.aps.org/doi/10.1103/PhysRevLett.71.2801.

27. *Ortega, J. E.* Quantum well states as mediators of magnetic coupling in superlattices / J. E. Ortega, F. J. Himpsel // Phys. Rev. Lett. — 1992. — Aug. — Vol. 69, issue 5. — P. 844—847. — URL: https://link.aps.org/doi/10.1103/PhysRevLett.69.844.

28. *Johnson, P. D.* Spin-polarized photoemission / P. D. Johnson // Reports on Progress in Physics. — 1997. — Nov. — Vol. 60, no. 11. — P. 1217. — URL: https://dx.doi.org/10.1088/0034-4885/60/11/002.

29. *Qiu, Z. Q.* Oscillatory interlayer magnetic coupling of wedged Co/Cu/Co sandwiches grown on Cu(100) by molecular beam epitaxy / Z. Q. Qiu, J. Pearson, S. D. Bader // Phys. Rev. B. — 1992. — Oct. — Vol. 46, issue 13. — P. 8659—8662. — URL: https://link.aps.org/doi/10.1103/PhysRevB.46.8659.

30. *Žutić, I.* Spintronics: Fundamentals and applications / I. Žutić, J. Fabian, S. Das Sarma // Rev. Mod. Phys. — 2004. — Apr. — Vol. 76, issue 2. — P. 323—410. — URL: https://link.aps.org/doi/10.1103/RevModPhys.76.323.

31. *Ahn, E. C.* 2D materials for spintronic devices / E. C. Ahn // npj 2D Materials and Applications. — 2020. — June. — Vol. 4, no. 1. — P. 17. — URL: https://doi.org/10.1038/s41699-020-0152-0.

32. *Barla, P.* Spintronic devices: a promising alternative to CMOS devices / P. Barla, V. K. Joshi, S. Bhat // Journal of Computational Electronics. — 2021. — Apr. — Vol. 20, no. 2. — P. 805—837. — URL: https://doi.org/10.1007/s10825-020-01648-6.

33. Electronic spin transport and spin precession in single graphene layers at room temperature / N. Tombros [et al.] // Nature. — 2007. — Aug. — Vol. 448, no. 7153. — P. 571—574. — URL: https://doi.org/10.1038/nature06037.

34. *Rashba, E.* Symmetry of energy bands in wurtzite-type crystals. II. Symmetry of bands taking into account spin interactions / E. Rashba, V. Sheka // Fizika tverdogo tela. — 1959. — Vol. 1, no. 2. — P. 162—176.

35. *Datta, S.* Electronic analog of the electro-optic modulator / S. Datta, B. Das // Appl. Phys. Lett. — 1990. — Vol. 56, no. 7. — P. 665—667. — URL: http://scitation.aip.org/content/aip/journal/apl/56/7/10.1063/1.102730.

36. Gate Control of Spin-Orbit Interaction in an Inverted $In_{0.53}Ga_{0.47}As/In_{0.52}Al_{0.48}As$ Heterostructure / J. Nitta [et al.] // Phys. Rev. Lett. — 1997. — Feb. — Vol. 78, issue 7. — P. 1335—1338. — URL: https://link.aps.org/doi/10.1103/PhysRevLett.78.1335.

37. Origin of Spin-Orbit Splitting for Monolayers of Au and Ag on W(110) and Mo(110) / A. M. Shikin [et al.] // Phys. Rev. Lett. — 2008. — Feb. — Vol. 100, issue 5. — P. 057601. — URL: https://link.aps.org/doi/10.1103/PhysRevLett.100.057601.

38. Quantum Cavity for Spin due to Spin-Orbit Interaction at a Metal Boundary / A. Varykhalov [et al.] // Phys. Rev. Lett. — 2008. — Dec. — Vol. 101, issue 25. — P. 256601. — URL: https://link.aps.org/doi/10.1103/PhysRevLett.101.256601.

39. Rashba-Type Spin-Orbit Splitting of Quantum Well States in Ultrathin Pb Films / J. H. Dil [et al.] // Phys. Rev. Lett. — 2008. — Dec. — Vol. 101, issue 26. — P. 266802. — URL: https://link.aps.org/doi/10.1103/PhysRevLett.101.266802.

40. Substrate-induced spin-orbit splitting of quantum-well and interface states in Au, Ag, and Cu layers of different thicknesses on W(110) and Mo(110) surfaces / A. M. Shikin [et al.] // Physics of the Solid State. — 2010. — July. — Vol. 52, no. 7. — P. 1515—1525. — URL: https://doi.org/10.1134/S1063783410070280.

41. New perspectives for Rashba spin–orbit coupling / A. Manchon [et al.] // Nature Materials. — 2015. — Sept. — Vol. 14, no. 9. — P. 871—882. — URL: https://doi.org/10.1038/nmat4360.

42. Rashba-like physics in condensed matter / G. Bihlmayer [et al.] // Nature Reviews Physics. — 2022. — Oct. — Vol. 4, no. 10. — P. 642—659. — URL: https://doi.org/10.1038/s42254-022-00490-y.

43. *D'yakonov*, *M. I.* Possibility of Orienting Electron Spins with Current / M. I. D'yakonov, V. I. Perel' // ZhETF Pis. — 1971. — Vol. 13, issue 11. — P. 657. — URL: http://jetpletters.ru/ps/0/article_24366.shtml.

44. Spin to Charge Conversion at Room Temperature by Spin Pumping into a New Type of Topological Insulator: α-Sn Films / J.-C. Rojas-Sánchez [et al.] // Phys. Rev. Lett. — 2016. — Mar. — Vol. 116, issue 9. — P. 096602. — URL: https://link.aps.org/doi/10.1103/PhysRevLett.116.096602.

45. *Lin*, *X.* Magnetization switching in van der Waals systems by spin-orbit torque / X. Lin, L. Zhu // Materials Today Electronics. — 2023. — Vol. 4. — P. 100037. — URL: https://www.sciencedirect.com/science/article/pii/S277294942300013X.

46. *Kane*, *C. L.* Quantum Spin Hall Effect in Graphene / C. L. Kane, E. J. Mele // Phys. Rev. Lett. — 2005. — Nov. — Vol. 95, issue 22. — P. 226801. — URL: http://link.aps.org/doi/10.1103/PhysRevLett.95.226801.

47. Experimental Observation of the Quantum Anomalous Hall Effect in a Magnetic Topological Insulator / C.-Z. Chang [et al.] // Science. — 2013. — Vol. 340, no. 6129. — P. 167—170. — URL: https://www.science.org/doi/abs/10.1126/science.1234414.

48. *Kitaev*, *A. Y.* Unpaired Majorana fermions in quantum wires / A. Y. Kitaev // Physics-Uspekhi. — 2001. — Oct. — Vol. 44, 10S. — P. 131. — URL: https://dx.doi.org/10.1070/1063-7869/44/10S/S29.

49. *Hasan, M. Z.* Colloquium: Topological insulators / M. Z. Hasan, C. L. Kane // Rev. Mod. Phys. — 2010. — Nov. — Vol. 82, issue 4. — P. 3045—3067. — URL: https://link.aps.org/doi/10.1103/RevModPhys.82.3045.

50. *Qi, X.-L.* Topological field theory of time-reversal invariant insulators / X.-L. Qi, T. L. Hughes, S.-C. Zhang // Phys. Rev. B. — 2008. — Nov. — Vol. 78, issue 19. — P. 195424. — URL: https://link.aps.org/doi/10.1103/PhysRevB.78.195424.

51. A tunable topological insulator in the spin helical Dirac transport regime / D. Hsieh [et al.] // Nature. — 2009. — Aug. — Vol. 460, no. 7259. — P. 1101—1105. — URL: https://doi.org/10.1038/nature08234.

52. Topological insulators in Bi_2Se_3, Bi_2Te_3 and Sb_2Te_3 with a single Dirac cone on the surface / H. Zhang [et al.] // Nature Physics. — 2009. — June. — Vol. 5, no. 6. — P. 438—442. — URL: https://doi.org/10.1038/nphys1270.

53. *Moore, J.* The next generation / J. Moore // Nature Physics. — 2009. — June. — Vol. 5, no. 6. — P. 378—380. — URL: https://doi.org/10.1038/nphys1294.

54. Electrical detection of charge-current-induced spin polarization due to spin-momentum locking in Bi_2Se_3 / C. H. Li [et al.] // Nature Nanotechnology. — 2014. — Mar. — Vol. 9, no. 3. — P. 218—224. — URL: https://doi.org/10.1038/nnano.2014.16.

55. Magnetization switching through giant spin–orbit torque in a magnetically doped topological insulator heterostructure / Y. Fan [et al.] // Nature Materials. — 2014. — July. — Vol. 13, no. 7. — P. 699—704. — URL: https://doi.org/10.1038/nmat3973.

56. Spin-transfer torque generated by a topological insulator / A. R. Mellnik [et al.] // Nature. — 2014. — July. — Vol. 511, no. 7510. — P. 449—451. — URL: https://doi.org/10.1038/nature13534.

57. Optimizing $\mathbf{Bi}_{2-x}\mathbf{Sb}_x\mathbf{Te}_{3-y}\mathbf{Se}_y$ solid solutions to approach the intrinsic topological insulator regime / Z. Ren [et al.] // Phys. Rev. B. — 2011. — Oct. — Vol. 84, issue 16. — P. 165311. — URL: https://link.aps.org/doi/10.1103/PhysRevB.84.165311.

58. Terahertz conductivity of topological surface states in Bi1.5Sb0.5Te1.8Se1.2 / C. S. Tang [et al.] // Scientific Reports. — 2013. — Dec. — Vol. 3, no. 1. — P. 3513. — URL: https://doi.org/10.1038/srep03513.

59. Quantized topological magnetoelectric effect of the zero-plateau quantum anomalous Hall state / J. Wang [et al.] // Phys. Rev. B. — 2015. — Aug. — Vol. 92, issue 8. — P. 081107. — URL: https://link.aps.org/doi/10.1103/PhysRevB.92.081107.

60. High-precision realization of robust quantum anomalous Hall state in a hard ferromagnetic topological insulator / C.-Z. Chang [et al.] // Nature Materials. — 2015. — May. — Vol. 14, no. 5. — P. 473—477. — URL: https://doi.org/10.1038/nmat4204.

61. Quantized Anomalous Hall Effect in Magnetic Topological Insulators / R. Yu [et al.] // Science. — 2010. — Vol. 329, no. 5987. — P. 61—64. — URL: https://www.science.org/doi/abs/10.1126/science.1187485.

62. *Pesin, D.* Spintronics and pseudospintronics in graphene and topological insulators / D. Pesin, A. H. MacDonald // Nature Materials. — 2012. — May. — Vol. 11, no. 5. — P. 409—416. — URL: https://doi.org/10.1038/nmat3305.

63. *Han, W.* Perspectives for spintronics in 2D materials / W. Han // APL Materials. — 2016. — Feb. — Vol. 4, no. 3. — P. 032401. — URL: https://doi.org/10.1063/1.4941712.

64. Magnetic topological insulators and quantum anomalous hall effect / X. Kou [et al.] // Solid State Communications. — 2015. — Vol. 215/216. — P. 34—53. — URL: https://www.sciencedirect.com/science/article/pii/S0038109814004438.

65. Oxide spin-orbitronics: spin–charge interconversion and topological spin textures / F. Trier [et al.] // Nature Reviews Materials. — 2022. — Apr. — Vol. 7, no. 4. — P. 258—274. — URL: https://doi.org/10.1038/s41578-021-00395-9.

66. Valleytronics in 2D materials / J. R. Schaibley [et al.] // Nature Reviews Materials. — 2016. — Aug. — Vol. 1, no. 11. — P. 16055. — URL: https://doi.org/10.1038/natrevmats.2016.55.

67. *Gilbert, M. J.* Topological electronics / M. J. Gilbert // Communications Physics. — 2021. — Apr. — Vol. 4, no. 1. — P. 70. — URL: https://doi.org/10.1038/s42005-021-00569-5.

68. Graphene products: introduction and market status. — 2023. — [Online; as of 20.09.2024]. https://www.graphene-info.com/graphene-products.

69. Graphene enabled products. — 2023. — [Online; as of 20.09.2024]. https://graphene-flagship.eu/about/first-10-years/products/.

70. Science and technology roadmap for graphene, related two-dimensional crystals, and hybrid systems / A. C. Ferrari [et al.] // Nanoscale. — 2015. — Vol. 7, issue 11. — P. 4598—4810. — URL: http://dx.doi.org/10.1039/C4NR01600A.

71. Recent Development of Graphene-Based Ink and Other Conductive Material-Based Inks for Flexible Electronics / D. S. Saidina [et al.] // Journal of Electronic Materials. — 2019. — June. — Vol. 48, no. 6. — P. 3428—3450. — URL: https://doi.org/10.1007/s11664-019-07183-w.

72. Graphene pads. — 2023. — [Online; as of 20.09.2024]. https://absoluteblack.cc/graphenpads-worlds-best-disc-brake-pads-disc-34-dura-ace.

73. *Bierman, J.* 4C Graphene compound / J. Bierman. — 2019. — [Online; as of 20.09.2024]. https://int.vittoria.com/pages/materials-1, https://www.bicyclerollingresistance.com/road-bike-reviews/vittoria-corsa-graphene2.

74. *Collomb, D.* Frontiers of graphene-based Hall-effect sensors / D. Collomb, P. Li, S. Bending // Journal of Physics: Condensed Matter. — 2021. — May. — Vol. 33, no. 24. — P. 243002. — URL: https://dx.doi.org/10.1088/1361-648X/abf7e2.

75. *Sun, J.* Application of graphene derivatives and their nanocomposites in tribology and lubrication: a review / J. Sun, S. Du // RSC Adv. — 2019. — Vol. 9, issue 69. — P. 40642—40661. — URL: http://dx.doi.org/10.1039/C9RA05679C.

76. Broadband image sensor array based on graphene–CMOS integration / S. Goossens [et al.] // Nature Photonics. — 2017. — June. — Vol. 11, no. 6. — P. 366—371. — URL: https://doi.org/10.1038/nphoton.2017.75.

77. Application of graphene in energy storage device – A review / A. Olabi [et al.] // Renewable and Sustainable Energy Reviews. — 2021. — Vol. 135. — P. 110026. — URL: https://www.sciencedirect.com/science/article/pii/S1364032120303178.

78. Graphene Acoustic Devices / H. Tian [et al.] // Graphene and Its Derivatives / ed. by I. Ahmad, F. I. Ezema. — Rijeka : IntechOpen, 2019. — Chap. 5. — URL: https://doi.org/10.5772/intechopen.81603.

79. *Wei*, *W.* Graphene-Based Electrode Materials for Neural Activity Detection / W. Wei, X. Wang // Materials. — 2021. — Vol. 14, no. 20. — P. 6170. — URL: https://www.mdpi.com/1996-1944/14/20/6170.

80. High-density transparent graphene arrays for predicting cellular calcium activity at depth from surface potential recordings / M. Ramezani [et al.] // Nature Nanotechnology. — 2024. — Jan. — URL: https://doi.org/10.1038/s41565-023-01576-z.

81. The electronic properties of graphene / A. H. Castro Neto [et al.] // Rev. Mod. Phys. — 2009. — Vol. 81. — P. 109.

82. *Yazyev*, *O. V.* Emergence of magnetism in graphene materials and nanostructures / O. V. Yazyev // Rep. Prog. Phys. — 2010. — Vol. 73, no. 5. — P. 056501. — URL: http://stacks.iop.org/0034-4885/73/i=5/a=056501.

83. Graphene spintronics / W. Han [et al.] // Nat. Nanotech. — 2014. — Vol. 9, no. 10. — P. 794—807.

84. Science and technology roadmap for graphene, related two-dimensional crystals, and hybrid systems / A. C. Ferrari [et al.] // Nanoscale. — 2015. — Vol. 7, no. 11. — P. 4598—4810.

85. Graphene spintronics: the European Flagship perspective / S. Roche [et al.] // 2D Mater. — 2015. — Vol. 2, no. 3. — P. 030202. — URL: http://stacks.iop.org/2053-1583/2/i=3/a=030202.

86. *Kane*, *C. L.* Z_2 Topological Order and the Quantum Spin Hall Effect / C. L. Kane, E. J. Mele // Phys. Rev. Lett. — 2005. — Sept. — Vol. 95, issue 14. — P. 146802. — URL: https://link.aps.org/doi/10.1103/PhysRevLett.95.146802.

87. *Phong*, *V. T.* Effective interactions in a graphene layer induced by the proximity to a ferromagnet / V. T. Phong, N. R. Walet, F. Guinea // 2D Materials. — 2017. — Dec. — Vol. 5, no. 1. — P. 014004. — URL: https://dx.doi.org/10.1088/2053-1583/aa9fca.

88. *Zhou, Y.* Realization of an Antiferromagnetic Superatomic Graphene: Dirac Mott Insulator and Circular Dichroism Hall Effect / Y. Zhou, F. Liu // Nano Letters. — 2021. — Jan. — Vol. 21, no. 1. — P. 230—235. — URL: https://doi.org/10.1021/acs.nanolett.0c03579.

89. Synthesis and characterization of triangulene / N. Pavliček [et al.] // Nature Nanotechnology. — 2017. — Apr. — Vol. 12, no. 4. — P. 308—311. — URL: https://doi.org/10.1038/nnano.2016.305.

90. Large magnetic exchange coupling in rhombus-shaped nanographenes with zigzag periphery / S. Mishra [et al.] // Nature Chemistry. — 2021. — June. — Vol. 13, no. 6. — P. 581—586. — URL: https://doi.org/10.1038/s41557-021-00678-2.

91. *Haldane, F. D. M.* Model for a Quantum Hall Effect without Landau Levels: Condensed-Matter Realization of the "Parity Anomaly" / F. D. M. Haldane // Phys. Rev. Lett. — 1988. — Oct. — Vol. 61, issue 18. — P. 2015—2018. — URL: https://link.aps.org/doi/10.1103/PhysRevLett.61.2015.

92. Quantum Spin Hall States and Topological Phase Transition in Germanene / P. Bampoulis [et al.] // Phys. Rev. Lett. — 2023. — May. — Vol. 130, issue 19. — P. 196401. — URL: https://link.aps.org/doi/10.1103/PhysRevLett.130.196401.

93. Magnetoelectric control of topological phases in graphene / H. Takenaka [et al.] // Phys. Rev. B. — 2019. — Sept. — Vol. 100, issue 12. — P. 125156. — URL: https://link.aps.org/doi/10.1103/PhysRevB.100.125156.

94. An epitaxial graphene platform for zero-energy edge state nanoelectronics / V. S. Prudkovskiy [et al.] // Nature Communications. — 2022. — Dec. — Vol. 13, no. 1. — P. 7814. — URL: https://doi.org/10.1038/s41467-022-34369-4.

95. Ultrahigh-mobility semiconducting epitaxial graphene on silicon carbide / J. Zhao [et al.] // Nature. — 2024. — Jan. — Vol. 625, no. 7993. — P. 60—65. — URL: https://doi.org/10.1038/s41586-023-06811-0.

96. Vacancy growth of monocrystalline SiC from Si by the method of self-consistent substitution of atoms / A. S. Grashchenko [et al.] // Catalysis Today. — 2022. — Vol. 397—399. — P. 375—378. — URL: https://www.sciencedirect.com/science/article/pii/S0920586121003680.

97. Semiconductor to metal transition in two-dimensional gold and its van der Waals heterostack with graphene / S. Forti [et al.] // Nature Communications. — 2020. — May. — Vol. 11, no. 1. — P. 2236. — URL: https://doi.org/10.1038/s41467-020-15683-1.

98. Observation of giant spin–orbit interaction in graphene and heavy metal heterostructures / A. M. Afzal [et al.] // RSC Adv. — 2019. — Vol. 9, issue 54. — P. 31797–31805. — URL: http://dx.doi.org/10.1039/C9RA06961E.

99. Induced superconductivity in graphene / H. B. Heersche [et al.] // Solid State Communications. — 2007. — Vol. 143, no. 1. — P. 72—76. — URL: https://www.sciencedirect.com/science/article/pii/S0038109807003031 ; Exploring graphene.

100. *Feigel'man, M. V.* Proximity-induced superconductivity in graphene / M. V. Feigel'man, M. A. Skvortsov, K. S. Tikhonov // JETP Letters. — 2008. — Feb. — Vol. 88, no. 11. — P. 747—751. — URL: https://doi.org/10.1134/S0021364008230100.

101. Controlling in-gap end states by linking nonmagnetic atoms and artificially-constructed spin chains on superconductors / L. Schneider [et al.] // Nature Communications. — 2020. — Sept. — Vol. 11, no. 1. — P. 4707. — URL: https://doi.org/10.1038/s41467-020-18540-3.

102. Spanning Fermi arcs in a two-dimensional magnet / Y.-J. Chen [et al.] // Nature Communications. — 2022. — Sept. — Vol. 13, no. 1. — P. 5309. — URL: https://doi.org/10.1038/s41467-022-32948-z.

103. Atmospheric stability and doping protection of noble-metal intercalated graphene on Ni(111) / D. Marchenko [et al.] // Applied Physics Letters. — 2011. — Vol. 98, no. 12. — P. 122111. — URL: https://doi.org/10.1063/1.3565248.

104. Room Temperature Ferromagnetism in Graphene/SiC(0001) System Intercalated by Fe and Co / S. O. Filnov [et al.] // physica status solidi (RRL) – Rapid Research Letters. — 2024. — Vol. 18, no. 3. — P. 2300336. — URL: https://onlinelibrary.wiley.com/doi/abs/10.1002/pssr.202300336.

105. Spin-orbit splitting of interface and quantum well states developed in thin Al layers on a W(110) surface / A. Rybkin [et al.] // Book of abstracts of 449. WE-Heraeus-Seminar "Rashba and related spin-orbit effects in metals". — 53604, Germany, Bad Honnef, Hauptstrasse 5 : Physikzentrum, 2010. — P. 44.

106. Rashba effect at magnetic metal surfaces / O. Krupin [et al.] // Phys. Rev. B. — 2005. — Vol. 71. — 201403(R).

107. Rashba Effect in the Graphene/Ni(111) System / Yu. S. Dedkov [et al.] // Phys. Rev. Lett. — 2008. — Mar. — Vol. 100, issue 10. — P. 107602. — URL: https://link.aps.org/doi/10.1103/PhysRevLett.100.107602.

108. Is There a Rashba Effect in Graphene on $3d$ Ferromagnets? / O. Rader [et al.] // Phys. Rev. Lett. — 2009. — Vol. 102. — P. 057602.

109. *Sakurai*, *J.* Modern Quantum Mechanics / J. Sakurai, J. Napolitano. — Addison-Wesley, 2011. — URL: https://www.google.ru/books/edition/_/N4I-AQAACAAJ?hl=en&sa=X&ved=2ahUKEwiEqZCVpJyHAxVTJxAIHUYaAjMQ8fIDegQIAxAn.

110. *Elliott*, *R. J.* Spin-Orbit Coupling in Band Theory—Character Tables for Some "Double" Space Groups / R. J. Elliott // Phys. Rev. — 1954. — Oct. — Vol. 96, issue 2. — P. 280—287. — URL: https://link.aps.org/doi/10.1103/PhysRev.96.280.

111. *Dresselhaus*, *G.* Spin-Orbit Interaction and the Effective Masses of Holes in Germanium / G. Dresselhaus, A. F. Kip, C. Kittel // Phys. Rev. — 1954. — July. — Vol. 95, issue 2. — P. 568—569. — URL: https://link.aps.org/doi/10.1103/PhysRev.95.568.

112. *Schlipf*, *M.* Dynamic Rashba-Dresselhaus Effect / M. Schlipf, F. Giustino // Phys. Rev. Lett. — 2021. — Dec. — Vol. 127, issue 23. — P. 237601. — URL: https://link.aps.org/doi/10.1103/PhysRevLett.127.237601.

113. *Kramers*, *H. A.* Théorie générale de la rotation paramagnétique dans les cristaux / H. A. Kramers // Proceedings of the Royal Netherlands Academy of Arts and Sciences (in French). — 1930. — T. 33, n° 6-10. — P. 959-972. — URL : https://dwc.knaw.nl/DL/publications/PU00015981.pdf.

114. *LaShell, S.* Spin Splitting of an Au(111) Surface State Band Observed with Angle Resolved Photoelectron Spectroscopy / S. LaShell, B. A. McDougall, E. Jensen // Phys. Rev. Lett. — 1996. — Oct. — Vol. 77, issue 16. — P. 3419—3422. — URL: https://link.aps.org/doi/10.1103/PhysRevLett.77.3419.

115. *Rotenberg, E.* Spin-Orbit Coupling Induced Surface Band Splitting in Li/W(110) and Li/Mo(110) / E. Rotenberg, J. W. Chung, S. D. Kevan // Phys. Rev. Lett. — 1999. — May. — Vol. 82, issue 20. — P. 4066—4069. — URL: https://link.aps.org/doi/10.1103/PhysRevLett.82.4066.

116. *Petersen, L.* A simple tight-binding model of spin–orbit splitting of sp-derived surface states / L. Petersen, P. Hedegård // Surface Science. — 2000. — Vol. 459, no. 1. — P. 49—56. — URL: https://www.sciencedirect.com/science/article/pii/S0039602800004416.

117. Origin of Spin-Orbit Splitting for Monolayers of Au and Ag on W(110) and Mo(110) / A. M. Shikin [et al.] // Phys. Rev. Lett. — 2008. — Feb. — Vol. 100, issue 5. — P. 057601. — URL: https://link.aps.org/doi/10.1103/PhysRevLett.100.057601.

118. *Bychkov, Yu. A.* Properties of a two-dimensional electron gas with lifted spectral degeneracy / Yu. A. Bychkov, E. I. Rashba // Pis'ma v ZHETF. — 1984. — Vol. 39, no. 2. — P. 66—69.

119. A first-principles study on the Rashba effect in surface systems / M. Nagano [et al.] // Journal of Physics: Condensed Matter. — 2009. — Jan. — Vol. 21, no. 6. — P. 064239. — URL: https://dx.doi.org/10.1088/0953-8984/21/6/064239.

120. Scaling law for Rashba-type spin splitting in quantum-well films / R. Noguchi [et al.] // Phys. Rev. B. — 2021. — Nov. — Vol. 104, issue 18. — P. L180409. — URL: https://link.aps.org/doi/10.1103/PhysRevB.104.L180409.

121. Band-structure topologies of graphene: Spin-orbit coupling effects from first principles / M. Gmitra [et al.] // Phys. Rev. B. — 2009. — Dec. — Vol. 80, issue 23. — P. 235431. — URL: https://link.aps.org/doi/10.1103/PhysRevB.80.235431.

122. Graphene spintronics / W. Han [et al.] // Nature Nanotechnology. — 2014. — Vol. 9. — P. 794—807.

123. Experimental Demonstration of xor Operation in Graphene Magnetologic Gates at Room Temperature / H. Wen [et al.] // Phys. Rev. Applied. — 2016. — Apr. — Vol. 5, issue 4. — P. 044003. — URL: https://link.aps.org/doi/10.1103/PhysRevApplied.5.044003.

124. Transport Properties of Graphene in the High-Current Limit / A. Barreiro [et al.] // Phys. Rev. Lett. — 2009. — Aug. — Vol. 103, issue 7. — P. 076601. — URL: https://link.aps.org/doi/10.1103/PhysRevLett.103.076601.

125. *Cho, S.* Gate-tunable graphene spin valve / S. Cho, Y.-F. Chen, M. S. Fuhrer // Applied Physics Letters. — 2007. — Sept. — Vol. 91, no. 12. — P. 123105. — URL: https://doi.org/10.1063/1.2784934.

126. Intrinsic and Rashba spin-orbit interactions in graphene sheets / H. Min [et al.] // Phys. Rev. B. — 2006. — Oct. — Vol. 74, issue 16. — P. 165310. — URL: https://link.aps.org/doi/10.1103/PhysRevB.74.165310.

127. *Bernevig, B. A.* Quantum Spin Hall Effect / B. A. Bernevig, S.-C. Zhang // Phys. Rev. Lett. — 2006. — Mar. — Vol. 96, issue 10. — P. 106802. — URL: https://link.aps.org/doi/10.1103/PhysRevLett.96.106802.

128. Engineering a Robust Quantum Spin Hall State in Graphene via Adatom Deposition / C. Weeks [et al.] // Phys. Rev. X. — 2011. — Oct. — Vol. 1, issue 2. — P. 021001. — URL: https://link.aps.org/doi/10.1103/PhysRevX.1.021001.

129. Giant Topological Insulator Gap in Graphene with $5d$ Adatoms / J. Hu [et al.] // Phys. Rev. Lett. — 2012. — Dec. — Vol. 109, issue 26. — P. 266801. — URL: https://link.aps.org/doi/10.1103/PhysRevLett.109.266801.

130. Transport study of graphene adsorbed with indium adatoms / Z. Jia [et al.] // Phys. Rev. B. — 2015. — Feb. — Vol. 91, issue 8. — P. 085411. — URL: https://link.aps.org/doi/10.1103/PhysRevB.91.085411.

131. *Chandni, U.* Transport in indium-decorated graphene / U. Chandni, E. A. Henriksen, J. P. Eisenstein // Phys. Rev. B. — 2015. — June. — Vol. 91, issue 24. — P. 245402. — URL: https://link.aps.org/doi/10.1103/PhysRevB.91.245402.

132. Long- versus Short-Range Scattering in Doped Epitaxial Graphene / C. Straßer [et al.] // Nano Letters. — 2015. — May. — Vol. 15, no. 5. — P. 2825–2829. — URL: https://doi.org/10.1021/nl504155f.

133. *Elias, J. A.* Unexpected Hole Doping of Graphene by Osmium Adatoms / J. A. Elias, E. A. Henriksen // Annalen der Physik. — 2020. — Vol. 532, no. 2. — P. 1900294. — URL: https://onlinelibrary.wiley.com/doi/abs/10.1002/andp.201900294.

134. *Brey, L.* Spin-orbit coupling in graphene induced by adatoms with outer-shell p orbitals / L. Brey // Phys. Rev. B. — 2015. — Dec. — Vol. 92, issue 23. — P. 235444. — URL: https://link.aps.org/doi/10.1103/PhysRevB.92.235444.

135. Spatial variation of a giant spin-orbit effect induces electron confinement in graphene on Pb islands / F. Calleja [et al.] // Nat. Phys. — 2015. — Vol. 11, no. 1. — P. 43—47.

136. Spin-Orbit Coupling Induced Gap in Graphene on Pt(111) with Intercalated Pb Monolayer / I. I Klimovskikh [et al.] // ACS Nano. — 2017. — Vol. 11, issue 1. — P. 368—374. — URL: https://pubs.acs.org/doi/10.1021/acsnano.6b05982.

137. Evidence of large spin-orbit coupling effects in quasi-free-standing graphene on Pb/Ir(1 1 1) / M. M. Otrokov [et al.] // 2D Materials. — 2018. — June. — Vol. 5, no. 3. — P. 035029. — URL: https://doi.org/10.1088/2053-1583/aac596.

138. Colossal enhancement of spin-orbit coupling in weakly hydrogenated graphene / J. Balakrishnan [et al.] // Nat. Phys. — 2013. — Vol. 9, no. 5. — P. 284—287.

139. Enhanced spin–orbit coupling in dilute fluorinated graphene / A. Avsar [et al.] // 2D Mater. — 2015. — Vol. 2, no. 4. — P. 044009. — URL: http://stacks.iop.org/2053-1583/2/i=4/a=044009.

140. Spin–orbit proximity effect in graphene / A. Avsar [et al.] // Nat. Commun. — 2014. — Vol. 5. — P. 4875.

141. Quantum Spin Hall States and Topological Phase Transition in Germanene / P. Bampoulis [et al.] // Phys. Rev. Lett. — 2023. — May. — Vol. 130, issue 19. — P. 196401. — URL: https://link.aps.org/doi/10.1103/PhysRevLett.130.196401.

142. Germanene: the germanium analogue of graphene / A. Acun [et al.] // Journal of Physics: Condensed Matter. — 2015. — Oct. — Vol. 27, no. 44. — P. 443002. — URL: https://dx.doi.org/10.1088/0953-8984/27/44/443002.

143. *Liu, C.-C.* Quantum Spin Hall Effect in Silicene and Two-Dimensional Germanium / C.-C. Liu, W. Feng, Y. Yao // Phys. Rev. Lett. — 2011. — Aug. — Vol. 107, issue 7. — P. 076802. — URL: https://link.aps.org/doi/10.1103/PhysRevLett.107.076802.

144. *Martins, C.* Coulomb correlations in 4d and 5d oxides from first principles—or how spin–orbit materials choose their effective orbital degeneracies / C. Martins, M. Aichhorn, S. Biermann // Journal of Physics: Condensed Matter. — 2017. — May. — Vol. 29, no. 26. — P. 263001. — URL: https://dx.doi.org/10.1088/1361-648X/aa648f.

145. Maximal Rashba-like spin splitting via kinetic-energy-coupled inversion-symmetry breaking / V. Sunko [et al.] // Nature. — 2017. — Sept. — Vol. 549, no. 7673. — P. 492—496. — URL: https://doi.org/10.1038/nature23898.

146. The Rashba Scale: Emergence of Band Anti-crossing as a Design Principle for Materials with Large Rashba Coefficient / C. Mera Acosta [et al.] // Matter. — 2020. — Vol. 3, no. 1. — P. 145—165. — URL: https://www.sciencedirect.com/science/article/pii/S2590238520302393.

147. Relativistic Corrections to the Band Structure of Tetrahedrally Bonded Semiconductors / F. Herman [et al.] // Phys. Rev. Lett. — 1963. — Dec. — Vol. 11, issue 12. — P. 541—545. — URL: https://link.aps.org/doi/10.1103/PhysRevLett.11.541.

148. *Martin, W. C.* Table of Spin-Orbit Energies for p-Electrons in Neutral Atomic (core)np Configurations / W. C. Martin // J Res Natl Bur Stand A Phys Chem. — United States, 1971. — Mar. — Vol. 75A, no. 2. — P. 109—111.

149. Electronic and Magnetic Properties of Quasifreestanding Graphene on Ni / A. Varykhalov [et al.] // Phys. Rev. Lett. — 2008. — Vol. 101. — P. 157601.

150. Tunable Fermi level and hedgehog spin texture in gapped graphene / A. Varykhalov [et al.] // Nature Communications. — 2015. — July. — Vol. 6, no. 1. — P. 7610. — URL: https://doi.org/10.1038/ncomms8610.

151. *Kuemmeth, F.* Giant spin rotation under quasiparticle-photoelectron conversion: Joint effect of sublattice interference and spin-orbit coupling / F. Kuemmeth, E. I. Rashba // Phys. Rev. B. — 2009. — Dec. — Vol. 80, issue 24. — P. 241409. — URL: https://link.aps.org/doi/10.1103/PhysRevB.80.241409.

152. *Rashba, E. I.* Graphene with structure-induced spin-orbit coupling: Spin-polarized states, spin zero modes, and quantum Hall effect / E. I. Rashba // Phys. Rev. B. — 2009. — Apr. — Vol. 79, issue 16. — P. 161409. — URL: http://link.aps.org/doi/10.1103/PhysRevB.79.161409.

153. *Tan, X.-D.* Gate tunable spin transport in graphene with Rashba spin-orbit coupling / X.-D. Tan, X.-P. Liao, L. Sun // Superlattices and Microstructures. — 2016. — Vol. 98. — P. 473—491. — URL: https://www.sciencedirect.com/science/article/pii/S0749603616304591.

154. *Sawińska, J.* Complex spin texture of Dirac cones induced via spin-orbit proximity effect in graphene on metals / J. Sawińska, J. I. Cerdá // Phys. Rev. B. — 2018. — Aug. — Vol. 98, issue 7. — P. 075436. — URL: https://link.aps.org/doi/10.1103/PhysRevB.98.075436.

155. *Voloshina, E.* Realistic Large-Scale Modeling of Rashba and Induced Spin–Orbit Effects in Graphene/High-Z-Metal Systems / E. Voloshina, Y. Dedkov // Advanced Theory and Simulations. — 2018. — Vol. 1, no. 10. — P. 1800063.

156. *Sawińska, J.* Spin–orbit proximity effect in graphene on metallic substrates: decoration versus intercalation with metal adatoms / J. Sawińska, J. I. Cerdá // New Journal of Physics. — 2019. — July. — Vol. 21, no. 7. — P. 073018. — URL: https://doi.org/10.1088%2F1367-2630%2Fab2bc7.

157. *Heisenberg, W.* Zur Theorie des Ferromagnetismus / W. Heisenberg // Zeitschrift für Physik (in German). — 1928. — Sep. — Jg. 49, Nr. 9. — S. 619–636. — URL: https://doi.org/10.1007/BF01328601.

158. *Stoner, E. C.* Collective electron ferromagnetism / E. C. Stoner // Proceedings of the Royal Society of London. Series A. Mathematical and Physical Sciences. — 1938. — Vol. 165, no. 922. — P. 372—414. — URL: https://royalsocietypublishing.org/doi/abs/10.1098/rspa.1938.0066.

159. Zeeman-type spin splitting controlled by an electric field / H. Yuan [et al.] // Nature Physics. — 2013. — Sept. — Vol. 9, no. 9. — P. 563—569. — URL: https://doi.org/10.1038/nphys2691.

160. *Mera Acosta*, *C.* Zeeman-type spin splitting in nonmagnetic three-dimensional compounds / C. Mera Acosta, A. Fazzio, G. M. Dalpian // npj Quantum Materials. — 2019. — Aug. — Vol. 4, no. 1. — P. 41. — URL: https://doi.org/10.1038/s41535-019-0182-z.

161. Giant Magnetic Band Gap in the Rashba-Split Surface State of Vanadium-Doped BiTeI: A Combined Photoemission and Ab Initio Study / I. I. Klimovskikh [et al.] // Scientific Reports. — 2017. — June. — Vol. 7, no. 1. — P. 3353. — URL: https://doi.org/10.1038/s41598-017-03507-0.

162. Rashba-like spin splitting around non-time-reversal-invariant momenta / L. L. Tao [et al.] // Phys. Rev. B. — 2023. — June. — Vol. 107, issue 23. — P. 235138. — URL: https://link.aps.org/doi/10.1103/PhysRevB.107.235138.

163. Asymmetric band gaps in a Rashba film system / C. Carbone [et al.] // Phys. Rev. B. — 2016. — Mar. — Vol. 93, issue 12. — P. 125409. — URL: https://link.aps.org/doi/10.1103/PhysRevB.93.125409.

164. *Xiao*, *D.* Valley-Contrasting Physics in Graphene: Magnetic Moment and Topological Transport / D. Xiao, W. Yao, Q. Niu // Phys. Rev. Lett. — 2007. — Dec. — Vol. 99, issue 23. — P. 236809. — URL: https://link.aps.org/doi/10.1103/PhysRevLett.99.236809.

165. Gated silicene as a tunable source of nearly 100% spin-polarized electrons / W.-F. Tsai [et al.] // Nature Communications. — 2013. — Feb. — Vol. 4, no. 1. — P. 1500. — URL: https://doi.org/10.1038/ncomms2525.

166. *Haugen*, *H.* Spin transport in proximity-induced ferromagnetic graphene / H. Haugen, D. Huertas-Hernando, A. Brataas // Phys. Rev. B. — 2008. — Mar. — Vol. 77, issue 11. — P. 115406. — URL: https://link.aps.org/doi/10.1103/PhysRevB.77.115406.

167. *Semenov*, *Y. G.* Spin field effect transistor with a graphene channel / Y. G. Semenov, K. W. Kim, J. M. Zavada // Appl. Phys. Lett. — 2007. — Vol. 91, no. 15. — URL: http://scitation.aip.org/content/aip/journal/apl/91/15/10.1063/1.2798596.

168. Integration of the Ferromagnetic Insulator EuO onto Graphene / A. G. Swartz [et al.] // ACS Nano. — 2012. — Vol. 6, no. 11. — P. 10063—10069. — URL: https://doi.org/10.1021/nn303771f ; PMID: 23083411.

169. *Bora, M.* Magnetic proximity effect in two-dimensional van der Waals heterostructure / M. Bora, P. Deb // Journal of Physics: Materials. — 2021. — May. — Vol. 4, no. 3. — P. 034014. — URL: https://dx.doi.org/10.1088/2515-7639/abf884.

170. High-Temperature Magnetism in Graphene Induced by Proximity to EuO / D. V. Averyanov [et al.] // ACS Applied Materials & Interfaces. — 2018. — Vol. 10, no. 24. — P. 20767—20774. — URL: https://doi.org/10.1021/acsami.8b04289 ; PMID: 29806934.

171. Exploring the interfacial coupling between graphene and the antiferromagnetic insulator $MnPSe_3$ / X. Yi [et al.] // Phys. Rev. B. — 2023. — Sept. — Vol. 108, issue 12. — P. 125427. — URL: https://link.aps.org/doi/10.1103/PhysRevB.108.125427.

172. Realization of quantum anomalous Hall effect in graphene from $n-p$ codoping-induced stable atomic adsorption / X. Deng [et al.] // Phys. Rev. B. — 2017. — Mar. — Vol. 95, issue 12. — P. 121410. — URL: https://link.aps.org/doi/10.1103/PhysRevB.95.121410.

173. Epitaxial B-Graphene: Large-Scale Growth and Atomic Structure / D. Yu. Usachov [et al.] // ACS Nano. — 2015. — Vol. 9, no. 7. — P. 7314—7322. — URL: http://dx.doi.org/10.1021/acsnano.5b02322.

174. Large-Scale Sublattice Asymmetry in Pure and Boron-Doped Graphene / D. Yu. Usachov [et al.] // Nano Lett. — 2016. — Vol. 16, no. 7. — P. 4535—4543.

175. Atomic-scale control of graphene magnetism by using hydrogen atoms / H. González-Herrero [et al.] // Science. — 2016. — Vol. 352, no. 6284. — P. 437—441.

176. Emergent ferromagnetism near three-quarters filling in twisted bilayer graphene / A. L. Sharpe [et al.] // Science. — 2019. — Vol. 365, no. 6453. — P. 605—608. — URL: https://www.science.org/doi/abs/10.1126/science.aaw3780.

177. *Santos, E. J. G.* Magnetism of substitutional Co impurities in graphene: Realization of single π vacancies / E. J. G. Santos, D. Sánchez-Portal, A. Ayuela // Phys. Rev. B. — 2010. — Mar. — Vol. 81, issue 12. — P. 125433. — URL: https://link.aps.org/doi/10.1103/PhysRevB.81.125433.

178. *Zhou, Y.* Realization of an Antiferromagnetic Superatomic Graphene: Dirac Mott Insulator and Circular Dichroism Hall Effect / Y. Zhou, F. Liu // Nano Letters. — 2021. — Vol. 21, no. 1. — P. 230—235. — URL: ttps://doi.org/10.1021/acs.nanolett.0c03579.

179. *Hubbard, J.* Electron correlations in narrow energy bands / J. Hubbard, B. H. Flowers // Proceedings of the Royal Society of London. Series A. Mathematical and Physical Sciences. — 1963. — Vol. 276, no. 1365. — P. 238—257. — URL: https://royalsocietypublishing.org/doi/abs/10.1098/rspa.1963.0204.

180. Quantum spin liquid emerging in two-dimensional correlated Dirac fermions / Z. Y. Meng [et al.] // Nature. — 2010. — Apr. — Vol. 464, no. 7290. — P. 847—851. — URL: https://doi.org/10.1038/nature08942.

181. Electrically Tunable Quantum Anomalous Hall Effect in Graphene Decorated by $5d$ Transition-Metal Adatoms / H. Zhang [et al.] // Phys. Rev. Lett. — 2012. — Feb. — Vol. 108, issue 5. — P. 056802. — URL: https://link.aps.org/doi/10.1103/PhysRevLett.108.056802.

182. *Chang, C.-Z.* Quantum anomalous Hall effect in time-reversal-symmetry breaking topological insulators / C.-Z. Chang, M. Li // Journal of Physics: Condensed Matter. — 2016. — Feb. — Vol. 28, no. 12. — P. 123002. — URL: https://dx.doi.org/10.1088/0953-8984/28/12/123002.

183. *Klitzing, K. v.* New Method for High-Accuracy Determination of the Fine-Structure Constant Based on Quantized Hall Resistance / K. v. Klitzing, G. Dorda, M. Pepper // Phys. Rev. Lett. — 1980. — Aug. — Vol. 45, issue 6. — P. 494—497. — URL: https://link.aps.org/doi/10.1103/PhysRevLett.45.494.

184. *Paalanen, M. A.* Quantized Hall effect at low temperatures / M. A. Paalanen, D. C. Tsui, A. C. Gossard // Phys. Rev. B. — 1982. — Apr. — Vol. 25, issue 8. — P. 5566—5569. — URL: https://link.aps.org/doi/10.1103/PhysRevB.25.5566.

185. *Büttiker, M.* Absence of backscattering in the quantum Hall effect in multi-probe conductors / M. Büttiker // Phys. Rev. B. — 1988. — Nov. — Vol. 38, issue 14. — P. 9375—9389. — URL: https://link.aps.org/doi/10.1103/PhysRevB.38.9375.

186. *Simon*, *B.* Holonomy, the Quantum Adiabatic Theorem, and Berry's Phase / B. Simon // Phys. Rev. Lett. — 1983. — Dec. — Vol. 51, issue 24. — P. 2167—2170. — URL: https://link.aps.org/doi/10.1103/PhysRevLett.51.2167.

187. *Banerjee*, *D.* Quantum Hall Effect and Berry Phase / D. Banerjee, P. Bandyopadhyay // Modern Physics Letters B. — 1994. — Vol. 08, no. 26. — P. 1643—1653. — URL: https://doi.org/10.1142/S0217984994001588.

188. *Berry*, *M. V.* Quantal phase factors accompanying adiabatic changes / M. V. Berry // Proceedings of the Royal Society of London. A. Mathematical and Physical Sciences. — 1984. — Vol. 392, no. 1802. — P. 45—57. — URL: https://royalsocietypublishing.org/doi/abs/10.1098/rspa.1984.0023.

189. Quantized Hall Conductance in a Two-Dimensional Periodic Potential / D. J. Thouless [et al.] // Phys. Rev. Lett. — 1982. — Aug. — Vol. 49, issue 6. — P. 405—408. — URL: https://link.aps.org/doi/10.1103/PhysRevLett.49.405.

190. *Watson*, *A. B.* Mathematical aspects of the Kubo formula for electrical conductivity with dissipation / A. B. Watson, D. Margetis, M. Luskin // Japan Journal of Industrial and Applied Mathematics. — 2023. — Sept. — Vol. 40, no. 3. — P. 1765—1795. — URL: https://doi.org/10.1007/s13160-023-00613-7.

191. Dirac-fermion-mediated ferromagnetism in a topological insulator / J. G. Checkelsky [et al.] // Nature Physics. — 2012. — Oct. — Vol. 8, no. 10. — P. 729—733. — URL: https://doi.org/10.1038/nphys2388.

192. Topological quantum materials / K. L. Wang [et al.] // MRS Bulletin. — 2020. — May. — Vol. 45, no. 5. — P. 373—379. — URL: https://doi.org/10.1557/mrs.2020.122.

193. 2D ferromagnetism in europium/graphene bilayers / I. S. Sokolov [et al.] // Mater. Horiz. — 2020. — Vol. 7, issue 5. — P. 1372—1378. — URL: http://dx.doi.org/10.1039/C9MH01988J.

194. High-Temperature Magnetism in Graphene Induced by Proximity to EuO / D. V. Averyanov [et al.] // ACS Applied Materials & Interfaces. — 2018. — Vol. 10, no. 24. — P. 20767—20774. — URL: https://doi.org/10.1021/acsami.8b04289 ; PMID: 29806934.

195. Quantum Anomalous Hall Effects in Graphene from Proximity-Induced Uniform and Staggered Spin-Orbit and Exchange Coupling / P. Högl [et al.] // Phys. Rev. Lett. — 2020. — Mar. — Vol. 124, issue 13. — P. 136403. — URL: https://link.aps.org/doi/10.1103/PhysRevLett.124.136403.

196. Quantum Anomalous Hall and Spin Hall Effects in Magnetic Graphene / T. S. Ghiasi [et al.]. — 2023. — arXiv: 2312.07515 [cond-mat.mes-hall].

197. *Averin, D.* Quantum computation with quasiparticles of the fractional quantum Hall effect / D. Averin, V. Goldman // Solid State Communications. — 2001. — Vol. 121, no. 1. — P. 25—28. — URL: https://www.sciencedirect.com/science/article/pii/S0038109801004471.

198. Fractional quantum anomalous Hall effect in multilayer graphene / Z. Lu [et al.] // Nature. — 2024. — Feb. — Vol. 626, no. 8000. — P. 759—764. — URL: https://doi.org/10.1038/s41586-023-07010-7.

199. Observation of fractionally quantized anomalous Hall effect / H. Park [et al.] // Nature. — 2023. — Oct. — Vol. 622, no. 7981. — P. 74—79. — URL: https://doi.org/10.1038/s41586-023-06536-0.

200. Non-Abelian braiding of graph vertices in a superconducting processor / T. I. Andersen [et al.] // Nature. — 2023. — June. — Vol. 618, no. 7964. — P. 264—269. — URL: https://doi.org/10.1038/s41586-023-05954-4.

201. Time-resolved photoemission apparatus achieving sub-20-meV energy resolution and high stability / Y. Ishida [et al.] // Review of Scientific Instruments. — 2014. — Dec. — Vol. 85, no. 12. — P. 123904. — URL: https://doi.org/10.1063/1.4903788.

202. Gigantic Surface Lifetime of an Intrinsic Topological Insulator / M. Neupane [et al.] // Phys. Rev. Lett. — 2015. — Sept. — Vol. 115, issue 11. — P. 116801. — URL: https://link.aps.org/doi/10.1103/PhysRevLett.115.116801.

203. Emergent photovoltage on SmB6 surface upon bulk-gap evolution revealed by pump-and-probe photoemission spectroscopy / Y. Ishida [et al.] // Scientific Reports. — 2015. — Feb. — Vol. 5, no. 1. — P. 8160. — URL: https://doi.org/10.1038/srep08160.

204. *Hüfner, S.* Photoelectron spectroscopy: principles and applications / S. Hüfner. — Berlin Heidelberg : Springer-Verlag, 1995.

205. *Himpsel, F. J.* Angle-resolved measurements of the photoemission of electrons in the study of solids / F. J. Himpsel // Adv. Phys. — 1983. — Vol. 32, no. 1. — P. 1—51.

206. *Seah, M. P.* Quantitative electron spectroscopy of surfaces: a standard data base for electron inelastic mean free paths in solids / M. P. Seah, W. A. Dench // Surf. Interface Anal. — 1979. — Vol. 1, no. 1. — P. 2—11.

207. *Feibelman, P. J.* Photoemission spectroscopy—Correspondence between quantum theory and experimental phenomenology / P. J. Feibelman, D. E. Eastman // Phys. Rev. B. — 1974. — Dec. — Vol. 10, issue 12. — P. 4932—4947. — URL: https://link.aps.org/doi/10.1103/PhysRevB.10.4932.

208. Handbook of X-Ray Photoelectron Spectroscopy / J. F. Moulder [et al.] //. — 1992. — URL: https://api.semanticscholar.org/CorpusID:133719866.

209. *Yeh, J.* Atomic subshell photoionization cross sections and asymmetry parameters: $1 \leqslant Z \leqslant 103$ / J. Yeh, I. Lindau // Atomic Data and Nuclear Data Tables. — 1985. — Vol. 32, no. 1. — P. 1—155. — URL: https://www.sciencedirect.com/science/article/pii/0092640X85900166.

210. *Park, C.-H.* Spin Polarization of Photoelectrons from Topological Insulators / C.-H. Park, S. G. Louie // Phys. Rev. Lett. — 2012. — Aug. — Vol. 109, issue 9. — P. 097601. — URL: https://link.aps.org/doi/10.1103/PhysRevLett.109.097601.

211. Photoelectron spin-flipping and texture manipulation in a topological insulator / C. Jozwiak [et al.] // Nature Physics. — 2013. — May. — Vol. 9, no. 5. — P. 293—298. — URL: https://doi.org/10.1038/nphys2572.

212. Photoemission of Bi_2Se_3 with Circularly Polarized Light: Probe of Spin Polarization or Means for Spin Manipulation? / J. Sánchez-Barriga [et al.] // Phys. Rev. X. — 2014. — Mar. — Vol. 4, issue 1. — P. 011046. — URL: https://link.aps.org/doi/10.1103/PhysRevX.4.011046.

213. *Jozwiak, C. A.* New Spin on Photoemission Spectroscopy : PhD thesis / Jozwiak C. A. — University of California, Berkeley, 2010. — URL: https://escholarship.org/uc/item/54b701zz.

214. Reply to “Comment on ‘Spin–Orbit Coupling Induced Gap in Graphene on Pt(111) with Intercalated Pb Monolayer”’ / I. I. Klimovskikh [et al.] // ACS Nano. — 2017. — Nov. — Vol. 11, no. 11. — P. 10630—10632. — URL: https://doi.org/10.1021/acsnano.7b06779.

215. Quantum Cavity for Spin due to Spin-Orbit Interaction at a Metal Boundary / A. Varykhalov [et al.] // Phys. Rev. Lett. — 2008. — Dec. — Vol. 101, issue 25. — P. 256601. — URL: https://link.aps.org/doi/10.1103/PhysRevLett.101.256601.

216. Substrate-induced spin-orbit splitting of quantum-well and interface states in Au, Ag, and Cu layers of different thicknesses on W(110) and Mo(110) surfaces / A. M. Shikin [et al.] // Physics of the Solid State. — 2010. — July. — Vol. 52, no. 7. — P. 1515—1525. — URL: https://doi.org/10.1134%2FS1063783410070280.

217. Ordered Vacancy Network Induced by the Growth of Epitaxial Graphene on Pt(111) / G. Otero [et al.] // Phys. Rev. Lett. — 2010. — Nov. — Vol. 105, issue 21. — P. 216102. — URL: https://link.aps.org/doi/10.1103/PhysRevLett.105.216102.

218. Epitaxial growth and structural property of graphene on Pt(111) / M. Gao [et al.] // Appl. Phys. Lett. — 2011. — Vol. 98, no. 3. — P. 033101. — URL: https://doi.org/10.1063/1.3543624.

219. Strain-Driven Moiré Superstructures of Epitaxial Graphene on Transition Metal Surfaces / P. Merino [et al.] // ACS Nano. — 2011. — July. — Vol. 5, no. 7. — P. 5627—5634. — URL: https://doi.org/10.1021/nn201200j.

220. Hole doping, hybridization gaps, and electronic correlation in graphene on a platinum substrate / J. Hwang [et al.] // Nanoscale. — 2017. — Vol. 9, issue 32. — P. 11498—11503. — URL: http://dx.doi.org/10.1039/C7NR03080K.

221. Chemistry below graphene: Decoupling epitaxial graphene from metals by potential-controlled electrochemical oxidation / I. Palacio [et al.] // Carbon. — 2018. — Vol. 129. — P. 837—846. — URL: http://www.sciencedirect.com/science/article/pii/S0008622317313374.

222. Preparation of graphene bilayers on platinum by sequential chemical vapour deposition / J. Halle [et al.] // Phys. Chem. Chem. Phys. — 2019. — Vol. 21, issue 6. — P. 3140—3144. — URL: http://dx.doi.org/10.1039/C8CP07569G.

223. Monolayer charge-neutral graphene on platinum with extremely weak electron-phonon coupling / W. Yao [et al.] // Phys. Rev. B. — 2015. — Sept. — Vol. 92, issue 11. — P. 115421. — URL: https://link.aps.org/doi/10.1103/PhysRevB.92.115421.

224. *Kohn, W.* Self-Consistent Equations Including Exchange and Correlation Effects / W. Kohn, L. J. Sham // Phys. Rev. — 1965. — Nov. — Vol. 140, 4A. — A1133—A1138. — URL: https://link.aps.org/doi/10.1103/PhysRev.140.A1133.

225. *Giarrusso, S.* Exchange-Correlation Energy Densities and Response Potentials: Connection between Two Definitions and Analytical Model for the Strong-Coupling Limit of a Stretched Bond / S. Giarrusso, P. Gori-Giorgi // The Journal of Physical Chemistry A. — 2020. — Mar. — Vol. 124, no. 12. — P. 2473—2482. — URL: https://doi.org/10.1021/acs.jpca.9b10538.

226. Scaling deep learning for materials discovery / A. Merchant [et al.] // Nature. — 2023. — Dec. — Vol. 624, no. 7990. — P. 80—85. — URL: https://doi.org/10.1038/s41586-023-06735-9.

227. Neural-network density functional theory / Y. Li [et al.]. — 2024. — arXiv: 2403.11287 [physics.comp-ph].

228. *Ozaki, T.* Variationally optimized atomic orbitals for large-scale electronic structures / T. Ozaki // Phys. Rev. B. — 2003. — Apr. — Vol. 67, issue 15. — P. 155108. — URL: https://link.aps.org/doi/10.1103/PhysRevB.67.155108.

229. *Ozaki, T.* Numerical atomic basis orbitals from H to Kr / T. Ozaki, H. Kino // Phys. Rev. B. — 2004. — May. — Vol. 69, issue 19. — P. 195113. — URL: https://link.aps.org/doi/10.1103/PhysRevB.69.195113.

230. *Troullier, N.* Efficient pseudopotentials for plane-wave calculations / N. Troullier, J. L. Martins // Physical review B. — 1991. — Vol. 43, no. 3. — P. 1993. — URL: https://doi.org/10.1103/PhysRevB.43.1993.

231. *Perdew, J. P.* Accurate and simple analytic representation of the electron-gas correlation energy / J. P. Perdew, Y. Wang // Phys. Rev. B. — 1992. — June. — Vol. 45, issue 23. — P. 13244—13249. — URL: https://link.aps.org/doi/10.1103/PhysRevB.45.13244.

232. *Perdew, J. P.* Generalized Gradient Approximation Made Simple / J. P. Perdew, K. Burke, M. Ernzerhof // Phys. Rev. Lett. — 1996. — Oct. — Vol. 77, issue 18. — P. 3865—3868.

233. *Blöchl*, *P. E.* Projector augmented-wave method / P. E. Blöchl // Phys. Rev. B. — 1994. — Dec. — Vol. 50, no. 24. — P. 17953—17979.

234. *Kresse*, *G.* Efficient iterative schemes for ab initio total-energy calculations using a plane-wave basis set / G. Kresse, J. Furthmüller // Phys. Rev. B. — 1996. — Oct. — Vol. 54, no. 16. — P. 11169—11186.

235. *Kresse*, *G.* From ultrasoft pseudopotentials to the projector augmented-wave method / G. Kresse, D. Joubert // Phys. Rev. B. — 1999. — Jan. — Vol. 59, no. 3. — P. 1758—1775.

236. *Koelling*, *D. D.* A technique for relativistic spin-polarised calculations / D. D. Koelling, B. N. Harmon // J. Phys. C: Sol. St. Phys. — 1977. — Vol. 10, no. 16. — P. 3107.

237. A consistent and accurate ab initio parametrization of density functional dispersion correction (DFT-D) for the 94 elements H-Pu / S. Grimme [et al.] // J. Chem. Phys. — 2010. — Vol. 132, no. 15. — P. 154104.

238. *Grimme*, *S.* Effect of the damping function in dispersion corrected density functional theory / S. Grimme, S. Ehrlich, L. Goerigk // J. Comput. Phys. — 2011. — Vol. 32, no. 7. — P. 1456—1465.

239. Efficient linearization of the augmented plane-wave method / G. K. H. Madsen [et al.] // Phys. Rev. B. — 2001. — Oct. — Vol. 64, issue 19. — P. 195134. — URL: https://link.aps.org/doi/10.1103/PhysRevB.64.195134.

240. WIEN2k, An Augmented Plane Wave Plus Local Orbitals Program for Calculating Crystal Properties / P. Blaha [et al.]. — Austria : Vienna University of Technology, 2001.

241. Unfolding the band structure of disordered solids: From bound states to high-mobility Kane fermions / O. Rubel [et al.] // Phys. Rev. B. — 2014. — Sept. — Vol. 90, issue 11. — P. 115202. — URL: https://link.aps.org/doi/10.1103/PhysRevB.90.115202.

242. *Momma*, *K. VESTA3* for three-dimensional visualization of crystal, volumetric and morphology data / K. Momma, F. Izumi // Journal of Applied Crystallography. — 2011. — Dec. — Vol. 44, no. 6. — P. 1272—1276. — URL: https://doi.org/10.1107/S0021889811038970.

243. *Nečas, D.* Gwyddion: an open-source software for SPM data analysis / D. Nečas, P. Klapetek // Cent. Eur. J. Phys. — 2012. — Vol. 10, issue 1. — P. 181—188.

244. Spin structure of the Shockley surface state on $\mathrm{Au}(111)$ / M. Hoesch [et al.] // Phys. Rev. B. — 2004. — June. — Vol. 69, issue 24. — P. 241401. — URL: https://link.aps.org/doi/10.1103/PhysRevB.69.241401.

245. *Qi, X.-L.* Topological insulators and superconductors / X.-L. Qi, S.-C. Zhang // Rev. Mod. Phys. — 2011. — Oct. — Vol. 83, issue 4. — P. 1057—1110. — URL: https://link.aps.org/doi/10.1103/RevModPhys.83.1057.

246. Nondegenerate Metallic States on Bi(114): A One-Dimensional Topological Metal / J. W. Wells [et al.] // Phys. Rev. Lett. — 2009. — Mar. — Vol. 102, issue 9. — P. 096802. — URL: https://link.aps.org/doi/10.1103/PhysRevLett.102.096802.

247. Observation of Unconventional Quantum Spin Textures in Topological Insulators / D. Hsieh [et al.] // Science. — 2009. — Vol. 323, no. 5916. — P. 919—922. — URL: https://www.science.org/doi/abs/10.1126/science.1167733.

248. *Dil, J. H.* Spin and angle resolved photoemission on non-magnetic low-dimensional systems / J. H. Dil // Journal of Physics: Condensed Matter. — 2009. — Sept. — Vol. 21, no. 40. — P. 403001. — URL: https://dx.doi.org/10.1088/0953-8984/21/40/403001.

249. Spin-Resolved Photoemission of Surface States of $\mathrm{W}(110)-(1\times 1)\mathrm{H}$ / M. Hochstrasser [et al.] // Phys. Rev. Lett. — 2002. — Nov. — Vol. 89, issue 21. — P. 216802. — URL: https://link.aps.org/doi/10.1103/PhysRevLett.89.216802.

250. Strong Rashba-Type Spin Polarization of the Photocurrent from Bulk Continuum States: Experiment and Theory for Bi(111) / A. Kimura [et al.] // Phys. Rev. Lett. — 2010. — Aug. — Vol. 105, issue 7. — P. 076804. — URL: https://link.aps.org/doi/10.1103/PhysRevLett.105.076804.

251. *Krasovskii, E. E.* Rashba polarization of bulk continuum states / E. E. Krasovskii, E. V. Chulkov // Phys. Rev. B. — 2011. — Apr. — Vol. 83, issue 15. — P. 155401. — URL: https://link.aps.org/doi/10.1103/PhysRevB.83.155401.

252. *Gaylord*, *R. H.* Spin-orbit-interaction-induced surface resonance on W(011) / R. H. Gaylord, S. D. Kevan // Phys. Rev. B. — 1987. — Dec. — Vol. 36, issue 17. — P. 9337—9340. — URL: https://link.aps.org/doi/10.1103/PhysRevB.36.9337.

253. *Rotenberg*, *E.* Evolution of Fermi Level Crossings versus H Coverage on $W(110)$ / E. Rotenberg, S. D. Kevan // Phys. Rev. Lett. — 1998. — Mar. — Vol. 80, issue 13. — P. 2905—2908. — URL: https://link.aps.org/doi/10.1103/PhysRevLett.80.2905.

254. *Bylander*, *D. M.* Self-consistent relativistic calculation of the energy bands and cohesive energy of W / D. M. Bylander, L. Kleinman // Phys. Rev. B. — 1984. — Feb. — Vol. 29, issue 4. — P. 1534—1539. — URL: https://link.aps.org/doi/10.1103/PhysRevB.29.1534.

255. *Krasovskii*, *E. E.* Augmented Fourier components method for constructing the crystal potential in self-consistent band-structure calculations / E. E. Krasovskii, F. Starrost, W. Schattke // Phys. Rev. B. — 1999. — Apr. — Vol. 59, issue 16. — P. 10504—10511. — URL: https://link.aps.org/doi/10.1103/PhysRevB.59.10504.

256. *Koelling*, *D. D.* A technique for relativistic spin-polarised calculations / D. D. Koelling, B. N. Harmon // Journal of Physics C: Solid State Physics. — 1977. — Aug. — Vol. 10, no. 16. — P. 3107. — URL: https://dx.doi.org/10.1088/0022-3719/10/16/019.

257. Photoemission study of surface state intensity resonance and dispersion of Be2C(100) / C.-T. Tzeng [et al.] // Surface Science. — 1999. — Vol. 423, no. 2. — P. 232—242. — URL: https://www.sciencedirect.com/science/article/pii/S0039602898009108.

258. *Papaconstantopoulos*, *D. A.* Handbook of the band structure of elemental solids / D. A. Papaconstantopoulos. — New York : Plenum Press, 1986.

259. *Krasovskii*, *E. E.* Calculation of the wave functions for semi-infinite crystals with linear methods of band theory / E. E. Krasovskii, W. Schattke // Phys. Rev. B. — 1999. — June. — Vol. 59, issue 24. — R15609—R15612. — URL: https://link.aps.org/doi/10.1103/PhysRevB.59.R15609.

260. Unconventional Fermi surface spin textures in the $Bi_xPb_{1-x}/Ag(111)$ surface alloy / F. Meier [et al.] // Phys. Rev. B. — 2009. — June. — Vol. 79, issue 24. — P. 241408. — URL: https://link.aps.org/doi/10.1103/PhysRevB.79.241408.

261. Spin texture of time-reversal symmetry invariant surface states on W(110) / D. Kutnyakhov [et al.] // Scientific Reports. — 2016. — July. — Vol. 6, no. 1. — P. 29394. — URL: https://doi.org/10.1038/srep29394.

262. Tilted Dirac cone on W(110) protected by mirror symmetry / A. Varykhalov [et al.] // Phys. Rev. B. — 2017. — June. — Vol. 95, issue 24. — P. 245421. — URL: https://link.aps.org/doi/10.1103/PhysRevB.95.245421.

263. Existence of topological nontrivial surface states in strained transition metals: W, Ta, Mo, and Nb / D. Thonig [et al.] // Phys. Rev. B. — 2016. — Oct. — Vol. 94, issue 15. — P. 155132. — URL: https://link.aps.org/doi/10.1103/PhysRevB.94.155132.

264. *Chiang, T.-C.* Photoemission studies of quantum well states in thin films / T.-C. Chiang // Surface Science Reports. — 2000. — Vol. 39, no. 7. — P. 181—235. — URL: https://www.sciencedirect.com/science/article/pii/S0167572900000066.

265. Quantum-well and tight-binding analyses of spin-polarized photoemission from Ag/Fe(001) overlayers / N. V. Smith [et al.] // Phys. Rev. B. — 1994. — Jan. — Vol. 49, issue 1. — P. 332—338. — URL: https://link.aps.org/doi/10.1103/PhysRevB.49.332.

266. *Lindgren, S. Å.* Discrete Valence-Electron States in Thin Metal Overlayers on a Metal / S. Å. Lindgren, L. Walldén // Phys. Rev. Lett. — 1987. — Dec. — Vol. 59, issue 26. — P. 3003—3006. — URL: https://link.aps.org/doi/10.1103/PhysRevLett.59.3003.

267. Probing interfacial properties with Bloch electrons: Ag on Cu(111) / M. A. Mueller [et al.] // Phys. Rev. B. — 1989. — Sept. — Vol. 40, issue 8. — P. 5845—5848. — URL: https://link.aps.org/doi/10.1103/PhysRevB.40.5845.

268. *Lindgren, S. Å.* Electron-Energy-Band Determination by Photoemission from Overlayer States / S. Å. Lindgren, L. Walldén // Phys. Rev. Lett. — 1988. — Dec. — Vol. 61, issue 25. — P. 2894—2897. — URL: https://link.aps.org/doi/10.1103/PhysRevLett.61.2894.

269. Probing the Ground State Electronic Structure of a Correlated Electron System by Quantum Well States: $Ag/Ni(111)$ / A. Varykhalov [et al.] // Phys. Rev. Lett. — 2005. — Dec. — Vol. 95, issue 24. — P. 247601. — URL: https://link.aps.org/doi/10.1103/PhysRevLett.95.247601.

270. Quantum well states of sp- and d-character in thin Au overlayers on W(110) / A. M. Shikin [et al.] // Phys. Rev. B. — 2002. — Jan. — Vol. 65, issue 7. — P. 075403. — URL: https://link.aps.org/doi/10.1103/PhysRevB.65.075403.

271. Spin-polarized photoemission from quantum well and interface states (invited) / C. Carbone [et al.] // Journal of Applied Physics. — 1994. — Nov. — Vol. 76, no. 10. — P. 6966—6971. — URL: https://doi.org/10.1063/1.358059.

272. Hybridization and the effective mass of quantum-well states in magnetic multilayers / P. D. Johnson [et al.] // Phys. Rev. B. — 1994. — Sept. — Vol. 50, issue 12. — P. 8954—8956. — URL: https://link.aps.org/doi/10.1103/PhysRevB.50.8954.

273. Probing Interface Electronic Structure with Overlayer Quantum-Well Resonances: $Al/Si(111)$ / L. Aballe [et al.] // Phys. Rev. Lett. — 2001. — Sept. — Vol. 87, issue 15. — P. 156801. — URL: https://link.aps.org/doi/10.1103/PhysRevLett.87.156801.

274. Umklapp-Mediated Quantization of Electronic States in Ag Films on Ge(111) / S.-J. Tang [et al.] // Phys. Rev. Lett. — 2006. — June. — Vol. 96, issue 21. — P. 216803. — URL: https://link.aps.org/doi/10.1103/PhysRevLett.96.216803.

275. *Tang, S.-J.* Modification of Surface States in Ultrathin Films via Hybridization with the Substrate: A Study of Ag on Ge / S.-J. Tang, T. Miller, T.-C. Chiang // Phys. Rev. Lett. — 2006. — Jan. — Vol. 96, issue 3. — P. 036802. — URL: https://link.aps.org/doi/10.1103/PhysRevLett.96.036802.

276. Probing Quasiparticle States Bound by Disparate Periodic Potentials / P. Moras [et al.] // Phys. Rev. Lett. — 2006. — Nov. — Vol. 97, issue 20. — P. 206802. — URL: https://link.aps.org/doi/10.1103/PhysRevLett.97.206802.

277. Influence of the substrate bands on the *sp*-levels topology of Ag films on Ge(111) / P. Moras [et al.] // Phys. Rev. B. — 2009. — Nov. — Vol. 80, issue 20. — P. 205418. — URL: https://link.aps.org/doi/10.1103/PhysRevB.80.205418.

278. *Matsuda, I.* In-plane dispersion of the quantum-well states of the epitaxial silver films on silicon / I. Matsuda, T. Ohta, H. W. Yeom // Phys. Rev. B. — 2002. — Feb. — Vol. 65, issue 8. — P. 085327. — URL: https://link.aps.org/doi/10.1103/PhysRevB.65.085327.

279. Surface State Scattering at a Buried Interface / F. Schiller [et al.] // Phys. Rev. Lett. — 2005. — Sept. — Vol. 95, issue 12. — P. 126402. — URL: https://link.aps.org/doi/10.1103/PhysRevLett.95.126402.

280. *Shikin, A. M.* Valence-band splitting in $\mathrm{Mg/W(110)}$: Neither spin-orbit nor parity effect / A. M. Shikin, O. Rader // Phys. Rev. B. — 2007. — Aug. — Vol. 76, issue 7. — P. 073407. — URL: https://link.aps.org/doi/10.1103/PhysRevB.76.073407.

281. Photoemission of a Quantum Cavity with a Nonmagnetic Spin Separator / C. Koitzsch [et al.] // Phys. Rev. Lett. — 2005. — Sept. — Vol. 95, issue 12. — P. 126401. — URL: https://link.aps.org/doi/10.1103/PhysRevLett.95.126401.

282. Non-free-electron momentum- and thickness-dependent evolution of quantum well states in the $\mathrm{Cu/Co/Cu(001)}$ system / E. Rotenberg [et al.] // Phys. Rev. B. — 2006. — Feb. — Vol. 73, issue 7. — P. 075426. — URL: https://link.aps.org/doi/10.1103/PhysRevB.73.075426.

283. *Himpsel, F. J.* Quantum well states in Ni/Cu/Ni spin valve structures / F. J. Himpsel, O. Rader // Applied Physics Letters. — 1995. — Aug. — Vol. 67, no. 8. — P. 1151—1153. — URL: https://doi.org/10.1063/1.114991.

284. Extended energy range of Ag quantum-well states in Ag(111)/Au(111)/W(110) / A. M. Shikin [et al.] // Phys. Rev. B. — 2000. — July. — Vol. 62, issue 4. — R2303—R2306. — URL: https://link.aps.org/doi/10.1103/PhysRevB.62.R2303.

285. Spin Polarization of Quantum Well States in Ag Films Induced by the Rashba Effect at the Surface / K. He [et al.] // Phys. Rev. Lett. — 2008. — Sept. — Vol. 101, issue 10. — P. 107604. — URL: https://link.aps.org/doi/10.1103/PhysRevLett.101.107604.

286. Tunable Spin Gaps in a Quantum-Confined Geometry / E. Frantzeskakis [et al.] // Phys. Rev. Lett. — 2008. — Nov. — Vol. 101, issue 19. — P. 196805. — URL: https://link.aps.org/doi/10.1103/PhysRevLett.101.196805.

287. Breakup of Quasiparticles in Thin-Film Quantum Wells / S.-J. Tang [et al.] // Phys. Rev. Lett. — 2004. — Nov. — Vol. 93, issue 21. — P. 216804. — URL: https://link.aps.org/doi/10.1103/PhysRevLett.93.216804.

288. Parity of substrate bands probed by quantum well states of an overlayer / D. V. Vyalikh [et al.] // Phys. Rev. B. — 2007. — Oct. — Vol. 76, issue 15. — P. 153406. — URL: https://link.aps.org/doi/10.1103/PhysRevB.76.153406.

289. Quantum-size effects in the electronic structure of low-dimensional metallic systems / A. M. Shikin [et al.] // Applied Physics A. — 2009. — Mar. — Vol. 94, no. 3. — P. 449—453. — URL: https://doi.org/10.1007/s00339-008-4915-2.

290. Spin-orbit interaction and Dirac cones in d-orbital noble metal surface states / R. Requist [et al.] // Phys. Rev. B. — 2015. — Jan. — Vol. 91, issue 4. — P. 045432. — URL: https://link.aps.org/doi/10.1103/PhysRevB.91.045432.

291. Effective mass enhancement and ultrafast electron dynamics of Au(111) surface state coupled to a quantum well / A. Varykhalov [et al.] // Phys. Rev. Res. — 2020. — Mar. — Vol. 2, issue 1. — P. 013343. — URL: https://link.aps.org/doi/10.1103/PhysRevResearch.2.013343.

292. Room Temperature Electrical Detection of Spin Polarized Currents in Topological Insulators / A. Dankert [et al.] // Nano Letters. — 2015. — Dec. — Vol. 15, no. 12. — P. 7976—7981. — URL: https://doi.org/10.1021/acs.nanolett.5b03080.

293. Out-of-plane polarization induced in magnetically-doped topological insulator $Bi_{1.37}V_{0.03}Sb_{0.6}Te_2Se$ by circularly polarized synchrotron radiation above a Curie temperature / A. M. Shikin [et al.] // Applied Physics Letters. — 2016. — Nov. — Vol. 109, no. 22. — P. 222404. — URL: https://doi.org/10.1063/1.4969070.

294. Anomalously large gap and induced out-of-plane spin polarization in magnetically doped 2D Rashba system: V-doped BiTeI / A. M. Shikin [et al.] // 2D Materials. — 2017. — Mar. — Vol. 4, no. 2. — P. 025055. — URL: https://dx.doi.org/10.1088/2053-1583/aa65bd.

295. Control over topological insulator photocurrents with light polarization / J. W. McIver [et al.] // Nature Nanotechnology. — 2012. — Feb. — Vol. 7, no. 2. — P. 96—100. — URL: https://doi.org/10.1038/nnano.2011.214.

296. Zero-bias photocurrent in ferromagnetic topological insulator / N. Ogawa [et al.] // Nature Communications. — 2016. — July. — Vol. 7, no. 1. — P. 12246. — URL: https://doi.org/10.1038/ncomms12246.

297. Ultrafast helicity control of surface currents in topological insulators with near-unity fidelity / C. Kastl [et al.] // Nature Communications. — 2015. — Mar. — Vol. 6, no. 1. — P. 6617. — URL: https://doi.org/10.1038/ncomms7617.

298. Local photocurrent generation in thin films of the topological insulator Bi_2Se_3 / C. Kastl [et al.] // Applied Physics Letters. — 2012. — Dec. — Vol. 101, no. 25. — P. 251110. — URL: https://doi.org/10.1063/1.4772547.

299. Surface spin-polarized currents generated in topological insulators by circularly polarized synchrotron radiation and their photoelectron spectroscopy indication / A. M. Shikin [et al.] // Physics of the Solid State. — 2016. — Aug. — Vol. 58, no. 8. — P. 1675—1686. — URL: https://doi.org/10.1134/S1063783416080266.

300. Room-Temperature High-Frequency Transport of Dirac Fermions in Epitaxially Grown Sb_2Te_3- and Bi_2Te_3-Based Topological Insulators / P. Olbrich [et al.] // Phys. Rev. Lett. — 2014. — Aug. — Vol. 113, issue 9. — P. 096601. — URL: https://link.aps.org/doi/10.1103/PhysRevLett.113.096601.

301. Cyclotron-resonance-assisted photocurrents in surface states of a three-dimensional topological insulator based on a strained high-mobility HgTe film / K.-M. Dantscher [et al.] // Phys. Rev. B. — 2015. — Oct. — Vol. 92, issue 16. — P. 165314. — URL: https://link.aps.org/doi/10.1103/PhysRevB.92.165314.

302. Photon drag effect in $(Bi_{1-x}Sb_x)_2Te_3$ three-dimensional topological insulators / H. Plank [et al.] // Phys. Rev. B. — 2016. — Mar. — Vol. 93, issue 12. — P. 125434. — URL: https://link.aps.org/doi/10.1103/PhysRevB.93.125434.

303. Opto-electronic characterization of three dimensional topological insulators / H. Plank [et al.] // Journal of Applied Physics. — 2016. — Oct. — Vol. 120, no. 16. — P. 165301. — URL: https://doi.org/10.1063/1.4965962.

304. *Hosur, P.* Circular photogalvanic effect on topological insulator surfaces: Berry-curvature-dependent response / P. Hosur // Phys. Rev. B. — 2011. — Jan. — Vol. 83, issue 3. — P. 035309. — URL: https://link.aps.org/doi/10.1103/PhysRevB.83.035309.

305. Tuning a Schottky barrier in a photoexcited topological insulator with transient Dirac cone electron-hole asymmetry / M. Hajlaoui [et al.] // Nature Communications. — 2014. — Jan. — Vol. 5, no. 1. — P. 3003. — URL: https://doi.org/10.1038/ncomms4003.

306. Ultrafast Optical Excitation of a Persistent Surface-State Population in the Topological Insulator Bi_2Se_3 / J. A. Sobota [et al.] // Phys. Rev. Lett. — 2012. — Mar. — Vol. 108, issue 11. — P. 117403. — URL: https://link.aps.org/doi/10.1103/PhysRevLett.108.117403.

307. Ultrafast photodoping and effective Fermi-Dirac distribution of the Dirac particles in Bi_2Se_3 / A. Crepaldi [et al.] // Phys. Rev. B. — 2012. — Nov. — Vol. 86, issue 20. — P. 205133. — URL: https://link.aps.org/doi/10.1103/PhysRevB.86.205133.

308. Measurement of Intrinsic Dirac Fermion Cooling on the Surface of the Topological Insulator Bi_2Se_3 Using Time-Resolved and Angle-Resolved Photoemission Spectroscopy / Y. H. Wang [et al.] // Phys. Rev. Lett. — 2012. — Sept. — Vol. 109, issue 12. — P. 127401. — URL: https://link.aps.org/doi/10.1103/PhysRevLett.109.127401.

309. Evidence of reduced surface electron-phonon scattering in the conduction band of Bi_2Se_3 by nonequilibrium ARPES / A. Crepaldi [et al.] // Phys. Rev. B. — 2013. — Sept. — Vol. 88, issue 12. — P. 121404. — URL: https://link.aps.org/doi/10.1103/PhysRevB.88.121404.

310. *Semenov, Y. G.* Tunable photogalvanic effect on topological insulator surfaces via proximity interactions / Y. G. Semenov, X. Li, K. W. Kim // Phys. Rev. B. — 2012. — Nov. — Vol. 86, issue 20. — P. 201401. — URL: https://link.aps.org/doi/10.1103/PhysRevB.86.201401.

311. Ultrafast spin-polarization control of Dirac fermions in topological insulators / J. Sánchez-Barriga [et al.] // Phys. Rev. B. — 2016. — Apr. — Vol. 93, issue 15. — P. 155426. — URL: https://link.aps.org/doi/10.1103/PhysRevB.93.155426.

312. Laser-induced persistent photovoltage on the surface of a ternary topological insulator at room temperature / J. Sánchez-Barriga [et al.] // Applied Physics Letters. — 2017. — Apr. — Vol. 110, no. 14. — P. 141605. — URL: https://doi.org/10.1063/1.4979596.

313. Ultrafast energy- and momentum-resolved surface Dirac photocurrents in the topological insulator Sb_2Te_3 / K. Kuroda [et al.] // Phys. Rev. B. — 2017. — Feb. — Vol. 95, issue 8. — P. 081103. — URL: https://link.aps.org/doi/10.1103/PhysRevB.95.081103.

314. Coherent control over three-dimensional spin polarization for the spin-orbit coupled surface state of Bi_2Se_3 / K. Kuroda [et al.] // Phys. Rev. B. — 2016. — Oct. — Vol. 94, issue 16. — P. 165162. — URL: https://link.aps.org/doi/10.1103/PhysRevB.94.165162.

315. *Kronik, L.* Surface photovoltage phenomena: theory, experiment, and applications / L. Kronik, Y. Shapira // Surface Science Reports. — 1999. — Vol. 37, no. 1. — P. 1—206. — URL: https://www.sciencedirect.com/science/article/pii/S0167572999000023.

316. Surface photovoltage effects on p-GaAs (100) from core-level photoelectron spectroscopy using synchrotron radiation and a laser / S. Tanaka [et al.] // Phys. Rev. B. — 2001. — Sept. — Vol. 64, issue 15. — P. 155308. — URL: https://link.aps.org/doi/10.1103/PhysRevB.64.155308.

317. *Oka, T.* Photovoltaic Hall effect in graphene / T. Oka, H. Aoki // Phys. Rev. B. — 2009. — Feb. — Vol. 79, issue 8. — P. 081406. — URL: https://link.aps.org/doi/10.1103/PhysRevB.79.081406.

318. Enhanced photogalvanic effect in graphene due to Rashba spin-orbit coupling / M. Inglot [et al.] // Phys. Rev. B. — 2015. — May. — Vol. 91, issue 19. — P. 195428. — URL: https://link.aps.org/doi/10.1103/PhysRevB.91.195428.

319. Broadband photovoltaic effect of n-type topological insulator Bi_2Te_3 films on p-type Si substrates / Z. Wang [et al.] // Nano Research. — 2017. — June. — Vol. 10, no. 6. — P. 1872—1879. — URL: https://doi.org/10.1007/s12274-016-1369-2.

320. Ultra-broadband and high response of the Bi_2Te_3–Si heterojunction and its application as a photodetector at room temperature in harsh working environments / J. Yao [et al.] // Nanoscale. — 2015. — Vol. 7, issue 29. — P. 12535—12541. — URL: http://dx.doi.org/10.1039/C5NR02953H.

321. Dirac-fermion-mediated ferromagnetism in a topological insulator / J. G. Checkelsky [et al.] // Nature Physics. — 2012. — Oct. — Vol. 8, no. 10. — P. 729—733. — URL: https://doi.org/10.1038/nphys2388.

322. Hedgehog spin texture and Berry's phase tuning in a magnetic topological insulator / S.-Y. Xu [et al.] // Nature Physics. — 2012. — Aug. — Vol. 8, no. 8. — P. 616—622. — URL: https://doi.org/10.1038/nphys2351.

323. Massive Dirac Fermion on the Surface of a Magnetically Doped Topological Insulator / Y. L. Chen [et al.] // Science. — 2010. — Vol. 329, no. 5992. — P. 659—662. — URL: https://www.science.org/doi/abs/10.1126/science.1189924.

324. Carrier dependent ferromagnetism in chromium doped topological insulator $Cr_y(Bi_xSb_{1-x})_{2-y}Te_3$ / B. Li [et al.] // Physics Letters A. — 2013. — Vol. 377, no. 31. — P. 1925—1929. — URL: https://www.sciencedirect.com/science/article/pii/S0375960113004908.

325. Tailoring Magnetic Doping in the Topological Insulator Bi_2Se_3 / J.-M. Zhang [et al.] // Phys. Rev. Lett. — 2012. — Dec. — Vol. 109, issue 26. — P. 266405. — URL: https://link.aps.org/doi/10.1103/PhysRevLett.109.266405.

326. *Larson, P.* Electronic structure and magnetism in Bi_2Te_3, Bi_2Se_3, and Sb_2Te_3 doped with transition metals (Ti–Zn) / P. Larson, W. R. L. Lambrecht // Phys. Rev. B. — 2008. — Nov. — Vol. 78, issue 19. — P. 195207. — URL: https://link.aps.org/doi/10.1103/PhysRevB.78.195207.

327. Low-temperature ferromagnetism in a new diluted magnetic semiconductor $Bi_{2-x}Fe_xTe_3$ / V. A. Kul'bachinskii [et al.] // Journal of Experimental and Theoretical Physics Letters. — 2001. — Apr. — Vol. 73, no. 7. — P. 352—356. — URL: https://doi.org/10.1134/1.1378118.

328. A topological insulator surface under strong Coulomb, magnetic and disorder perturbations / L. A. Wray [et al.] // Nature Physics. — 2011. — Jan. — Vol. 7, no. 1. — P. 32—37. — URL: https://doi.org/10.1038/nphys1838.

329. *Rosenberg, G.* Surface magnetic ordering in topological insulators with bulk magnetic dopants / G. Rosenberg, M. Franz // Phys. Rev. B. — 2012. — May. — Vol. 85, issue 19. — P. 195119. — URL: https://link.aps.org/doi/10.1103/PhysRevB.85.195119.

330. *D'yakonov, M. I.* Charge relaxation in an anisotropic medium and in low-dimensional media / M. I. D'yakonov, A. S. Furman // Sov. Phys. JET. — 1987. — Vol. 65, no. 3. — P. 574. — URL: http://jetp.ras.ru/cgi-bin/dn/e_065_03_0574.pdf.

331. Ultrafast electron dynamics at the Dirac node of the topological insulator Sb_2Te_3 / S. Zhu [et al.] // Scientific Reports. — 2015. — Aug. — Vol. 5, no. 1. — P. 13213. — URL: https://doi.org/10.1038/srep13213.

332. Generic New Platform for Topological Quantum Computation Using Semiconductor Heterostructures / J. D. Sau [et al.] // Phys. Rev. Lett. — 2010. — Jan. — Vol. 104, issue 4. — P. 040502. — URL: https://link.aps.org/doi/10.1103/PhysRevLett.104.040502.

333. Antiferromagnetic spintronics / V. Baltz [et al.] // Rev. Mod. Phys. — 2018. — Feb. — Vol. 90, issue 1. — P. 015005. — URL: https://link.aps.org/doi/10.1103/RevModPhys.90.015005.

334. Giant Rashba-type spin splitting in bulk BiTeI / K. Ishizaka [et al.] // Nature Materials. — 2011. — July. — Vol. 10, no. 7. — P. 521–526. — URL: https://doi.org/10.1038/nmat3051.

335. Spin-texture inversion in the giant Rashba semiconductor BiTeI / H. Maaß [et al.] // Nature Communications. — 2016. — May. — Vol. 7, no. 1. — P. 11621. — URL: https://doi.org/10.1038/ncomms11621.

336. *Eremeev, S. V.* Giant Rashba-type spin splitting at polar surfaces of BiTeI / S. V. Eremeev, I. A. Nechaev, E. V. Chulkov // JETP Letters. — 2012. — Dec. — Vol. 96, no. 7. — P. 437–444. — URL: https://doi.org/10.1134/S0021364012190071.

337. Ideal Two-Dimensional Electron Systems with a Giant Rashba-Type Spin Splitting in Real Materials: Surfaces of Bismuth Tellurohalides / S. V. Eremeev [et al.] // Phys. Rev. Lett. — 2012. — June. — Vol. 108, issue 24. — P. 246802. — URL: https://link.aps.org/doi/10.1103/PhysRevLett.108.246802.

338. Disentanglement of Surface and Bulk Rashba Spin Splittings in Noncentrosymmetric BiTeI / G. Landolt [et al.] // Phys. Rev. Lett. — 2012. — Sept. — Vol. 109, issue 11. — P. 116403. — URL: https://link.aps.org/doi/10.1103/PhysRevLett.109.116403.

339. Giant Ambipolar Rashba Effect in the Semiconductor BiTeI / A. Crepaldi [et al.] // Phys. Rev. Lett. — 2012. — Aug. — Vol. 109, issue 9. — P. 096803. — URL: https://link.aps.org/doi/10.1103/PhysRevLett.109.096803.

340. Massive Dirac Fermion on the Surface of a Magnetically Doped Topological Insulator / Y. L. Chen [et al.] // Science. — 2010. — Vol. 329, no. 5992. — P. 659–662. — URL: https://www.science.org/doi/abs/10.1126/science.1189924.

341. Hedgehog spin texture and Berry's phase tuning in a magnetic topological insulator / S.-Y. Xu [et al.] // Nature Physics. — 2012. — Aug. — Vol. 8, no. 8. — P. 616–622. — URL: https://doi.org/10.1038/nphys2351.

342. Signatures of in-plane and out-of-plane magnetization generated by synchrotron radiation in magnetically doped and pristine topological insulators / A. M. Shikin [et al.] // Phys. Rev. B. — 2018. — June. — Vol. 97, issue 24. — P. 245407. — URL: https://link.aps.org/doi/10.1103/PhysRevB.97.245407.

343. Dirac gap opening and Dirac-fermion-mediated magnetic coupling in antiferromagnetic Gd-doped topological insulators and their manipulation by synchrotron radiation / A. M. Shikin [et al.] // Scientific Reports. — 2019. — Mar. — Vol. 9, no. 1. — P. 4813. — URL: https://doi.org/10.1038/s41598-019-41137-w.

344. Gap Opening Mechanism at the Dirac Point in the Electronic Spectrum of Gd-Doped Topological Insulator / A. M. Shikin [et al.] // Physics of the Solid State. — 2020. — Feb. — Vol. 62, no. 2. — P. 338–349. — URL: https://doi.org/10.1134/S1063783420020183.

345. Signatures of temperature driven antiferromagnetic transition in the electronic structure of topological insulator $MnBi_2Te_4$ / D. A. Estyunin [et al.] // APL Materials. — 2020. — Feb. — Vol. 8, no. 2. — P. 021105. — URL: https://doi.org/10.1063/1.5142846.

346. Magnetophotocurrent in BiTeI with Rashba spin-split bands / N. Ogawa [et al.] // Phys. Rev. B. — 2013. — July. — Vol. 88, issue 3. — P. 035130. — URL: https://link.aps.org/doi/10.1103/PhysRevB.88.035130.

347. Electrically Controlled Spin Injection from Giant Rashba Spin–Orbit Conductor BiTeBr / Z. Kovács-Krausz [et al.] // Nano Letters. — 2020. — July. — Vol. 20, no. 7. — P. 4782–4791. — URL: https://doi.org/10.1021/acs.nanolett.0c00458.

348. Photocontrol of Dirac electrons in a bulk Rashba semiconductor / N. Ogawa [et al.] // Phys. Rev. B. — 2014. — Sept. — Vol. 90, issue 12. — P. 125122. — URL: https://link.aps.org/doi/10.1103/PhysRevB.90.125122.

349. Spin-Filter Device Based on the Rashba Effect Using a Nonmagnetic Resonant Tunneling Diode / T. Koga [et al.] // Phys. Rev. Lett. — 2002. — Mar. — Vol. 88, issue 12. — P. 126601. — URL: https://link.aps.org/doi/10.1103/PhysRevLett.88.126601.

350. Universal Intrinsic Spin Hall Effect / J. Sinova [et al.] // Phys. Rev. Lett. — 2004. — Mar. — Vol. 92, issue 12. — P. 126603. — URL: https://link.aps.org/doi/10.1103/PhysRevLett.92.126603.

351. Topologically non-trivial superconductivity in spin–orbit-coupled systems: bulk phases and quantum phase transitions / S. Tewari [et al.] // New Journal of Physics. — 2011. — June. — Vol. 13, no. 6. — P. 065004. — URL: https://dx.doi.org/10.1088/1367-2630/13/6/065004.

352. *Fu, L.* Superconducting Proximity Effect and Majorana Fermions at the Surface of a Topological Insulator / L. Fu, C. L. Kane // Phys. Rev. Lett. — 2008. — Mar. — Vol. 100, issue 9. — P. 096407. — URL: https://link.aps.org/doi/10.1103/PhysRevLett.100.096407.

353. Non-Abelian statistics and topological quantum information processing in 1D wire networks / J. Alicea [et al.] // Nature Physics. — 2011. — May. — Vol. 7, no. 5. — P. 412–417. — URL: https://doi.org/10.1038/nphys1915.

354. Proposal for realizing Majorana fermions in chains of magnetic atoms on a superconductor / S. Nadj-Perge [et al.] // Phys. Rev. B. — 2013. — July. — Vol. 88, issue 2. — P. 020407. — URL: https://link.aps.org/doi/10.1103/PhysRevB.88.020407.

355. Anomalously large gap and induced out-of-plane spin polarization in magnetically doped 2D Rashba system: V-doped BiTeI / A. M. Shikin [et al.] // 2D Materials. — 2017. — Mar. — Vol. 4, no. 2. — P. 025055. — URL: https://dx.doi.org/10.1088/2053-1583/aa65bd.

356. Entanglement and manipulation of the magnetic and spin–orbit order in multiferroic Rashba semiconductors / J. Krempaský [et al.] // Nature Communications. — 2016. — Oct. — Vol. 7, no. 1. — P. 13071. — URL: https://doi.org/10.1038/ncomms13071.

357. Spin-resolved electronic structure of ferroelectric α-GeTe and multiferroic $Ge_{1-x}Mn_xTe$ / J. Krempaský [et al.] // Journal of Physics and Chemistry of Solids. — 2019. — Vol. 128. — P. 237—244. — URL: https://www.sciencedirect.com/science/article/pii/S0022369717314531.

358. Mapping polarization induced surface band bending on the Rashba semiconductor BiTeI / C. J. Butler [et al.] // Nature Communications. — 2014. — June. — Vol. 5, no. 1. — P. 4066. — URL: https://doi.org/10.1038/ncomms5066.

359. Imaging ambipolar two-dimensional carriers induced by the spontaneous electric polarization of a polar semiconductor BiTeI / Y. Kohsaka [et al.] // Phys. Rev. B. — 2015. — June. — Vol. 91, issue 24. — P. 245312. — URL: https://link.aps.org/doi/10.1103/PhysRevB.91.245312.

360. Effect of Rashba splitting on ultrafast carrier dynamics in BiTeI / A. S. Ketterl [et al.] // Phys. Rev. B. — 2021. — Feb. — Vol. 103, issue 8. — P. 085406. — URL: https://link.aps.org/doi/10.1103/PhysRevB.103.085406.

361. Electric field effect in atomically thin carbon films / K. S. Novoselov [et al.] // Science. — 2004. — Vol. 306, no. 5696. — P. 666—669.

362. Two-dimensional gas of massless Dirac fermions in graphene / K. S. Novoselov [et al.] // Nature. — 2005. — Vol. 438. — P. 197.

363. *Geim, A. K.* The rise of graphene / A. K. Geim, K. S. Novoselov // Nat. Mater. — 2007. — Vol. 6. — P. 183.

364. Utilization of a buffered dielectric to achieve high field-effect carrier mobility in graphene transistors / D. B. Farmer [et al.] // Nano Lett. — 2009. — Vol. 9, no. 12. — P. 4474—4478.

365. Graphene field-effect transistors with high on/off current ratio and large transport band gap at room temperature / F. Xia [et al.] // Nano Lett. — 2010. — Vol. 10, no. 2. — P. 715—718.

366. *Pesin, D.* Spintronics and pseudospintronics in graphene and topological insulators / D. Pesin, A. H. MacDonald // Nat. Mater. — 2012. — Vol. 11, no. 5. — P. 409—416.

367. Ultrafast electronic response of graphene to a strong and localized electric field / E. Gruber [et al.] // Nat. Commun. — 2016. — Vol. 7. — P. 13948.

368. Towards wafer-size graphene layers by atmospheric pressure graphitization of silicon carbide / K. V. Emtsev [et al.] // Nature Materials. — 2009. — Vol. 8, issue 3. — P. 203—207. — URL: https://doi.org/10.1038/nmat2382.

369. *Starke, U.* Epitaxial graphene on SiC(0001) and SiC(000$\bar{1}$): from surface reconstructions to carbon electronics / U. Starke, C. Riedl // J. Phys.: Condens. Matter. — 2009. — Vol. 21. — P. 134016. — URL: https://doi.org/10.1088/0953-8984/21/13/134016.

370. Atomic-Scale Morphology and Electronic Structure of Manganese Atomic Layers Underneath Epitaxial Graphene on SiC(0001) / T. Gao [et al.] // ACS Nano. — 2012. — Vol. 6, no. 8. — P. 6562—6568.

371. Modification of electronic structure of quasi-free-standing graphene via adsorption and intercalation of Mn atoms / A. A. Gogina [et al.] // ZhETF. — 2021. — Vol. 159, no. 6. — P. 1028. — URL: http://jetp.ras.ru/cgi-bin/e/index/r/159/6/p1028?a=list.

372. Intercalation Synthesis of Cobalt Silicides under Graphene Grown on Silicon Carbide / G. S. Grebenyuk [et al.] // Physics of the Solid State. — 2020. — Vol. 62, issue 3. — P. 519—528.

373. The investigation of cobalt intercalation underneath epitaxial graphene on 6H-SiC(0001) / Y. Zhang [et al.] // Nanotechnology. — 2017. — Vol. 28, issue 7. — P. 075701.

374. Quasi-Freestanding Graphene on SiC(0001) by Ar-Mediated Intercalation of Antimony: A Route Toward Intercalation of High-Vapor-Pressure Elements / S. Wolff [et al.] // Annalen der Physik. — 2019. — Vol. 531, no. 11. — P. 1900199.

375. Ambipolar doping in quasifree epitaxial graphene on SiC(0001) controlled by Ge intercalation / K. V. Emtsev [et al.] // Phys. Rev. B. — 2011. — Sept. — Vol. 84, issue 12. — P. 125423. — URL: https://link.aps.org/doi/10.1103/PhysRevB.84.125423.

376. Intercalation of graphene on SiC(0001) via ion implantation / A. Stöhr [et al.] // Phys. Rev. B. — 2016. — Aug. — Vol. 94, issue 8. — P. 085431. — URL: https://link.aps.org/doi/10.1103/PhysRevB.94.085431.

377. Mini-Dirac cones in the band structure of a copper intercalated epitaxial graphene superlattice / S. Forti [et al.] // 2D Materials. — 2016. — Vol. 3, issue 3. — P. 035003. — URL: https://doi.org/10.1088/2053-1583/3/3/035003.

378. *Silly*, *M. G.* Electronic properties of zero-layer graphene on 6H-SiC(0001) substrate decoupled by silicon intercalation / M. G. Silly, G. Li, Y. J. Dappe // Surface and Interface Analysis. — 2014. — Vol. 46, no. 12/13. — P. 1273—1277. — URL: https://analyticalsciencejournals.onlinelibrary.wiley.com/doi/abs/10.1002/sia.5574.

379. Structural, chemical, and magnetic properties of cobalt intercalated graphene on silicon carbide / R. Hönig [et al.] // Nanotechnology. — 2019. — Vol. 30. — P. 025702.

380. Magnetic properties of ultrathin Co films on Si(111) and $CoSi_2$ surfaces / J. S. Tsay [et al.] // Journal of Applied Physics. — 1999. — Vol. 85, no. 8. — P. 4967—4969.

381. *Wang*, *Q.* Molecular Precursor Induced Surface Reconstruction at Graphene/Pt(111) Interfaces / Q. Wang, R. Pang, X. Shi // J. Phys. Chem. C. — 2015. — Oct. — Vol. 119, no. 39. — P. 22534—22541. — URL: https://doi.org/10.1021/acs.jpcc.5b06842.

382. Interaction, growth, and ordering of epitaxial graphene on SiC0001 surfaces: A comparative photoelectron spectroscopy study / K. V. Emtsev [et al.] // Phys. Rev. B. — 2008. — Apr. — Vol. 77, issue 15. — P. 155303. — URL: https://link.aps.org/doi/10.1103/PhysRevB.77.155303.

383. *Riedl*, *C.* Structural and electronic properties of epitaxial graphene on SiC(0 0 0 1): a review of growth, characterization, transfer doping and hydrogen intercalation / C. Riedl, C. Coletti, U. Starke // Journal of Physics D: Applied Physics. — 2010. — Sept. — Vol. 43, no. 37. — P. 374009. — URL: https://dx.doi.org/10.1088/0022-3727/43/37/374009.

384. Structural properties of the graphene-SiC(0001) interface as a key for the preparation of homogeneous large-terrace graphene surfaces / C. Riedl [et al.] // Phys. Rev. B. — 2007. — Dec. — Vol. 76, issue 24. — P. 245406. — URL: https://link.aps.org/doi/10.1103/PhysRevB.76.245406.

385. *Mateo*, *P. M.* Structural characterization of epitaxial graphene : Dissertation / Mateo Pablo Merino. — Universidad Autónoma de Madrid, 2014. — URL: https://wp.icmm.csic.es/esisna/wp-content/uploads/sites/26/2018/03/Thesis_P_MERINO.pdf.

386. Quasi-Free-Standing Epitaxial Graphene on SiC Obtained by Hydrogen Intercalation / C. Riedl [et al.] // Phys. Rev. Lett. — 2009. — Dec. — Vol. 103, issue 24. — P. 246804. — URL: https://link.aps.org/doi/10.1103/PhysRevLett.103.246804.

387. *Mårtensson*, *P.* Morphology, Atomic and Electronic Structure of 6H-SiC(0001) Surfaces / P. Mårtensson, F. Owman, L. I. Johansson // physica status solidi (b). — 1997. — Vol. 202, no. 1. — P. 501—528. — URL: https://doi.org/10.1002/1521-3951(199707)202:1%3C501::AID-PSSB501%3E3.0.CO;2-H.

388. Electronic decoupling of an epitaxial graphene monolayer by gold intercalation / I. Gierz [et al.] // Phys. Rev. B. — 2010. — June. — Vol. 81, issue 23. — P. 235408. — URL: https://link.aps.org/doi/10.1103/PhysRevB.81.235408.

389. *Yazdi*, *G. R.* Epitaxial Graphene on SiC: A Review of Growth and Characterization / G. R. Yazdi, T. Iakimov, R. Yakimova // Crystals. — 2016. — Vol. 6, no. 5. — P. 53. — URL: https://www.mdpi.com/2073-4352/6/5/53.

390. Graphene p-n junction formed on SiC(0001) by Au intercalation / Y. Sohn [et al.] // Journal of the Korean Physical Society. — 2021. — Jan. — Vol. 78, no. 1. — P. 40—44. — URL: https://doi.org/10.1007/s40042-020-00010-0.

391. Advances in two-dimensional heterostructures by mono-element intercalation underneath epitaxial graphene / S. Wu [et al.] // Progress in Surface Science. — 2021. — Vol. 96, no. 3. — P. 100637. — URL: https://www.sciencedirect.com/science/article/pii/S0079681621000253.

392. *Emtsev*, *K.* Dissertation “Electronic and structural characterizations of unreconstructed SiC(0001) surfaces and the growth of graphene overlayers” / K. Emtsev. — Friedrich-Alexander-Universität Erlangen-Nürnberg, 2009.

393. Electronic Structure of Epitaxial Graphene Layers on SiC: Effect of the Substrate / F. Varchon [et al.] // Phys. Rev. Lett. — 2007. — Sept. — Vol. 99, issue 12. — P. 126805. — URL: https://link.aps.org/doi/10.1103/PhysRevLett.99.126805.

394. Manipulation of electronic property of epitaxial graphene on SiC substrate by Pb intercalation / J. Wang [et al.] // Phys. Rev. B. — 2021. — Feb. — Vol. 103, issue 8. — P. 085403. — URL: https://link.aps.org/doi/10.1103/PhysRevB.103.085403.

395. Cobalt Intercalation of Graphene on Silicon Carbide / G. S. Grebenyuk [et al.] // Physics of the Solid State. — 2019. — Vol. 61, no. 7. — P. 1316—1326.

396. *Johansson, L. I.* High-resolution core-level study of 6H-SiC(0001) / L. I. Johansson, F. Owman, P. Mårtensson // Phys. Rev. B. — 1996. — May. — Vol. 53, issue 20. — P. 13793—13802. — URL: https://link.aps.org/doi/10.1103/PhysRevB.53.13793.

397. *Hönig, R.* Dissertation“Photoemission microscopy and spectroscopy of cobalt-intercalated graphene on silicon carbide” / R. Hönig. — Technischen Universität Dortmund, 2019.

398. XPS and HRTEM characterization of cobalt–nickel silicide thin films / M. García-Méndez [et al.] // Applied Surface Science. — 2000. — Vol. 161, issue 1. — P. 61—73. — URL: https://doi.org/10.1016/S0169-4332(00)00122-7.

399. Interfacial Reaction of Co on Si(100) by Using Medium-Energy Ion-Scattering Spectroscopy and X-ray Photoelectron Spectroscopy / J. Nam [et al.] // J. Korean Phy. Soc. — 1999. — Vol. 35, 9(2). — P. 546. — URL: https://www.jkps.or.kr/journal/view.html?uid=3753&vmd=Full.

400. *Zhao, J.* Characterization of Cobalt Silicide Formation by X-ray Photoelectron Spectroscopy. I. CoSi / J. Zhao, D. M. Poirier // Surface Science Spectra. — 2000. — Vol. 7, no. 4. — P. 322—328. — URL: https://doi.org/10.1116/1.1376319.

401. *Tedesco, J. L.* Conducting atomic force microscopy studies of nanoscale cobalt silicide Schottky barriers on Si(111) and Si(100) / J. L. Tedesco, J. E. Rowe, R. J. Nemanich // Journal of Applied Physics. — 2009. — Vol. 105, no. 8. — P. 083721. — URL: https://doi.org/10.1063/1.3100212.

402. *Appelbaum, A.* Study of cobalt-disilicide formation from cobalt monosilicide / A. Appelbaum, R. V. Knoell, S. P. Murarka // Journal of Applied Physics. — 1985. — Vol. 57, no. 6. — P. 1880—1886.

403. The (2×2) reconstructions on the surface of cobalt silicides: Atomic configuration at the annealed Co/Si(111) interface / V. Kotlyar [et al.] // Surface Science. — 2017. — Vol. 662. — P. 6—11. — URL: https://doi.org/10.1016/j.susc.2017.03.010.

404. Effect of high temperature deposition on $CoSi_2$ phase formation / C. M. Comrie [et al.] // Journal of Applied Physics. — 2013. — Vol. 113, no. 23. — P. 234902.

405. *Ommen, A. H. van*. Properties of $CoSi_2$ formed on (001) Si / A. H. van Ommen, C. W. T. Bulle-Lieuwma, C. Langereis // Journal of Applied Physics. — 1988. — Vol. 64, no. 5. — P. 2706—2716.

406. Electron-phonon coupling in graphene placed between magnetic Li and Si layers on cobalt / D. Yu. Usachov [et al.] // Phys. Rev. B. — 2018. — Feb. — Vol. 97, issue 8. — P. 085132. — URL: https://link.aps.org/doi/10.1103/PhysRevB.97.085132.

407. Controlled assembly of graphene-capped nickel, cobalt and iron silicides / O. Vilkov [et al.] // Scientific Reports. — 2013. — Vol. 3, issue 1. — P. 2168. — URL: https://doi.org/10.1038/srep02168.

408. *Pan, Z. J.* Electronic structure and transport properties of doped CoSi single crystal / Z. J. Pan, L. T. Zhang, J. S. Wu // Journal of Applied Physics. — 2007. — Vol. 101, no. 3. — P. 033715.

409. Annealing studies of the Co/Si(111) interface / C. Pirri [et al.] // Solid State Communications. — 1986. — Vol. 57, no. 5. — P. 361—364.

410. Non-destructive characterization of the uniformity of thin cobalt disilicide films by Raman microprobe measurements / A. Perez-Rodriguez [et al.] // Thin Solid Films. — 1994. — Vol. 251, no. 1. — P. 45—50.

411. Influence of annealing ambience on the formation of cobalt silicides / F.-M. Liu [et al.] // Chemical Physics Letters. — 2003. — Vol. 372, no. 1. — P. 15—21.

412. Raman spectroscopic studies of the formation processes of cobalt silicide thin films / F. M. Liu [et al.] // Thin Solid Films. — 2005. — Vol. 471, no. 1/2. — P. 257—263.

413. *Narozhnyi, V. N.* Studying the magnetic properties of CoSi single crystals / V. N. Narozhnyi, V. N. Krasnorussky // Journal of Experimental and Theoretical Physics. — 2013. — May. — Vol. 116, no. 5. — P. 780—784.

414. Magnetic Properties of Single-Crystalline CoSi Nanowires / K. Seo [et al.] // Nano Letters. — 2007. — May.

415. Effect of $CoSi_2$ buffer layer on structure and magnetic properties of Co films grown on Si (001) substrate / B. Hu [et al.] // Chinese Physics B. — 2015. — Jan. — Vol. 24, no. 1. — P. 017502.

416. Anisotropy and orientational dependence of magnetization reversal processes in epitaxial ferromagnetic thin films / C. Daboo [et al.] // Phys. Rev. B. — 1995. — June. — Vol. 51, issue 22. — P. 15964—15973.

417. Magnetic switching and in-plane uniaxial anisotropy in ultrathin Ag/Fe/Ag(100) epitaxial films / R. P. Cowburn [et al.] // Journal of Applied Physics. — 1995. — Vol. 78, no. 12. — P. 7210—7219.

418. *Liu, C.* Synthesis of magnetic spinel ferrite $CoFe_2O_4$ nanoparticles from ferric salt and characterization of the size-dependent superparamagnetic properties: / C. Liu, A. J. Rondinone, Z. J. Zhang // Pure and Applied Chemistry. — 2000. — Vol. 72, no. 1/2. — P. 37—45.

419. *Ojha, V. H.* Investigation of structural and magnetic properties of strained $CoFe_2O_4$ nanoparticles / V. H. Ojha, K. M. Kant // Journal of Physics and Chemistry of Solids. — 2021. — Vol. 148. — P. 109655.

420. Superparamagnetic bimetallic iron–palladium nanoalloy: synthesis and characterization / R. Nazir [et al.] // Nanotechnology. — 2008. — Apr. — Vol. 19, no. 18. — P. 185608.

421. *Varykhalov, A.* Graphene grown on Co(0001) films and islands: Electronic structure and its precise magnetization dependence / A. Varykhalov, O. Rader // Phys. Rev. B. — 2009. — Vol. 80. — P. 035437.

422. Chemical vapour deposition of graphene on Ni(111) and Co(0001) and intercalation with Au to study Dirac-cone formation and Rashba splitting / J. Sánchez-Barriga [et al.] // Diamond and Related Materials. — 2010. — Vol. 19, no. 7. — P. 734—741. — URL: https://www.sciencedirect.com/science/article/pii/S0925963510000671.

423. Intact Dirac Cones at Broken Sublattice Symmetry: Photoemission Study of Graphene on Ni and Co / A. Varykhalov [et al.] // Phys. Rev. X. — 2012. — Dec. — Vol. 2, issue 4. — P. 041017. — URL: https://link.aps.org/doi/10.1103/PhysRevX.2.041017.

424. Disorder and Defect Healing in Graphene on Ni(111) / P. Jacobson [et al.] // The Journal of Physical Chemistry Letters. — 2012. — Jan. — Vol. 3, no. 1. — P. 136—139. — URL: https://doi.org/10.1021/jz2015007.

425. Stone–Wales Defect in Graphene / S. K. Tiwari [et al.] // Small. — 2023. — Vol. 19, no. 44. — P. 2303340. — URL: https://onlinelibrary.wiley.com/doi/abs/10.1002/smll.202303340.

426. Cobalt-assisted recrystallization and alignment of pure and doped graphene / D. Yu. Usachov [et al.] // Nanoscale. — 2018. — Vol. 10, issue 25. — P. 12123—12132. — URL: http://dx.doi.org/10.1039/C8NR03183E.

427. *Kang, M. H.* Density functional study of the Au-intercalated graphene/Ni(111) surface / M. H. Kang, S. C. Jung, J. W. Park // Phys. Rev. B. — 2010. — Aug. — Vol. 82, issue 8. — P. 085409. — URL: https://link.aps.org/doi/10.1103/PhysRevB.82.085409.

428. *Sojka, F.* LEEDLab / F. Sojka, T. Fritz. — 2018.

429. *Sutter, P.* Graphene on Pt(111): Growth and substrate interaction / P. Sutter, J. T. Sadowski, E. Sutter // Phys. Rev. B. — 2009. — Dec. — Vol. 80, issue 24. — P. 245411. — URL: https://link.aps.org/doi/10.1103/PhysRevB.80.245411.

430. *Tersoff, J.* Theory and Application for the Scanning Tunneling Microscope / J. Tersoff, D. R. Hamann // Phys. Rev. Lett. — 1983. — June. — Vol. 50, issue 25. — P. 1998—2001. — URL: https://link.aps.org/doi/10.1103/PhysRevLett.50.1998.

431. Pt_5Gd as a Highly Active and Stable Catalyst for Oxygen Electroreduction / M. Escudero-Escribano [et al.] // J. Am. Chem. Soc. — 2012. — Vol. 134, no. 40. — P. 16476—16479. — URL: https://doi.org/10.1021/ja306348d.

432. Alloys of platinum and early transition metals as oxygen reduction electrocatalysts / J. Greeley [et al.] // Nat. Chem. — 2009. — Sept. — Vol. 1. — P. 552—556. — URL: https://doi.org/10.1038/nchem.367.

433. The enhanced activity of mass-selected Pt_xGd nanoparticles for oxygen electroreduction / A. Velázquez-Palenzuela [et al.] // J. Catal. — 2015. — Vol. 328. — P. 297—307. — URL: http://www.sciencedirect.com/science/article/pii/S0021951714003479.

434. Benchmarking Pt-based electrocatalysts for low temperature fuel cell reactions with the rotating disk electrode: oxygen reduction and hydrogen oxidation in the presence of CO (review article) / C. M. Pedersen [et al.] // Electrochim. Acta. — 2015. — Vol. 179. — P. 647—657. — URL: http://www.sciencedirect.com/science/article/pii/S0013468615007951.

435. Tuning the activity of Pt alloy electrocatalysts by means of the lanthanide contraction / M. Escudero-Escribano [et al.] // Science. — 2016. — Vol. 352, no. 6281. — P. 73—76. — URL: https://science.sciencemag.org/content/352/6281/73.

436. Investigating the coverage dependent behaviour of CO on Gd/Pt(111) / E. T. Ulrikkeholm [et al.] // Phys. Chem. Chem. Phys. — 2016. — Vol. 18, issue 43. — P. 29732—29739. — URL: http://dx.doi.org/10.1039/C6CP04575H.

437. First-principles study of the effect of compressive strain on oxygen adsorption in Pd/Ni/Cu-alloy-core@Pd/Ir-alloy-shell catalysts / J. R. De Lile [et al.] // New J. Chem. — 2019. — Vol. 43, issue 21. — P. 8195—8203. — URL: http://dx.doi.org/10.1039/C9NJ01705D.

438. Visualizing Chemical Reactions Confined under Graphene / R. Mu [et al.] // Angew. Chem. Int. Ed. — 2012. — Vol. 51, no. 20. — P. 4856—4859. — URL: https://onlinelibrary.wiley.com/doi/abs/10.1002/anie.201200413.

439. Graphene cover-promoted metal-catalyzed reactions / Y. Yao [et al.] // Proc. Natl. Acad. Sci. USA. — 2014. — Vol. 111, no. 48. — P. 17023—17028. — URL: https://www.pnas.org/content/111/48/17023.

440. Catalysis with two-dimensional materials and their heterostructures / D. Deng [et al.] // Nat. Nanotechnol. — 2016. — Mar. — Vol. 11. — P. 218—230. — URL: https://doi.org/10.1038/nnano.2015.340.

441. *Shaari, N.* Graphene in electrocatalyst and proton conductiong membrane in fuel cell applications: An overview / N. Shaari, S. Kamarudin // Renew. Sust. Energ. Rev. — 2017. — Vol. 69. — P. 862—870. — URL: http://www.sciencedirect.com/science/article/pii/S1364032116303707.

442. Reconstructed Fermi surface in graphene on Ir(111) by Gd-Ir surface alloying / I. Klimovskikh [et al.] // Carbon. — 2019. — Vol. 147. — P. 182—186. — URL: http://www.sciencedirect.com/science/article/pii/S0008622319301575.

443. Introducing strong correlation effects into graphene by gadolinium intercalation / S. Link [et al.] // Phys. Rev. B. — 2019. — Sept. — Vol. 100, issue 12. — P. 121407. — URL: https://link.aps.org/doi/10.1103/PhysRevB.100.121407.

444. *Naumov, I. I.* Gap opening in graphene by simple periodic inhomogeneous strain / I. I. Naumov, A. M. Bratkovsky // Phys. Rev. B. — 2011. — Dec. — Vol. 84, issue 24. — P. 245444. — URL: https://link.aps.org/doi/10.1103/PhysRevB.84.245444.

445. Complementary doping of van der Waals materials through controlled intercalation for monolithically integrated electronics / M. Ke [et al.] // Nano Research. — 2020. — URL: https://doi.org/10.1007/s12274-020-2634-y.

446. Pt_xGd alloy formation on Pt(111): Preparation and structural characterization / E. T. Ulrikkeholm [et al.] // Surf. Sci. — 2016. — Vol. 652. — P. 114—122. — URL: http://www.sciencedirect.com/science/article/pii/S0039602816000832.

447. *Sernelius, B. E.* Core-level spectra from graphene / B. E. Sernelius // Phys. Rev. B. — 2015. — Jan. — Vol. 91, issue 4. — P. 045402. — URL: https://link.aps.org/doi/10.1103/PhysRevB.91.045402.

448. Core level shifts of intercalated graphene / U. A. Schröder [et al.] // 2D Mater. — 2016. — Nov. — Vol. 4, no. 1. — P. 015013. — URL: https://doi.org/10.1088%2F2053-1583%2F4%2F1%2F015013.

449. Synthesis and Transfer of High-Quality Graphene Grown on Al_2O_3(0001)/Pt(111) Template Wafers / K. Verguts [et al.] // ECS J. Solid State Sci. Technol. — 2018. — Vol. 7, issue 12. — P. M195—M200. — URL: http://ma.ecsdl.org/content/MA2018-01/10/846.abstract.

450. Quantum anomalous Hall effect in graphene from Rashba and exchange effects / Z. Qiao [et al.] // Phys. Rev. B. — 2010. — Oct. — Vol. 82, issue 16. — 161414(R). — URL: https://link.aps.org/doi/10.1103/PhysRevB.82.161414.

451. Non-Trivial Band Topology Criteria for Magneto-Spin-Orbit Graphene / A. V. Eryzhenkov [et al.] // Symmetry. — 2023. — Vol. 15, no. 2. — P. 516. — URL: https://www.mdpi.com/2073-8994/15/2/516.

452. *Chen, L.* Rashba spin–orbit coupling induced rectified currents in monolayer graphene with exchange field and sublattice potential / L. Chen, F. Li, X.-M. Ding // Chinese Physics B. — 2023. — Aug. — Vol. 32, no. 8. — P. 087103. — URL: https://dx.doi.org/10.1088/1674-1056/acc932.

453. *Offidani, M.* Anomalous Hall Effect in 2D Dirac Materials / M. Offidani, A. Ferreira // Phys. Rev. Lett. — 2018. — Sept. — Vol. 121, issue 12. — P. 126802. — URL: https://link.aps.org/doi/10.1103/PhysRevLett.121.126802.

454. Enhanced photogalvanic effect in graphene due to Rashba spin-orbit coupling / M. Inglot [et al.] // Phys. Rev. B. — 2015. — May. — Vol. 91, issue 19. — P. 195428. — URL: http://link.aps.org/doi/10.1103/PhysRevB.91.195428.

455. Gate-Tunable Reversible Rashba–Edelstein Effect in a Few-Layer Graphene/2H-TaS_2 Heterostructure at Room Temperature / L. Li [et al.] // ACS Nano. — 2020. — May. — Vol. 14, no. 5. — P. 5251—5259. — URL: https://doi.org/10.1021/acsnano.0c01037.

456. Magnetotransport and current-induced spin transfer torque in a ferromagnetically contacted graphene / B. Zhou [et al.] // J. Phys.: Condens. Matter. — 2010. — Vol. 22, no. 44. — P. 445302. — URL: http://stacks.iop.org/0953-8984/22/i=44/a=445302.

457. Spin current formation at the graphene/Pt interface for magnetization manipulation in magnetic nanodots / A. M. Shikin [et al.] // Applied Physics Letters. — 2014. — Vol. 105, no. 4. — P. 042407. — URL: https://doi.org/10.1063/1.4891361.

458. *Dyrda, A.* Current-induced spin polarization and spin-orbit torque in graphene / A. Dyrda, J. Barnaś // Phys. Rev. B. — 2015. — Oct. — Vol. 92, issue 16. — P. 165404. — URL: http://link.aps.org/doi/10.1103/PhysRevB.92.165404.

459. Proximity Effects Induced in Graphene by Magnetic Insulators: First-Principles Calculations on Spin Filtering and Exchange-Splitting Gaps / H. X. Yang [et al.] // Phys. Rev. Lett. — 2013. — Jan. — Vol. 110, issue 4. — P. 046603. — URL: http://link.aps.org/doi/10.1103/PhysRevLett.110.046603.

460. *Buša, J.* Rippled Graphene as an Ideal Spin Inverter / J. Buša, M. Pudlák, R. Nazmitdinov // Symmetry. — 2023. — Vol. 15, no. 8. — P. 1593. — URL: https://www.mdpi.com/2073-8994/15/8/1593.

461. Engineering a Robust Quantum Spin Hall State in Graphene via Adatom Deposition / C. Weeks [et al.] // Phys. Rev. X. — 2011. — Oct. — Vol. 1, issue 2. — P. 021001. — URL: https://link.aps.org/doi/10.1103/PhysRevX.1.021001.

462. Spin–orbit proximity effect in graphene / A. Avsar [et al.] // Nature Communications. — 2014. — Sept. — Vol. 5, no. 1. — P. 4875. — URL: https://doi.org/10.1038/ncomms5875.

463. *Ng, S.-W.* Graphene-based two-dimensional Janus materials / S.-W. Ng, N. Noor, Z. Zheng // NPG Asia Materials. — 2018. — Apr. — Vol. 10, no. 4. — P. 217–237. — URL: https://doi.org/10.1038/s41427-018-0023-8.

464. Anisotropic Rashba splitting in Pt-based Janus monolayers PtXY (X,Y = S, Se, or Te) / P. A. L. Sino [et al.] // Nanoscale Adv. — 2021. — Vol. 3, issue 23. — P. 6608–6616. — URL: http://dx.doi.org/10.1039/D1NA00334H.

465. *Gong, Q.* Rashba Splitting and Electronic Valley Characteristics of Janus Sb and Bi Topological Monolayers / Q. Gong, G. Zhang // International Journal of Molecular Sciences. — 2022. — Vol. 23, no. 14. — P. 7629. — URL: https://www.mdpi.com/1422-0067/23/14/7629.

466. Nanostructural origin of giant Rashba effect in intercalated graphene / M. Krivenkov [et al.] // 2D Materials. — 2017. — July. — Vol. 4, no. 3. — P. 035010. — URL: https://dx.doi.org/10.1088/2053-1583/aa7ad8.

467. Proximity-induced spin-orbit effects in graphene on Au / A. López [et al.] // Phys. Rev. B. — 2019. — Feb. — Vol. 99, issue 8. — P. 085411. — URL: https://link.aps.org/doi/10.1103/PhysRevB.99.085411.

468. Rashba splitting of 100 meV in Au-intercalated graphene on SiC / D. Marchenko [et al.] // Applied Physics Letters. — 2016. — Apr. — Vol. 108, no. 17. — P. 172405. — URL: https://doi.org/10.1063/1.4947286.

469. Epitaxial graphene/silicon carbide intercalation: a minireview on graphene modulation and unique 2D materials / N. Briggs [et al.] // Nanoscale. — 2019. — Vol. 11, issue 33. — P. 15440–15447. — URL: http://dx.doi.org/10.1039/C9NR03721G.

470. High thermal stability quasi-free-standing bilayer graphene formed on 4H–SiC(0001) via platinum intercalation / C. Xia [et al.] // Carbon. — 2014. — Vol. 79. — P. 631—635. — URL: https://www.sciencedirect.com/science/article/pii/S0008622314007672.

471. Surface intercalation of gold underneath a graphene monolayer on SiC(0001) studied by scanning tunneling microscopy and spectroscopy / B. Premlal [et al.] // Applied Physics Letters. — 2009. — July. — Vol. 94, no. 26. — P. 263115. — URL: https://doi.org/10.1063/1.3168502.

472. Fabrication of a single layer graphene by copper intercalation on a SiC(0001) surface / K. Yagyu [et al.] // Applied Physics Letters. — 2014. — Feb. — Vol. 104, no. 5. — P. 053115. — URL: https://doi.org/10.1063/1.4864155.

473. Spin-induced band modifications of graphene through intercalation of magnetic iron atoms / S. J. Sung [et al.] // Nanoscale. — 2014. — Vol. 6, issue 7. — P. 3824—3829. — URL: http://dx.doi.org/10.1039/C3NR04178F.

474. Fabrication and mechanism of Pb-intercalated graphene on SiC / D. Yang [et al.] // Applied Surface Science. — 2021. — Vol. 569. — P. 151012. — URL: https://www.sciencedirect.com/science/article/pii/S0169433221020699.

475. Intrinsic Spin Hall Effect in Platinum: First-Principles Calculations / G. Y. Guo [et al.] // Phys. Rev. Lett. — 2008. — Mar. — Vol. 100, issue 9. — P. 096401. — URL: https://link.aps.org/doi/10.1103/PhysRevLett.100.096401.

476. Variation of the character of spin-orbit interaction by Pt intercalation underneath graphene on Ir(111) / I. I. Klimovskikh [et al.] // Phys. Rev. B. — 2015. — Oct. — Vol. 92, issue 16. — P. 165402. — URL: https://link.aps.org/doi/10.1103/PhysRevB.92.165402.

477. *Jain*, *V.* The Gaussian-Lorentzian Sum, Product, and Convolution (Voigt) functions in the context of peak fitting X-ray photoelectron spectroscopy (XPS) narrow scans / V. Jain, M. C. Biesinger, M. R. Linford // Applied Surface Science. — 2018. — Vol. 447. — P. 548—553. — URL: https://www.sciencedirect.com/science/article/pii/S0169433218308766.

478. Electronic Structure of Pentacene on Ni(110): Comparison with Graphene / D. Usachov [et al.] // Fullerenes, Nanotubes and Carbon Nanostructures. — 2010. — Vol. 18, no. 4—6. — P. 487—492. — URL: https://doi.org/10.1080/1536383X.2010.487786.

479. *Meier, F.* Measuring spin polarization vectors in angle-resolved photoemission spectroscopy / F. Meier, J. H. Dil, J. Osterwalder // New Journal of Physics. — 2009. — Dec. — Vol. 11, no. 12. — P. 125008. — URL: https://dx.doi.org/10.1088/1367-2630/11/12/125008.

480. *Reohr, W. e. a.* Memories of tomorrow / W. e. a. Reohr // IEEE Circuits and Devices. — 2002. — Vol. 18, issue 5. — P. 17—27.

481. *Slonczewski, J. C.* Conductance and exchange coupling of two ferromagnets separated by a tunneling barrier / J. C. Slonczewski // Phys. Rev. B. — 1989. — Vol. 39. — P. 6995.

482. Exchange-biased magnetic tunnel junctions and application to nonvolatile magnetic random access memory / S. S. P. Parkin [et al.] // Journal of Applied Physics. — 1999. — Vol. 85. — P. 5828.

483. Giant tunnelling magnetoresistance at room temperature with MgO(100) tunnel barriers / S. S. P. Parkin [et al.] // Nature Materials. — 2004. — Vol. 3. — P. 862—867.

484. The Promise of Nanomagnetics and Spintronics for Future Logic and Universal Memory / S. A. Wolf [et al.] // Proceedings of the IEEE. — 2010. — Vol. 98, issue 12. — P. 2155—2168.

485. Spintronics based random access memory: a review / S. Bhatti [et al.] // Materials Today. — 2017. — Vol. 20, issue 9. — P. 530—548.

486. *Wang, K. L.* Low-power non-volatile spintronic memory: STT-RAM and beyond / K. L. Wang, J. G. Alzate, P. Khalili Amiri // J. Phys. D: Appl. Phys. — 2013. — Vol. 46. — P. 5074003.

487. Two-terminal spin–orbit torque magnetoresistive random access memory / N. Sato [et al.] // Nature Electronics. — 2018. — Vol. 1. — P. 508—511.

488. *Zhu, L.* Switching of Perpendicular Magnetization by Spin–Orbit Torque / L. Zhu // Advanced Materials. — 2023. — Vol. 35, no. 48. — P. 2300853. — URL: https://onlinelibrary.wiley.com/doi/abs/10.1002/adma.202300853.

489. *Yu, G.* Two-terminal MRAM with a spin / G. Yu // Nature Electronics. — 2018. — Vol. 1. — P. 496—497.

490. *Endoh, T.* A Recent Progress of Spintronics Devices for Integrated Circuit Applications / T. Endoh, H. Honjo // J. Low Power Electron. Appl. — 2018. — Vol. 8, issue 44.

491. Perpendicular switching of a single ferromagnetic layer induced by in-plane current injection / I. M. Miron [et al.] // Nature. — 2011. — Vol. 476. — P. 189—193.

492. Spin-transfer torque generated by a topological insulator / A. R. Mellnik [et al.] // Nature. — 2014. — Vol. 511. — P. 449—451.

493. Magnetic and structural properties of Co/Pt multilayers / C.-J. Lin [et al.] // Journal of Magnetism and Magnetic Materials. — 1991. — Vol. 93. — P. 194—206.

494. Nonadiabatic Spin Transfer Torque in High Anisotropy Magnetic Nanowires with Narrow Domain Walls / O. Boulle [et al.] // Phys. Rev. Lett. — 2008. — Vol. 101, issue 21. — P. 216601. — URL: https://link.aps.org/doi/10.1103/PhysRevLett.101.216601.

495. Domain Wall Spin Torquemeter / I. M. Miron [et al.] // Phys. Rev. Lett. — 2009. — Vol. 102, issue 13. — P. 137202. — URL: https://link.aps.org/doi/10.1103/PhysRevLett.102.137202.

496. Current-driven spin torque induced by the Rashba effect in a ferromagnetic metal layer / I. M. Miron [et al.] // Nature Materials. — 2010. — Vol. 9. — P. 230—234.

497. Electric Manipulation of Spin Relaxation Using the Spin Hall Effect / K. Ando [et al.] // Phys. Rev. Lett. — 2008. — July. — Vol. 101, issue 3. — P. 036601. — URL: https://link.aps.org/doi/10.1103/PhysRevLett.101.036601.

498. Writable Magnetic Element : patent US20120098077A1 : Int .Cl. H01L 29/82 / G. Gaudin [et al.] ; ICREA [et al.]. — No. 12/959,980 ; req. 12/03/2010 ; publ. 04/26/2012. — 6 p. : il.

499. *Moser, J.* Current-induced cleaning of graphene / J. Moser, A. Barreiro, A. Bachtold // Appl. Phys. Lett. — 2007. — Vol. 91, issue 7. — P. 163513. — URL: http://dx.doi.org/10.1063/1.2789673.

500. Toward Wafer Scale Fabrication of Graphene Based Spin Valve Devices / A. Avsar [et al.] // Nano Lett. — 2011. — Vol. 11. — P. 2363—2368.

501. *Castro Neto, A. H.* Impurity-Induced Spin-Orbit Coupling in Graphene / A. H. Castro Neto, F. Guinea // Phys. Rev. Lett. — 2009. — July. — Vol. 103, issue 2. — P. 026804. — URL: https://link.aps.org/doi/10.1103/PhysRevLett.103.026804.

502. Spatial variation of a giant spin–orbit effect induces electron confinement in graphene on Pb islands / F. Calleja [et al.] // Nature Physics. — 2015. — Vol. 11. — P. 43—47.

503. A two-dimensional spin field-effect switch / W. Yan [et al.] // Nature Communications. — 2016. — Vol. 7. — P. 13372.

504. Colossal enhancement of spin–orbit coupling in weakly hydrogenated graphene / J. Balakrishnan [et al.] // Nature Physics. — 2013. — Vol. 9. — P. 284—287.

505. *Zhang, H.* Equilibrium spin current in graphene with Rashba spin-orbit coupling / H. Zhang, Z. Ma, J.-F. Liu // Scientific Reports. — 2014. — Vol. 4. — P. 6464.

506. Hybridization of graphene and a Ag monolayer supported on Re(0001) / M. Papagno [et al.] // Phys. Rev. B. — 2013. — Vol. 88, issue 23. — P. 235430. — URL: https://link.aps.org/doi/10.1103/PhysRevB.88.235430.

507. Comparison of electronic structure and template function of single-layer graphene and a hexagonal boron nitride nanomesh on Ru(0001) / T. Brugger [et al.] // Phys. Rev. B. — 2009. — Vol. 79, issue 4. — P. 045407. — URL: https://link.aps.org/doi/10.1103/PhysRevB.79.045407.

508. Controlling the Electronic Structure of Bilayer Graphene / T. Ohta [et al.] // Science. — 2006. — Vol. 313, issue 5789. — P. 951—954.

509. Quasiparticle dynamics in graphene / A. Bostwick [et al.] // Nature Physics. — 2007. — Vol. 3. — P. 36—40.

510. Electronic structures of an epitaxial graphene monolayer on SiC(0001) after gold intercalation: a first-principles study / F.-C. Chuang [et al.] // Nanotechnology. — 2011. — Vol. 22. — P. 275704.

511. Electronic structures of an epitaxial graphene monolayer on SiC(0001) after metal intercalation (metal = Al, Ag, Au, Pt, and Pd): A first-principles study / C.-H. Hsu [et al.] // Appl. Phys. Lett. — 2012. — Vol. 100. — P. 063115.

512. Gold intercalation of different 6H-SiC(0001) surface reconstructions / A. A. Gogina [et al.] // Materials Chemistry and Physics. — 2024. — Vol. 323. — P. 129612. — URL: https://www.sciencedirect.com/science/article/pii/S0254058424007375.

513. Critical role of orbital hybridization in the Dzyaloshinskii-Moriya interaction of magnetic interfaces / L. Zhu [et al.] // Communications Physics. — 2022. — June. — Vol. 5, no. 1. — P. 151. — URL: https://doi.org/10.1038/s42005-022-00932-0.

514. *Dedkov*, *Yu. S.* Electronic and magnetic properties of the graphene–ferromagnet interface / Yu. S. Dedkov, M. Fonin // New J. Phys. — 2010. — Vol. 12. — P. 125004.

515. Highly spin-polarized Dirac fermions at the graphene/Co interface / D. Marchenko [et al.] // Phys. Rev. B. — 2015. — June. — Vol. 91, issue 23. — P. 235431. — URL: http://link.aps.org/doi/10.1103/PhysRevB.91.235431.

516. *Yazyev*, *O. V.* Defect-induced magnetism in graphene / O. V. Yazyev, L. Helm // Phys. Rev. B. — 2007. — Mar. — Vol. 75, issue 12. — P. 125408. — URL: http://link.aps.org/doi/10.1103/PhysRevB.75.125408.

517. *Červenka*, *J.* Room-temperature ferromagnetism in graphite driven by two-dimensional networks of point defects / J. Červenka, M. Katsnelson, C. Flipse // Nat. Phys. — 2009. — Vol. 5, no. 11. — P. 840–844.

518. Missing Atom as a Source of Carbon Magnetism / M. M. Ugeda [et al.] // Phys. Rev. Lett. — 2010. — Mar. — Vol. 104, issue 9. — P. 096804. — URL: http://link.aps.org/doi/10.1103/PhysRevLett.104.096804.

519. Spin-half paramagnetism in graphene induced by point defects / R. Nair [et al.] // Nat. Phys. — 2012. — Vol. 8, no. 3. — P. 199–202.

520. *Boukhvalov*, *D. W.* Hydrogen on graphene: Electronic structure, total energy, structural distortions and magnetism from first-principles calculations / D. W. Boukhvalov, M. I. Katsnelson, A. I. Lichtenstein // Phys. Rev. B. — 2008. — Jan. — Vol. 77, issue 3. — P. 035427. — URL: http://link.aps.org/doi/10.1103/PhysRevB.77.035427.

521. Evidence for Spin-Flip Scattering and Local Moments in Dilute Fluorinated Graphene / X. Hong [et al.] // Phys. Rev. Lett. — 2012. — June. — Vol. 108, issue 22. — P. 226602. — URL: http://link.aps.org/doi/10.1103/PhysRevLett.108.226602.

522. Interface-Induced Room-Temperature Ferromagnetism in Hydrogenated Epitaxial Graphene / A. J. M. Giesbers [et al.] // Phys. Rev. Lett. — 2013. — Oct. — Vol. 111, issue 16. — P. 166101. — URL: http://link.aps.org/doi/10.1103/PhysRevLett.111.166101.

523. Effect of noble-metal contacts on doping and band gap of graphene / A. Varykhalov [et al.] // Phys. Rev. B. — 2010. — Vol. 82. — 121101(R).

524. Symmetry breaking in few layer graphene films / A. Bostwick [et al.] // New J. Phys. — 2007. — Vol. 9, no. 10. — P. 385. — URL: http://stacks.iop.org/1367-2630/9/i=10/a=385.

525. M. Mucha-Kruczyński [et al.] // Phys. Rev. B. — 2008. — Vol. 77. — P. 195403.

526. *Kaya*, *S.* On the magnetization of single crystals of cobalt / S. Kaya // Sci. Rep. Tohoku Imp. Univ. — 1928. — Vol. 17. — P. 1157.

527. Spin-polarized low-energy electron microscopy study of the magnetic microstructure of ultra-thin epitaxial cobalt films on W(110) / H. Pinkvos [et al.] // Ultramicroscopy. — 1992. — Vol. 47, no. 4. — P. 339—345. — URL: http://www.sciencedirect.com/science/article/pii/030439919290163E.

528. Spin resolved photoemission study of Co(0001) films / M. Getzlaff [et al.] // J. Magn. Magn. Mat. — 1996. — Vol. 161. — P. 70—88.

529. Spin-polarized photoemission at interfaces of noble metals with Co and Fe / D. Hartmann [et al.] // J. Magn. Magn. Mat. — 1993. — Vol. 121. — P. 160—162.

530. *Besenbacher*, *F.* Scanning tunnelling microscopy studies of metal surfaces / F. Besenbacher // Rep. Prog. Phys. — 1996. — Vol. 59. — P. 1737—1802.

531. *Mamy*, *R.* Growth of Co on Au(lll): a photoemission study / R. Mamy // Surf. Sci. — 1995. — Vol. 322. — P. 337—341.

532. Structural and electronic characterization of Co nanostructures on Au(332) / M. J. Prieto [et al.] // Surf. Sci. — 2013. — Vol. 617. — P. 87—93.

533. *Monserrat, B.* Phonon-assisted spin splitting in centrosymmetric crystals / B. Monserrat, D. Vanderbilt // arXiv:1711.06274v1. —. — URL: https://arxiv.org/abs/1711.06274v1.

534. *Nielsen, L. P.* The Nucleation and Growth of Au on Ni(110) and Ni(111): A Scanning Tunneling Microscopy Study : PhD thesis / Nielsen Lars Pleth. — University of Aarhus, 1995. — URL: https://phys.au.dk/fileadmin/site_files/publikationer/phd/Lars_Pleth_Nielsen.pdf.

535. Atomic-Scale Determination of Misfit Dislocation Loops at Metal-Metal Interfaces / J. Jacobsen [et al.] // Phys. Rev. Lett. — 1995. — July. — Vol. 75, issue 3. — P. 489—492. — URL: https://link.aps.org/doi/10.1103/PhysRevLett.75.489.

536. Spin structure of spin-orbit split surface states in a magnetic material revealed by spin-integrated photoemission / D. Yu. Usachov [et al.] // Phys. Rev. B. — 2020. — June. — Vol. 101, issue 24. — P. 245140. — URL: https://link.aps.org/doi/10.1103/PhysRevB.101.245140.

537. *Nielsen, L. P.* The Nucleation and Growth of Au on Ni(110) and Ni(111): A Scanning Tunneling Microscopy Study : PhD thesis / Nielsen Lars Pleth. — University of Aarhus, 1995. — URL: https://phys.au.dk/fileadmin/site_files/publikationer/phd/Lars_Pleth_Nielsen.pdf.

538. Modification of Shockley states induced by surface reconstruction in epitaxial Ag films on Cu(111) / A. Bendounan [et al.] // Phys. Rev. B. — 2003. — Apr. — Vol. 67, issue 16. — P. 165412. — URL: https://link.aps.org/doi/10.1103/PhysRevB.67.165412.

539. Direct Detection of Circularly Polarized Light Using Chiral Copper Chloride–Carbon Nanotube Heterostructures / J. Hao [et al.] // ACS Nano. — 2021. — Apr. — Vol. 15, no. 4. — P. 7608—7617. — URL: https://doi.org/10.1021/acsnano.1c01134.

540. Direct Detection of Near-Infrared Circularly Polarized Light via Precisely Designed Chiral Perovskite Heterostructures / X. Zhang [et al.] // ACS Applied Materials & Interfaces. — 2022. — Aug. — Vol. 14, no. 32. — P. 36781—36788. — URL: https://doi.org/10.1021/acsami.2c07208.

541. Detectors of circularly polarized radiation based on semiconductor heterostructures with a Schottky barrier CoPt / A. V. Kudrin [et al.] // FTT. — 2018. — Vol. 60, no. 11. — P. 2236. — URL: https://journals.ioffe.ru/articles/viewPDF/46669.

542. Far-infrared detection using Weyl semimetals : patent WO2018/017976 A1 : Int .Cl. H01L 31/18, H01L 31/0224 / C.-K. Chan [et al.] ; MIT, TRDF, CIT. — No. PCT/US2017/043329 ; req. 07/21/2017 ; publ. 01/25/2018, priority 07/21/2016. — 24 p. : il.

543. Method for determining the sign of circular polarization of laser radiation : patent RU2452924 C1 : Int .Cl. G01J 4/04 / G. M. Mikheev, V. A. Aleksandrov, A. S. Saushin ; G. M. Mikheev, V. A. Aleksandrov. — No. 2010153472/28 ; req. 12/27/2010 ; publ. 06/10/2012, bul. No. 16 (Russian Federation). — 10 p. : il.

544. Graphene photonics and optoelectronics / F. Bonaccorso [et al.] // Nature Photonics. — 2010. — Sept. — Vol. 4, no. 9. — P. 611—622. — URL: https://doi.org/10.1038/nphoton.2010.186.

545. *Tredicucci, A.* Device Concepts for Graphene-Based Terahertz Photonics / A. Tredicucci, M. S. Vitiello // IEEE Journal of Selected Topics in Quantum Electronics. — 2014. — Vol. 20. — P. 130—138. — URL: https://api.semanticscholar.org/CorpusID:24679073.

546. Systems and methods for graphene photodetectors : patent WO2014089454A3 : Int .Cl. H01L29/15 / D. Englung, R.-J. Shiue, X. Gan ; T. T. O. C. U. I. T. C. O. N. York. — No. PCT/US2013/073613 ; req. 12/06/2013 ; publ. 06/12/2014, priority 12/07/2012. — 2 p. : il.

547. Mid-Infrared Optoelectronic Devices Based on Two-Dimensional Materials beyond Graphene: Status and Trends / R. Cao [et al.] // Nanomaterials. — 2022. — Vol. 12, no. 13. — P. 2260. — URL: https://www.mdpi.com/2079-4991/12/13/2260.

548. Ubiquitous Spin-Orbit Coupling in a Screw Dislocation with High Spin Coherency / L. Hu [et al.] // Phys. Rev. Lett. — 2018. — Aug. — Vol. 121, issue 6. — P. 066401. — URL: https://link.aps.org/doi/10.1103/PhysRevLett.121.066401.

549. Topological nature of step-edge states on the surface of the topological crystalline insulator $Pb_{0.7}Sn_{0.3}Se$ / D. Iaia [et al.] // Phys. Rev. B. — 2019. — Apr. — Vol. 99, issue 15. — P. 155116. — URL: https://link.aps.org/doi/10.1103/PhysRevB.99.155116.

550. *Ran, Y.* One-dimensional topologically protected modes in topological insulators with lattice dislocations / Y. Ran, Y. Zhang, A. Vishwanath // Nature Physics. — 2009. — Vol. 5, no. 4. — P. 298—303. — URL: https://doi.org/10.1038/nphys1220.

551. Topological states on the gold surface / B. Yan [et al.] // Nature Communications. — 2015. — Vol. 6, no. 1. — P. 10167. — URL: https://doi.org/10.1038/ncomms10167.

552. Distinct multiple fermionic states in a single topological metal / M. M. Hosen [et al.] // Nature Communications. — 2018. — Aug. — Vol. 9, no. 1. — P. 3002. — URL: https://doi.org/10.1038/s41467-018-05233-1.

553. Quantum-Size Effects in Ultra-Thin Gold Films on Pt(111) Surface / Y. M. Koroteev [et al.] // Materials. — 2024. — Vol. 17, no. 1. — P. 63. — URL: https://www.mdpi.com/1996-1944/17/1/63.

554. *Momma, K.* VESTA3 for three-dimensional visualization of crystal, volumetric and morphology data / K. Momma, F. Izumi // J. Appl. Crystallogr. — 2011. — Dec. — Vol. 44, no. 6. — P. 1272—1276. — URL: https://doi.org/10.1107/S0021889811038970.

555. Structure and magnetism of hcp(0001) and fcc(001) thin cobalt films on a clean and carbon-reconstructed W(110) surface / A. Bettac [et al.] // Surface Science. — 2000. — Vol. 454—456. — P. 936—941. — URL: https://www.sciencedirect.com/science/article/pii/S0039602800001849.

556. Superconductivity of Cobalt in Thin Films / N. Banu [et al.] // arXiv: Superconductivity. — 2017. — URL: https://api.semanticscholar.org/CorpusID:119098787.

557. *Nguyen, D.-L.* Theoretical prediction of superconductivity in monolayer CoO_2 / D.-L. Nguyen, C.-R. Hsing, C.-M. Wei // Nanoscale. — 2019. — Vol. 11, issue 36. — P. 17052—17057. — URL: http://dx.doi.org/10.1039/C9NR03954F.

558. Signature of Superconductivity in Orthorhombic CoSb Monolayer Films on $SrTiO_3$(001) / C. Ding [et al.] // ACS Nano. — 2019. — Sept. — Vol. 13, no. 9. — P. 10434—10439. — URL: https://doi.org/10.1021/acsnano.9b04223.

559. Enhanced Superconductivity and Rashba Effect in a Buckled Plumbene-Au Kagome Superstructure / W.-H. Chen [et al.] // Advanced Science. — 2023. — Vol. 10, no. 17. — P. 2300845. — URL: https://onlinelibrary.wiley.com/doi/abs/10.1002/advs.202300845.

560. Superconductivity in the Surface State of Noble Metal Gold and its Fermi Level Tuning by EuS Dielectric / P. Wei [et al.] // Phys. Rev. Lett. — 2019. — June. — Vol. 122, issue 24. — P. 247002. — URL: https://link.aps.org/doi/10.1103/PhysRevLett.122.247002.

Author's list of publications on the dissertation subject

1. Large spin-orbit splitting in light quantum films: Al/W(110) / A. G. Rybkin, A. M. Shikin, V. K. Adamchuk, D. Marchenko, C. Biswas, A. Varykhalov, O. Rader // Phys. Rev. B. — 2010. — Vol. 82, issue 23. — P. 233403. — URL: https://link.aps.org/doi/10.1103/PhysRevB.82.233403.

2. Spin-dependent avoided-crossing effect on quantum-well states in Al/W(110) / A. G. Rybkin, A. M. Shikin, D. Marchenko, A. Varykhalov, O. Rader // Phys. Rev. B. — 2012. — Vol. 85, issue 4. — P. 045425. — URL: https://link.aps.org/doi/10.1103/PhysRevB.85.045425.

3. Topology of spin polarization of the $5d$ states on W(110) and Al/W(110) surfaces / A. G. Rybkin, E. E. Krasovskii, D. Marchenko, E. V. Chulkov, A. Varykhalov, O. Rader, A. M. Shikin // Phys. Rev. B. — 2012. — Vol. 86, issue 3. — P. 035117. — URL: https://link.aps.org/doi/10.1103/PhysRevB.86.035117.

4. Magneto-Spin–Orbit Graphene: Interplay between Exchange and Spin–Orbit Couplings / A. G. Rybkin, A. A. Rybkina, M. M. Otrokov, O. Yu. Vilkov, I. I. Klimovskikh, A. E. Petukhov, M. V. Filianina, V. Yu. Voroshnin, I. P. Rusinov, A. Ernst, A. Arnau, E. V. Chulkov, A. M. Shikin // Nano Letters. — 2018. — Vol. 18, no. 3. — P. 1564—1574. — URL: https://doi.org/10.1021/acs.nanolett.7b01548 ; PMID: 29365269.

5. A new approach for synthesis of epitaxial nano-thin Pt_5Gd alloy via intercalation underneath a graphene / A. G. Rybkin, A. A. Rybkina, A. V. Tarasov, D. A. Pudikov, I. I. Klimovskikh, O. Yu. Vilkov, A. E. Petukhov, D. Yu. Usachov, D. A. Estyunin, V. Yu. Voroshnin, A. Varykhalov, G. Di Santo, L. Petaccia, E. F. Schwier, K. Shimada, A. Kimura, A. M. Shikin // Applied Surface Science. — 2020. — Vol. 526. — P. 146687. — URL: https://www.sciencedirect.com/science/article/pii/S0169433220314446.

6. Sublattice Ferrimagnetism in Quasifreestanding Graphene / A. G. Rybkin, A. V. Tarasov, A. A. Rybkina, D. Yu. Usachov, A. E. Petukhov, A. V. Eryzhenkov, D. A. Pudikov, A. A. Gogina, I. I. Klimovskikh, G. Di Santo, L. Petaccia, A. Varykhalov, A. M. Shikin // Phys. Rev. Lett. —

2022. — Vol. 129, issue 22. — P. 226401. — URL: https://link.aps.org/doi/10.1103/PhysRevLett.129.226401.

7. Robust ferrimagnetism in quasi-freestanding graphene / A. G. Rybkin, A. V. Tarasov, A. A. Gogina, A. V. Eryzhenkov, A. A. Rybkina // Pis'ma v ZHETF. — 2023. — Vol. 117, issue 8. — P. 626. — URL: http://jetpletters.ru/ps/2418/article_35652.shtml.

8. Quasi-freestanding graphene on SiC(0001) via cobalt intercalation of zero-layer graphene / A. A. Rybkina, S. O. Filnov, A. V. Tarasov, D. V. Danilov, M. V. Likholetova, V. Yu. Voroshnin, D. A. Pudikov, D. A. Glazkova, A. V. Eryzhenkov, I. A. Eliseyev, V. Yu. Davydov, A. M. Shikin, A. G. Rybkin // Phys. Rev. B. — 2021. — Vol. 104, issue 15. — P. 155423. — URL: https://link.aps.org/doi/10.1103/PhysRevB.104.155423.

9. Effect of gold intercalation on the electronic structure of graphene on Co-Si/SiC(0001) / A. A. Rybkina, S. O. Filnov, D. A. Glazkova, O. Yu. Vilkov, K. A. Bokai, D. A. Pudikov, A. M. Shikin, A. G. Rybkin // FTT (in Russian). — 2022. — Vol. 64, no. 8. — P. 1122. — URL: https://journals.ioffe.ru/articles/viewPDF/52716.

10. Origin of Giant Rashba Effect in Graphene on Pt/SiC / A. A. Rybkina, A. A. Gogina, A. V. Tarasov, Y. Xin, V. Yu. Voroshnin, D. A. Pudikov, I. I. Klimovskikh, A. E. Petukhov, K. A. Bokai, C. Yuan, Z. Zhou, A. M. Shikin, A. G. Rybkin // Symmetry. — 2023. — Vol. 15, no. 11. — P. 2052. — URL: https://www.mdpi.com/2073-8994/15/11/2052.

11. Magnetic effects in the electronic structure of new quantum materials / A. M. Shikin, A. A. Rybkina, D. A. Estunin, D. A. Glazkova, A. V. Tarasov, D. Y. Usachov, A. G. Rybkin // Quantum structures for post-silicon electronics / ed. by A. V. Latyshev. — Novosibirsk, Parallel' : Minobrnauki Rossii; Institut fiziki poluprovodnikov im. A. V. Rzhanova SO RAN, 2023. — P. 111—128. — URL: https://www.isp.nsc.ru/nauka/izdaniya/kvantovye-struktury-dlya-postkremnievoj-elektroniki.

12. Giant Rashba splitting in graphene due to hybridization with gold / D. Marchenko, A. Varykhalov, M. R. Scholz, G. Bihlmayer, E. I. Rashba, A. Rybkin, A. M. Shikin, O. Rader // Nature Communications. — 2012. — Vol. 3, no. 1. — P. 1232. — URL: https://doi.org/10.1038/ncomms2227.

13. The graphene/Au/Ni interface and its application in the construction of a graphene spin filter / A. A. Rybkina, A. G. Rybkin, V. K. Adamchuk, D. Marchenko, A. Varykhalov, J. Sánchez-Barriga, A. M. Shikin // Nanotechnology. — 2013. — Vol. 24, no. 29. — P. 295201. — URL: https://doi.org/10.1088/0957-4484/24/29/295201.

14. Induced spin–orbit splitting in graphene: the role of atomic number of the intercalated metal and π–d hybridization / A. M. Shikin, A. G. Rybkin, D. Marchenko, A. A. Rybkina, M. R. Scholz, O. Rader, A. Varykhalov // New Journal of Physics. — 2013. — Vol. 15, no. 1. — P. 013016. — URL: https://doi.org/10.1088/1367-2630/15/1/013016.

15. Nontrivial spin structure of graphene on Pt(111) at the Fermi level due to spin-dependent hybridization / I. I. Klimovskikh, S. S. Tsirkin, A. G. Rybkin, A. A. Rybkina, M. V. Filianina, E. V. Zhizhin, E. V. Chulkov, A. M. Shikin // Phys. Rev. B. — 2014. — Vol. 90, issue 23. — P. 235431. — URL: https://link.aps.org/doi/10.1103/PhysRevB.90.235431.

16. Observation of Single-Spin Dirac Fermions at the Graphene/Ferromagnet Interface / D. Usachov, A. Fedorov, M. M. Otrokov, A. Chikina, O. Vilkov, A. Petukhov, A. G. Rybkin, Y. M. Koroteev, E. V. Chulkov, V. K. Adamchuk, A. Grüneis, C. Laubschat, D. V. Vyalikh // Nano Letters. — 2015. — Vol. 15, no. 4. — P. 2396—2401. — URL: https://doi.org/10.1021/nl504693u ; PMID: 25734657.

17. Gigantic 2D laser-induced photovoltaic effect in magnetically doped topological insulators for surface zero-bias spin-polarized current generation / A. M. Shikin, V. Yu. Voroshin, A. G. Rybkin, K. A. Kokh, O. E. Tereshchenko, Y. Ishida, A. Kimura // 2D Materials. — 2018. — Vol. 5, no. 1. — P. 015015. — URL: https://doi.org/10.1088/2053-1583/aa928a.

18. Advanced graphene recording device for spin–orbit torque magnetoresistive random access memory / A. A. Rybkina, A. G. Rybkin, I. I. Klimovskikh, P. N. Skirdkov, K. A. Zvezdin, A. K. Zvezdin, A. M. Shikin // Nanotechnology. — 2020. — Vol. 31, no. 16. — P. 165201. — URL: https://doi.org/10.1088/1361-6528/ab6470.

19. Non-monotonic variation of the Kramers point band gap with increasing magnetic doping in BiTeI / A. M. Shikin, A. A. Rybkina, D. A. Estyunin, I. I. Klimovskikh, A. G. Rybkin, S. O. Filnov, A. V. Koroleva, E. V. Shevchenko, M. V. Likholetova, V. Yu. Voroshnin, A. E. Petukhov, K. A. Kokh, O. E. Tereshchenko, L. Petaccia, G. Di Santo, S. Kumar, A. Kimura, P. N. Skirdkov, K. A. Zvezdin, A. K. Zvezdin // Scientific Reports. — 2021. — Vol. 11, no. 1. — P. 23332. — URL: https://doi.org/10.1038/s41598-021-02493-8.

20. Graphene spin filter : patent RU 2585404 C1 : Int. Cl. G01R 33/05 / A. M. Shikin, A. A. Rybkina, A. G. Rybkin, A. B. Tsyganov, V. K. Adamchuk ; applicant federalnoe gosudarstvennoe byudzhetnoe obrazovatelnoe uchrezhdenie vysshego obrazovaniya "Sankt-Peterburgskij gosudarstvennyj universitet" (SPbGU) ; patent attorney A. A. Matveev. — No. 2015113131/28 ; req. 04/09/2015 ; publ. 05/27/2016, bul. no. 15. — 11 p. : il.

21. Device for recording of information for magnetoresistive RAM : patent RU 2677564 C1 : Int. Cl. G11C 11/16 / A. M. Shikin, A. A. Rybkina, A. G. Rybkin, I. I. Klimovskikh, P. N. Skirdkov ; applicant federalnoe gosudarstvennoe byudzhetnoe obrazovatelnoe uchrezhdenie vysshego obrazovaniya "Sankt-Peterburgskij gosudarstvennyj universitet" (SPbGU) ; patent attorney A. A. Matveev. — No. 2017138165 ; req. 11/01/2017 ; publ. 01/17/2019, bul. no. 2. — 16 p. : il.

22. Infrared detector of circularly polarized radiation based on graphene : patent RU 2805784 C1 : Int. Cl. G01J 4/04 / A. G. Rybkin, A. A. Rybkina, A. V. Tarasov, A. V. Eryzhenkov, A. M. Shikin ; applicant federalnoe gosudarstvennoe byudzhetnoe obrazovatelnoe uchrezhdenie vysshego obrazovaniya "Sankt-Peterburgskij gosudarstvennyj universitet" (SPbGU) ; patent attorneys A. A. Matveev, T. I. Matveeva, I. F. Leonov. — No. 2023109819 ; req. 04/17/2023 ; publ. 10/24/2023, bul. no. 30. — 11 p. : il.

23. Program for recording photoelectron spectra (XPS spectra) : certificate of state registration of the computer program 2020610365 / A. G. Rybkin, D. Y. Usachev, E. V. Zhizhin, D. A. Pudikov ; applicant federalnoe gosudarstvennoe byudzhetnoe obrazovatelnoe uchrezhdenie vysshego obra-

zovaniya "Sankt-Peterburgskij gosudarstvennyj universitet" (SPbGU). — No. 2019666984 ; req. 12/19/2019 ; publ. 01/13/2020.